# Lattice Discretization Effects on the QCD Phase Structure at Zero Chemical Potential and the Roberge-Weiss Endpoint

Dissertation
zur Erlangung des Doktorgrades
der Naturwissenschaften

vorgelegt beim Fachbereich Physik
der Johann Wolfgang Goethe-Universität
in Frankfurt am Main

von
Christopher Czaban
aus Hanau

Frankfurt am Main 2018
D30

vom Fachbereich Physik der
Johann Wolfgang Goethe-Universität als Dissertation angenommen.

Dekan: Prof. Dr. O. Philipsen

Gutachter: Prof. Dr. O. Philipsen
Prof. Dr. M. Wagner

Datum der Disputation:

# Contents

# Abstract

*Quantum chromodynamics* is the theory of the strong interaction between quarks and gluons. Due to *Confinement*, at lower energies quarks and gluons are bound into colorless states called *hadrons*. QCD is also *asymptotically free*, i.e. at large energies or densities it enters a deconfined state, termed *quark-gluon plasma (QGP)*, where quarks and gluons are quasi-free. This transition occurs at an energy scale around 200 MeV where QCD cannot be treated perturbatively. Instead it can be formulated on a space-time grid. The resulting theory, *lattice quantum chromodynamics (LQCD)*, can be simulated efficiently on high performance parallel-computing clusters. In recent years *graphic processing units (GPUs)*, which outperform CPUs in terms of parallel-computing and memory bandwidth capabilities, became very popular for LQCD computations. In this work the QCD deconfinement transition is studied using CL$^2$QCD, a LQCD application that runs efficiently on GPUs. Furthermore, CL$^2$QCD is extended by a Rational Hybrid Monte Carlo algorithm for Wilson fermions to allow for simulations of an odd number of flavors $N_f$.

Due to the *sign-problem* LQCD simulations are restricted to zero or very small baryon densities, where, in the limit of infinite quark mass QCD has a first order deconfinement phase transition associated to the breaking of the global centre symmetry. Including dynamical quarks breaks this symmetry explicitly. Lowering their mass weakens the first order transition until it terminates in a second order $Z_2$ point. Beyond this point the transition is merely an analytic crossover. As the lattice spacing is decreased, the reduction of discretization errors causes the region of first order transitions to expand towards lower masses. In this work the deconfinement critical point with $N_f = 2$ and 3 flavors of standard Wilson fermions is studied. To this end several kappa values are simulated on $N_\tau = 6, 8, 10$ ($N_\tau = 4$) for $N_f = 2$ ($N_f = 3$) and various aspect ratios $N_\mathrm{s}/N_\tau$ so as to extrapolate to the thermodynamic limit, applying finite size scaling . For $N_f = 2$ an estimate is done if and when a continuum extrapolation is possible.

The chiral and deconfinement phase transitions at zero density for light and heavy quarks, respectively, have analytic continuations to purely imaginary chemical potential $\mu_i$, where no sign-problem exists and LQCD simulations can be applied. At some critical value $\mu_{i,c}$, the transitions meet the endpoint of the *Roberge-Weiss* transition between adjacent $Z_3$ sectors. For light and heavy quarks the transition lines meet in a triple point, while for intermediate masses they meet in a second order point. At the boundary between these regimes the junction is a tricritical point, as shown in studies with $N_f = 2, 3$ flavors of staggered and Wilson quarks on $N_\tau = 4$ lattices. Employing finite size scaling the nature of this point as a function of the quark mass is studied in this work for $N_f = 2$ flavors of Wilson fermions with a temporal lattice extent of $N_\tau = 6$. Of particular interest is the change of the location of tricritical points compared to an earlier study on $N_\tau = 4$.

# Deutsche Zusammenfassung

Das Standard Modell der Teilchenphysik repräsentiert den heutigen Wissensstand über die Theorien zur Beschreibung von drei der vier fundamentalen Wechselwirkungen der Natur, durch welche sich physikalische Objekte (z.B. Felder, Teilchen oder Systeme von Teilchen) gegenseitig beeinflussen. Die durch das Standardmodell beschriebenen Wechselwirkungen sind die elektromagnetische, die schwache und die starke Wechselwirkung. Eine Beschreibung der vergleichsweise schwachen Gravitation, wie sie durch die allgemeine Relativitätstheorie gegeben ist, konnte bisher durch keine Theorie in das Standardmodell integriert werden. Das Standardmodell basiert auf Quantenfeldtheorien, deren fundamentale Objekte Quantenfelder sind, welche in diskreten Schritten angeregt werden können. Diese Anregungen repräsentieren, unter Verwendung der entsprechenden Darstellung, die elementaren Teichen. Die enthaltenen Quantenfeldtheorien sowie die von ihnen beschriebenen Teilchen respektieren die Gesetze der speziellen Relativitätstheorie. Einen hohen Grad an Akzeptanz erlangte das Standardmodell, als es 1970 möglich wurde, die Existenz der sogenannten *Quarks* experimentell nachzuweisen. Bei diesen handelt es sich um die fundamentalen Bausteine der Materie, welche neben der elektrischen Ladung auch eine sogenannte *Farbladung* tragen und mittels der starken Wechselwirkung miteinander wechselwirken. Diese wird durch die im Standardmodell enthaltene Quantenfeldtheorie namens *Quantenchromodynamik (QCD)* beschrieben, welche auch Gegenstand dieser Arbeit ist. Die Austauschteilchen der starken Wechselwirkung sind die sogenannten *Gluonen*, welche ebenfalls eine Farbladung tragen. Die Besonderheit der Gluonen liegt darin, dass sie aufgrund der nicht abelschen Natur der Eichgruppe der QCD nicht nur die starke Kraft zwischen den Quarks vermitteln, sondern auch mit sich selbst wechselwirken. Diese Selbstwechselwirkung steht im Zusammenhang mit einer besonderen, als *color confinement* bezeichneten Eigenschaft der QCD und führt auf nicht-triviale Weise dazu, dass die anziehende Kraft zwischen zwei Quarks mit steigender Separation zunimmt. Ab einer gewissen Distanz, wird es für das System energetisch gesehen günstiger, ein neues Quark-Antiquark Paar aus der in dem gluonischen Bindungsfeld befindlichen Energie zu erzeugen. Dies hat zur Folge, das Quarks und Gluonen bei niedrigen Energien stets in gebundene Zustände, sogenannten *Hadronen*, konfiniert sind und somit nicht als freie Teilchen beobachtet werden können. Desweiteren müssen gebundene Zustände aus Quarks stets in farbneutralen Zuständen auftreten. Andererseits besitzt die QCD eine weitere besondere Eigenschaft, die als *asymptotische Freiheit* bezeichnet wird und zur Folge hat, dass die anziehende Kraft nachlässt, sobald der Abstand der wechselwirkenden Quarks klein wird und beziehungsweise oder deren Impulse groß sind. Die Stärke der Wechselwirkung zwischen den Quarks lässt sich über eine laufenden Kopplung quantifizieren, die bei Energien, welche etwa der intrinsischen Energieskala der QCD ($\Lambda_{\mathrm{QCD}} = 200\mathrm{MeV}$) entsprechen, maximal, d.h. $\mathcal{O}(1)$ wird. Die dazu korrespondierende Längenskala liegt im Femtometerbereich.

Aufgrund der starken Kopplung, ist die QCD in diesem Energiebereich nicht perturbativ, d.h. nicht störungstheoretisch, behandelbar. Die derzeit effizienteste Methode in diesem Energiebereich (im Vakuum)

stellt die numerische Untersuchung der QCD im Rahmen von Gittereichtheorien dar, indem die kontinuierliche Raum-Zeit durch ein endliches Gitter diskretisiert wird, dessen Punkte durch einen endlichen Abstand $a$ separiert sind. Auf diese Weise konnten bereits Berechnungen zahlreicher Hadronenmassen durchgeführt werden, die eine extrem genaue Übereinstimmung mit Experimenten liefern. Der dazu verwendete Zugang zur QCD über den auf dem Prinzip der kleinsten Wirkung basierenden Pfadintegralformalismus ist besonders gut zur numerischen Behandlung mittels Computern geeignet, da sich das Pfadintegral der Theorie, nach einer *Wick-Rotation*, d.h. nach analytischer Fortsetzung in den euklidischen Raum, stochastisch durch Monte Carlo Simulationen approximativ lösen lässt. Durch diesen notwendigen Übergang erhält man reelle (statt komplexe) Phasenfaktoren im Pfadintegral, die den Boltzmannfaktoren in der statistischen Physik entsprechen. Um bei endlichen Rechenressourcen eine möglichst genaue Approximation des hochdimensionalen Pfadintegrals gewährleisten zu können, findet die Methode des *importance sampling* Anwendung, bei welcher mittels einer Wahrscheinlichkeitsverteilung größeres Gewicht auf die wahrscheinlicheren Feldkonfigurationen des Phasenraums gelegt wird, also jene, die einen großen Beitrag zum Pfadintegral liefern. Die Wahrscheinlichkeitsverteilung wird dabei durch die Phasen- bzw. Boltzmannfaktoren dargestellt. Diese enthalten die QCD Wirkung, bei welcher zwischen einem reinen, die Bosonen der Theorie beschreibenden Eichanteil und einem fermionischen Anteil unterschieden wird. Diese Unterscheidung ist mit unter durch die chirale Symmetrie der Fermionen motiviert, die bei der Konstruktion von Gitterwirkungen ein eigenes Problemfeld eröffnet.

Für die Konstruktion des fermionischen Anteils der Gitter-QCD Wirkung bestehen verschiedene Möglichkeiten, solange diese für verschwindenden Gitterabstand $a \to 0$ in die Kontinuumswirkung übergehen. Heute gibt es eine Vielzahl an Gitterwirkungen, die auf verschiedene Weise das wohlbekannte *Dopplerproblem* behandeln. Dieses hängt mit der Realisierung der chiralen Symmetrie der Fermionen auf einem Gitter zusammen und tritt bei naiver Diskretisierung der Theorie auf, d.h. wenn die Ableitungen in der Wirkungen einfach durch endliche Differenzen ersetzt werden. In letzterem Fall enthält die Theorie sechzehn statt einem einzelnen Fermion. Insbesondere ist es nicht möglich Gitter-QCD Wirkungen zu konstruieren, die zur gleichen Zeit dopplerfrei, lokal, translationsinvariant und chiral-symmetrisch sind. Dieses Problem ist im *Nielsen-Ninomiya-Theorem* formuliert. Die älteste Form der Diskretisierung sind *Wilson-Fermionen*. Dabei wird das Dopplerproblem gelöst, indem den unphysikalischen Fermionmoden eine zusätzliche Masse verliehen wird, welche im Kontinuumslimes proportional zu $1/a$ divergiert, wodurch sie von der Theorie entkoppeln. Allerdings wird bei diesem Vorgehen die chirale Symmetrie explizit gebrochen. Ein weiterer Nachteil besteht darin, dass Diskretisierungsfehler bereits in führender Ordnung $\mathcal{O}(a)$ auftreten. Aus diesem Grund werden für gewöhnlich verbesserte Wilson Diskretisierungen verwendet, in welchen zusätzliche oder modifizierte Terme die führende Ordnung der Gitteartefakte eliminieren. Beispiele dafür sind *Clover-* oder *Twisted-Mass-Fermionen*. Ein zu beachtender Aspekt ist dabei allerdings, dass durch die zusätzlichen Terme eventuell unphysikalische Modifikationen nicht ausgeschlossen werden können. Eine weitere, aufgrund der im Vergleich zu Wilson-Fermionen sehr viel geringeren numerischen Kosten, sehr häufig verwendete Fermiondiskretisierung sind *Staggered-Fermionen*. Bei diesen wird durch Spin Diagonalisierung der Dirac-Matritzen die Anzahl der Doppler auf vier reduziert. Zur weiteren Reduktion der Fermionenanzahl auf eins findet das kontrovers diskutierte *rooting* Verfahren Anwendung, dessen Auswirkungen auf die Physik noch nicht vollständig verstanden sind. Weitere Möglichkeiten der Diskretisierung sind *Overlap-* oder *Domain-Wall-Fermionen*. Bei diesen wird auf komplizierte Weise eine Variante der chrialen Symmetrie auf dem Gitter erhalten, allerdings

besteht der Nachteil dieser Formulierungen in den hohen numerischen Kosten, aus welchem Grund diese heute noch eher selten Anwendung finden.

Der fermionische Anteil der QCD Wirkung kann aufgrund der Grassmann-Natur der fermionischen Felder exakt ausintegriert werden. Dadurch erhält man die Fermiondeterminante, die wiederum als pseudofermionisches (Bosonen mit der gleichen Anzahl an Freiheitsgraden wie fermionische Variablen) Pfadintegral dargestellt werden kann, welches im Phasenfaktor die inverse Fermionmatrix enthält. Die Wirkung der inversen Fermionmatrix auf die bosonischen Feldvariablen lässt sich effizient mittels Krylov-Unterraum-Verfahren (Beispielsweise Conjugate-Gradient) lösen, da die inverse Fermionmatrix dünnbesetzt ist. Unter anderem macht die Berechnung dieses algebraischen Systems die Gitter-QCD zu einem der aufwändigsten Computerprobleme der heutigen Zeit, welches nur unter Verwendung von Hochleistungs-Rechenclustern effizient behandelt werden kann. Die rechnerischen Kosten steigen dabei umso stärker an, je kleiner die zu berechnende Fermionmasse ist, da die Konditionszahl der in den algebraischen Rechnungen zu verwendenden Fermionmatrix dadurch verschlechtert wird. Ein weiterer Faktor, der die rechnerischen Kosten enorm steigen lässt, ist durch die Anforderungen an ein zu berechnendes System gegeben, welches ausreichend groß sein soll, um endliche Volumeneffekte zu minimieren und sich gleichzeitig dem Kontinuumslimes annähern soll, was durch einen kleinen Gitterabstand $a$ realisiert werden kann. Dies impliziert eine große Menge an zu berechnenden Gitterpunkten. Zu den Problemstellungen dabei gehören die hohen Anforderungen an die benötigten Speicherbandbreiten sowie die effiziente Parallelisierung. Daher erfreuen sich *Graphics Processing Unit (GPU)*-Lösungen zunehmender Beliebtheit, da diese dafür optimiert sind, sehr häufig zu wiederholende Operationen auf enorme Datenmengen anzuwenden. Diese Fähigkeit, in welcher CPUs leistungsmäßig bei weitem von GPUs übertroffen werden, ist von großer Wichtigkeit für Gitter-QCD Anwendungen, da in diesen das Gitter auf natürliche Weise auf die Einheiten innerhalb einer GPU aufgeteilt werden kann. Dazu kommt, dass GPUs beim Erfüllen dieser Aufgabe wesentlich strom- und kosteneffizienter sind als CPUs. Zu den bekanntesten Herstellern von GPUs gehören NVIDIA und AMD. NVIDIA veröffentlichte zur Steuerung und Programmierung der GPUs einen eigenen, vergleichsweise einfach zu verwendenden Standard namens *CUDA*, auf dem gegenwärtig viele Gitter-QCD Anwendungen basieren, welcher jedoch ausschließlich der Programmierung von NVIDIA GPUs dient. Ein anderes, hardwareunabhängiges framework, welches im Allgemeinen die Programmierung von heterogenen Computerarchitekturen erlaubt, ist der in Zusammenarbeit von AMD, IBM, Intel, NVIDIA und Apple entworfene Standard *OpenCL (Open Computing Language)*.

Für die für diese Arbeit durchgeführten Gitter-QCD Simulationen wurde die von der Gitter-QCD Gruppe in Frankfurt entwickelte Software CL$^2$QCD verwendet. Diese besteht aus einem C++ Hostprogramm, welches für die algorithmische Logik sowie Lese- und Schreiboperationen der Daten zuständig ist. Darüber hinaus kontrolliert das Hostprogramm die Gitter-QCD Funktionen, welche in OpenCL geschrieben wurden und sowohl auf GPUs als auch auf CPUs ausgeführt werden können. Aufgrund der Verwendung von OpenCL ist die Applikation hardwareunabhängig, d.h. sie kann sowohl auf AMD als auch auf NVIDIA Grafikkarten betrieben werden. Die Anwendung ist auf Problemstellungen bei endlicher Temperatur ausgelegt und verfügt über die Möglichkeit unverbesserte sowie verbesserte Wilson-Fermionen, aber auch reine Eichtheorie, zu simulieren. Desweiteren ist kürzlich im Rahmen einer Doktorarbeit in der Frankfurter Gitter-QCD Gruppe der Staggered-Formalismus und im Rahmen der vorliegenden Arbeit die Möglichkeit zur Simulation der drei Quark-Flavor Theorie in der unverbesserten Wilson-Formulierung implementiert worden. Im Allgemeinen wurde beim Design von CL$^2$QCD auf

Eigenschaften der Erweiterungsfähigkeit, Wartungsfreundlichkeit sowie Skalierbarkeit gesetzt, wobei im Zusammenhang damit stark auf die Einhaltung der *Clean Code* Prinzipien geachtet wurde.

Gitter-QCD bei endlichen Temperaturen erfordert in vielen Fällen die größtenteils gleichzeitige Durchführung hunderter Simulationen auf Computing-Clustern, um bei einer Vielzahl variierender Simulationsparameter thermale Phasenübergänge zu lokalisieren. Dies führt bei rein manuellem Vorgehen unweigerlich zu einer großen Fehleranfälligkeit. Aus diesem Grund wurde zur effizienten und fehlerfreien Bewältigung der Menge an Simulationen während dieser Arbeit in der Entwicklung einer auf der Unix-Shell *Bash* basierende Software partizipiert. Diese bietet neben der Organisation und Strukturierung der erzeugten Daten sowie fehlerfreien Durchführung, Verwaltung und Überwachung der Simulationen auch die Möglichkeit entsprechende Informationen über letztere in einer Datenbank zu speichern und diese zusammengefasst auszugeben. Diese als *BaHaMas* bezeichnete Software wurde bereits im Rahmen eines Vortrags eines Gruppenmitglieds auf einer Konferenz präsentiert und wird künftig neben CL$^2$QCD auf der Entwicklungsplattform GitHub frei zur Verfügung stehen.

Die oben beschriebene Eigenschaft der asymptotischen Freiheit impliziert bei extrem großen Temperaturen ($\approx 10^{12}$)K und beziehungsweise oder Dichten ($\approx 10^{15}\mathrm{g/cm}^3$) einen Übergang in eine Phase, die als Quark-Gluon Plasma (QGP) bezeichnet wird. Diese Phase ist durch das Aufbrechen der Bindungen zwischen Quarks und Gluonen charakterisiert, sodass diese nicht mehr in hadronischen Zuständen konfiniert sind, sondern als quasi-freie Teilchen vorliegen. Die für den thermischen Übergang in diese Phase notwendigen Temperaturen waren kurz nach der Entstehung des Universums vorhanden oder entstehen auf mikroskopischem Raum während Schwerionen-Kollisionen, wie sie beispielsweise in aktuellen Beschleuniger-Experimenten des *Large Hadron Colliders (LHC)* am Forschungsinstitut *CERN*, der Europäischen Organisation für Kernforschung, durchgeführt werden. Der Übergang zum Quark-Gluon Plasma über extrem hohe Dichten wird in der Natur im Inneren von Neutronensternen vermutet. Darüber hinaus, werden bei noch größeren Dichten Übergänge in verschiedene, farbsupraleitende Phasen erwartet, welche durch die Bildung von Quark-Cooperpaaren entstehen. Bei bestimmten Temperaturen und Dichten wird durch theoretische Argumentation sowie Modellbetrachtungen ein Phasenübergang erster Ordnung vermutet, was zur Zeit aufgrund oben genannter Probleme allerdings noch nicht belegt werden kann. Dieser Phasenübergang erster Ordnung würde irgendwann bei kleineren Dichten und höheren Temperaturen in einem Phasenübergangspunkt zweiter Ordnung der $Z_2$ Universalitätsklasse enden. Nach diesem Endpunkt wäre der Übergang analytischer Natur, d.h. nicht sprunghaft in den thermodynamischen Ordnungsparametern oder deren Ableitungen. Ein solcher Übergang wird auch als *crossover* bezeichnet. Klarheit über diesen Verlauf zu schaffen, ist gegenwärtig von sehr großem Interesse und ist Ziel aufwändiger experimenteller sowie theoretischer Untersuchungen. Gegenwärtig und künftig durchgeführte Beschleuiniger-Experimente decken dafür ein großes Spektrum an Strahlenergien und Werten des chemischen Potentials ab. Zu diesen Experimenten gehören jene, die am LHC (enorm große Energie bei kleineren Dichten), an der *Facility for Antiproton and Ion Research (FAIR)* (moderate Energien bei höheren Dichten) bei der *Gesellschaft für Schwerionenforschung (GSI)* und am *Relativistic Heavy Ion Collider (RHIC)* (Energie und Dichten etwa zwischen LHC und FAIR) stattfinden. Die theoretische Untersuchung dieses Übergangs kann aufgrund der nicht-linearen Dynamik der QCD und ihrer großen Kopplung in diesem Energiebereich nicht mit störungstheoretischen Methoden durchgeführt werden. Untersuchungen mit Hilfe verschiedener Modelle sind zwar möglich, jedoch basieren diese auf Annahmen und Näherungen. Die oben beschriebene Gitter-QCD hingegen stellt zwar eine Methode

zur Untersuchung aus sog. *first principles* (ohne Annahmen oder Näherungen) dar, scheitert jedoch, da die Fermiondeterminante bei endlichem chemischen Potential komplex wird und nicht mehr positiv (semi-)definit ist. Dies sorgt für einen stark oszillierenden Integranden im Pfadintegral, sodass dessen Bestandteile nicht mehr als Wahrscheinlichkeitsmaß (notwendig für das importance sampling in Monte Carlo Simulationen) interpretiert werden können. Dieses Problem ist auch als *Vorzeichenproblem* bekannt. Dadurch sind Gitter-QCD Simulationen faktisch auf verschwindendes oder sehr kleines chemisches Potential $\mu$ beschränkt. Bei letzterem konnte allerdings mit Hilfe der Gitter-QCD verifiziert werden, dass es sich tatsächlich um einen crossover Übergang handelt, der bei Temperaturen um 150-170 MeV stattfindet.

Die Untersuchungen des Bereichs bei $\mu = 0$ sind allerdings bei Weitem noch nicht abgeschlossen und werfen zahlreiche Fragen auf. Beispielsweise sind einige Aspekte der Phasenstruktur in den Limites verschwindender $(m_q \to 0)$ und unendlich großer $(m_q \to \infty)$ Quarkmasse sowie die Bereiche dazwischen ungeklärt. Neben der Quarkmasse hängt die Art des Phasenübergangs auch von der Anzahl der Flavor $N_f$ ab. Für die für den Phasenübergang relevanten Energiebereiche liefert nur die Dynamik der zwei beziehungsweise drei leichtesten Quarks wichtige Beiträge. Aus diesem Grund werden auch in den meisten Gitter-QCD Studien nur die zwei leichtesten Quarks, d.h. up und down Quark oder zusätzlich das strange Quark inkludiert. Weiterhin kann die Masse der up und down Quarks näherungsweise als entartet, d.h. als gleich schwer angenommen werden. In einigen Arbeiten, zu denen auch die vorliegende Arbeit zählt, wird zusätzlich der Fall von drei entarteten Quarkmassen betrachtet, d.h. up, down und strange Quark werden als gleich schwer angenommen. Die Untersuchung des Phasenübergangs im sogenannten chiralen Limes für $(m_q \to 0)$ ist von großem Interesse, da durch diesen indirekt Einblicke in die Natur des Phasenübergangs bei $\mu > 0$ gewonnen werden können. Es besteht die begründete Vermutung, dass in diesem Limes inklusive kleiner (auch physikalischer) Quarkmassen die nötige Temperatur zum Übergang zum QGP gleich oder sehr ähnlich zu jener ist, bei welcher die Wiederherstellung der chiralen Symmetrie erfolgt. Der Ordnungsparameter, der letzteres signalisiert, ist das chirale Kondensat $\langle \bar{\psi}\psi \rangle$, welches beim Übergang in die chiral-symmetrische Phase bei entsprechend hoher Temperaturen verschwindet. Der Phasenübergang für $N_f = 3$ (drei entartete Quarkmassen) und $m_q \to 0$ ist erster Ordnung. Für steigende Massen wird dieser Übergang abgeschwächt bis er in einem Punkt zweiter Ordnung der $Z_2$ Universalitätsklasse endet und darüber hinaus bei mittleren Quarkmassen als crossover Übergang vorliegt. Für $N_f = 2$ und $m_{u,d} \to 0$ werden aktuell zwei mögliche Szenarien diskutiert: Während das eine Szenario die Möglichkeit für einen Übergang erster Ordnung beinhaltet, enthält das andere Szenario die Möglichkeit eines Überganges zweiter Ordnung, welcher zur $O(4)$ Universalitätsklasse gehört. Nur das erste Szenario, mit der Möglichkeit eines Überganges erster Ordnung, würde für endliche Quarkmassen $m_{u,d} > 0$ einen sehr kleinen Bereich mit Übergängen erster Ordnung implizieren, welcher bei einer bestimmten Quarkmasse in einem $Z_2$ Punkt enden würde. Dieser $Z_2$ Punkt wäre mit jenem der $N_f = 3$ Theorie über eine Linie solcher Punkte im Bereich variierender up, down Quarkmasse $m_{u,d}$ und strange Quarkmasse $m_s$ (d.h. $N_f = 2 + 1$ Quarkflavors) verbunden. Im zweite Ordnung $O(4)$ Szenario für $N_f = 2$ und $m_{u,d} \to 0$ würde diese Linie, ausgehend vom $Z_2$ Punkt bei $N_f = 3$, in einem trikritischen Punkt bei bestimmten Massen $0 < m_s < \infty$ und $m_{u,d} = 0$ münden. Dieser trikritische Punkt repräsentiert den Übergangspunkt zwischen den Linien zweiter Ordnung, die zu den $Z_2$ und $O(4)$ Universalitätsklassen gehören. Das Hauptproblem bei der Unterscheidung beider Szenarien ist, dass diese sehr nahe beieinander liegen und durch aktuelle Simulationen nur sehr schwer voneinander zu unterscheiden sind. Neben

widersprüchlichen Ergebnissen aus Studien, die unterschiedliche Fermiondiskretisierungen verwenden, kommt die Problematik der Diskretisierungsfehler hinzu, welche die kritischen Quarkmassen an den Phasenübergangspunkten zweiter Ordnung betreffen: Bei Verwendung feinerer Gitter (d.h. Reduktion der Diskretisierungsfehler), die allerdings wesentlich kostspieliger sind, wird eine Reduktion dieser Massen hin zu kleineren, ebenfalls kostspieligeren Massen erwartet, wodurch das Problem der Unterscheidung beider Szenarien weiter forciert wird.

In der vorliegenden Arbeit wird dieses Problemfeld bei $\mu = 0$ jedoch nicht untersucht und wird daher nicht tiefgehender diskutiert. Stattdessen liegt einer der Schwerpunkte auf dem Bereich um den Grenzfall unendlich schwerer Quarkmassen $m_q \to \infty$, welcher reine Eichtheorie beschreibt und in dem ein mit dem Bruch der Zentrums-Symmetrie assoziierter Phasenübergang erster Ordnung existiert. Bei endlichen Quarkmassen (d.h. unter Beachtung dynamischer Fermionen) wird die Zentrums-Symmetrie explizit gebrochen und der Übergang erster Ordnung wird hin zu kleineren Quarkmassen abgeschwächt bis er schließlich bei unterschiedlichen Massen für $N_f = 2, 3$ und $N_f = 2 + 1$ in einem $Z_2$ Punkt endet. Hier stellt sich, ähnlich wie im chiralen Limes, die Frage, welche Werte die für die $Z_2$ Punkte repräsentativen kritischen Quarkmassen im Kontinuumslimes annehmen. Dabei wird beim Übergang zu kleinerem Gitterabstand eine Reduktion dieser Massen erwartet. Um diese Frage zu beantworten, muss eine Extrapolation über die kritischen Massen, extrahiert von einer Reihe feiner werdender Gittern hin zu $a \to 0$, durchgeführt werden. Aufgrund der Relation $T_\mathrm{c} = 1/a(\beta_\mathrm{c})N_\tau$ wird der Gitterabstand $a$ hauptsächlich durch die temporale Gitterausdehnung $N_\tau$ kontrolliert. Der Parameter $\beta$ entspricht der inversen Gitterkopplung und wird dazu verwendet, bei fixierter temporaler Ausdehnung $N_\tau$ die Temperatur zu kontrollieren. In dieser Arbeit wurden die kritischen Massen von Gittern mit den temporalen Ausdehnungen $N_\tau = 6, 8$ und 10 extrahiert für (unverbesserte) Wilson-Fermionen mit $N_f = 2$ Flavors. Dabei wurde erwartungsgemäß bei steigender temporaler Ausdehung eine deutliche Reduktion des Gitterabstandes $a$ festgestellt. Die Extraktion der $Z_2$ Punkte im thermodynamischen Limes ($V \to \infty$) unendlich großen Volumens erfolgte dabei über *finite size scaling* Analysen, welche die Simulation von Gittern unterschiedlicher, ausreichend großer räumlicher Ausdehnung $N_\mathrm{s}$ erfordern. Im Bereich schwerer Massen spielen fermionischen Freiheitsgrade eine untergeordnete Rolle und das System wird hauptsächlich über gluonischen Freiheitsgrade bestimmt. Aus diesem Grund ist der entsprechende Ordnungsparameter der *Polyakovloop*. Die finite size scaling Analysen basieren daher auf geeigneten Observablen des letzteren. Das Ergebnis der Studie lässt vermuten, dass Gitter der temporalen Ausdehnungen $N_\tau = 6, 8$ und 10 noch nicht ausreichend sind, um über eine Extrapolation die Position der $Z_2$ Punkte im Kontinuum zu erhalten. Die Ergebnisse aus den $N_\tau = 6$ und 8 Simulationen zeigen zwar deutlich den erwarteten Trend hin zu kleineren Massen, allerdings liefern die $N_\tau = 10$ Daten aufgrund der geringen Statistik und der dadurch implizierten großen Fehlern noch kein klares Bild und sind nur als vorläufiges Ergebnis zu betrachten. Zur Identifikation der $Z_2$ Punkte wurden anstelle der Quarkmassen über Hadronenspektroskopie die leichtesten hadronischen Freiheitsgrade der Theorie, bestimmt, welche die pseudoskalaren Mesonen, d.h. die Pionen der Theorie sind. Diese sind vergleichsweise einfach zu berechnen und benötigen keine zusätzliche Renormierung. Für die Berechnungen derer Massen $m_\mathrm{PS}$ wurden $T = 0$ Konfigurationen (erzeugt bei hinreichend großer temporaler Gitterausdehnung $N_\tau$) verwendet, für deren Erzeugung bei Werten der Gitterkopplung simuliert wurde, die an den entsprechenden Phasenübergängen in den Simulationen bei endlicher Temperatur bestimmt wurden. Der Wert des Gitterabstandes $a$ wurde über die *Wilson-Flow* Methode ermittelt. Die Auswertung der Ergebnisse zeigte, dass der Gitterabstand $a$ sowie die verwendeten räumlichen Gitterausdehnungen noch

in Bereichen liegen, in welchen sowohl starke Diskretisierungseffekte als auch endliche Volumeneffekte vorliegen. Dies äußerte sich beispielsweise durch die pseudoskalare Masse, die in Gittereinheiten noch größer eins ist, d.h. $am_{\mathrm{PS}} > 1$ beziehungsweise $a < 1/m_{\mathrm{PS}}$. Die Ausdehnung des Teilchen, gegeben durch die *Compton-Wellenlänge* $\lambda_c = 1/m_{\mathrm{PS}}$, kann also nicht durch den verwendeten Gitterabstand $a$ aufgelöst werden. Dadurch verlieren die extrahierten pseudoskalaren Massen an Aussagekraft. Es zeigte sich jedoch, dass bei Gittern der temporalen Ausdehnung $N_\tau = 10$ zunehmend Bereiche des Gitterabstandes $a$ erschlossen werden, in denen Diskretisierungseffekte erstmals milder werden, sodass $am_{\mathrm{PS}} \approx 1$. Ein Beispiel für nicht ausreichend große Volumina zeigte sich an den Resultaten der finite size scaling Analysen, in welchen keine Fits an die Daten mit guten $\chi^2_{\mathrm{NDF}}$ Werten möglich waren. Dies lässt sich durch die beobachteten endlichen Volumeneffekte erklären, welche die Observable, auf denen die finite size scaling Analysen basieren, stark betrifft beziehungsweise verzerrt. Eine Verbesserung brachte die Verwendung eines Korrekturterms, der die endlichen Volumeneffekte in den finite size scaling Analysen zwar zu berücksichtigen scheinte, bei welchem allerdings nicht vollständig verstanden werden konnte, ob dieser im untersuchten Parameterbereich tatsächlich physikalisch motiviert werden kann.

Auf Basis der simulierten Daten konnte in dem gegeben zeitlich Rahmen und mit den verfügbaren Rechenressourcen zwar noch kein Kontinuumsergebnis gewonnen werden, jedoch lässt sich zusammenfassend sagen, dass ein solider Ausgangspunkt für ein solches gewonnen werden konnte. Desweiteren schaffen die erhaltenen Daten Möglichkeiten zum Vergleich mit anderen Studien, die auf anderen Verfahren beruhen oder andere Fermiondiskretisierungen verwenden. Zur Zeit werden in der Gitter-QCD Gruppe in Frankfurt Simulationen durchgeführt, welche die vorläufigen von $N_\tau = 10$ Gittern gewonnen Ergebnisse konsolidieren und neue Erkenntnisse von $N_\tau = 12$ Gittern hinzufügen sollen. Der zu erwartende Fortschritt könnte erstmals Abschätzungen über die Position der $Z_2$ Punkte in der Kontinuumstheorie ermöglichen.

Die Studie wurde auf identische Weise für $N_f = 3$ Quarkflavors auf relativ groben Gittern mit temporaler Ausdehnung von $N_\tau = 4$ wiederholt. Dabei bestand die Absicht allerdings nicht in einer Kontinuumsextrapolation, sondern vielmehr in einem Test des im Rahmen dieser Arbeit in die CL$^2$QCD Applikation implementierten und zur Simulation von $N_f = 3$ Flavors notwendigen Rational Hybrid Monte Carlo Algorithmus für Wilson-Fermionen. Da kein durch die gleiche Methode gewonnener Referenzwert in der Literatur gefunden wurde, konnte das Ergebnis noch nicht abschließend verifiziert werden, allerdings lässt der Vergleich mit dem Ergebnis aus einem *strong coupling expansion* Modell sowie einer Gitter-QCD Simulation, in der eine Extrapolation durchgeführt wird, die auf einer *hopping expansion* basierenden Approximation der Fermiondeterminante basiert, den Schluss auf einen erfolgreichen Test zu. Desweiteren ist das Ergebnis konsistent mit der Erwartung, die aus der Betrachtung der Ergebnisse der Simulationen der $N_f = 2$ Flavor Theorie entsteht.

Ein weiterer Fokus dieser Arbeit liegt auf der Untersuchung der QCD Phasenstruktur bei rein imaginärem chemischen Potential $\mu_i$, welches eine analytische Fortsetzung der Theorie bei $\mu = 0$ darstellt. In diesem Fall besitzt die Theorie kein Vorzeichenproblem, da die Fermiondeterminante wieder reell wird, sodass Simulationen bei endlichen Werten des rein imaginären chemischen Potentials problemlos ausgeführt werden können. Als weitere Konsequenz aus der Verwendung eines rein imaginären chemischen Potentials ergeben sich neue Symmetrien der Zustandssumme der Theorie. Zum einen ist diese nun reflexionssymmetrisch in $\mu_i$, zum anderen besitzt die Zustandssumme nun eine bestimmte Periodizität in $\mu_i$. Diese wird auch als *Roberge-Weiss (RW) Symmetrie* bezeichnet, und impliziert bei bestimmten kritischen

Werten $\mu_{i,c}$ einen Übergang zwischen den $Z_3$ Zentrumssektoren. Die $Z_3$ Sektoren lassen sich anhand der Phase des Polyakovloops unterscheiden. Die Übergänge zwischen den Sektoren zeichnen sich durch eine besondere Phasenstruktur aus, die strukturell jener bei $\mu = 0$ ähnelt und die ausgenutzt werden kann, um indirekt Erkenntnisse über die Natur der Phasenübergänge bei endlichem, reellem $\mu \geq 0$ zu gewinnen. Diese besondere Phasenstruktur ist ein Resultat des Zusammenkommens der Übergänge zwischen den $Z_3$ Sektoren und den thermalen Phasenübergängen die sich von $\mu = 0$ analytisch in den Bereich imaginären chemischen Potentials fortsetzen. Für hohe Temperaturen handelt es sich bei den Übergängen zwischen den $Z_3$ Sektoren um Übergänge erster Ordnung, während die Übergänge bei niedrigen Temperaturen analytischer Natur sind. Beide Bereiche sind durch einen Punkt verbunden, der auch als RW-Endpunkt bezeichnet wird. Die Natur dieses Punktes ist eine Funktion der Masse und der Anzahl der Flavors. Im Allgemeinen ist dieser Punkt bei kleinen sowie bei großen Fermionmassen ein Tripelpunkt, während er bei mittleren Massen einen Übergang zweiter Ordnung der $Z_2$ Universalitätsklasse darstellt. Die Tripelpunkte kommen aufgrund der Übereinkunft dreier Übergänge erster Ordnung zustande: Die sich fortsetzenden chiralen/deconfinement Übergänge erster Ordnung bei $\mu = 0$ und die Übergänge erster Ordnung zwischen den $Z_3$ Sektoren. Die $Z_2$ Punkte ergeben sich aus letzteren und den analytischen crossover Übergängen, die sich von $\mu = 0$ bei mittleren Massen zu $\mu_{i,c}$ fortsetzen, da der Verbindungspunkt zwischen einem Übergang erster Ordnung und einem crossover Übergang ein Übergang zweiter Ordnung sein muss. An den Verbindungspunkten zwischen den Bereichen der Tripelpunkte und der $Z_2$ Punkte ist der RW-Endpunkt ein trikritischer Punkt, in welchem die Koexistenz dreier unterschiedlicher Phasen endet. Bei Betrachtung der Phasenstruktur unter Variation der Masse sowie der Anzahl der Flavors sind die Tripelpunkte, so wie die $Z_2$ Punkte bei $\mu = 0$, kontinuierlich verbunden und stellen Linien dar, welche die Bereiche der Tripelpunkte und der $Z_2$ Punkte voneinander abgrenzen. Die $Z_2$ Punkte bei $\mu = 0$ sind mit den trikritischen Punkten bei $\mu_{i,c}$ durch $Z_2$ Linien zwischen $\mu = 0$ und $\mu_{i,c}$ verbunden. Insbesondere lässt sich, wie oben bereits angedeutet, die Tatsache ausnutzen, dass das Verhalten einer $Z_2$ Linie, die aus einem trkritischen Punkt hervorgeht beziehungsweise in einem solchen endet, durch trikritische Skalierungsgesetze bestimmt ist. Das bedeutet, bei Kenntnis des trikritischen Punktes und eines Teils der $Z_2$ Linie zwischen $\mu = 0$ und $\mu_{i,c}$ lässts sich mit Hilfe eines trikritischen Skalierungsgesetzes eine Extrapolation bis hin zu reellem $\mu$ durchführen.

In der vorliegenden Arbeit liegt der Fokus auf der Lokalisierung der trikritischen Punkte für $N_f = 2$ Wilson-Fermionflavors sowohl im Bereich leichter als auch schwerer Fermionmassen. Die Strategie basiert hier, wie auch bei $\mu = 0$, zwar noch immer auf finite size scaling Analysen, allerdings unterscheiden sich letztere von denen bei $\mu = 0$ signifikant. Der wesentliche Unterschied liegt darin, dass in Simulationen bei $\mu = 0$ der Parameter $\beta$ zunächst auf den der kritischen Temperatur entsprechenden Wert eingestellt werden muss, bei dem der thermische Übergang stattfindet, während in Simulationen bei $\mu_{i,c}$ das System bei jedem Wert der inversen Kopplung $\beta$ kritisch ist. Dies ist dadurch zu verstehen, dass der RW-Endpunkt, an welchem sich das System bei $\mu_{i,c}$ befindet, den Übergang bzw. die Koexistenz zwischen den Phasen darstellt, die den $Z_3$ Sektoren zugeschrieben werden. Dies hat große Implikationen für das strukturelle Vorgehen in den finite size scaling Analysen. Zur Unterscheidung der verschiedenen Phasen wird hier der Imaginärteil des Polyakovloop verwendet, da sich dieser im Zusammenhang mit der Phase des Polyakovloop bei einem bestimmten Wert von $\mu_{i,c}$ als geeigneter Ordnungsparameter erweist. Die durchgeführte Studie bildet die Fortsetzung einer bereits zuvor in der Gitter-QCD Gruppe in Frankfurt durchgeführten Studie. Dabei hat der Übergang von Gittern mit temporaler Ausdehnung

$N_\tau = 4$ zu feineren Gittern mit $N_\tau = 6$ stattgefunden. Gleichzeitig wurde die Statistik im Vergleich zur Vorstudie sowie die Methoden zur Untersuchung und Extraktion der Ordnung der Phasenübergänge signifikant verbessert. Im Vergleich zeigt sich, das die qualitativen Erkenntnisse im wesentlich unverändert sind, allerdings hat sich erwartungsgemäß aufgrund der durch die Verwendung der feineren Gitter reduzierten Diskretisierungsfehler ein Versatz der trikritischen Linien hin zu kleineren Massen ergeben. Weiterhin wurden im Zuge der Studie die auftretenden endlichen Volumeneffekte besser verstanden. Die gewonnenen Daten eröffnen weiterhin der Vergleich mit Resultaten von Studien, die auf anderen Fermiondiskretisierungen basieren.

# Chapter 1

# Introduction

At present the Standard Model constitutes our current knowledge of elementary particle physics. It successfully describes the known elementary particles and, except for gravity, the interaction forces between them, which are the electromagnetic, the weak and the strong interaction. Gravity only becomes relevant at extremely high energies which are currently not accessible, and thus still can be neglected. While many attempts are undertaken to include gravity into the Standard model success has yet to happen. Through the standard model the interaction forces are formulated in terms of quantum field theories which can be characterized by symmetry groups. The fundamental objects of these quantum field theories are matter fields which can be classified into three families of quarks and leptons which can interact through the mentioned forces. The electromagnetic and the weak interaction can be unified to the electroweak interaction, characterized by a $SU(2) \times U(1)$ symmetry group. These forces are also related to the part of the Standard Model required for the leptons and quarks to have a mass, namely the Higgs-sector [1, 2], which could be experimentally verified by the discovery of the Higgs-boson in an experiment conducted at the *Large Hadron Collider (LHC)* run by the *European Organization for Nuclear Research (CERN)* in Genf [3, 4] in 2012. The Higgs-boson was postulated already in 1964 by Robert Brout and Francois Englert [1] followed just a few days later by a similar but independent work by Peter Higgs [2]. In 2013, just about two years after Robert Brouts passing away, Peter Higgs and Francois Englert were awarded the Nobel prize for their works from 1964.

However, it is interesting to note that more than 95% of the mass of our visible universe is not explained through the Higgs-mechanism but through the binding energy caused by the strong interaction, responsible for the formation of hadronic bound states out of quarks and gluons as well as for the binding between nucleons inside atomic nuclei. The strong interaction is described by quantum chromodynamics (QCD), the quantum field theory of quarks, the fundamental constituents of atomic nuclei (protons and neutrons), and gluons, the force carriers mediating the strong interaction between themselves and the quarks. QCD is characterized by the non-abelian symmetry group $SU(3)$. The quarks as fermionic particles are the fundamental matter fields of QCD and come in six flavors: up ($\approx 3$ MeV), down ($\approx 5$ MeV), strange ($\approx 95$ MeV), charm ($\approx 1.3$ GeV), bottom ($\approx 4.3$ GeV), top ($\approx 173$ GeV). QCD includes eight flavorless gluons, the gauge bosons of the theory, which can be deduced from group theoretical considerations.

When the theory was formulated in the early seventies of the past century as a non-Abelian gauge field theory [5–8], neither the existence of quarks nor of gluons was experimentally proven. Spectroscopy of hadrons in 1964 led to first indications of quarks possibly being the constituents of the proton and neutron which caused Murray Gell-Mann and Georg Zweig to independently formulate the quark hypothesis [9,

10] which (roughly spoken) states that quarks in combinations of two or three are the building blocks of all the observed hadrons.

Initially problems with the statistics of quarks were encountered but then later on resolved by the introduction of an additional degree of freedom termed *color* [11], which is the analog of the electric charge in the electromagnetic interaction, mediated by photons, the gauge bosons of quantum electrodynamics (QED). The number of possible colors $N_c$ corresponds to the order of the symmetry group, i.e. in case of QCD which has a $SU(3)$ symmetry, $N_c = 3$. Evidence for the number of colors present in QCD could be found in electron-electron scattering experiments in which the measured cross-section is predicted by perturbation theory to be proportional to the number of colors $N_c$. Moreover, the cross-section increases as a function of energy each time the mass threshold for the production of another quark flavor is reached, which allows to verify the number of flavors $N_f$. QCD exclusively concerns particles with color charge. Quarks have three possible color charges, which are labeled by red, green and blue. Antiquarks carry the corresponding anti-color. Quarks always come in color-neutral bound states (color singlets) which can be realized for instance either by a combination of three quarks with (anti-)red, (anti-)green and (anti-)blue which are (anti-)baryons or by a combination of two quarks carrying a color and the corresponding anti-color which are the (anti-)mesons, the bosonic counterparts of baryons[1]. The charge of gluons consists of a color and an anti-color implying a color change of the quarks exchanging the gluons. Moreover, the color charge of the gluons causes self-interactions due to which, as a consequence, the attractive force between quarks does not diminish as the distance between them is increased. Instead, the attractive force rises and the potential energy of the binding between the quarks rises linearly with separation. At a certain separation of the quarks, nature favors the creation of new quarks instead of allowing for a further increase in the binding energy. In theory the gluonic field between the quarks is described to be confined in a narrow region denoted as flux tube. The phenomenon is formulated in terms of the color *confinement* hypothesis which says that only color-neutral states can exist, i.e. hadrons like the proton, neutron or pion, but color-charged particles can never be isolated. Moreover, the self-interaction of the gluons implies the possibility for the existence of states made up purely from gluons, so-called glueballs, which are subject to actual research [13]. Quarks and Gluons interact at a length scale of $\mathcal{O}(1)$ which corresponds to the QCD mass scale of $\Lambda_{\text{QCD}} = 200$ MeV. At these energies the QCD coupling $\alpha_s$ is $\approx 1$ and perturbation theory only becomes applicable if the energy involved in the process is $E \gg \Lambda_{\text{QCD}}$. In the low energy regime of hadrons QCD has to be treated with non-perturbative methods like lattice gauge theory. A further important peculiarity about QCD, already mentioned above, is that the chromodynamic binding energy between the quarks, i.e. the constituents of the nucleons (proton and neutron), makes up more than $95\%$ of a nucleons mass due to the energy-mass equivalence. The binding energy of the gluonic field is not solely responsible for the large chromodynamic binding energy, but also the kinetic energy carried by the hadrons constituents. Note that the chromodynamic binding energy is very hard to investigate due to the complex structure of hadrons which in total comprises valence quarks, sea quarks, gluons and virtual particles.

However, experiments in 1968 involving high-energy, deep inelastic electron-nucleon scattering at the Stanford Linear Accelerator Center (SLAC) [14, 15] showed indications for the existence of quarks which was further strongly backed up by following experiments of scattering neutrinos and antineutrinos on nucleons [16]. In these experiments the constituent's momentum distribution was revealed as well as

[1]Exotic color singlets consisting of more than three quarks have been postulated, for instance tetraquarks or pentaquarks, and are subject to current research [12]

the angular dependence of the scattering which showed the spin of the constituents to be $\frac{1}{2}$. Comparison between electron and neutrino scattering yielded the average squared electric charge of the constituents. Overall the experimental results and analysis thereof were sufficient to justify the hypothesis about the existence of quarks [17] which was further backed up in 1975 by increased energy and precision scattering experiments involving charm spectroscopy. Around the same time Wilczek, Gross and Politzer [7, 8] formulated the concept of asymptotic freedom (for which they received the Nobel prize in 2004), a property which causes the coupling $\alpha_s$ between quarks to become weaker as the energy is increased and the distance between them is decreased. Experimental verification of asymptotic freedom followed soon after from deep inelastic scattering experiments.

The only possibility to measure a direct signature of a quark was the observation of a *jet*, which is a shower of hadrons into which a quark fragments and whose existence was still questionable at that time. Again in 1975, evidence for jets was found from data recorded during experiments run at the electron-positron collider SPEAR at SLAC [18, 19]. The process of interest was $e^+e^- \rightarrow q\bar{q} \rightarrow \text{jet} + \text{jet}$. Since the jets were not directly visible by eye, an intricate analysis was carried out involving the so called *sphericity tensor* [20] used to investigate the angular distribution of the jet axis with respect to the incident beam.

Evidence for the existence of gluons[2] was pursued with less interest at that time. One of the reasons gluons are harder to detect is that they do not scatter leptons directly as quarks do. First signs indicating their existence were found from the analysis of lepton nucleon scattering, which showed that the momentum sum rule of nucleon structure functions could not be saturated by the quarks and antiquarks contained in the nucleon. This led to the assumption that about half of a fast nucleon's momentum must be carried by flavorless constituents for which suited candidates were the gluons predicted by QCD. Stronger indications were found by observing scaling violations in lepton nucleon scattering processes, which became gradually more distinct over the years as the precision and the possible kinematic range of the measurements increased. For the first time scaling violations compatible with QCD predictions were observed in 1978. Further processes yielding increasing but still weak indications were lepton pair productions in hadronic oscillations [22]. Though an effect that could clearly and definitely be explained by gluons was not discovered and thus the task remained to either find clear evidence for the existence of gluons or against it, invalidating QCD.

To summarize it briefly, the key steps in this process were taken in 1979 with experiments (starting in 1978) taking place at the electron-positron collider PETRA of the research facility *Deutsches Elektronen-Synchrotron* (DESY), which was the first of its kind to reach $e^+e^-$ center-of-mass energies in the 30 GeV range. In this year results showed first evidence that the QCD prediction about gluons was correct: Multihadron states generated in $e^+e^-$ collisions were analyzed, leading the TASSO collaboration to find signatures of gluon jets generated by hard gluon Bremsstrahlung. In this electron positron collision an intermediate photon is produced which itself turns into a quark-antiquark pair as it decays. Some of the final state quarks sometimes would emit a gluon before it hadronizes. Among the final multihadron states TASSO observed planar and three-jet configurations which were produced by this radiated gluon. A few month later the spin 1 nature of hard gluons was verified, as well, followed by many more investigations about the quark-gluon interaction strength, the gluon self-coupling and about properties of the gluon jets. Overall the discovery of the gluon and consequently the verification of QCD is attributable to a tight and

[2]Initially the term "gluon" was introduced by Gell-Mann in 1962 (without using the notion of color) to denote a hypothetical neutral vector field which strongly couples to the baryon current [21].

successful interplay of theory and experiment. A comprehensive summary about the discovery of the gluon can for instance be found in [23]. Today QCD is widely accepted and strongly established since no mismatch between QCD and experiment has been found. For an overview of experimental tests of QCD see for instance [24].

Coming back to asymptotic freedom and confinement, these properties of QCD imply the existence of a quark-gluon plasma (QGP) a state of hot and dense matter with a huge energy density, in which quarks and gluons can virtually move freely. Such a state is assumed to have existed in the first tens of microseconds of the onset of the universe. While today in nature such a state probably only exists in the center of neutron stars, in a laboratory setting the creation of a QGP requires the use of heavy-ion colliders. In heavy-ion collisions the colliding nuclei exhibit a large energy density and the partons (quarks and gluons) interact through inelastic collisions until a thermal equilibrium is reached - the QGP. Due to the pressure of the interior of the volume the QGP expands and thus cools down until a critical temperature is reached at which hadronization of the partons sets in. An indication for the formation of a QGP are the aforementioned jets: In heavy-ion collisions jets naturally occur in a large number. If the energy-density is large enough for a QGP formation a smaller number of jets can be observed. This is due to the particles being heavily slowed down within the QGP and thus lacking the necessary energy for the creation of a jet. Such experiments are conducted at the *Gesellschaft für Schwerionenforschung (GSI)* in Darmstadt, at CERN and at the *Relativistic Heavy Ion Collider (RHIC)* on Long Island, New York, where the investigation of the phase transition from the confined state to the QGP is of particular interest. Recent measurements at large energies but low densities indicate that this transition is rather a *crossover* (an analytic, non-sharp or smeared out) transition type. If the nature of this transition would change from a crossover to a real phase transition, i.e. a first order transition, further evidence for the existence of the QGP would be found. Such a change would be marked by a second order critical point. The search for such a transition is ongoing in present and upcoming experiments covering a wide range of energies at moderate and larger baryo-chemical densities at the LHC, at RHIC and at the *Facility for Antiproton and Ion Research (FAIR)* at GSI, as well [25].

Theoretical predictions about the nature of this phase transition are hampered due to a variety of problems and thus up to date remain an extremely challenging field of research. Currently one of the most efficient approaches is to treat the problem in a numerical setting with lattice gauge theory. The advantage of this approach is that no assumptions whatsoever are needed, i.e. the equations of the full theory are directly evaluated at any temperature from first principles by the means of high-end computers. Not long ago, the technology of graphics processing units (GPUs) has been introduced to the field [26], yielding a huge gain in computational performance, since GPUs are perfectly suited to parallel problems (and come with a high memory bandwidth) as they are present in the case of the evaluation of LQCD equations. At present the main supplier for GPUs in this field is NVIDIA which offers its framework CUDA for programming the GPUs. An alternative is given by the OpenCL [27] standard, a framework to program not only GPUs but in general heterogenic computing architectures and is developed by the Khronos Working Group. The advantage is its vendor independency which allows the use of (for instance) GPUs from AMD which in the past have been somewhat lower in cost compared to NVIDIA GPUs. The software CL$^2$QCD used in this thesis for lattice quantum chromodynamics computations consists of two parts: The host part which is written in C++ and an OpenCL part, responsible for the performance intensive computations.

Using lattice quantum chromodynamics calculations the QCD crossover transition at a temperature of 150-170 MeV at zero chemical potential could be verified already [28]. The drawback is that lattice QCD calculations currently only work at zero or sufficiently small chemical potential (a measure for the particle-antiparticle ratio), i.e. (roughly spoken) at small particle densities. At larger densities the *sign problem* spoils the numerical evaluation of the lattice QCD path integral. Alternatively, a purely imaginary chemical potential can be chosen for which there is no sign problem. Then, using lattice QCD calculations as a basis, information about the area at real chemical potential can be obtained by intricate extrapolation techniques like analytical continuation via truncated polynomials [29, 30]. Approximations are introduced by the latter for which reason such techniques are only justified up to real chemical potentials about ($\mu/T \lesssim 1$) [31].

However, in the region where lattice QCD calculations can be carried out, i.e. at zero or small chemical potential as well as purely imaginary chemical potential, the nature of the phase transition can be studied as a function of the quark mass, which is one of the two main goals of this work. Doing so on the one hand-side can help to obtain additional insights about the region at larger chemical potential. This is due to the phase structure at unphysical quark masses which imposes certain constraints on the physical region. On the other hand-side this problem is interesting in its own right and investigating it, important knowledge and further understanding about the QCD phase structure can be gathered. Throughout this work I will discuss these topics and explain how they relate to symmetries of QCD present in the limits of zero and infinite quark masses. In lattice QCD additional complications are introduced by the discretization of the space-time and by the finite volume. These complications manifest in terms of lattice artifacts and finite size effects. Using an arbitrarily fine discretization and large volume is not possible due to finite computational resources. The standard way of dealing with these effects is to simulate a series of successively finer lattices and larger volumes and to perform continuum extrapolations and finite size scaling analyses. These techniques will be elucidated in the course of this thesis. The second main goal of this thesis is to lay the foundation for a continuum extrapolation of the phase structure of QCD at zero chemical potential in the heavy quark mass region, which would be the first of its kind.

In chapter 2 lattice QCD is briefly introduced. Chapter 3 treats relevant theoretical aspects about thermodynamics and lattice QCD thermodynamics which will be useful or even necessary for readers unfamiliar with the topic. Moreover approaches will be discussed to study lattice QCD at non-zero baryon density (non-zero chemical potential). This is followed by a discussion about the QCD phase diagram and in particular the QCD phase structure at zero and imaginary chemical potential. In these sections I will try to cover parts of the progress in this field to further motivate the subject of this thesis. Afterwards in chapter 4 data analysis methods used for this work will be explained and algorithmic details will be elucidated. In particular I will describe the Rational Hybrid Monte Carlo for simulating an odd number of quark flavors, which was implemented into the CL$^2$QCD simulation software. Furthermore a brief presentation about CL$^2$QCD and BaHaMAS, a **B**ash **H**andler to **M**onitor and **A**dministrate **S**imulations, will be given. Chapter 5 is divided into the presentation of the result achieved at zero and purely imaginary chemical potential. Each part is preceded with an explanation about the strategy pursued to study the QCD phase structure on lattices. Finally, chapter 6 closes this thesis by giving conclusions and perspectives about this work.

# Chapter 2

# Lattice Quantum Chromodynamics (LQCD)

This chapter serves as a brief reminder and summary of the central equations of Quantum Chromodynamics (QCD), the theory of strongly interacting particles and its discretized version, Lattice Quantum Chromodynamics (LQCD). I will provide the minimal theoretical framework needed to make the work self contained for which reason this chapter is not to be regarded as a lengthy and comprehensive introduction into the complex topic of QCD. It mainly concentrates on providing the ingredients necessary for the construction of its discretized version, LQCD, and hence will be restricted to the theoretical scope needed for this work.

LQCD is formulated in Euclidean space-time, which is an imperative condition if Monte Carlo methods are to be applied since in Minkowski space the Boltzmann factor used in the path integral, discussed in section 2.2, would be complex and thus rapidly oscillating. In QCD the transition to Euclidean metric is done via an analytic continuation based on the introduction of an imaginary time often referred to as Wick rotation [32], for which the standard conventions are

$$t_{\mathrm{E}} = it_{\mathrm{M}}, \quad \mathcal{L}_{\mathrm{E}} = -\mathcal{L}_{\mathrm{M}}, \quad -S_{\mathrm{E}} = iS_{\mathrm{M}}, \tag{2.1}$$

where the subscripts E and M refer to Euclidean and Minkowskian, respectively. As an implication the relative minus sign between space and time components vanish, i.e. there is no discrimination between them anymore. Here this transition is not further discussed. Instead, the starting point will be the theory formulated in Euclidean space-time.

I will start by discussing the Euclidean correlation function, which is a major object in lattice field theories in general. This allows me to subsequently make a natural link to the path integral, the central quantity of LQCD, as it is a different way of writing the euclidean correlation function and at the same time serves as a quantization prescription for QCD. The ensuing sections will focus on the components of the path integral, which are the fields of the theory and the respective actions. The starting point will be the continuous version of these quantities and afterwards I will show how to discretize them. Having done this I will discuss the Polyakov loop, an important observable that was heavily employed to produce the results for this work. The last topic of this chapter addresses renormalization and the link to the continuum limit. Whenever it is not possible to strive into detail and the reader feels the need to fill in the gap, he is referred to the respective literature [33–35] on which I based this chapter.

## 2.1 Euclidean Correlation Functions

The Euclidean correlator is given by

$$\langle O_2(t)O_1(0)\rangle = \frac{1}{Z}\mathrm{Tr}\left[\,\mathrm{e}^{-(T-t)\hat{\mathrm{H}}}\hat{\mathrm{O}}_2\,\mathrm{e}^{-t\hat{\mathrm{H}}}\hat{\mathrm{O}}_1\right], \tag{2.2}$$

On the right-hand side the quantities $\hat{\mathrm{O}}_1$ and $\hat{\mathrm{O}}_2$ are generic operators for the creation or annihilation of particle states or for measuring observables. Note, $t$ and $T$ are Euclidean time distances and are not to be interpreted as physical times since we are operating in Euclidean metric. In particular, $T$ is a formal maximal time distance and will be taken to infinity. The hermitian Hamiltonian operator $\hat{\mathrm{H}}$ of the system measures the energies of the system by acting on the corresponding eigentstates $\hat{\mathrm{H}}|n\rangle = E_n|n\rangle$ and governs the time evolution. The partition function[1] $Z$ serves as a normalization factor and can be evaluated by writing the trace in terms of a Basis of normalized physical eigenvectors $|n\rangle$

$$Z = \mathrm{Tr}\left[\,\mathrm{e}^{-T\hat{\mathrm{H}}}\right] = \sum_n \langle n|\,\mathrm{e}^{-T\hat{\mathrm{H}}}|n\rangle = \,\mathrm{e}^{-TE_n}. \tag{2.3}$$

The right-hand side of eq. (2.2) can be evaluated in the same fashion

$$\langle O_2(t)O_1(0)\rangle = \frac{\sum_{m,n}\langle m|\hat{\mathrm{O}}_2|n\rangle\langle n|\hat{\mathrm{O}}_1|m\rangle\,\mathrm{e}^{-t\Delta E_n}\,\mathrm{e}^{-(T-t)\Delta E_m}}{1+\,\mathrm{e}^{-T\Delta E_1}+\,\mathrm{e}^{-T\Delta E_2}+\ldots}, \tag{2.4}$$

where $\Delta E_n$ is the energy difference between $E_n$ and the vacuum energy $E_0$. Taking the limit $T\to\infty$ only the states $|m\rangle$ equal to the vacuum state $|0\rangle$ survive and the last expression becomes

$$\lim_{T\to\infty}\langle O_2(t)O_1(0)\rangle = \sum_n \langle 0|\hat{\mathrm{O}}_2|n\rangle\langle n|\hat{\mathrm{O}}_1|0\rangle\,\mathrm{e}^{-tE_n}, \tag{2.5}$$

which is a central equation in lattice field theories and allows to compute the energy spectrum and matrix elements of a theory. For instance the operators $\hat{\mathrm{O}}_2$ and $\hat{\mathrm{O}}_1$ can be chosen as $\hat{\mathrm{O}}_p(t')$ and $\hat{\mathrm{O}}_p^\dagger(0)$ so that they create a specific particle state $|p\rangle$ at a time $t=0$ and destroy it at a time $t=t'$. In order to extract the ground state energy of this state one considers eq. (2.5) for large times $t'$ and obtains ($T\to\infty$ assumed)

$$\left\langle O_p(t')O_p^\dagger(0)\right\rangle = \left|\langle p|\hat{\mathrm{O}}_p^\dagger|0\rangle\right|^2\,\mathrm{e}^{-tE_p}+\ldots, \tag{2.6}$$

where the the subleading terms are suppressed if $t'$ is large enough.

## 2.2 The LQCD Path Integral

There are several ways to quantize a theory. In conjunction with LQCD the path integral approach is used for quantization, which can be used to express the Euclidean correlator from the previous section 2.1:

$$\langle O_2(t)O_1(0)\rangle = \frac{1}{Z}\int \mathcal{D}\mathcal{U}\,\mathcal{D}\psi\mathcal{D}\bar{\psi}O_2\left[\psi,\bar{\psi},U\right]O_1\left[\psi,\bar{\psi},U\right]\,\mathrm{e}^{-S_\mathrm{F}\left[\psi,\bar{\psi}\right]-S_G[U]}, \tag{2.7}$$

$$Z = \int \mathcal{D}\mathcal{U}\,\mathcal{D}\psi\mathcal{D}\bar{\psi}\,\mathrm{e}^{-S_\mathrm{F}\left[\psi,\bar{\psi}\right]-S_G[U]}. \tag{2.8}$$

As before, $Z$ is the partition function. The right-hand side of eq. (2.7) is a path integral and thus an integration over all possible configurations of the classical fermion fields $\psi,\bar{\psi}$ as well as gauge fields $U$,

[1] The name is borrowed from the partition function in statistical mechanics, as it is structurally equivalent.

which together constitute the degrees of freedom of LQCD. Here, all quantities contained in this path integral are already quantized. This is not surprising since the path integral can be derived by replacing the continuous space-timeby a discrete lattice, which at the same time serves as an ultraviolet regulator. Such a regularization is essential in order to compute finite quantities in the framework of QCD[2]. Roughly spoken, the path integral can be derived by algebraic manipulations like the introduction of small Euclidean time steps from the right-hand side of eq. (2.2). For QCD this derivation is quite lengthy due to the notational complexity and will not be given here[3]. While in eq. (2.2) there are still the field operators $\hat{\mathrm{O}}$, in eq. (2.7) these field operators became functionals $O\left[\psi, \bar{\psi}, U\right]$ of the fields. These are in general complex numbers for which reason the position within the path integral is unimportant. The transition takes place during the derivation of the path integral, when the field operators act on the field states. The integration measure for the fermion and gauge fields are given by

$$\mathcal{D}\psi = \prod_{x\in\Lambda}\prod_{f,\alpha,c} \mathrm{d}\psi^{(f)}(x)^{\alpha}_{c} \qquad \mathcal{DU} = \prod_{x\in\Lambda}\prod_{\mu=1}^{4} \mathrm{d}U_{\mu}(x). \tag{2.9}$$

In fact the path integral measures constitute products of measures including all quark field components and all gauge fields for every lattice site. Since the path integral is to be evaluated in a numerical simulation of a finite lattice the boundary conditions imposed on it play an important role as they determine the topology of the underyling manifold. In most applications translational invariance preserving toroidal boundary conditions are chosen. In particular the gauge fields $U$ are implemented with periodic for space and times directions while fermionic fields are implemented with anti-periodic boundary conditions time direction, i.e.

$$U_{\mu}(\mathbf{x}, t+T) = U_{\mu}(\mathbf{x}, t) \qquad \psi(\mathbf{x}, t+T) = -\psi(\mathbf{x}, t). \tag{2.10}$$

The reason for this are the statistics that have to be obeyed by the different particle species, namely Bose/Einstein statistics for the gauge fields and Fermi statistics for the fermion fields. The quantization of QCD via the path integral can be summarized as follows:

- Discretization of the continuous space-time via a lattice. The degrees of freedom are given by the classical fields in the path integral, which are solely defined on the lattice sites.
- The Euclidean action is discretized (see following sections). The continuum version has to result from taking the limit $a \to \infty$.
- Operators in the Euclidean correlator become functionals of the classical fields in the path integral.
- Euclidean correlators can be computed by evaluation of the functionals and weighting them according to the Boltzmann weight factor.

In general, lattice field theories and statistical mechanics are structurally equivalent for which reason analytical and in particular numerical methods suited for statistical mechanics can be applied to lattice field theories. This yields the possibility to compute the path integral with Monte Carlo methods which will be picked up again in section 4.2.

[2]Outside of lattice field theory other means for regularization exist, for instance dimensional regularization, Paui-Villars or the introduction of a momentum cutoff.

[3]The concepts can be easily learned from simpler theories like quantum mechanics or a scalar field theory. A detailed derivation and discussion of the QCD path integral can be found in [36].

As a last remark, note, that it cannot be clear a priori whether an action that is discretized in a certain way and used in the path integral gives rise to expectation values of physical observables. In order to do so, Euclidean correlators computed with the path integral must obey a certain set of axioms. Only then the necessary quantum mechanical Hilbert space for the Minkowski theory can be reconstructed. For a detailed treatment see [37, 38].

## 2.3 Continuum QCD

The constituents of the QCD action are the fundamental fields of the theory, the quarks and the gluons. The quarks as matter fields are spin-$\frac{1}{2}$ fermion fields

$$\psi^{(f)}(x)_{\substack{\alpha \\ c}}, \qquad \bar{\psi}^{(f)}(x)_{\substack{\alpha \\ c}}, \tag{2.11}$$

whose components are Grassmann valued variables with space-timeargument $x$, a Dirac index $\alpha = 1, \ldots, 4$ and a color index $c = 1, 2, 3$. This is to be understood as 3 color components per Dirac component and consequently each field has 12 components in total. The index $f$ refers to the quark flavor with $f = 1, \ldots, N_f$. Note that $\bar{\psi}^{(f)}(x)$ in the Euclidean path integral is an independent integration variable. If the indices of the fields are omitted it means that matrix/vector notation is used. The gluons are described by the gauge potential

$$A_\mu(x)_{cd} \tag{2.12}$$

that carries a space-timeargument $x$, as well. These fields are Lie algebra elements of the non-abelian gauge group of QCD which is $SU(3)$ and thus represent traceless, hermitian $3 \times 3$ matrices whose components are indexed by the color indices $c$ and $d$. Moreover they constitute vector fields with an orientation in space-timecharacterized by the Lorentz index $\mu = 1, \ldots, 4$. The gluon field has an expansion in terms of color components $i = 1, \ldots, 8$

$$A_\mu(x) = \sum_{i=1}^{8} A_\mu^i(x) T_i, \tag{2.13}$$

where $T_i$ are the generators of the algebra of $SU(3)$ providing a basis for traceless hermitian $3 \times 3$ matrices.

The fermionic part of the QCD action is a bilinear functional in the fields $\psi^{(f)}(x), \bar{\psi}^{(f)}(x)$ and contains a term coupling them to the gluonic field $A_\mu(x)_{cd}$. Written explicitly in all indices (Einstein summation convention is assumed) it reads

$$S_{\mathrm{F}}[\psi, \bar{\psi}, A] = \sum_{f=1}^{N_f} \int \mathrm{d}^4x \; \bar{\psi}^{(f)}(x)_{\substack{\alpha \\ c}} \left( (\gamma_\mu)_{\alpha\beta} (\delta_{cd} \partial_\mu + i A_\mu(x)_{cd}) + m^{(f)} \delta_{\alpha\beta} \delta_{cd} \right) \psi^{(f)}(x)_{\substack{\beta \\ d}}. \tag{2.14}$$

The expression contains a sum over all quark flavors taken into account which identically couple to the gauge field $A_\mu$. Aside from the mass $m^{(f)}$ the different flavors differ only in their electrical charge but this is irrelevant for strong interactions. Here additionally the 4 different Euclidean Dirac $4 \times 4$ $\gamma$-matrices appear which mix the Dirac components of the fermion fields in a different way for each value of $\mu$. In eq. (2.14) the mass term is trivial in both Dirac and color space and thus the product of the quark fields is equivalent to a simple vector product. The kinetic term containing the partial derivative is only trivial in color space but since there is a contraction with $\gamma_\mu$ a mixing of the Dirac components takes place.

The term coupling the quark fields to the gauge field is neither trivial in color nor in Dirac space as it is contracted with $\gamma_\mu$, as well. The term on the right-hand side of eq. (2.14) is expressed compactly as

$$S_{\mathrm{F}}[\psi,\bar{\psi},A]=\sum_{f=1}^{N_f}\int \mathrm{d}^4x\ \bar{\psi}^{(f)}(x)_{\underset{c}{\alpha}}D(x)^{\alpha\beta}_{cd}\psi^{(f)}(x)_{\underset{d}{\beta}}. \tag{2.15}$$

where $D(x)^{\alpha\beta}_{cd}$ (the part in the brackets in eq. (2.14)) represents the Dirac operator. In order for the fermion action to be gauge invariant with respect to $SU(3)$ rotations in color space

$$S_{\mathrm{F}}[\psi,\bar{\psi},A]=S_{\mathrm{F}}[\psi^{'},\bar{\psi}^{'},A^{'}], \tag{2.16}$$

the quark and gauge fields are required to transform like

$$\begin{aligned}\psi(x)\rightarrow\psi^{'}(x)&=\Omega(x)\psi(x)\\ \bar{\psi}(x)\rightarrow\bar{\psi}^{'}(x)&=\bar{\psi}(x)\Omega^{\dagger}(x)\\ A_\mu(x)\rightarrow A^{'}_\mu(x)&=\Omega(x)A_\mu(x)\Omega^{\dagger}(x)+i(\partial_\mu\Omega(x))\Omega^{\dagger}(x).\end{aligned} \tag{2.17}$$

The properties of $A_\mu(x)$ of being hermitian and traceless are preserved by this transformation.

The gluonic action of QCD is given by

$$S_{\mathrm{G}}[A]=\frac{1}{2g^2}\int \mathrm{d}^4x\ \mathrm{Tr}[F_{\mu\nu}(x)F_{\mu\nu}(x)], \tag{2.18}$$

with the field strength tensor

$$F_{\mu\nu}(x)=-i\left[D_\mu(x),D_\nu(x)\right]=\partial_\mu A_\nu(x)-\partial_\nu A_\mu(x)+i\left[A_\mu(x),A_\nu(x)\right], \tag{2.19}$$

where $D_\mu(x)$ is the covariant derivative

$$D_\mu(x)=\partial_\mu+iA_\mu(x). \tag{2.20}$$

By construction the action is invariant under the last transformation of (2.17) and thus

$$S_{\mathrm{G}}[A^{'}]=S_{\mathrm{G}}[A]. \tag{2.21}$$

After rewriting the field strength tensor $F_{\mu\nu}(x)$ with some lines of algebra in terms of the color components of the gauge field $A_\mu$, the action becomes

$$S_{\mathrm{G}}[A]=\frac{1}{4g^2}\sum_{i=1}^{8}\int \mathrm{d}^4x\ F^{(i)}_{\mu\nu}(x)F^{(i)}_{\mu\nu}(x), \tag{2.22}$$

where the expression for $F^{(i)}_{\mu\nu}(x)$ reads

$$F^{(i)}_{\mu\nu}(x)=\partial_\mu A^i_\nu(x)-\partial_\nu A^i_\mu(x)-f_{ijk}A^j_\mu(x)A^k_\nu(x). \tag{2.23}$$

The last term on the right-hand side leads to terms being cubic and quadratic in the action (2.22) implying self interactions of the gluons and thus inducing the phenomenon of color confinement.

## 2.4 Discretization of QCD

The first step towards a discretized theory of QCD is the introduction of a 4D lattice $\Lambda$ in which the continuous space-timeis embedded

$$\Lambda = \{n = (n_1, n_2, n_3, n_4) \mid n_1, n_2, n_3 = 0, \ldots, N_\sigma - 1; n_4 = 0, \ldots, N_T - 1\}. \tag{2.24}$$

The lattice points labeled by $n$ are separated by the lattice spacing $a$. The fermion fields now live on the lattice points only and for notational convenience the space-timeargument $x = an$ now can be replaced by $n$:

$$\psi(n), \quad \bar{\psi}(n). \tag{2.25}$$

The partial derivative acting on the fermion field is discretized symmetrically

$$\partial_\mu \psi(x) \to \frac{\psi(n + \hat{\mu}) - \psi(n - \hat{\mu})}{2a}, \tag{2.26}$$

where $\hat{\mu}$ is a unit vector in direction $\mu$. The space-timeintegral gets replaced by a sum over the lattice points

$$\int \mathrm{d}^4 x \to a^4 \sum_{n \in \Lambda}. \tag{2.27}$$

A naive application of these prescriptions leads to terms in the fermion action like $\bar{\psi}(n)\psi(n + \hat{\mu})$ which break the gauge invariance. This can be seen easily from applying a gauge transformation according to (2.17) on this term. The gauge invariance can be preserved by the introduction of fields $U_\mu(n)$ with an directional Lorentz index $\mu$. They belong to the $SU(3)$ gauge group and are required to transform in the following way

$$U_\mu(n) \to U'_\mu(n) = \Omega(n) U_\mu(n) \Omega^\dagger(n + \hat{\mu}). \tag{2.28}$$

The fields $U_\mu(n)$ are then attached to the fermion fields in the discretized partial derivative leading to gauge invariant terms in the fermion action like $\bar{\psi}(n) U_\mu(n) \psi(n + \hat{\mu})$. They can be thought of as living on the links connecting the lattice points. For this reason the fields $U_\mu(n)$ are commonly referred to as link variables. They take on the role of the gluon fields in the continuum. Note that in contrast to $U_\mu(n)$, which are elements of $SU(3)$, the continuum gluon fields $A_\mu(x)$ are elements of the algebra of $SU(3)$. The fields $U_\mu(n)$ are also called lattice gauge transporters and can be written in the form

$$U_\mu(n) = \exp\left(iaA_\mu(n)\right), \tag{2.29}$$

where $A_\mu(n)$ are just the algebra valued lattice gauge fields of the continuum placed on discrete lattice points $n$. In LQCD the link variables $U_\mu(n)$ are the fundamental fields to be integrated over in the path integral formalism. These are all the prerequisites necessary to construct LQCD. In the following section I will introduce Wilson's lattice version of the gauge action, the first formulation of lattice gauge theory.

## 2.5 The Wilson Gauge Action

Simply put, the idea for the construction of the Wilson gauge or gluon action is to build and sum the shortest possible closed loops of link variables on the lattice. Such a loop is given by the so called plaquette

$$P_{\mu\nu}(n) = U_\mu(n) U_\nu(n + \hat{\mu}) U^\dagger_\mu(n + \hat{\nu}) U^\dagger_\nu(n), \tag{2.30}$$

which is a product of link variables along a closed path of links connecting four adjacent lattice points. The trace of the plaquette is a gauge invariant quantity. The Wilson gauge action is then given by [39]

$$S_G[U] = \frac{\beta}{3} \sum_{n\in\Lambda} \sum_{\mu\leq\nu} \mathrm{ReTr}\left[\mathbb{1} - P_{\mu\nu}(n)\right], \tag{2.31}$$

where the trace is in the color space. The parameter $\beta$ is the inverse lattice coupling and refers to the lattice gauge coupling $g$ via

$$\beta = \frac{6}{g^2}. \tag{2.32}$$

The action $S_{\mathrm{G}}[U]$ is positive and due to the trace gauge invariant under gauge rotations.

## 2.6 Wilson Fermion Discretization

Applying naively the discretization prescriptions listed in section 2.4 in order to obtain the fermion action leads to an expression that on the lattice suffers from a problem named *species doubling*. A rigorous analysis would be quite lengthy for which reason I will restrain from presenting one, although, the important points can be summarized as follows: The common way to study the problem is to compute and examine the momentum space quark propagator $\tilde{D}^{-1}(p)$ which reveals that it has 16 poles of which 15, the so called doublers, are unphysical. The implication is there are 16 degenerate flavors of the same fermion in the continuum. These copies can be forbidden as asymptotic states but they still contribute in loops as for instance it is the case for the renormalization group $\beta$ function. A possible solution proposed by Wilson is to add an extra term to the Dirac operator which takes care of the doublers in an elaborate way. This term vanishes for the physical pole while for each unphysical pole it contributes $2/a$ leading to a total mass of $m + 2l/a$, where $l$ is the number of momentum components causing the unphysical poles. In the limit of $a \to 0$ the doubler contributions become very heavy and consequently decouple from the theory. Implementing this term in the position space Dirac operator leads to the following action for $N_f$ fermion flavors

$$S_{\mathrm{F}}[\psi, \bar{\psi}, U] = \sum_{f=1}^{N_f} a^4 \sum_{n,m\in\Lambda} \bar{\psi}^{(f)}(n) D^{(f)}(n|m) \psi^{(f)}(m), \tag{2.33}$$

where $D^{(f)}(n|m)$ is Wilson's complete Dirac operator [39] (often also referred to by Wilson fermion matrix)

$$D^{(f)}(n|m) = \left(m_0^{(f)} + \frac{4}{a}\right) \delta_{\alpha\beta}\delta_{ab}\delta_{nm} - \frac{1}{2a} \sum_{\mu=\pm1}^{\pm4} (\mathbb{1} - \gamma_\mu)_{\alpha\beta} U_\mu(n)_{ab} \delta_{n+\hat{\mu},m}, \tag{2.34}$$

written in a particularly compact way as the sum runs over negative $\mu$ values leading to terms $\gamma_{-\mu} = -\gamma_\mu$. Additionally it gets often rescaled by factoring out $m_0^{(f)} + 4/a$ which leads to

$$C\, D'^{(f)}(n|m) = C \left(\delta_{\alpha\beta}\delta_{ab}\delta_{nm} - \kappa \sum_{\mu=\pm1}^{\pm4} (\mathbb{1} - \gamma_\mu)_{\alpha\beta} U_\mu(n)_{ab} \delta_{n+\hat{\mu},m}\right), \tag{2.35}$$

with $D'^{(f)}(n|m)$ being the rescaled version of the Wilson Dirac operator and

$$\kappa = \frac{1}{2(am_0^{(f)} + 4)}, \qquad C = m_0^{(f)} + \frac{4}{a}. \tag{2.36}$$

The real parameter $\kappa$ is called *hopping parameter* [4] , used in Monte Carlo Simulations with Wilson fermions to indirectly control the bare quark mass $m_0$. Note that for free fermion fields, i.e. $U_\mu = \mathbb{1}$, the bare quark mass $m_0$ equals the physical quark mass and setting $m_0 = 0$ in eq. (2.36) leads to massless fermions for a value of $\kappa = 1/8$. This does not hold if the fermions are in an external gauge field, i.e. $U_\mu \neq \mathbb{1}$. In this case the bare quark mass gets an additional mass renormalization due to quantum corrections caused by the coupling to the external gauge field and massless fermions are obtained for some negative value of $m_0$ or $\kappa \geq 1/8$, respectively. In the fermion action the fields $\psi^{(f)}(x)$ and $\bar{\psi}^{(f)}(x)$ are then typically rescaled, as well, in order to absorb the factor $C$ and $a^4$ (stemming from the discretized space-timeintegral in the fermion action)

$$\psi^{(f)}(n) \to a^2\sqrt{C}\psi^{(f)}(n), \qquad \bar{\psi}^{(f)}(n) \to a^2\sqrt{C}\bar{\psi}^{(f)}(m). \tag{2.37}$$

Thus the fermion action becomes

$$S_{\mathrm{F}}[\psi, \bar{\psi}, U] = \sum_{f=1}^{N_f} \sum_{n,m\in\Lambda} \psi^{(f)}(n) D^{(f)}(n|m) \bar{\psi}^{(f)}(m), \tag{2.38}$$

with $D^{(f)}(n|m)$ and $\psi^{(f)}(n), \bar{\psi}^{(f)}(m)$ given by eqs. (2.35) and (2.37).

### Symmetry Aspects

The price for having obtained a lattice formulation of the Dirac operator is the loss of many continuum symmetries like translational or rotational invariance of which only discretized versions exist on the lattice, though, these symmetries can be recovered in the continuum as $a \to 0$. Two other important symmetry operations of the Wilson Dirac operator (for e.g. the construction of hadron interpolators) existing in the continuum and on the lattice alike are charge conjugation $\mathcal{C}$ which transforms particles into antiparticles and parity $\mathcal{P}$ transformations for reflections in euclidean space. Furthermore the Wilson Dirac operator obeys a relation called $\gamma_5$-hermiticity [5] , i.e.

$$D^\dagger = \gamma_5 D \gamma_5 \;\Leftrightarrow\; (\gamma_5 D)^\dagger = \gamma_5 D. \tag{2.39}$$

This property establishes the hermiticity of $D^\dagger D$, which will turn out to be extremely important in the context of Monte Carlo simulations (see section 4.2). Moreover $\gamma_5$-hermiticity is not specific to the Wilson Dirac operator. In fact almost all Dirac operators feature this symmetry. One of it's characteristics is that the Dirac operators eigenvalues are either real or come in complex conjugate pairs. As a last point I want to address another problem of utmost significance, namely the explicit breaking of chiral symmetry on the lattice. The Dirac operator as given in eq. (2.15) is, in the massless case, clearly invariant under chiral rotations

$$\psi(x) \to \psi'(x) = \mathrm{e}^{i\alpha\gamma_5}\psi(x), \quad \bar{\psi}(x) \to \bar{\psi}'(x) = \mathrm{e}^{i\alpha\gamma_5}\bar{\psi}(x), \tag{2.40}$$

since $\{\gamma_5, D\} = 0$. In contrast, for the Wilson Dirac operator, eq. (2.34), this is not true anymore ($m_0 = 0$ assumed) [43, 44]. What spoils the invariance is the additional diagonal term, as well as the unit matrix in $(\mathbb{1} - \gamma_5)$ which both do not commute with $\gamma_5$ and are a consequence of the term added by Wilson in order to overcome the aforementioned species doubling problem.

[4] The name hopping parameter originates from analysing Wilson fermions in the limit of heavy quark masses where $\kappa$ is small and thus serves as expansion parameter. From this analysis fermions are exposed to be paths of link variables referred to as fermion lines [40–42]. Moreover the fermion determinant turns out to be interpretable as closed fermion lines or fermion loops.

[5] It is simple to prove this relation by multiplying $\gamma_5$ from both sides to eq. (2.34). The diagonal term is unaffected whereas in the second term there is a change from $(\mathbb{1} - \gamma_5)$ to $(\mathbb{1} + \gamma_5)$. The sum over negative and positive $\mu$ values can be exploited to recover $(\mathbb{1} - \gamma_5)$ and together with the $\delta$-function the position of the gauge field $U_\mu$ can be exchanged $n \leftrightarrow m$.

### The Nielsen-Ninomiya Theorem and Chiral Symmetry Breaking

It is not possible to find a different expression to remove the doublers and to preserve chiral symmetry at the same time. This fact is expressed in terms of the Nielsen-Ninomiya theorem [45–48]. Considering the case of free fermions and a Dirac operator with translational invariance,

$$D\, \mathrm{e}^{ipx} u = \tilde{D}(p)\, \mathrm{e}^{ipx} u, \tag{2.41}$$

(where $\tilde{D}(p)$ is the momentum space propagator, given by a $4 \times 4$ complex matrix, and $u$ is a constant spinor) a simplified version of the theorem states that one of the following properties has to be sacrificed:

1. $\tilde{D}(p)$ is local, i.e. is analytic in the momentum components $p_\mu$ with a period of $2\pi/a$.
2. $\tilde{D}(p)$ assumes its continuum form $\tilde{D}(p) = i \sum_\mu \gamma_\mu p_\mu + O(ap^2)$ for $ap_\mu \ll \pi$.
3. $\tilde{D}(p)$ is invertible for all non-vanishing momentum components (mod $2\pi/a$), i.e. there is no species doubling.
4. Continuum chiral symmetry, i.e. $\{\gamma_5, D\}$.

To obtain a sensible continuum theory the properties 1 and 2 can't be relinquished. Neither can property 4, as long as chiral symmetry ought to exist in its continuous form. This renders property 3, species doubling, inevitable. If a theory is excepted to be non-chiral, as it is the case for QCD, there are three possibilities for remedy:

1. Using Wilson fermions, i.e. having the Wilson term taking care of the doublers but breaking chiral symmetry explicitly,
2. using staggered fermions which come in four copies but feature a $U(1)$ chiral symmetry,
3. using Ginsparg-Wilson fermions which have no doubling problem and have a lattice-version of chiral symmetry.

Regarding the last point there is no contradiction with the Nielsen-Ninomiya theorem since chiral symmetry is realized in a different way than it has been originally assumed for proving the theorem [49]. I conclude this section by addressing another issue regarding the use of Wilson fermions, namely the question whether the axial anomaly comes out correctly in the continuum limit. This has been extensively studied and the answer turned out be positive (see for instance [50] and refs. therein).

### Other Fermion Discretizations

The Wilson fermion discretization presented above was the first discretization discovered and represents just one particular choice. Today it is still widely used in many studies since the computational costs are moderate and they are fairly simple to implement and to use. Examples of alternatives include the following:

*Twisted Mass* fermions [51] represent a doublet of unimproved Wilson fermions with a chirally twisted mass term added. The doublet is then interpreted as the up/down isospin doublet. They have the advantage that for spectral observables the leading discretization errors vanish under a certain choice of parameters.

The drawback is that parity and isospin are violated by cut-off effects implying potentially undesirable features, for instance a neutral pion with the quantum numbers of the vacuum.

Another variant of Wilson fermions are *clover* Wilson fermions [52], which add another term, the Sheikholeslami-Wohlert term, to reduce the lattice actifacts to be $O(a^2)$. There are numerous individual actions which differ mainly by the kind of links included in the discretized derivatives (and possibly into the *SW* term). These links can be thin links guaranteeing certain properties like locality and positivity, or variants of smeared links causing better statistical behavior of various observables.

Then there are *Staggered* fermions [53]. They reduce the number of doublers to four by a redistribution of the degrees of freedom between the lattice sites. For this discretization smearing depicts an important technique used to reduce the effect of high-momentum gluons whose exchange causes the interactions mixing the different *tastes* of the remaining doublers. An advantage of the staggered discretization is the preservation of a residual chiral symmetry. The disadvantage that triggered a lot of controversy in the community in the past is the need to take the root of the determinant of the Dirac operator. Actions currently used for this discretization are the *asqtad* and *HISQ* actions.

More sophisticated discretizations preserve lattice chiral symmetry but are computationally very expensive. Examples are *Domain-Wall* and *Overlap* fermions [54–57].

## 2.7 Wilson and Polyakov Loops

In this section I will introduce two important gauge invariant observables of quantum fields - the Wilson and Polyakov loop [58] which are closely linked to each other. I will briefly explain how to construct them and provide a physical interpretation. The Polyakov loop will be further motivated in the context of finite temperature QCD in section 3.2.2. Both of these observables are gauge invariant quantities constructed purely from ordered products of link variables and allow to determine the potential between two static color sources.

### The Wilson Loop

As a starting point we consider a Wilson loop which is basically given by the trace over a product of link variables along a closed circuit and can be expressed as

$$L[U] = \mathrm{Tr}\left[\prod_{n,\mu\in\mathcal{L}} U_\mu(n)\right]. \tag{2.42}$$

In this expression $\mathcal{L}$ indicates the closed loop along which the link variables $U_\mu$ are multiplied. The simplest form of a Wilson loop is just a planar loop which is realized by a rectangle situated in the lattice $\Lambda$ such that it has a temporal and only one spatial component. Apparently the smallest planar Wilson loop is the plaquette (see eq. (2.30)). These types of Wilson loops can generally be described in terms of its four constituents which are two so-called Wilson lines $S$ along a common spatial direction and two temporal transporters $T$, i.e.

$$W_\mathcal{L}[U] = \mathrm{Tr}\Big[S(\mathbf{m},\mathbf{n},n_\tau)T^\dagger(\mathbf{n},n_\tau)S^\dagger(\mathbf{m},\mathbf{n},0)T(\mathbf{m},n_\tau)\Big]. \tag{2.43}$$

To proceed, we choose the temporal gauge $A_\mu = 0$ which implies $U_\mu = \mathbb{1}$ according to eq. (2.29). This step is not necessary but simplifies the interpretation of the Wilson loop. The last equation then simply

reads

$$W_{\mathcal{L}}[U] = \mathrm{Tr}\Big[S(\mathbf{m},\mathbf{n},n_\tau)S^\dagger(\mathbf{m},\mathbf{n},0)\Big]. \tag{2.44}$$

from which it becomes apparent that the Wilson loop is the correlator of two temporally separated Wilson lines. Using the key equation (2.2) the expectation value of the Wilson loop can be computed. Comparing the gauge transformation properties of the Wilson lines with those of a quark-antiquark pair expressed as a product of fields $\psi(\mathbf{m})\bar{\psi}(\mathbf{n})$ (which are in fact the same) it can be reasoned that the states with non-vanishing overlap involved in this correlator describe a static quark-antiquark pair sitting at $\mathbf{m}$ and $\mathbf{n}$. For a more rigorous reasoning it has to be shown using the definition of quark fields on the lattice that the quark propagator reduces to the Wilson line $S(\mathbf{m},\mathbf{n})$ in the heavy quark mass limit. However, for sufficiently large times the expectation value can be extracted from the correlator as

$$\langle W_{\mathcal{L}}\rangle = C\,\mathrm{e}^{-tE_{q\bar{q}}}\left(1+\mathcal{O}\left(\mathrm{e}^{-t\Delta E}\right)\right). \tag{2.45}$$

$C$ is the amplitude and $E_{q\bar{q}}$ is the ground state energy of the correlator corresponding to the static quark-antiquark potential $V(r)$ where $r = a\,|\mathbf{m}-\mathbf{n}|$ is the distance between the quark and the antiquark. The time argument is given by the product of lattice spacing and time slice, $t = an_\tau$. In the sub-leading terms $\Delta E$ is the exponentially suppressed difference to the first excited energy level of the quark-antiquark pair including additional particle-antiparticle combinations with vacuum quantum numbers. It is worth noting that using non-planar Wilson loops it is possible to compute the potential $V(r)$ for non-integer multiples of $a$ since in this case the Wilson loop has more than one spatial component. This can be of importance for instance if restoration of rotational invariance when approaching the continuum limit is to be studied. Another point concerns the investigation of gluonic bound states (glueballs) for which Wilson loops can be used as operators. This allows to calculate the mass spectrum of such states, see e.g. [59].

### The Polyakov Loop

We consider again the product

$$\prod_{n,\mu\in\mathcal{L}} U_\mu(n) = S(\mathbf{m},\mathbf{n},N_\tau)T^\dagger(\mathbf{n},N_\tau)S^\dagger(\mathbf{m},\mathbf{n},0)T(\mathbf{m},N_\tau), \tag{2.46}$$

but this time $n_t$ assumes the value of $N_\tau$, i.e. the temporal extent of the lattice. Instead of utilizing the temporal gauge as before (which is not possible due to the periodic boundary conditions) a gauge is used in which the spatial links are set to unity. Then the Wilson loop consists of two disconnected temporal paths $T^\dagger(\mathbf{n},N_\tau)T(\mathbf{m},N_\tau)$ of opposite orientation winding around the temporal boundary of the lattice. Taking the trace of each of the disconnected parts separately yields two gauge invariant quantities

$$P(\mathbf{n}) = \mathrm{Tr}\left[\prod_{j=0}^{N_\tau-1} U_4(\mathbf{n},j)\right], \tag{2.47}$$

which are named Polyakov loops. It can be used likewise to compute the static quark-antiquark potential by repeating the same procedure as for the Wilson loop. The expression for the expectation value is then given by the correlator of the Polyakov loops spatially separated by the distance $r = a\,|\mathbf{m}-\mathbf{n}|$

$$\langle P(\mathbf{m})P(\mathbf{n})\rangle = C\,\mathrm{e}^{-aN_\tau E_{q\bar{q}}}\left(1+\mathcal{O}\left(\mathrm{e}^{-aN_\tau\Delta E}\right)\right). \tag{2.48}$$

It is important to remark, that the equality between the quark-antiquark potential as derived from the Wilson loop and the Polyakov loop are not rigorously proven. There is only a proof that the string tension of the quark-antiquark potential extracted from the Polyakov loop correlator is bounded from above by the one of the Wilson loop correlator [60].

An alternative introduction of the Polyakov loop, as it is comprehensibly illustrated in [34] for QED without dynamical fermions, is to start from the continuum theory with a partition function of a system containing an infinitely heavy quark coupled to a fluctuating gauge potential. The field operator acting on the states can be used together with the Dirac equation to derive the expression for the Wilson line in a straight forward way. The QCD version is then given by

$$L(\mathbf{x}) = \text{Tr } \mathrm{e}^{P \int_0^\beta \mathrm{d}x_4 A_4(\mathbf{x},x_4)}, \tag{2.49}$$

which on the lattice translates to the Polyakov loop in eq. (2.47). The expectation value of the Polyakov loop is an order parameter for the deconfinement phase transition of QCD without dynamical quarks. For this reason I will continue the discussion and motivation about the Polyakov later in chapter 3.

## 2.8 Continuum Limit and Renormalization

In order for LQCD to describe QCD in the continuum the lattice action is required to transition into its continuum counterpart in the limit $a \to 0$. However, this is only the naive continuum limit. In fact there is an infinite number of lattice actions that reduce to the QCD action as $a \to 0$ because there is a certain freedom in the construction of a lattice action[6]. This requirement alone is insufficient in order to assure the existence of a continuum limit that correctly describes QCD. The reason is that LQCD requires the evaluation of a path integral whose results are observables $\Theta(g(a), a)$ which do non-trivially depend on the lattice spacing $a$. For numerical calculations this implies the existence of a range of values of the coupling $g$ in which the correlation length $\hat{\xi}$ (in lattice units) [7] of the system diverges, i.e. $\hat{\xi}(g) \underset{g\to g^*}{\longrightarrow} \infty$. This corresponds to a phase transition at which the physical scales become large in physical units in contrast to the lattice which becomes successively finer. As the correlation length diverges the underlying lattice structure looses its meaning. Only if the possibility for such a transition is given LQCD is able to describe QCD in the continuum. An observable $\Theta$ with a mass dimension of $d$ must approach a finite value for $a \to 0$,

$$\Theta(g(a), a) = \left(\frac{1}{a}\right)^d \hat{\Theta}(g(a)) \underset{a\to 0}{\longrightarrow} \Theta_{\text{phys}}, \tag{2.50}$$

which assumes the corresponding lattice quantity $\hat{\Theta}(g)$ to diverge. At the same time the lattice coupling approaches its critical value, $g \to g^*$. In order to keep physics constant, $g$ has to be tuned to $g^*$ in a particular way. This can be realized by fixing $\Theta(g(a), a)$ at its physical value $\Theta_{\text{phys}}$ and determining $g(a) = a(\Theta_{\text{phys}})^{1/d}$ as function of $a$ [8].

A practical example in terms of LQCD is given by the phase diagram for Wilson fermions for which the control parameters are the inverse lattice gauge coupling $\beta = 6/g^2$ and the hopping parameter

[6] This allows for the construction of improved lattice actions which enable the extraction for physical results at larger lattice spacings.

[7] The correlation length corresponds to the inverse of the smallest mass of the system, i.e. for QCD this is the pion mass $m_\pi$.

[8] The dependence of the coupling on $a$ can be understood intuitively by considering successively finer lattices. To fix the physical volume, the number of lattice sites and links must be increased by which the coupling has to be tuned accordingly to the changing dynamics of the system.

$\kappa = 1/(2am + 8)$, where $m$ is the bare (i.e. non-renormalized) quark mass. In the limiting case of $\kappa = 0$ (infinitely heavy quarks) pure gauge theory with no dynamical fermions is obtained. In this limit the Wilson and Polyakov loop act as true order parameters for the distinction between a confined phase at $\beta \geq 0$ and a deconfined phase in the limit of $\beta \to \infty$, separated by a phase transition occurring at some critical value $\beta_c$. Another limiting case is that of free dynamical lattice fermions at $\beta = \infty$ ($g = 0$). Computing the quark propagators for the free theory, the correlation length can be shown to be given by the inverse of the quark mass. Consequently the correlation length diverges for $\kappa = 1/8$. At $\beta = 0$, results from strong coupling expansion calculations indicate that the quark mass vanishes at $\kappa \approx 1/4$. The points where the quark mass vanishes are also the points where the mass of the Goldstone modes (the pions) of the system (associated with chiral symmetry breaking) vanishes. At finite values of $\beta$ the quark mass vanishes at some $\kappa$ value $1/4 > \kappa_{ch}(\beta) > 1/8$, where $\kappa_{ch}(\beta)$ defines the so called *chiral curve*. Consequently, fixing $\beta$ and tuning $\kappa$ from 0 to $\kappa_{ch}(\beta)$ the quark mass is decreased from $\infty$ to 0. The pion mass is reduced to 0 at $\kappa_{ch}(\beta)$, as well. The continuum limit can be approached in different ways. One possibility for a mass-independent renormalization scheme is to follow the chiral curve given by $\kappa_{ch}(\beta)$. Another, mass-dependent scheme is to use mass ratios like $m_\pi/m_\rho$ which for a given $\beta$ will assume its experimental value at some value of $k < \kappa_{ch}(\beta)$. At this point the scale can be set (determining the lattice spacing $a$) for which different scale-setting methods exist. This can be repeated for a series of increasing values of $\beta$ which yields a curve along which $a$ decreases to zero and that terminates at $\kappa_{ch}(\beta = \infty) = 1/8$. Note, that the lattice spacing $a$ also depends on the dynamics of sea quarks and thus is a function of $\beta$ and $\kappa$, implying that lines of constant $\beta$ are not lines of constant $a$. As a last remark, note that this discussion is held on a rather qualitative level and only has the intention of showing that establishing a true continuum result typically requires several LQCD simulations that subsequently have to be subjected to a complex analysis.

### The Renormalization Group Equation

The tuning described above is commonly referred to as the *running* of the bare parameters and can be studied by means of the renormalization group theory. The corresponding renormalization group equation to express this condition is

$$\frac{\mathrm{d}\Theta(g(a), a)}{\mathrm{d}\ln a} = \left(\frac{\partial}{\partial \ln a} + \beta\frac{\partial}{\partial g}\right)\Theta(g(a), a) = \mathcal{O}\left(\left(\frac{a}{\hat{\xi}}\right)^2 \ln\left(\frac{a}{\hat{\xi}}\right)\right), \tag{2.51}$$

where

$$\beta = \frac{\partial g}{\partial \ln a}, \tag{2.52}$$

is the renormalization group beta function[9], which determines the lattice couplings dependency on $a$. For small $g$ it can be determined from perturbation theory and reads up to second leading order:

$$\begin{aligned} \beta(g) =& -\beta_0 g^3 - \beta_1 g^5 + \mathcal{O}\left(g^7\right) \\ \beta_0 =& \frac{1}{(4\pi)^2}\left(\frac{11}{3}N - \frac{2}{3}N_f\right) \\ \beta_1 =& \frac{1}{(4\pi)^4}\left(\frac{34}{3}N - \frac{10}{3}N\,N_f - \frac{N^2-1}{N}N_f\right). \end{aligned} \tag{2.53}$$

[9] Not to be mistaken for the inverse lattice gauge coupling.

This can be used together with eq. (2.52) to find

$$a(g) = \frac{1}{\Lambda_L}(\beta_0 g^2)^{\frac{\beta_1}{2\beta_0^2}}\ \mathrm{e}^{-\frac{1}{2\beta_0 g^2}}\left(1 + \mathcal{O}\left(g^2\right)\right). \tag{2.54}$$

The introduced energy scale $\Lambda_L$ is a result of the renormalization of the theory [10]. It stems from solving eq. (2.52) via separation of the integration variables and subsequent integration. Note, that $\Lambda_L$ depends on the regularization scheme, i.e. different action lead to different values of $\Lambda_L$ whose ratios can be related by tree-level perturbation calculation. The running coupling $g(a)$ can be obtained by inversion:

$$g(a)^{-2} = \beta_0 \ln\left(a^{-2}\Lambda_L^{-2}\right) + \frac{\beta_1}{\beta_0}\ln\left(\ln\left(a^{-2}\Lambda_L^{-2}\right)\right) + \mathcal{O}\left(\frac{1}{\ln\left(a^2\Lambda_L^2\right)}\right). \tag{2.55}$$

As long as $N_f < 11N/2$ a decrease in the lattice spacing $a$ leads to a decrease of the coupling $g$ in a way such that the physical observable in eq. (2.50) remains constant. This important property is referred to as *asymptotic freedom*.

**The True Continuum Limit $a \to 0$ & $V \to \infty$**

As already indicated above, the inverse lattice coupling (c.f. eq. (2.32)) cannot simply be driven to $\beta \to \infty$ in order to arrive at the continuum limit $a \to 0$ as it would also imply $V \to 0$. Ideally before approaching the continuum limit, the infinite volume limit is taken, i.e. $N_\sigma \to \infty$ and $N_T \to \infty$. Taking the infinite volume limit $V \to \infty$ and reducing the lattice spacing $a$ to zero is also referred to as the *true continuum limit*. Apparently in a numerical simulation neither one or the other is possible. Instead in practice an extrapolation to $a \to 0$ is performed by computing physical observables for several values of $\beta$ while keeping the physical volume $L = aN_\sigma, T = aN_T$ fixed. Additionally the computations have to be repeated for different physical volumes in order to allow for an extrapolation to the infinite volume limit $V \to \infty$. Note, that finite temperature simulations of QCD ($N_\tau \ll N_\mathrm{s}$) introduce another (a thermal) phase transition related to the critical temperature $T_\mathrm{c}$, where QCD enters the deconfined phase (the quark-gluon plasma ). This thermal phase transition will be topic later on, starting in section 3. For the transitions discussed above the setting of zero temperature QCD was assumed, i.e. a large enough temporal extent $N_\tau$ such that the system stays in the confined phase. However, in lattice simulations of finite temperature QCD sometimes one has to cope with an interplay of the thermal transition and the transitions discussed above which further complicates things.

[10] This property is referred to as *dimensional transmutation*. $\Lambda_L$ can be combined with $a$ according to the standard $b_0$ convention [61]: $-\ln\left(a^2\Lambda_L^2\right) = 1/(b_0 g^2) + b_1/b_0 \ln(b_0 g^2) + \mathcal{O}(g^2)$

# Chapter 3

# LQCD Thermodynamics

From the modern renormalization-group approach we know that systems undergoing phase transitions fall into universality classes, i.e. close to a critical point the behavior of the system only depends on its dimensionalities, symmetries and range of interactions of the relevant order parameter. At finite temperature and density the system under investigation is rather three-dimensional because we are interested in its equilibrium statistical mechanics with three spatial dimensions. A temporal development is not taking place. To put it on a more formal ground, we are considering the system with Euclidean metric, where the temporal direction can be seen as a way to incorporate temperature into the systems thermodynamics. The temporal direction $N_\tau = 1/(aT)$ is fixed and small compared to the spatial size $N_\mathrm{s}$ of the box. At present LQCD is used to study systems in equilibrium rather than the evolution and decay dynamics of the system.

Keeping this in mind, in non-perturbative QCD at finite temperature and density we concern ourselves with numerous questions addressing the phase transition from the hadronic phase to the QGP and its nature predicted by QCD. In this work we are interested in the QCD phase transition at zero and at imaginary chemical potential. In particular, we look at the QCD phase transition as a function of the quark mass and investigate its nature mainly at heavy quark masses but at small quark mass, as well. This chapter provides the necessary pieces of theoretical background for these studies. The first part of section 3.1 starts with a very qualitative reminder of the different possible types of thermal phase transitions. This is followed by somewhat more technical passages about the theoretical means to detect phase transitions and how to determine their nature. Additionally the important concept of critical exponents, universality and the closely related topic of scaling laws will be discussed. The following sections 3.2 and 3.3 will enter the field of LQCD at finite temperature and zero as well as non-zero density. There I will explain how the QCD deconfinement and chiral transitions are related to the breaking of the center and chiral symmetries in the heavy and light quark mass region. The switching on of a chemical potential and its implication, the sign problem of QCD, will be explained as well as possible approaches to it, which includes a topic central to this work: a purely imaginary chemical potential. As a natural way to proceed I chose to put a brief and qualitative introduction about the notorious QCD phase diagram next in section 3.4. This serves as a starting point for the last part of this chapter, which contains a more detailed treatment about the phase structure of QCD on the lattice as a function of the quark mass while the chemical potential is fixed at zero and at the critical value of the purely imaginary chemical potential, denoted as *Roberge-Weiss (RW) plane*. The chapter is based on the presentations found in [33, 34, 50, 62–64] as well as on published studies which will be cited at the appropriate places.

## 3.1 Reminder: Phase Transitions in Statistical Mechanics

In a thermodynamic system matter can exist in different states. The possible forms of matter are fluid, vapor [1], solid and in some cases plasma. At specific values of thermodynamic quantities like temperature and pressure phase transitions between the different states of matter take place. This leads to non-analyticities in the free energy of the system as a function of thermodynamic parameters. A well known example is $H_2O$ which has transitions between ice and water, water and vapor as well as vapor and ice. The transitions are apparently accompanied by a drastic change of the properties of the substance. Depending on the type of the transition this can happen in a continuous or discontinuous way. According to the modern classification of phase transitions one distinguishes between two types of transition, motivated by the Ehrenfest classification [65]:

- First order phase transition
  If the temperature of the system is turned up until the point where it undergoes a phase transition, the temperature remains constant for a while as latent heat is added. The system absorbs a specific amount of energy per volume. During this process the two phases of the substance coexist which means that in some regions the transition is complete while in others it is not. For instance, coming back to the $H_2O$ example, at the first order transition between water and vapor the water is not turned instantly into vapor but there is rather a turbulent mixture of water and vapor bubbles. For a theoretical treatment one looks at order parameters showing a discontinuity at the transition. Their values are zero in one phase and non-zero in another phase. Examples for such order parameters are the net-magnetization in a ferromagnetic system or differences in the densities of a system at liquid/gas transitions.

- Second order phase transition
  Second order transitions are characterized by a divergence of the correlation length of the system and other quantities like the heat capacity. Moreover power-laws can be found for correlations near the critical point. The order parameter remains continuous. A typical example is a ferromagnetic system for which the order parameter is the magnetization. It is zero above and non-zero below the critical temperature. Much more can be said about second order phase transition. Some aspects are discussed in section 3.1.2.

From a theoretical view, phase transitions are often related to symmetry breaking which gives rise to order parameters. A distinction is made between spontaneous and explicit symmetry breaking. Roughly speaking, the first happens due to the system spontaneously falling into a specific state for instance due to a critical temperature that is reached. The latter one is temperature independent and depends on a quantity of the system. For instance a magnetic background field breaks the symmetry in a magnetic system explicitly. In many cases states of higher temperature (above the critical temperature) have larger symmetry content in contrast to states with lower temperature (e.g. magnetization in a ferromagnet) but there are exceptions, one of which I will discuss later in the context of QCD. Matter can change its properties rapidly in the absence of singularities, as well. Such a transition is denoted by *analytic crossover*.

[1] For the sake of completeness and correctness, gas should be mentioned, as well, since there is a strict distinction between the terms vapor and gas. For the sake of simplicity I will will not further discuss this distinction

- Crossover
  A rapid and drastic change of the physical properties of a system when a certain parameter is changed. Some quantities like the specific heat reach their maximum but do not become non-analytic. The system "crosses over" from one phase into another. A crossover is not unusual as there exist many examples. For instance water displays this kind of transition in a certain region at large temperature and pressure.

Note that according to the theorem of Lee and Yang [66, 67] non-analytic phase transitions can only occur in the thermodynamic limit $V \to \infty$ of infinitely many particles. In LQCD the partition function as a functional integral over a compact group with a bounded exponential is a analytic function of temperature T, chemical potential $\mu$ and the volume $V$. For this reason the identification of a true phase transition can only be achieved by carrying out finite size scaling (FSS) analyses on a series of increasing and, in particular, sufficiently large volumes. As a consequence, on finite volumes, where different phases are connected by a smooth analytic transition, no specific temperature value $T_\mathrm{c}$ exists at which a phase transition occurs. Instead, analytic transitions take place in a small range of temperature values. However, of course it is still necessary and important to identify a single value of the temperature at which the transition takes place. Such a temperature value for a smooth analytic transition is then referred to as pseudo-critical.

### 3.1.1 Localization of Phase Transitions

The localization of a thermal phase boundary requires to adjust the parameters of the theory to their critical values. For LQCD these parameters are the inverse lattice coupling $\beta$ (controlling the temperature), the quark mass $m_q$ and the chemical potential $\mu$. In lattice simulations with finite volumes there are no non-analytic phase transitions for which reason the critical values of the parameters are actually pseudo-critical. A common approach to find the transition, two of these parameters can be kept constant and the remaining one is varied. In this work the phase transition was located by tuning the temperature while fixing a combination of quark mass and chemical potential. As the pseudo-critical values are approached thermodynamic observables begin to change rapidly and exhibit strong fluctuations $\delta O = O - \langle O \rangle$. The thermodynamic variables of interest are the ones giving the strongest signals at a phase boundary. In the case of QCD these are typically the chiral condensate $\langle \bar{\psi}\psi \rangle$ and the Polyakov loop $P$. The fluctuations can be studied by statistical means and therefore one looks at quantities constructed from the central moments $\mu_n = \langle (\delta O)^n \rangle$. The most important ones for investigating phase transitions include

$$\mu_2 = \left\langle (\delta O)^2 \right\rangle, \qquad B_n = \frac{\mu_n}{(\mu_2)^{\frac{n}{2}}} = \frac{\langle (\delta O)^n \rangle}{\langle (\delta O)^2 \rangle^{\frac{n}{2}}}, \qquad \text{with } \delta O = O - \langle O \rangle . \tag{3.1}$$

where the second central moment $\mu_2$ is just the variance of $O$ which reaches its maximum on the phase boundary as the observable is constantly jumping between two phases. For the so-called standardized central moments $B_n$ there are in particular two interesting cases. Setting $n = 3$ gives the *skewness* which is a measure for the lopsidedness of a distribution. Positively and negatively skewed data extends more to the right and left, respectively. At a phase boundary the skewness is expected to vanish since there the distribution of $O$ is symmetric because the system equally visits all the phases. Setting $n = 4$ gives the *kurtosis* which is a measure for the weight in the tails of a distribution. The kurtosis take on the value 3 for a normal distribution whereas a value $> 3$ means that there is more weight in the tails than

expected from a normal distribution. For instance, the kurtosis of the Polyakov loop $P$ evaluated at the deconfinement transition of QCD reaches its minimum which implies that the distribution of $P$ has the least weight in its tails. $B_4$ is sometimes also referred to as the Binder cumulant [68] whose definition differs trivially by subtraction and multiplication of constants but provides exactly the same information. Here we will always use the definition of the kurtosis. In statistical mechanics the susceptibility $\chi_O$ takes on the role of $\mu_2$ to which it is proportionally linked. The central moments $\mu_n$ are proportional to the n-th order derivatives of the free energy of the system, which I will explain further below in section 3.1.3. The quantities discussed above are used in this work to investigate the nature of the QCD phase transition on the lattice and their practical application will be demonstrated in chapter 5 about the results of this work.

### Identifying the Phase Transition Type

After having located the phase boundary the next step is to identify the nature of the transition. The susceptibility $\chi_O$ diverges at a first and second order transition whereas it saturates for a crossover. The kurtosis $B_4$ takes on particular values that differ for a first or second order or a crossover-type transition. This task turns out to be challenging since, as mentioned before, on finite volumes transitions are analytic everywhere and thus a first or second order transition cannot be observed directly. Instead one examines the behavior of the susceptibility $\chi_O$ as well as $B_4$ which scale differently on a series of increasing volumes for the different types of transitions. This procedure is called finite size scaling (FSS). The remaining part of the section will be dedicated to this problem.

### Remarks about the Susceptibility $\chi_O \sim \left\langle (\delta O)^2 \right\rangle$

Susceptibilities come in many different forms. A general expression for susceptibilities in statistical mechanics systems is given by the connected correlation function

$$\chi_O = \int \mathrm{d}^3x \mathrm{d}^3y \left( \langle O(x)O(y) \rangle - \langle O(x) \rangle \langle O(y) \rangle \right). \tag{3.2}$$

If instead the spatial averages $\bar{O}$ are inserted translational invariance can be used to simplify $\chi_O$ to

$$\chi_O = V \left( \left\langle \bar{O}^2 \right\rangle - \left\langle \bar{O} \right\rangle^2 \right). \tag{3.3}$$

Note that the connected correlation function can typically be obtained from second order derivatives of the free energy $F$ of the system with respect to quantities of interest. This is particularly important when finite size scaling studies are performed since the free energy carries the information needed to derive scaling laws for quantities near a second order critical point. At such a point different theories share something that is called a universality class (see section 3.1.2) which means they scale in the same way with respect to the volume. This property can be used to learn something from simpler theories about the finite size scaling of more complex theories. For instance in magnetic spin systems the susceptibility is obtained from the second order derivative of the free energy $F$ of the system with respect to the magnetic field or the temperature. Since $F$ is an extensive quantity in thermodynamics often the energy density $f = F/V$ is studied, where $V$ is the volume. The magnetic susceptibility $\chi_h$ of the magnetization $M$ can then be defined as

$$\chi_h = -\frac{1}{T} \left. \frac{\partial^2 f(h,t)}{\partial h^2} \right|_t = \frac{1}{V} \left\langle (\delta M)^2 \right\rangle, \tag{3.4}$$

where $h = B/T$ is the reduced magnetic field and $t = |T - T_c| / T_c$ is the reduced temperature. The definition is likewise given for $\chi_t$. Note that in (3.3) spatial averages were used whereas for (3.4) extensive quantities were used which implies different volume factors. Therefore caution should be exercised in using the different definitions.

### 3.1.2 Critical Exponents and Universality

Critical exponents and universality are discussed most readily in the context of magnetic systems exhibiting a second order transition that separates a paramagnetic from a ferromagnetic phase. A well known testing ground to study magnetic spin systems is the two or three dimensional Ising model. Moreover, studying these rather simple models helps to learn something about more complex theories. For instance, the $3D$ Ising model and QCD (in a certain range of parameters) share the same universality class, a term I will explain further below. In order to convey the main ideas about the behavior of systems at second order transitions, it is enough to consider the simple the $2D$ Ising model The model possess a global $Z_2$ symmetry, i.e. the energy of the system is unchanged under a global interchange of up and down spins. Very similar ideas also apply to quantum field theories. Moreover, QCD (in a certain range of parameters) and the $3D$ Ising model share the same universality class, a term I will explain further below. For the $2D$ Ising model the partition function encoding its thermodynamical properties and its Hamiltonian are given by

$$Z = \sum_c \mathrm{e}^{-\beta H(J,B)}, \qquad H = -J \sum_{n,i} s(n)s(n+i) - B \sum_n s(n), \tag{3.5}$$

where $c$ is the index labeling the configurations and $n$ is labeling the lattice sites. The Hamiltonian $H$, as a function of the coupling $J$ and an external magnetic field $B$, takes only into account nearest neighbor couplings. $\beta$ is the inverse temperature. The sum is over the number of configurations given by $2^N$ with the number of lattice sites $N$. The key quantities to study the thermodynamic properties and the phase transition of this system are

$$F = -T \ln Z, \qquad M = \frac{1}{N}\frac{\partial F}{\partial B}, \qquad \chi = \frac{\partial M}{\partial B}, \qquad C = -T\frac{\partial^2 F}{\partial T^2}. \tag{3.6}$$

$F$ is the free energy which is the thermodynamic potential for this system. The magnetization $M$ is a function of the temperature $T$ and the external magnetic field $B$. Evaluating the expression for $M$ in eq. (3.6) gives

$$M = \left\langle \frac{1}{N} \sum_{n=1}^{N} s(n) \right\rangle. \tag{3.7}$$

It serves as an order parameter to distinguish between the paramagnetic and ferromagnetic phase. For a zero magnetic field $B$ it gives a non-zero expectation value below a critical temperature $T_c$ (the Curie temperature in the Ising model) which spontaneously breaks the $Z_2$ symmetry of the system. $M$ vanishes as the temperature is driven towards $T_c$. In the phase above $T_c$ the $Z_2$ symmetry is restored and the magnetization remains zero. On the second level of derivatives of the free energy there are $\chi$, the magnetic susceptibility that measures the effect of the magnetic field on the spins, and the specific heat $C$ that shows how the system reacts to changes in the temperature. Evaluating the expression for $\chi$ in eq. (3.6) shows

that it is a sum over the spin-spin correlation function $\Gamma(n)$ [2],

$$\chi = \frac{1}{T}\sum_n \Gamma(n), \qquad \Gamma(n) = \langle s(n)s(0)\rangle - \langle s(0)\rangle^2 . \tag{3.8}$$

At a certain critical temperature $T_\mathrm{c}$ the net magnetization $\langle s(0)\rangle$ is expected to vanish so that the spin-spin correlation function reduces to $\Gamma(n) = \langle s(n)s(0)\rangle$. As $\chi$ is a sum over the spin correlations, it can diverge in the thermodynamic limit, if the dynamics of the system develop sufficient long range correlations. Above $T_\mathrm{c}$ the correlation function falls of exponentially, i.e.

$$\Gamma(n) \sim \ \mathrm{e}^{-\frac{|n|}{\xi(T)}}, \qquad \text{for } \ T > T_\mathrm{c}. \tag{3.9}$$

The spins might be disordered but the system may save energy by allowing spins in certain regions to point into the same direction. In the relation above $\xi(T)$ is the correlation length which is a measure for the spatial distance over which the spins are correlated (c.f fig. 3.1). Below $T_\mathrm{c}$ the magnetization is non-zero and thus average fields have to be subtracted as it is done in eq. (3.8) but the behavior is still described by eq. (3.9). The subtraction of the average fields shows the fluctuations away from perfect order.

It has been observed experimentally for magnetic systems that all of the quantities in eq. (3.6) in the vicinity of a critical point $T_\mathrm{c}$ display power-law behavior as a function of the temperature, i.e. they become free from any dependence on a length scale like $\xi$. This implies that characteristic fluctuations occur over all length scales, a property that applies to many other systems as well. These powers are given in form of the critical exponents $\alpha, \gamma, \delta, \beta, \nu$ and $\eta$. Typically the behavior is defined via the reduced temperature $t = (T - T_\mathrm{c})/T_\mathrm{c}$. The physical quantities are related to the critical exponents as follows:

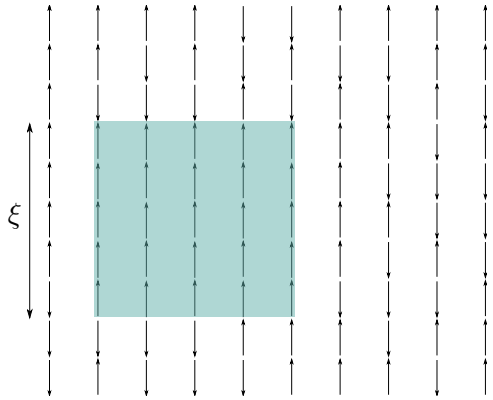


Figure 3.1: A ferromagnetic fluctuation of length $\xi$.

- magnetization $M \sim (-t)^\beta$,
- susceptibility $\chi \sim |t|^{-\gamma}$,
- correlation function

$$\Gamma(n) \sim \begin{cases} \mathrm{e}^{-\frac{|n|}{\xi}} & |n| \gg \xi \\ |n|^{-d+2+\eta} & |n| \ll \xi, \end{cases}$$

  where $d$ is the systems dimensionality,
- specific heat $C \sim |t|^{-\alpha}$, and
- correlation length $\xi \sim |t|^{-\nu}$.

The effect of an infinitesimal $B$ field on the system at $T = T_\mathrm{c}$ is determined by $\delta$:

- $M, \chi \sim B^{1/\delta}$, for both $M$ and $\chi$ likewise.

[2] After computing the derivative $\chi = \partial M/\partial B$ translational invariance was used to simplify the appearing spin sums.

The important piece of information is that at a critical point the correlation length diverges, leading to huge fluctuations and singularities in some thermodynamic quantities even if the coupling of the system is short ranged. The characteristic length scales disappear and the thermodynamic quantities follow scale-invariant power laws determined by the critical exponents.

Universality classes describe classes of systems that have the same power behavior at a critical point. In some ferromagnets the behavior of thermodynamic quantities at a phase transition is determined by the same critical indices as it is the case for some liquid crystals. Within a universality class the collective behavior is characterized by

- the dimensionality of a system,
- the symmetries of the local variables in the energy of the system,
- the symmetries of the coupling between the local variables, and
- the range of couplings in the energy.

The universality classes are characterized by spin models as they can be solved analytically or inexpensively by numerical means in contrast to more complicated theories like QCD. In fact, for QCD and many other systems usually several universality classes are of relevance because in such systems the related global symmetries are determined dynamically in the vicinity of a critical point.

### 3.1.3 Scaling Laws

#### Scaling of the Free Energy

A de facto standard framework for the description of universality classes and critical phenomena in general is Wilsons renormalization-group approach that was introduced in 1974 and comprehensibly presented in his detailed work [69]. The analysis relies on a variation of the length scale at which the physics are investigated. Some time before the onset of Wilsons renormalization-group theory Widom [70] proposed a hypothesis about the behavior of a magnetic system near a critical point. He assumed that experimental findings might be explained if the free energy density ($f = F/V$) has a certain form under the transformation of the length scale. According to his hypothesis under a scaling of the length $L \to bL$ with an arbitrary factor $b$ the singular part of the free energy density is expected to behave like

$$f_s(t,h) = b^{-d} f_s(t',h'), \quad t' = b^{y_t} t, \quad h' = b^{y_h} h, \tag{3.10}$$

with the reduced temperature $t$ as before and the reduced field $h = B/T$. The so called temperature and magnetic exponents $y_t$ and $y_h$ are yet to be determined. Eq. (3.10) and the relations between the free energy and the thermodynamic observables like the magnetization, specific heat and susceptibility (c.f. eq. (3.6)) can be used to write critical exponents in terms of $y_t$ and $y_h$:

$$\begin{aligned} \alpha = 2 - \frac{d}{y_t}, \quad \beta = \frac{d - y_h}{y_t}, \quad \gamma = \frac{2y_h - d}{y_t}, \\ \delta = \frac{y_h}{d - y_h}, \quad \nu = \frac{1}{y_t}, \quad \eta = 2 + d - 2y_h. \end{aligned} \tag{3.11}$$

The exponents $y_t$ and $y_h$ can be determined using the renormalization-group approach by seeing how the fields $t$ and $h$ flow under renormalization. This then gives access to the critical exponents which can be compared with experimental observations.

### Scaling Properties in QCD

In [71] it was proposed to study scaling properties of QCD with an effective Hamiltonian in analogy to spin models,

$$\frac{H_{\text{eff}}}{T} = \tau\mathcal{E} + h\mathcal{M}, \tag{3.12}$$

that controls the dynamics and the universal critical behavior in the vicinity of a second order point. $\mathcal{E}$ and $\mathcal{M}$ are extensive energy-like and magnetization-like operators with their respective couplings[1] $\tau$ and $h$. In QCD finite values of the quark mass break all global symmetries explicitly for which reason they are non-trivially related to the symmetries of $H_{\text{eff}}$. Thus it can be expected that the QCD operators $O = \{\langle\bar{\psi}\psi\rangle, P, \ldots\}$ and the relevant couplings $\beta, m_q$ are mixtures [2] of $\mathcal{E}, \mathcal{M}$ and $\tau, h$, respectively. Renormalization-group arguments show that the scaling hypothesis for the singular part of the free energy density (c.f. eq. (3.10)) can be applied, i.e.

$$f_s = b^{-d} f_s(b^{y_t}\tau, b^{y_h}h). \tag{3.13}$$

The arbitrary scale factor $b$ can be set to $b = LT = N_{\text{s}}/N_\tau$ to give the spatial extent of the lattice in units of inverse temperature.

### Scaling of the Susceptibilities

Knowing the scaling form of the free energy density $f$ the scaling of related quantities like the temperature and magnetic field susceptibilities $\chi_\tau$ and $\chi_h$ near a second order critical point can be deduced:

$$\begin{aligned}
\chi_\tau &\sim b^{-d}\frac{\partial^2 f(\tau b^{y_\tau}, hb^{y_h})}{\partial\tau^2} = b^{-d+2y_\tau} f''(\tau b^{y_\tau}, hb^{y_h}) = b^{\alpha/\nu} f''(\tau b^{y_t}, hb^{y_h}),\\
\chi_h &\sim b^{-d}\frac{\partial^2 f(\tau b^{y_\tau}, hb^{y_h})}{\partial h^2} = b^{-d+2y_h} f''(\tau b^{y_\tau}, hb^{y_h}) = b^{\gamma/\nu} f''(tb^{y_\tau}, hb^{y_h}).
\end{aligned} \tag{3.14}$$

In the last step the relations in (3.11) have been used. As the scaling factor $b$ is arbitrary it can be set to the linear extent $L$ of the system. With the scaling factor $b = N_{\text{s}}/N_\tau$ chosen as before the following scaling relation can be obtained:

$$\chi_h/N_{\text{s}}^{\gamma/\nu} = \Phi(\tau N_{\text{s}}^{1/\nu}), \tag{3.15}$$

where $\Phi$ is a scaling function proportional to the second derivative of the free energy density $f$. In the previous paragraph I explained that the QCD operators are mixtures of energy-like and magnetization-like operators. Therefore, if $\chi$ is constructed from QCD operators $O = \{\langle\bar{\psi}\psi\rangle, P, \ldots\}$, its finite size scaling behavior will be dominated by the larger of $\gamma/\nu$ or $\alpha/\nu$. For the universality classes of QCD, $Z_2$, $O(4)$ and $O(2)$, this is $\gamma/\nu$. Thus, if $\chi_h/N_{\text{s}}^{\gamma/\nu}$ is plotted against $\tau N_{\text{s}}^{1/\nu}$ all curves from different volumes labeled by $N_{\text{s}}$ should coincide. It can be useful to rule out scenarios for the order of a phase transition by inserting the respective values of the critical exponents. For instance in the crossover regime the curves $\Phi(\tau N_{\text{s}}^{1/\nu})$ for different $N_{\text{s}}$ do not coincide for the second order value of $\gamma/\nu$.

[1] In the case of the Ising models discussed above, $\tau$ and $h$ are proportional to temperature and magnetic field.

[2] In [71] a thorough analysis and numerical study about the mixing of the LQCD observables has been done.

### Scaling of the Kurtosis ($B_4$)

For the kurtosis introduced in section 3.1.1 scaling relations can be derived likewise. As $B_4$ is constructed from moments of the fluctuations $\delta O$ it can be written in terms of fractions of derivatives of the free energy [3]. Following the presentation in [72] the expression for magnetization-like operators $M$ is given by derivatives with respect to $h$,

$$B_4(\tau,0) = \frac{F^{(4)}(\tau,h)\big|_{h=0}}{\left(F^{(2)}(\tau,h)\big|_{h=0}\right)^2} = \frac{N_\mathrm{s}^{4y_\tau}F^{(4)}(N_\mathrm{s}^{y_\tau}\tau,0)}{\left(N_\mathrm{s}^{2y_\tau}F^{(2)}(N_\mathrm{s}^{y_\tau}\tau,0)\right)^2} = \frac{F^{(4)}(N_\mathrm{s}^{y_\tau}\tau,0)}{\left(F^{(2)}(N_\mathrm{s}^{y_\tau}\tau,0)\right)^2}, \tag{3.16}$$

where

$$F^{(n)}(\tau,h) = \frac{\partial^n F(\tau,h)}{\partial h^n}. \tag{3.17}$$

In the second step of (3.16) the scaling of the free energy density was used, setting the scaling factor $b = N_\mathrm{s}$. Then $B_4(\tau,0)$ can be expanded around $\tau = 0$ which corresponds to the critical point at which the system undergoes a second order phase transition and obtain [4]

$$B_4(\tau,0,N_\tau) = \frac{F^{(4)}(0)}{\left(F^{(2)}(0)\right)^2} + A\tau N_\mathrm{s}^{1/\nu} + \mathcal{O}\left(\left(\tau N_\mathrm{s}^{1/\nu}\right)^3\right), \tag{3.18}$$

where $y_\tau = 1/\nu$ was used (see (3.11)). For $\tau > 0$, $B_4(\tau,0,N_\tau)$ is volume dependent but at $\tau = 0$ this dependency vanishes and the curves $B_4(\tau,0,N_\tau)$ for different $N_\tau$ intersect, i.e. they share the common value $B_4 = F^{(4)}(0)/\left(F^{(2)}(0)\right)^2$. This is no surprise as all the characteristic length scales of the system loose their meaning close to a critical point and $B_4(\tau,0,N_\tau)$ is expected to take on its universal value $B_4$ specific to the corresponding universality class. Therefore one can write

$$B_4(\tau,0,N_\tau) = B_4 + A\tau N_\mathrm{s}^{1/\nu} + \mathcal{O}(N_\mathrm{s}^{2/\nu}). \tag{3.19}$$

This equation can be used to simultaneously fit LQCD Data describing the curves $B_4(\tau,0,N_\tau)$, sharing the parameters $B_4$ and $A$. This procedure is nothing but a finite size scaling analysis. In this context of intersecting curves $B_4(\tau,0,N_\tau)$ the fitting procedure is sometimes referred to as intersection analysis of $B_4$ in the literature. In QCD the observables of interest are mixtures of energy-like and magnetization-like operators and in this case the kurtosis should be constructed respectively. Therefore one considers mixed derivatives of the free energy with respect to $\tau$ and $h$:

$$F^{(nm)}(\tau,h) = \frac{\partial^n}{\partial\tau^n}\frac{\partial^m}{\partial h^m}F(\tau,h). \tag{3.20}$$

In this case $B_4$ comes with an additional factor $N_\mathrm{s}^{y_\tau-y_h}$. To first order in $N_\mathrm{s}^{y_\tau-y_h}$ the result is

$$B_4(\tau,0,N_\tau) = \frac{F^{04}(N_\mathrm{s}^{y_\tau}\tau)}{\left(F^{02}(N_\mathrm{s}^{y_\tau}\tau)\right)^2}\left(1 + BN_\mathrm{s}^{y_\tau-y_h} + \mathcal{O}\left(N_\mathrm{s}^{2(y_\tau-y_h)}\right)\right), \tag{3.21}$$

and the expansion around $\tau = 0$ reads

$$B_4(\tau,0,N_\tau) = \left(B_4 + AtN_\mathrm{s}^{1/\nu} + \mathcal{O}(N_\mathrm{s}^{2/\nu})\right)\left(1 + BN_\mathrm{s}^{y_\tau-y_h} + \mathcal{O}\left(N_\mathrm{s}^{2(y_\tau-y_h)}\right)\right). \tag{3.22}$$

The full derivation is given in A.1. Note that $B_4(\tau,0,N_\tau)$ is volume dependent even for $\tau = 0$. However, for the universality classes relevant for QCD the difference $y_\tau - y_h$ is negative and thus the additional correction term $(1 + BN_\mathrm{s}^{y_\tau-y_h})$ becomes irrelevant for sufficiently large volumes.

[3] Note, that the free energy $F$ was used instead of the free energy density $f = F/V$ because the volume factors $V$ simply cancel out.

[4] The reason that there is no second order term is that the $Z_2$ point represents an inflection point of $B_4$.

**Summary of Exponents and Quantities Specific to Universality Classes and Transitions**

| | $Z_2$ Ising | $O(2)$ | $O(4)$ | $1^{st}$ order triple | Tricritical | Crossover |
|---|---|---|---|---|---|---|
| $B_4$ | 1.604 \| [73] | 1.242(2) \| [74] | 1.092(3) \| [75] | 1.5 | 2 | 3 |
| $\nu$ | 0.6301(4) | 0.6703(13) \| [76] | 0.7479(90) \| [75] | 1/3 | 1/2 | – |
| $\alpha$ | 0.1101(1) | -0.011(4) \| [76] | -0.25 \| [72] | – | – | – |
| $\gamma$ | 1.2373(2) | 1.3169(20) \| [76] | 1.477(18) \| [75] | 1 | 1 | – |
| $1/\nu$ | 1.5870(9) | 1.4917(29) | 1.337(16) \| [75] | 3 | 2 | – |
| $\alpha/\nu$ | 0.1747(2) | -0.0164(60) | -0.3342(40) | – | – | – |
| $\gamma/\nu$ | 1.9637(13) | 1.9646(50) | 1.9746(38) \| [75] | 3 | 1/2 | – |
| $y_t - y_h$ | -0.8944(6) | -0.9905(38) | -1.1546(100) | | | |

Table 3.1: Summary of critical exponents and $B_4$ for universality classes $Z_2$ Ising, $O(2)$ and $O(4)$ as well as for $1^{st}$ order triple, tricritical and crossover transitions. The values refer to the three-dimensional case. The values in blue color are just computed from the available non-colored entries in the tables. For the last row $1/2\nu(\alpha - \gamma) = y_t - y_h$ has been used.

Provided a reference for the values could be found in the literature, it is cited by the numbers $[xx]$.

Table 3.1 summarizes the critical exponents for the three universality classes $Z_2$ Ising, $O(2)$ and $O(4)$ for the 3-dimensional case relevant for QCD. Values of the exponents for $1^{st}$ order triple, tricritical and crossover transitions are listed, as well. The values of the $O(4)$ column have been determined (except $\alpha$ an $\alpha/\nu$) in [75] with Monte Carlo simulations of the three-dimensional classical $O(4)$ Heisenberg model whose universality class is considered a candidate for the finite temperature transition in QCD with two massless quark flavors. The estimated values present an update of the values obtained from the $4 - \varepsilon$ expansion method with errors reduced to about the half. The 3D $O(2)$ universality class is another possible candidate for the finite temperature transition in QCD with two massless quark flavors. The exponents have been determined in [76] for the N-vector model against the background of RG functions (seven loop order) of the 3D $\phi^4$ field theory using techniques related to Borel summation techniques.

## 3.2 Finite Temperature LQCD at Zero Baryon Density

The partition function of a statistical thermal system, given by

$$Z = \mathrm{Tr}\left[\, \mathrm{e}^{-\beta H}\right], \tag{3.23}$$

is equivalent to the partition function of the path integral formalism. In this expression $\beta$ corresponds to the inverse temperature, as it is the usual notation in statistical mechanics. In section 2.2 it was said that the path integral partition function in eq. (2.8) can be derived from the general euclidean partition function in eq. (2.3), where the factor $T$ in the exponential is a formal maximal temporal extent. In LQCD this is simply the temporal lattice extent given by the product $aN_\tau$ of lattice spacing and number of temporal lattice sites. The partition function can be obtained from the euclidean time transporter or transfer matrix

$\mathrm{e}^{-aH}$ that connects two temporal time slices:

$$Z = \int \prod_{\tau} \left( \mathcal{DU}_i(\tau, \mathbf{x}, ) \, \mathrm{e}^{-aH} \right) = \hat{\mathrm{Tr}} \left[ \left( \mathrm{e}^{-aH} \right)^{N_\tau} \right] = \hat{\mathrm{Tr}} \left[ \, \mathrm{e}^{-aN_\tau H} \right]. \tag{3.24}$$

A detailed derivation is presented in [50]. By comparing eq. (3.24) with eq. (3.23) it becomes apparent that the inverse temperature can be identified with the temporal extent of the lattice

$$\frac{1}{T} = aN_\tau \qquad (T \mathrel{\widehat{=}} \text{Temperature}). \tag{3.25}$$

In a correlation function like in eq. (2.2) taking the limit of $N_\tau \to \infty$ projects onto the vacuum expectation value, i.e. the expectation value at zero temperature. Of course, in numerical lattice simulations $N_\tau$ is always finite but if the intention is to study vacuum physics the temporal extent is chosen large enough such that it can be considered to approximate the limit $N_\tau \to \infty$ sufficiently well. Accordingly, in finite temperature simulations $N_\tau$ is chosen sufficiently small such that contributions from excited energy states with Boltzmann weights $\mathrm{e}^{-aN_\tau \Delta E}$ become significant. Small $N_\tau$ has further important physical implications: If fields are Fourier transformed to change between momentum and position space representation the associated Matsubara frequencies $l2\pi/(aN_\tau)$ for Bosons are discrete and limited to $(-\pi/a, \pi/a]$. The value of $l$ is restricted by $-N_\tau/2 + 1 \leq l \leq N_\tau/2$ and hence $N_\tau$ determines the number of possible Matsubara frequencies. This practically means there are fewer and coarser energy levels separated by $2\pi/(aN_\tau)$. For fermions there is and additional shift $\pi/(2aN_\tau)$ which leads to odd Matsubara frequencies. As the thermodynamic limit $V \to \infty$ is approached the Matsubara frequencies stay discrete due to the compactified time dimension opposed to the spatial components of the Fourier sum, which become continuous. This results in Feynman rules different from vacuum physics. For a thorough treatment of the topic see [36]. A further complication shows up when studying exponential decay properties in time direction of for instance particle propagators. At small $N_\tau$ there are only few time steps that can be followed so that the exponential curve cannot be well resolved. A method introduced in [77, 78] and discussed in detail in [50] suggests to deal with this problem by introducing different lattice spacings $a$ and $a_T$ in spatial and temporal direction, respectively. Then $N_\tau$ can be increased while fixing the physical temporal extent $L_T$ and keeping $L/L_T$ large, without having to increase the number of spatial lattice points $N$.

### 3.2.1 Controlling Temperature & Constraints on Lattice Paremeters

From eq. (3.25) it is apparent that the Temperature $T$ is a function of the number of temporal lattice sites $N_\tau$ and the lattice spacing $a$. Using $N_\tau$ the temperature can only be changed in discrete steps of a size depending on $a$ which in general is impractical. In contrast $a$ allows for a continuous variation of $T$. This for instance enables to scan precisely for the critical temperature $T_\mathrm{c}$ at which the system undergoes a thermal transition. Using this property it should be kept in mind, that different values of $a$ imply different cut-off effects. The parameter $a$ can only be controlled indirectly by the inverse lattice coupling $\beta(g(a))$ (eq. (2.32)). The relation between the lattice coupling $g$ and $a$ is stated in eq. (2.54). The snag with this relation is, that it is derived from perturbation theory which is not convergent for the lattice spacings accessible in current finite temperature lattice simulations. However, the lattice spacing $a$ can be determined by different scale setting methods, one of which is the Wilson flow method (see for instance [79]), which is used in this work.

If systematic errors like finite volume and discretization effects are to be avoided there are several conditions to be fulfilled. One such case for instance concerns discretization errors of hadron masses in a low temperature regime. The extent of a hadron is given by its Compton wavelength that is the inverse of the hadron mass. The Compton wavelength of the hadron should be significantly larger than the lattice spacing, i.e. $a \ll 1/m_{\mathrm{h}}$ or $am_h \ll 1$, respectively. If this condition is not met, the extraction of a hadron mass by means of a lattice calculation in a standard way will not yield a meaningful result. A common way of speaking about this is to say "the hadron falls through the lattice". However, at present there are situations, e.g. finite temperature simulations with heavy quarks, where it might not possible to access sufficiently small lattice spacings to meet this criterion due to computational restrictions. In fact often the lattice mass is $am_h \approx 1$ or even larger. If one desires to obtain a meaningful result in this case, more elaborate methods have to be consulted, like extracting the mass in the framework of *Heavy Quark Effective Theory (HQET)* or *Non-Relativistic Quantum Chromodyanmics (NRQCD)*. However, note that these are different theories and trying to employ HQET or NRQCD to solve or work around problems like $am_h > 1$ occuring in finite temperature LQCD simulations with e.g. Wilson fermions could turn out to a be difficult - not to say impossible - task, since matching quantities in both theories might simply not be possible. On the other handside the extent of the lightest degree of freedom should be small compared to the spatial extent of the system, in order to avoid finite volume effects. Together with the previous constraint this can be summarized as:

$$a \ll m_h^{-1} \ll aN_{\mathrm{s}}. \tag{3.26}$$

In simulations with large temperatures additional restrictions should be respected. As mentioned in the last section the Boltzmann weights become noticeable at sufficiently small temporal extent. This implies that screening masses scale like $m_h \sim T = 1/aN_\tau$. In conjunction with the right inequality of eq. (3.26) this implies

$$\frac{1}{T} = aN_\tau \ll aN_{\mathrm{s}}. \tag{3.27}$$

The left inequality implies

$$1 \gg am_h \sim aT = \frac{1}{N_\tau}. \tag{3.28}$$

In summary this combines to

$$N_\tau^{-1} \ll 1 \ll N_{\mathrm{s}} N_\tau^{-1}. \tag{3.29}$$

### 3.2.2 The QCD Deconfinement Transition

In this section I will discuss aspects of the QCD deconfinement transition, i.e. the transition at which QCD changes from the phase in which quarks and gluons are confined into the phase where they are deconfined - the quark-gluon plasma . The starting point will be Yang-Mills (pure gauge) theory, i.e. the quenched theory for which the quark determinant is set to unity implying infinitely heavy and thus static quarks. Against this background I will meet the announcement from section 2.7 to further motivate the Polyakov loop as an order parameter for the deconfinement transition As a natural follow up of the discussion I will address the $Z_3$ center symmetry of QCD as its breaking is associated to the deconfinement transition. I will also address the case of leaving pure gauge theory through the inclusion of dynamical fermions.

### The Polyakov Loop as Order Parameter for the Deconfinement Transition

We consider Yang-Mills theory where the quark determinant is set to unity and which is referred to as quenched QCD. This means the quarks are infinitely heavy and static. In section 2.7 it was shown that the static quark-antiquark potential can be extracted from the correlator of two Polyakov loops situated at spatial sites $\mathbf{m}$ and $\mathbf{n}$. In the language of thermodynamics, the potential is simply the free energy between a quark and an antiquark separated by $r = a\,|\mathbf{m} - \mathbf{n}|$, i.e.

$$\langle P(\mathbf{m}) P(\mathbf{n}) \rangle \propto \mathrm{e}^{-F_{\bar{q}q}(r)/T}. \tag{3.30}$$

For large distances separating the quark and the antiquark the correlator factorizes and because of its translational invariance can be expressed as the square of the absolute value of the Polyakov loop:

$$\lim_{r\to\infty} \langle P(\mathbf{m}) P(\mathbf{n}) \rangle = \langle P(\mathbf{m}) \rangle \langle P(\mathbf{n}) \rangle = |\langle P \rangle|^2 . \tag{3.31}$$

Then $|\langle P \rangle|$ represents the probability to observe a single static color charge with a purely timelike world line. The actual expectation value is computed by averaging over the spatial box and is related to the free energy needed to put an external static color source in the fundamental representation to the system:

$$\mathrm{e}^{-F_q/T} \propto |\langle P \rangle| = \left| \left\langle \frac{1}{N^3} \sum_{\mathbf{n}\in\Lambda} P(\mathbf{n}) \right\rangle \right| . \tag{3.32}$$

At low temperature the theory is expected to be in a phase where quarks are confined through flux tubes. These create a linear confining potential implying an energy per unit length of the flux tube. In this phase the Polyakov loop represents a heavy static quark impurity which requires an infinite free energy $F_q$ in order to be put into the system because it acts as the source of an "infinitely" long flux tube. Another way of seeing it is to view $F_q$ as the energy needed to remove a static quark to infinity. Doing so would infinitely extent the flux tube between two color sources resulting in a infinitely large free energy. Accordingly, in the thermodynamic limit, the expectation value $|\langle P \rangle|$ must vanish. In contrast in a finite box the free energy diverges as the linear spatial dimension of this box. As the system is heated a thermal transition to a deconfined phase is expected to take place at a temperature $T_\mathrm{c}$, consisting of a hot and dense quark-gluon plasma in which the gluons Debye-screen the quarks color field. If a quark in the fundamental representation of color $SU(3)$ is inserted into the plasma its field gets screened exponentially and thus is short-ranged. Moreover the string tension of the static quark-antiquark potential should vanish. Thus also the free energy of a static quark put into or removed from the system remains finite. This implies a non-vanishing expectation value $|\langle P \rangle|$ in the deconfined phase. Fundamental works about this topic are [80, 81]. It is also important to consider the two limiting cases of the theory in which the discussed properties can be readily read off. In the limit of $T \to 0$ of the low temperature phase $\mathrm{e}^{-F_q/T}$ vanishes and so clearly does the expectation value $|\langle P \rangle|$. The opposing limit $T \to \infty$ in the large temperature phase corresponds to infinitely large inverse lattice coupling, i.e. vanishing lattice coupling for which $U_0 = \mathbb{1}$. Accordingly, the expectation value of the Polyakov loop takes the value $|\langle P \rangle| = 3$ for $SU(3)$. The conclusion is that the Polyakov loop acts as an order parameter for pure gauge theory distinguishing between a confined phase where free charges cannot exist and a deconfined phase where single charges get screened and can be observed. This can be summarized as follows:

$$\begin{array}{llll} \langle P \rangle = 0 & \text{confinement} & T < T_\mathrm{c} & F_q \text{ is infinite} \\ \langle P \rangle \neq 0 & \text{deconfinement} & T > T_\mathrm{c} & F_q \text{ is finite} \end{array} \tag{3.33}$$

The order parameter has been studied for an effective 3-dimensional spin model with a global $Z_3$ symmetry [82]. Universality arguments led to the suggestion for a first order transition in the limit of infinitely heavy quark masses. This could be confirmed already some time ago by numerical simulations of quenched QCD.

### The $Z_3$ Center Symmetry in the limit $m_q \to \infty$

Of course, the phase transition needs to be associated to the breaking of a global symmetry group. The Polyakov loop as an order parameter is a locally gauge invariant quantity so the question arises if there is a global component related to $SU(3)$ color rotations that leaves the Polyakov loop non-invariant. The answer is yes such a transformation exists, namely the center transformation. A center transformation is a gauge transformation with $SU(3)$ matrices that are only periodic in time direction up to an additional factor,

$$\Omega(\mathbf{n}, t + N_\tau) = c\,\Omega(\mathbf{n}, t), \tag{3.34}$$

where $c$ belongs to the center of the group consisting of the cubic roots[5],

$$c = z\mathbb{1} \in Z(N) \qquad z = \mathrm{e}^{i\frac{2\pi n}{N}} \qquad n \in \{0, \ldots, N-1\}. \tag{3.35}$$

The $SU(3)$ center elements are thus given by

$$c \in \{\mathbb{1},\ \mathrm{e}^{i\frac{2\pi}{3}}\mathbb{1},\ \mathrm{e}^{-i\frac{2\pi}{3}}\mathbb{1}\}. \tag{3.36}$$

The transformation is applied to all temporal links in a given temporal times slice $n_4 = t_0$. The gauge action is invariant under such a transformation since it contains only trivially closed loops that go through the specific plane $n_4 = t_0$ one time for each direction, i.e. they have as many center elements in one direction as in the opposite. Since the center elements are proportional to the unit matrix they commute with every other group element and simply cancel out in the closed loops. For instance the center transformation of a plaquette in the time slice $n_4 = t_0$

$$P_{\mu\nu}(n) = U_\mu(\mathbf{n}, t_0)U_\nu(\mathbf{n} + \hat{\mu}, t_0)U_\mu^\dagger(\mathbf{n} + \hat{\nu}, t_0 + 1)U_\nu^\dagger(\mathbf{n}, t_0), \tag{3.37}$$

is given by

$$\begin{aligned} P_{\mu\nu}(n) \longrightarrow P'_{\mu\nu}(n) &= U_\mu(\mathbf{n}, t_0)zU_4(\mathbf{n} + \hat{\mu}, t_0)U_\mu^\dagger(\mathbf{n} + \hat{\nu}, t_0 + 1)z^\dagger U_4^\dagger(\mathbf{n}, t_0) \\ &= P_{\mu\nu}(n), \end{aligned} \tag{3.38}$$

which is invariant since $zz^\dagger = \mathbb{1}$. In contrast the Polyakov loop is sensitive to this transformation, since it is not a trivially closed loop but winds around the compact temporal direction picking up a factor $z$ when a center transformation is applied. This factor is not canceled because no other part of the loop is going

[5] A complex exponential can be written alternately in terms of a root, for instance $\exp(-i2\pi/3) = -\sqrt[3]{-1}$.

through the temporal boundary in the opposite direction. The transformation reads

$$\begin{aligned} P(\mathbf{n}) \longrightarrow P'(\mathbf{n}) &= \mathrm{Tr}\left[\Omega(\mathbf{n},t_0)\left(\prod_{n_4=t_0}^{N_\tau-1} U_4(\mathbf{n},n_4)\right)\Omega^{-1}(\mathbf{n},N_\tau)\right] \\ &= \mathrm{Tr}\left[\Omega(\mathbf{n},t_0)\left(\prod_{n_4=t_0}^{N_\tau-1} U_4(\mathbf{n},n_4)\right)\Omega^{-1}(\mathbf{n},t_0)c^{-1}\right] \\ &= z^*\mathrm{Tr}\left[\prod_{n_4=t_0}^{N_\tau-1} U_4(\mathbf{n},n_4)\right] \\ &= z^* P(\mathbf{n}). \end{aligned} \tag{3.39}$$

Considering again the two cases in eq. (3.33) it becomes apparent that the center symmetry breaks spontaneously above a critical temperature $T_\mathrm{c}$ where the Polyakov loop develops a ground state expectation value [83]. In the thermodynamic limit $\langle P\rangle$ is settled in one of the center sectors given by the cubic roots. In finite temperature LQCD simulations the finite volume leads to tunneling between the three sectors located at the points corresponding to the cubic roots in the complex plane, spoiling a reliable estimation of $\langle P\rangle$. Simulating larger volumes suppress this tunneling but the systematic error is not under control. Instead $\langle|P|\rangle$ can computed which, in the thermodynamic limit, coincides with the quantity of interest, $|\langle P\rangle|$ (c.f. eq. (3.32)) [6].

### Dynamical Fermions and $Z_3$ Symmetry

Including dynamical fermions implies having finite quark mass, i.e. leaving the quenched case where quarks are infinitely heavy and static. The quark mass is then controlled via the corresponding parameter. For instance for the Wilson discretization of fermions (see section 2.6) this parameter is the so called hopping parameter $\kappa$. In section section 2.2 it was already explained that fermions require anti-periodic boundary conditions in time. Under a center transformation

$$\begin{aligned} \psi(\mathbf{n},N_\tau) \to \psi'(\mathbf{n},N_\tau) &= \Omega(\mathbf{n},N_\tau)\psi(\mathbf{n},N_\tau) \\ &= -c\,\Omega(\mathbf{n},t_0)\psi(\mathbf{n},t_0), \end{aligned} \tag{3.40}$$

the only allowed value for the center element is $c = \mathbb{1}$. Thus taking into account dynamical fermions breaks the center symmetry explicitly. Another way of viewing it is to remember that the fermion determinant can be written as the exponential of a sum over all possible closed loops of gauge links including the ones winding non-trivially around the compactified time direction, i.e. Polyakov loops. Therefore the QCD action is not invariant anymore under a multiplication of the temporal gauge links in a time slice. Physically the pair production of the quarks screens the confining force which leads to string breaking of the potential between two quarks and therefore $F_q$ is always finite. In other words, the flux tube created by a color source represented by the Polyakov loop gets always terminated by the dynamical quarks in the system. An important implication is that a non-analytic phase transition as function of temperature is not necessary anymore. The confined and deconfined regions can be analytically connected by a crossover transition. It will be discussed later on that for large quark masses (small values of $\kappa$ for Wilson fermions) the deconfinement transition remains non-analytic in the thermodynamic limit but that it weakens and turns into a crossover as the quark masses are decreased. The Polyakov loop has a

[6] For $V \to \infty$ the distribution $\mathcal{P}(|P|)$ approaches a $\delta$-distribution.

non-vanishing expectation value for all values of the temperature and hence is not a true order parameter anymore. If a true order parameter is desired one has to seek for alternatives. One such alternative is investigated in [84] where a gauge invariant two-point function is studied that can be used to distinguish between phases of gauge theories with matter fields. However, the Polyakov loop still serves to determine the deconfinement transition by studying its distribution. The methods for doing so will be explained in the upcoming sections.

### Chiral Symmetry and Deconfinement in the Light Quark Mass Region

Lets move away from heavy quark masses all the way to the opposite limit of vanishing quark masses where chiral symmetry properties of QCD become relevant. At zero quark mass the classical QCD Lagrangian is invariant under chiral rotations which are characterized by the symmetry group

$$U_A(1) \times SU_L(N_f) \times SU_R(N_f), \tag{3.41}$$

consisting of the anomalous $U_A(1)$ that is broken down to $Z(N_f)$ by quantum corrections and $SU_L(N_f) \times SU_R(N_f)$ that is spontaneously broken to $SU_V(N_f)$, generating $N_f^2 - 1$ Goldstone bosons which are the pions $(\pi^+, \pi^0, \pi^-)$ for $N_f = 2$. The order parameter for distinguishing between a chirally broken and a chirally symmetric phase is the quark chiral condensate

$$\left\langle \bar{\psi}\psi \right\rangle = \frac{1}{N_s^3 N_\tau} \frac{\partial}{\partial m^{(f)}} \ln Z, \tag{3.42}$$

which assumes a non-zero value at a temperature $T < T_{\text{ch}}$ where chiral symmetry is spontaneously broken and a zero value at a temperature $T > T_{\text{ch}}$ where chiral symmetry is unbroken, i.e.

$$\begin{aligned} \left\langle \bar{\psi}\psi \right\rangle &= 0 \qquad \text{chirally broken phase} \qquad T < T_{\text{c}} \\ \left\langle \bar{\psi}\psi \right\rangle &\neq 0 \qquad \text{chirally symmetric phase} \qquad T > T_{\text{c}} \end{aligned} \tag{3.43}$$

The order of the phase transition in the limit $m_q \to 0$ can be either of first or second order and depends heavily on the number of flavors and their respective quark masses, about which I will tell more later in section 3.5.2. In the case of non-zero quark mass the chiral symmetry gets broken explicitly and the chiral condensate is $\left\langle \bar{\psi}\psi \right\rangle \neq 0$ for all values of $T$. Then a non-analytic phase transition is possible but not necessary anymore, i.e. the two phases can be connected by a smooth crossover transition. As it is the case for $\langle P \rangle$ the chiral condensate is no longer an order parameter in the strict sense but using it to study the phase transition is still perfectly legitimate. In LQCD chiral symmetry can be broken even for vanishing quark masses by the discretization, e.g. Wilson fermions (see section 2.6), or have a reduced version of chiral symmetry, as in the case of staggered fermions with a $U(1)$ chiral symmetry. There is an argument by A. Casher that relates chiral-symmetry breaking to the formation of bound states as well as to confinement. At the deconfinement transition the connections between the quarks break up and then naturally the question arises whether the temperatures $T_{\text{ch}}$ and $T_{\text{c}}$ coincide. This is a non-trivial problem because the forces between a quark and an antiquark do not simply vanish in the quark-gluon plasma phase and may still cause $\bar{q}q$ condensation. From numerical simulations it could be observed that the deconfined phase is entered at about the same temperature at which chiral symmetry is restored and thus the screened forces between quarks in the fundamental representation seem not to be sufficient to produce $\bar{q}q$ condensation. This problem received a lot attention and led to many controversies in the past. See for instance [85–87] where $T_{\text{ch}}$ has been determined for physical masses of $m_{u,d}$ and $m_s$ to be about

150MeV using $\langle\bar{\psi}\psi\rangle$ and $T_c$ has been determined from observables of $\langle P\rangle$ with a stronger signal at the deconfinement transition that resulted in a value of about 25-30MeV $> T_{ch}$. However, the findings of the past suggest that gluonic forces responsible for bound-state formation, confinement and flux tube formation do also give rise to chiral symmetry breaking.

## 3.3 Finite Temperature LQCD at Non-Zero Baryon Density

In the previous section I discussed lattice QCD at zero chemical potential which describes a system at balance between matter and antimatter. An example for a system that can be described with zero or almost zero chemical potential is the early universe where there was only a very small difference between matter and antimatter. In order to address problems such as heavy ion collisions or neutron stars the effect of non-zero baryon density has to be taken into account, which can be realized by an implementation of a non-vanishing chemical potential into the QCD partition function.

### 3.3.1 Introducing a Chemical Potential

In order to implement a chemical potential into the continuum theory we extent its grand canonical partition function by adding to the action the chemical potential $\mu$ times the Quark number $Q$:

$$Z(T,\mu) = \text{Tr } \mathrm{e}^{-(H-\mu Q)/T}. \tag{3.44}$$

The quark number $Q$ is related to the baryon number via $Q = 3B$ since If $n_q$ and $n_{\bar{q}}$ denotes the number of quarks and antiquarks, respectively, the baryon number is given by $B = 1/3(n_q - n_{\bar{q}})$. Correspondingly the net number of baryons can be expressed in terms of the relation between the baryon number and the quark number, $Q = 3B$. The quark chemical potential is related to the baryon chemical potential via $\mu = \mu_B/3$. The quark number $Q$ is given by the spatial integral over the temporal content of the four current $\bar{\psi}\gamma_\mu\psi$:

$$Q = \int \mathrm{d}^3x\bar{\psi}(x)\gamma_4\psi(x) = \int \mathrm{d}^3x\bar{\psi}^\dagger(x)\psi(x). \tag{3.45}$$

Under charge conjugation (turning particles into antiparticles) the quark number changes sign,

$$\begin{aligned} Q^C &= \int \mathrm{d}^3x\bar{\psi}^C(x)\gamma_4\psi^C(x) \\ &= \int \mathrm{d}^3x(-\bar{\psi}(x)\gamma_4\psi(x)) \\ &= -Q \end{aligned} \tag{3.46}$$

which corresponds to flipping the sign of the chemical potential in the partition function. Thus a positive chemical potential represents a net particle number and a negative chemical potential represents a net antiparticle number. Charge conjugating the partition function leads to the symmetry

$$Z(\mu) = Z(-\mu). \tag{3.47}$$

Implementing the chemical potential on the lattice in a naive way, i.e. by adding a term like $\bar{\psi}(x)\gamma_4\psi(x)$ to the Dirac operator multiplied by $\mu$, leads to the following behavior of the energy density,

$$\lim_{a\to 0}(\epsilon(\mu) - \epsilon(0)) \sim \left(\frac{\mu}{a}\right)^2, \tag{3.48}$$

which apparently diverges as the continuum is approached. The renormalization of the zero temperature theory must also be sufficient for finite temperature and density theory. The reason is that the microscopic short distance regime should be unaffected by the introduction of macroscopic quantities like baryon chemical potential or temperature. This clearly doesn't hold for a naive lattice implementation of the chemical potential. Considering the continuum theory sheds light on the situation [88]: The quark number is the conserved charge of the $U(1)$ global symmetry and being multiplied by $\mu$ it can be written in the form

$$\mu Q = -ig \int \mathrm{d}^3x A_4 j_4, \qquad A_4 = i\frac{\mu}{g}, \quad j_4 = \bar{\psi}(x)\gamma_4\psi(x). \tag{3.49}$$

Here $\mu$ is written in terms of an external $U(1)$ gauge field coupling to the temporal component of the fermion current $j_4$. This expression can be absorbed into the covariant derivative of the Dirac operator where it gives rise to the $U(1)$ symmetry of the quark fields and $A_0$ and protects against divergences. This symmetry gets broken by a naive lattice implementation. A solution is to implement the chemical potential as additional temporal link variable which acts as an external $U(1)$ gauge field, i.e.

$$U_0 = \mathrm{e}^{-a\mu} = \mathrm{e}^{iagA_0}. \tag{3.50}$$

Consider for instance the Dirac operator given in (2.34). In order to implement the chemical potential in this way the temporal part of the sum gets modified in the following way:

$$\begin{aligned} -\frac{1}{2a}\sum_{n\in\Lambda}\Big( & \mathrm{e}^{a\mu}\,(\mathbb{1}-\gamma_4)_{\alpha\beta}\,U_4(n)_{ab}\delta_{n+\hat{4},m} \\ & + \mathrm{e}^{-a\mu}\,(\mathbb{1}+\gamma_4)_{\alpha\beta}\,U_4^\dagger(n-\hat{4})_{ab}\delta_{n-\hat{4},m}\Big). \end{aligned} \tag{3.51}$$

This implementation features the following properties:

- At $\mu = 0$ the original action is recovered.
- If the exponential is expanded $\mu$ appears linearly in the leading order of $a$ term and thus reproduces the density term.
- Time reflection invariance is fulfilled.

The particle-antiparticle asymmetry is introduced by favoring propagation forward in time by $\exp(a\mu)$ while disfavoring propagation backward in time by $\exp(-a\mu)$. Note that the fermion determinant can be interpreted as a sum over closed loops. In such loops the factors $\exp(a\mu)$ cancel with the factors $\exp(-a\mu)$ unless a loop closes non-trivially in the compact time direction. In this case the chemical potential contributes with $\exp(a\mu)^{nN_\tau}$ where n is the winding number of the loop. A practical point to remark is that it is sufficient to multiply all timely links in one single time slice with $\exp(a\mu)^{N_\tau}$ instead of modifying all timely links with $\exp(a\mu)$. From the factor

$$\mathrm{e}^{a\mu N_\tau} = \mathrm{e}^{\frac{\mu}{T}} \tag{3.52}$$

it becomes apparent that the chemical potential enters again in the form $\mu/T$ as it is the case in (3.44). The chemical potential causes the Dirac operator to loose its $\gamma_5$-hermiticity, which is easy to verify. Consider the hopping portion of the Dirac operator with the chemical potential implemented:

$$D(U) = -\frac{1}{2a}\sum_{\pm 1}^{\pm 4}(\mathbb{1}-\gamma_\mu)_{\alpha\beta}\,U_\mu(n)_{ab}\delta_{n+\mu,m}\exp\left(\mathrm{sgn}(\mu)\,a\mu_q\,\delta_{|\mu|,4}\right). \tag{3.53}$$

Here I denoted the chemical potential with $\mu_q$ to avoid confusion with the directional index $\mu$ of the link variables. The sgn-function and the Kronecker-$\delta$ assure that the factor $\exp(a\mu)$ appears correctly in the respective terms. Complex conjugation of this relation is just

$$D^\dagger(U,\mu) = -\frac{1}{2a}\sum_{\pm 1}^{\pm 4}(\mathbb{1}-\gamma_\mu)_{\alpha\beta}\, U_\mu^\dagger(n)_{ab}\delta_{n+\mu,m}\exp\left(\mathrm{sgn}(\mu)\, a\mu_q\, \delta_{|\mu|,4}\right). \tag{3.54}$$

Multiplying $D(U)$ by $\gamma_5$ from the left and right gives:

$$\begin{aligned}
\gamma_5 D(U,\mu)\gamma_5 &= -\frac{1}{2a}\sum_{\pm 1}^{\pm 4}(\mathbb{1}+\gamma_\mu)_{\alpha\beta}\, U_\mu(n)_{ab}\delta_{n+\mu,m}\exp\left(\mathrm{sgn}(\mu)\, a\mu_q\, \delta_{|\mu|,4}\right), \\
&= -\frac{1}{2a}\sum_{\pm 1}^{\pm 4}(\mathbb{1}-\gamma_\mu)_{\alpha\beta}\, U_{-\mu}(n)_{ab}\delta_{n-\mu,m}\exp\left(-\mathrm{sgn}(\mu)\, a\mu_q\, \delta_{|\mu|,4}\right), \\
&= -\frac{1}{2a}\sum_{\pm 1}^{\pm 4}(\mathbb{1}-\gamma_\mu)_{\alpha\beta}\, U_\mu^\dagger(n)_{ab}\delta_{n+\mu,m}\exp\left(-\mathrm{sgn}(\mu)\, a\mu_q\, \delta_{|\mu|,4}\right).
\end{aligned} \tag{3.55}$$

From the first to the second it was used that negative $\mu$ can be considered like wise since the sum runs over positive and negative values. One just has to make to sure to change the sign for every occurrence of $\mu$. From the second to the third $\gamma_{-\mu} = -\gamma_\mu$ was used and that the complex conjugate of the link variables corresponds to its opposite directed counterpart. Then the lattice site index $n$ was renamed $n \leftrightarrow m$. Comparing the relations (3.54) and (3.55) shows that

$$\gamma_5 D(U,\mu)\gamma_5 \neq D^\dagger(U,\mu). \tag{3.56}$$

Instead a modified relation holds:

$$\gamma_5 D(U,\mu)\gamma_5 = D^\dagger(U,-\mu). \tag{3.57}$$

Note that this is not an invariance operation anymore. Together with the fact that $S_g[U^\dagger]$ and $DU^\dagger = DU$ we observe that the property $Z(\mu) = Z(-\mu)$ holds likewise on the lattice.

### 3.3.2 The Sign Problem

The spoiling of the $\gamma_5$-hermiticity leads to the problem that the fermion determinant potentially looses its reality. Consider

$$\det\left[D(\mu)\right] = \det{}^*\left[D(-\mu^*)\right], \tag{3.58}$$

which follows from (3.57) and shows that the fermion determinant is only real if $\mathrm{Re}(\mu) = 0$. If $\mu$ has a non-vanishing real part then the fermion determinant is complex which prevents an evaluation of the path integral by Monte Carlo methods, since the fermion determinant is part of the joint probability weight used for the importance sampling. If it is complex it cannot be interpreted anymore as probability weight. The integrand becomes complex and thus highly oscillatory in this case which makes it numerically extremely hard to evaluate. The positive and negative contributions to the path integral nearly cancel. To accurately obtain the difference between both would require an evaluation of the integral with extremely high precision which is unfeasible. The described condition is commonly referred to as the "sign-problem" and the problem posed by it becomes more severe the larger $\mathrm{Re}(\mu)$ is. One should not be deceived about this

term because there is nothing wrong with the theory at non-zero density. The nature of the sign-problem is simply inherent to systems containing particles and antiparticles and thus is part of the physics. Note that in theory all thermodynamic functions are real after the evaluation of the path integral because the imaginary parts of the fermion determinant cancel each other out. The complex determinant only becomes a problem in terms of the numerical evaluation of the path integral by Monte Carlo methods.

### 3.3.3 Possible Approaches

In the past a variety of techniques have been developed and explored in order to overcome the sign-problem. There are essentially two possibilities: Either one still uses Monte Carlo methods and tries to indirectly gather information about the theory at non-zero density by extrapolation techniques from regions where the sign-problem is absent or sufficiently mild, or one tries to use a conceptually new approach. In the following I will briefly address some of them.

#### Indirect Methods

The first kind of methods where one tries to learn something about the theory at finite chemical potential with extrapolation techniques. Note that all of these methods introduce additional systematic errors in one way or another and moreover break down for $\mu/T \geq 1$. These methods include the following:

#### Reweighting

Reweighting techniques are often used to interpolate between or to extrapolate from data produced in Monte Carlo Simulations. The essential idea is to produce an ensemble of configurations at specific values of a set of parameters and to perform measurements on this ensemble with respect to a different ensemble, corresponding to different values of the parameters. This is done by computing a reweighting factor which accounts for the difference between the two ensembles on each of the produced configurations. The reweighting factor is given by the ratio between the probability weights corresponding to the two different ensembles. In the context of the sign problem reweighting can be used for instance in the following two ways:

- Consider an estimate of some observable $O$ at some finite real value $\mu'$ of the chemical potential:

$$\langle O \rangle_{(\mu')} = \frac{\left\langle O \frac{\det M(\mu')}{\det M(0)} \right\rangle_{(0)}}{\left\langle \frac{\det M(\mu')}{\det M(0)} \right\rangle_{(0)}}. \tag{3.59}$$

  The estimate is measured on an ensemble produced at $\mu = 0$. The ratio $\det M(\mu)/\det M(0)$ is the reweighting factor and accounts for the difference between the ensemble at $\mu = 0$ and $\mu'$ and allows to measure the estimate of $O$ at $\mu' \neq 0$. Ref. [89] gives an introduction on the topic by studying reweighting in the d=2 ferromagnetic q=3 Potts model and the d=2 antiferromagnetic Ising model.

- The complex fermion determinant can be written in terms of its modulus times a complex phase factor, $|\det M| \exp(i\phi)$. The modulus is still used as part of the joint probability weight for the importance sampling while the complex phase factor is moved into the expectation value, i.e.

$$\langle O \rangle = \frac{\left\langle O \, \mathrm{e}^{i\phi} \right\rangle_{\mathrm{pq}}}{\left\langle \, \mathrm{e}^{i\phi} \right\rangle_{\mathrm{pq}}}, \tag{3.60}$$

where pq denotes "phase quenched". Although the spirit of the reweighting may not be obvious in this case, it is still a reweighting since the expectation value is taken with respect to the so called phase quenched weight $|\det M|$. Unsurprisingly the approach has its limitations. See for instance [90] for a detailed and comprehensive study about the validity of phase quenched QCD.

While the procedures are mathematically sound the practical application turns out to be very costly. In the first case this is due to the configuration-wise evaluation of the reweighting factor given by the ratio of determinants. In both cases the signal to noise ratio worsens exponentially because of the ratio of the partition functions appearing in the expressions, containing the difference of the free energies which are extensive quantities, $F = Vf$:

$$\frac{Z}{Z'} = \mathrm{e}^{\Omega \Delta f}, \tag{3.61}$$

with $\Omega = V/T$ and $\Delta f$ denotes the difference in the free energy densities. The second important problem is the overlap problem. It addresses the overlap between the probability functions of the different ensembles, for instance at $\mu = 0$ and $\mu' \neq 0$, which has to be sufficiently large in order for reweighting to work. A possible way to increase the overlap is to reweight in multiple parameters [91]. In section 4.1.2 I will discuss and explain reweighting in more detail because it is used a lot in the data analysis done in this work.

### Isospin Chemical Potential

A possibility to run Monte Carlo simulations at finite density is to consider two mass degenerate flavors with opposite chemical potential,

$$\mu_I \equiv \mu_u = -\mu_d, \tag{3.62}$$

where $\mu_I$ is the chemical potential linked to isospin [92]. The corresponding term in the Euclidean continuum Lagrangian reads $\mu_I(\bar{u}\gamma_4 u - \bar{d}\gamma_4 d)$. For this choice of the chemical potential The Dirac operators are block diagonal Consider the block diagonal structure of the Dirac operators

$$\begin{pmatrix} D(\mu_I & 0 \\ 0 & D(-\mu_I) \end{pmatrix} = \begin{pmatrix} D(\mu_I & 0 \\ 0 & \gamma_5 D^\dagger(\mu_I)\gamma_5 \end{pmatrix}, \tag{3.63}$$

where on the right-hand side the modified $\gamma_5$-hermiticity relation (eq. (3.57)) has been used. As a consequence a real positive determinant is obtained:

$$\det\left[D(\mu_I)\right] \det\left[\gamma_5 D^\dagger(\mu_I)\gamma_5\right] = \det\left[D(\mu_I)\right] \det\left[D^\dagger(\mu_I)\right] = \left|\det\left[D(\mu_I)\right]\right|^2. \tag{3.64}$$

Even though isospin is not conserved in the real world due to electroweak interactions it is still relevant as such a situation could possibly occur in for instance heavy ion collisions. Moreover, interesting finite density effects like charged pion condensation can be studied for isospin chemical potentials larger than the pion mass [93].

### Taylor Expansion

In this approach the philosophy is again to produce an ensemble of configurations at zero density and to expand the partition function in parameters causing the sign problem, i.e. the chemical potential $\mu$. Such a Taylor expansion of the partition function can only range up to the next non-analyticity which is given by

a phase transition. Since true phase transitions do not exist on finite volumes (in simulations of LQCD) [66, 67] the partition function is analytic everywhere. The Taylor expansion of some observable $O$ is given by

$$O(T,\mu) = \sum_{n=0}^{\infty} c_n(T) \left(\frac{\mu}{T}\right)^n, \quad c_n = \frac{1}{n!} \left.\frac{\partial^n O}{\partial \left(\frac{\mu}{T}\right)^n}\right|_{\mu=0}. \tag{3.65}$$

Due to the reflection symmetry of the partition function in $\mu$ the powers $n$ are depending on the observable either $n = 2k$ or $n = 2k+1$. In order to compute the coefficients $c_n$ in Monte Carlo simulations, the derivatives $\partial \langle O \rangle / \partial \mu$ have to be evaluated, containing expressions like $\partial \ln \det M / \partial \mu$. Higher order derivatives turn out to be rather complex expressions hard to evaluate numerically. A discussion of this problem can be found for instance in [94].

### Imaginary Chemical Potential

Simulations at purely imaginary chemical potential are a central topic of this work. For this reason I will only give a brief description here for completeness but I will provide a detailed discussion below in section 3.3.4. Using a purely imaginary chemical potential $\mu = i\mu_i$ in eq. (3.58) yields

$$\det\left[D(i\mu_i)\right] = \det{}^*\left[D(i\mu_i)\right], \tag{3.66}$$

and thus renders the fermion determinant real, allowing to simulate at finite values of $\mu_i$. Moreover the Dirac operator gets back its $\gamma_5$-hermiticity. Afterwards the Monte Carlo data can for instance be used again in conjunction with a Taylor expansion as described above by (3.65) followed by analytic continuation. An alternative is to exploit the phase structure at imaginary chemical potential in order to use universal scaling relations as they govern the behavior of the critical surfaces that can be followed into the region at real $\mu$.

### Canonical Partition Function from Imaginary Chemical Potential

The grand canonical ensemble and the canonical ensemble coincide in the thermodynamic limit and the grand canonical partition function, (3.44), can be obtained from the canonical one by an expansion in a power series of the fugacity variable $z = \exp(\mu/T)$,

$$Z(T,\mu,V) = \sum_Q \left(\mathrm{e}^{\frac{\mu}{T}}\right)^Q Z_Q(T,V). \tag{3.67}$$

Using a purely imaginary chemical potential the fugacity expansion is Fourier sum [95, 96] with a periodicity of $2\pi$ in $\mu_i/T$ and reads

$$Z(T,i\mu_i,V) = \sum_Q \left(\mathrm{e}^{\frac{i\mu_i}{T}}\right)^Q Z_Q(T,V).. \tag{3.68}$$

Inversion yields the canonical partition function at a fixed quark number $Q$:

$$Z_Q(T,V) = \frac{1}{2\pi} \int_{-\pi}^{\pi} \mathrm{d}\left(\frac{\mu_i}{T}\right)\ \mathrm{e}^{\frac{i\mu_i Q}{T}} Z(T,i\mu_i,V). \tag{3.69}$$

Computing $Z(T,i\mu_i,V)$ in Monte Carlo simulations with purely imaginary chemical potential and using them in (3.69) allows to determine the partition functions $Z_Q$ which in turn can be used in the fugacity

expansion in (3.67), see [97]. Note that the integrand of the Fourier integral in (3.69) is increasingly oscillating for larger quark number $Q$. This requires a larger number of samples in the interval $[-\pi, \pi]$ to reliably estimate the integral. Approaching the thermodynamic limit requires $Q \to \infty$. In practice this means that large $Q$ are necessary in this approach which quickly turns into a problem for the needed statistics of the Monte Carlo simulations. Even though the sign problem cannot be circumvented in this way the approach offers an interesting alternative. Attempts have been done to deal with the oscillating integrand by using combinations of multi-histogram reweighting and other involved methods, see e.g. [98, 99] and references therein.

### Direct Methods

The second way to study QCD at finite density includes techniques aiming at solving or bypassing the sign problem and to simulate directly at real finite values of the chemical potential. As this is not the topic of this work in the following I will only provide a rather incomplete list of these methods including the most popular options together with references.

Effective theories aim at eliminating or reducing the sign problem by truncation or by integrating out degrees of freedom linked to the sign problem. Well known approaches are for instance PNJL, sigma, Polyakov loop + quark meson models or theories involving strong coupling and hopping expansions. They typically have the $Z_3$ and/or chiral symmetry in common with QCD. Examples for discussions of these approaches are given in [100–103]. There are approaches starting straightly from QCD involving Dyson-Schwinger equations [104] or functional renormalization-group (FRG) methods [105]. Note that a general difficulty consists in the determination and control of systematic errors introduced when using these kind of theories.

### 3.3.4 Imaginary Chemical Potential and Restoration of the $Z_3$ Center Symmetry

The sign problem which was explained in section section 3.3.2 arises when a chemical potential with $\Re(\mu) \neq 0$ is turned on because the fermion determinant becomes complex. For a purely imaginary chemical potential the fermion determinant becomes real again and the $\gamma_5$-hermiticity of the Dirac operator is restored. In this case standard Monte Carlo methods can be applied without any further problem. A purely imaginary chemical potential has further important consequences [106]: The partition function

$$Z(T,\mu) = \text{Tr } \mathrm{e}^{-(H-\mu Q)/T}, \tag{3.70}$$

and thus thermodynamic functions become periodic in $\mu_i/T$. In section 3.3.1 I explained that the chemical potential is equivalent to an external $U(1)$ field (c.f. eq. (3.50)) that can be moved to the final time slice contributing with (c.f. eq. (3.52))

$$\mathrm{e}^{ia\mu_i N_\tau} = \mathrm{e}^{i\frac{\mu_i}{T}}, \quad T = \frac{1}{aN_\tau}. \tag{3.71}$$

Thus the imaginary chemical potential term can be attached to the fermionic field modifying its boundary condition. The fermion determinant in the partition function is then effectively evaluated at $\mu = 0$ and the fermion fields come with an additional phase factor as they wind through the boundary:

$$Z(i\mu_i/T) = \int \mathcal{D}\mathcal{U} \det D(\mu=0)\, \mathrm{e}^{-S_G}, \quad \psi(\mathbf{x}, t+T) = -\,\mathrm{e}^{i\frac{\mu_i}{T}}\psi(\mathbf{x},t). \tag{3.72}$$

In section section 3.2.2 I explained that including dynamical fermions break the $Z_3$ center symmetry explicitly because they require anti-periodic boundary conditions which under a center transformation only permits the trivial center element (see eq. (3.40)). However, with an imaginary chemical potential term attached any $Z_3$ transformation can be undone by a respective shift in the imaginary chemical potential. To see this consider the center transformations discussed in section 3.2.2,

$$\Omega(\mathbf{n}, t+N_\tau) = \mathrm{e}^{i\frac{2\pi n}{3}}\Omega(\mathbf{n},t). \tag{3.73}$$

Applying such a transformation leaves the partition function in (3.72) invariant but the fermion fields receive an additional factor

$$Z(i\mu_i/T + i2\pi n/3) = \int \mathcal{D}\mathcal{U} \det D(\mu=0)\, \mathrm{e}^{-S_G}, \quad \psi(\mathbf{x}, t+T) = -\,\mathrm{e}^{i\frac{2\pi n}{3}}\,\mathrm{e}^{i\frac{\mu_i}{T}}\psi(\mathbf{x},t). \tag{3.74}$$

Hence eq. (3.74) is the result of a center transformation on eq. (3.72) and thus describes equivalent physics. The important observation here is that the resultant new symmetry, sometimes referred to as *extended center symmetry*,

$$Z\left(i\frac{\mu_i}{T}\right) = Z\left(i\frac{\mu_i}{T} + i\frac{2\pi n}{3}\right), \tag{3.75}$$

shows a $2\pi/3$ periodicity of the partition function. In a way the center symmetry can be considered restored. Apparently the interval $[0, 2\pi)$ can be separated into three sectors which correspond to the three $Z_3$ center sectors that can be distinguished by the phase of the Polyakov loop, c.f. eq. (3.39). For $\mu_i/T = 0$ the expectation value of the Polyakov loop above the critical temperature $T_\mathrm{c}$ settles in the trivial vacuum, where $\langle P\rangle \sim 1$. For $\mu_i/T = 2\pi/3$ and $\mu_i/T = 4\pi/3$ it settles in rotated vacua, where $\langle P\rangle \sim z$ and $\langle P\rangle \sim z^2$, respectively. The partition function exhibits reflection symmetry,

$$Z(\mu_i) = Z(-\mu_i), \tag{3.76}$$

with respect to critical values of the imaginary chemical potential $\mu_{i,c}/T = 2\pi/3(n + 1/2)$. At these values there are transitions between the $Z_3$ sectors, commonly referred to as *Roberge-Weiss (RW)* transitions. At large temperatures these are first order transitions. Reducing the temperature, at some critical value $T_c$ the first order transition ends in the so called RW-endpoint. Below this point at $T < T_c$ the transition is an analytic crossover. This has been verified in numerical studies [29, 30]. From $\mu = 0$ the chiral/deconfinement transition analytically continues to purely imaginary values $\mu_i$ and meet the RW transitions in their endpoint, as shown schematically in fig. 3.2 for a fixed quark mass $m_q$. The nature of the chiral/deconfinement transition and the RW-endpoint is a function of $N_f, m_q$ and $\mu_{i,c}/T$, Around the chiral and heavy quark mass limits the chiral/deconfinement transition is of first order and the RW endpoint is a triple point. At intermediate masses the chiral/deconfinement transition is a crossover and the RW endpoint is second order $Z_2$ point. For certain masses chiral/deconfinement transition changes its nature as a function of $\mu_i/T$. Note, that there is a third possibility for the RW endpoint: For certain values of the quark mass it becomes a tricritical point, which separates mass regions where the RW endpoint is a triple point from those where it is a second order $Z_2$ point.

As mentioned above, the phase of the Polyakov loop distinguishes the $Z_3$ sectors which is indicated by the three-pointed star shapes, plotted in the different $Z_3$ sectors in fig. 3.2. At $(\mu_{i,c}/T)/(\pi/3) = 3$, where its phase points up-left in one sector and down-left in the other, the imaginary part $\mathrm{Im}(P)$ of the Polyakov loop is suitable as an order parameter to identify the different phases as well as the nature of the RW endpoint, as depicted in the right panel of fig. 3.2. A detailed explanation is given in the caption of fig. 3.2. The discussion will be continued in section 3.5.

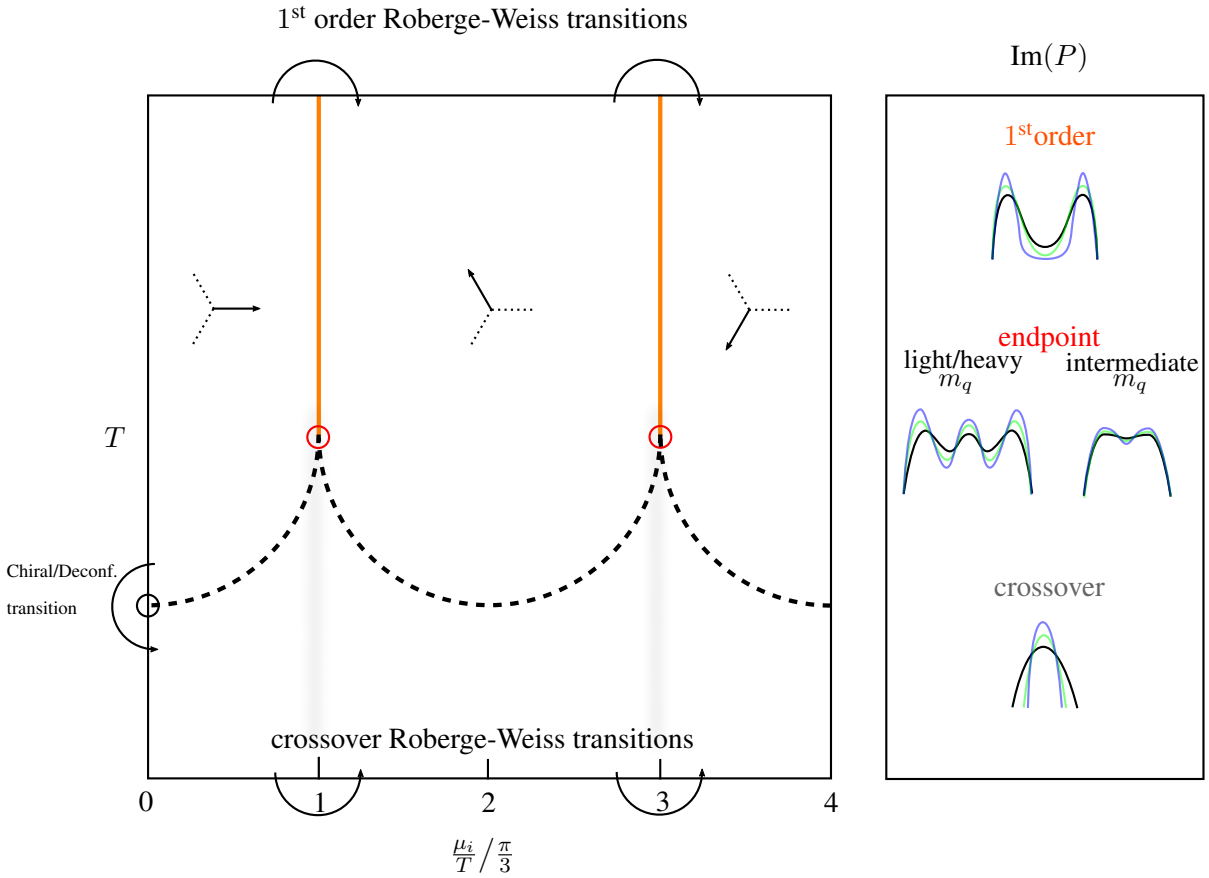


Figure 3.2: **Left panel:** shows the chiral/deconfinement and $Z_3$ transitions in the plane of temperature and imaginary chemical potential. Vertical lines represent the $Z_3$ transitions (colored solid lines for first order and blurred lines for crossover transitions). Dashed lines represent the analytic continuation of the chiral/deconfinement transitions. **Right panel:** qualitatively shows the expected shapes of the distribution of the imaginary part of the Polyakov loop at $(\mu_{i,c}/T)/(\pi/3) = 3$. At large $T > T_c$, where the RW transition is of first order, $\mathrm{Im}(P)$ shows a two peak structure characteristic for a two phase coexistence. At low $T < T_c$, where the RW transition is a crossover, $\mathrm{Im}(P)$ shows a one peak structure characteristic for a smooth, analytic transition. At $T_c$, where the RW transition ends in the RW endpoint, the shape of $\mathrm{Im}(P)$ additionally depends on the quark mass. For light/heavy quark masses, the RW endpoint a triple point where three phases coexist: The deconfined/chirally-symmetric phase in the left sector at $T > T_c$, the deconfined/chirally-symmetric phase in the right sector at $T > T_c$ and the confined/chirally-broken phase at $T < T_c$. Thus $\mathrm{Im}(P)$ shows a three peak structure. At intermediate quark masses, the RW endpoint is a second order $Z_2$ point. Consequently there is only a two phase coexistence consisting of the deconfined/chirally-symmetric phase in the left sector at $T > T_c$ and deconfined/chirally-symmetric phase in the right sector at $T > T_c$. At temperatures $T < T_c$ the confined/chirally-broken phase is reached through an analytic crossover. In this case $\mathrm{Im}(P)$ shows a two peak structure. Note, that in LQCD simulations the peak structure of the distributions of $\mathrm{Im}(P)$ becomes more distinct as the volume is increased, which is indicated through the different shapes, lying on top of each other.

## 3.4 The QCD Phase Diagram

One possibility to clearly represent thermodynamic properties of matter are phase diagrams whose axes correspond to thermodynamic control parameters. In a phase diagram different forms of matter can be found in different regions which can be separated by lines of phase or thermal transitions on which the different forms of matter coexist, i.e. are in equilibrium. Moreover, there can be critical points in which lines of phase transitions terminate or meet. A well know example for such a phase diagram is the one of $H_2O$, in which the control parameter pressure $P$ is plotted against the temperature $T$. $H_2O$ has three distinct phases: Water, ice and vapor. Between ice and water, water and vapor as well as between vapor and ice there are first order phase transitions. Furthermore $H_2O$ features the aforementioned critical points. One of these points is a triple point at which the three lines of first order transitions meet for a particular value of the temperature $T$ and pressure $P$. At this point the three phases exist at the same time. A further critical point is the endpoint at which the line of first order transitions between vapor and water terminate. This point represents a second order transition belonging to a $Z_2$ universality class. Beyond this point the transition is merely a rapid, continuous transformation between the two forms of $H_2O$, denoted as crossover. A conjectured phase diagram with similar properties exists for QCD, which I will discuss in the following on a very qualitative level. There the thermodynamic control parameters are temperature $T$ and baryochemical potential $\mu_B$. The QCD phase diagram is still understood only to a small extent but there is much effort to change this situation which led to the onset of many new research fields. The established structure of this phase diagram is largely conjectured, supported by model calculations, arguments regarding symmetries and first principle calculations. Furthermore, many theoretical investigations consider only three quarks: Two mass-degenerate light quarks (up and down) and one heavier quark (strange). This setting serves as a very good approximation to real physics since the dynamics of the quarks with much larger mass (charm, bottom and top) are negligible with respect to the quark sea. A schematic representation of how the QCD phase diagram might look like is shown in fig. 3.3. This illustration can be divided roughly into three sections: In the complete upper half, corresponding to extremely large temperatures, due to the asymptotic freedom of QCD a deconfined phase is expected termed as quark-gluon plasma. As the name suggests, in this state the dominant degrees of freedom are quarks and gluons. This is also a chirally-symmetric phase, i.e. where the chiral condensate vanishes, $\langle\bar{\psi}\psi\rangle = 0$. In lower left part of the phase diagram at vanishing $T$ and $\mu_B$ there is the vacuum, where the chiral symmetry is broken, signalled by a non-vanishing chiral condensate, $\langle\bar{\psi}\psi\rangle \neq 0$. If the reader is interested to read more about the chiral symmetry-breaking nature of the vacuum he is referred to the comprehensively written article about the QCD phase diagram by S. Hands [107]. At low $T$ and $\mu_B$, QCD is dominated by a gas of bound states, namely hadrons. Increasing $\mu_B$ while keeping $T$ small corresponds to increasing the number of quarks in the system, since antiquarks do not exist at low temperatures. At some point a region is entered in which at a chemical potential of about $\mu_B \approx 900$MeV a transition to nuclear matter is expected. This transition corresponds to ordinary atomic matter. Droplets of nuclear matter are surrounded by vacuum. At even larger values of $\mu_B$ one ends up on the right side of the lower half of the phase diagram where there is at unknown values of $\mu_B$ a transition to quark matter. To be more precise, diverse states of quark matter are conjectured, for instance a color-flavor-locked (CFL) phase at extremely large values of $\mu_B$. This is also termed as color superconducting quark matter. Before this area, at smaller $\mu_B$ values, there could be other phases referred to as non-CFL quark liquid whose properties are unknown at present. Hypotheses suggest these are other color superconducting phases.

The transition at low values of $\mu_B$ at extraordinarily large temperatures $T \approx 150$MeV or $\approx 10^{12}$K is characterized by the breaking up of the hadrons (mostly pions) and creation of a gas consisting of quarks, antiquarks and gluons but also photons, electrons and positrons. Subsequently the gas condenses more and more until the onset of the QGP. The temperatures at the transition between hadronic matter and QGP could only be realized in two situations so far: Shortly after the big bang in the first tens of microseconds as well as in high energy collision between heavy nuclei. For this reason this area is subject to intense experimental studies. These include ALICE at CERN or such conducted at the Relativistic Heavy Ion Collider (RHIC) at Brookhaven National Laboratory in New York, marked in fig. 3.3 in the respective areas. The described area including (especially) lower temperatures due to its non-perturbative nature can hardly be studied by purely analytic treatments of QCD and LQCD is currently probably the most efficient theoretical research method. LQCD calculations showed that the transition to the QGP is a crossover [28]. From lattice studies, indirect methods based on the latter and model calculations it was observed that the critical temperature $T_c$ at which the transition occurs decreases for larger values of $\mu_B$. Moreover, indications were found that along the transition a critical endpoint of a line of first order transitions could exist [91, 108] which consequently represents a second order point. Unfortunately due to the sign problem the possibility for LQCD calculations declines already at small values of $\mu_B$. For this reason the investigations are restricted mainly to the vertical $T = 0$ axis. While the curvature of the transition line can already be determined reliably by indirect methods like analytic continuation [109–113], it is still a long way to confirm or deny the existence of the critical endpoint. Many approaches are being developed which rather aim at solving the sign problem and to study the QCD phase diagram directly at finite $\mu_B$. These include Lefschetz thimbles [114, 115], complex Langevin simulations [116, 117], density of state methods [118, 119] as well as canonical approaches [120, 121]. Following the transition line to smaller $T_c$ and $\mu_B$ eventually the lower half of the phase diagram is reached where the meaning of the transition changes from a transition between hadronic matter and QGP to a transition between hadronic matter and quark matter. The nature of the transition in this region is still an open question, for a review about the progress and an explanation about different possible scenarios see for instance [122]. However, the thermal transition at $\mu_B = 0$ is still subject of intensive theoretical research. This is not only due to its relevance for the study of the early universe but also because it offers a vast abundance of opportunities to establish a deep theoretical understanding of this area. One of these opportunities consists in exploring the properties of this transition as well as identifying what influences its nature. For instance from thermodynamic arguments it is apparent that the nature of the thermal transition is a function of the quark mass. Moreover, theoretical considerations of QCD revealed a dependence on the number of flavors taken into account, e.g. only the two mass degenerate up and down quarks or additionally the heavier strange quark. It shall be for LQCD to identify the nature of the transition for given quark masses and number of flavors. As expected, this brings about new challenges. One of the main problems in LQCD consists in controlling discretization effects which, as it is well known for some time (c.f. [123] an refs. therein), significantly influence the position of the endpoints of the lines of phase transitions. Until this very day, a precise treatment leading to final conclusions about the location of these endpoints in the continuum theory, i.e. for vanishing lattice spacing $a \to 0$, remains a challenge. The remaining part of the chapter will be devoted to the question about the nature of the transition at $\mu_B = 0$ and how it changes as a function of the quark mass, the number of flavors and the lattice spacing. Moreover the analytic continuation to purely imaginary values of $\mu$ will be discussed, where QCD possesses an even richer

phase structure. Principally, there the same questions apply as for $\mu = 0$ and trying to answer them can indeed help to restrict the phase diagram at $\mu = 0$.

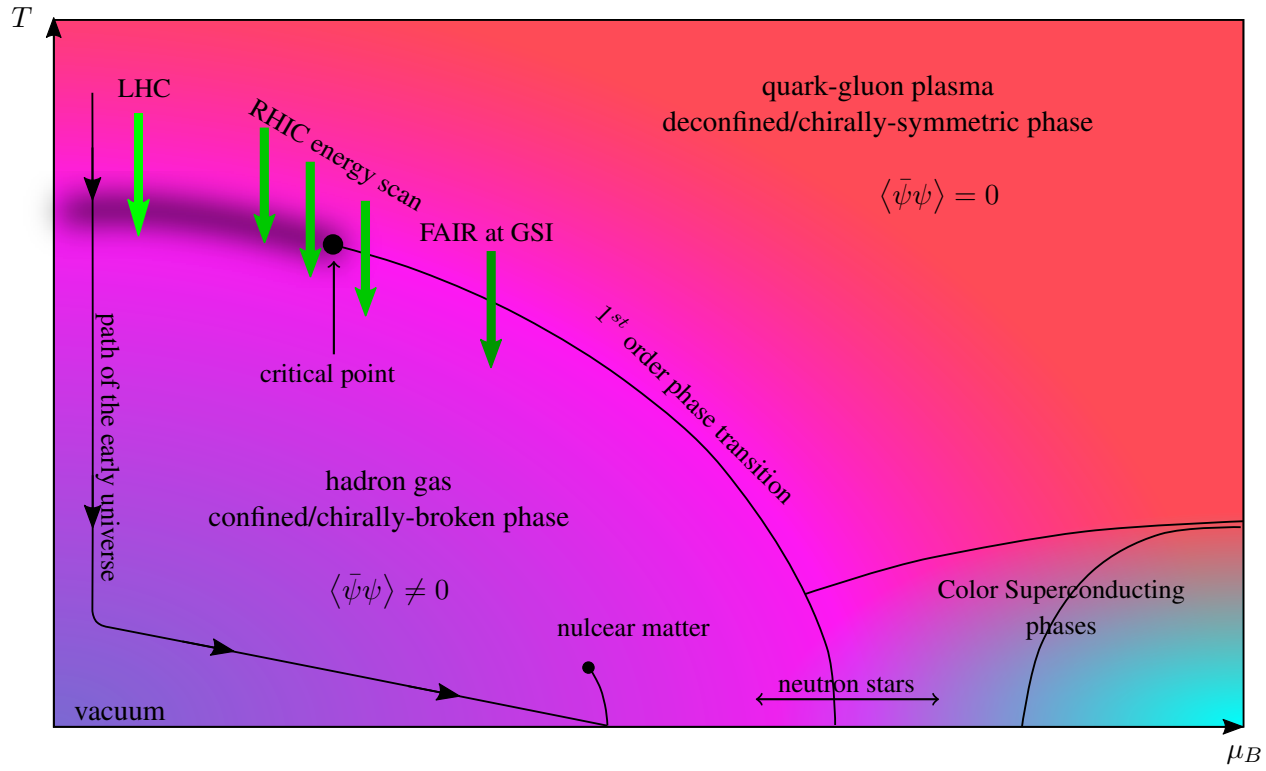


Figure 3.3: Schematic illustraition of a possible phase structure of $N_f = 2 + 1$ flavor QCD in the $(T, \mu_B)$-plane.

## 3.5 The QCD Phase Structure at Zero and Imaginary Chemical Potential from the Lattice

The nature of the thermal phase transition as a function of the quark masses at a fixed value of the chemical potential $\mu$ can be most readily presented in a quark mass diagram, as shown in fig. 3.5 for $\mu = 0$, where the masses of the up and down quarks, $m_u, m_d$ are considered degenerate and thus are plotted as $m_{u,d}$ over the strange quark mass $m_s$. In contrast to the $(T, \mu_B)$-diagram (fig. 3.3) there is no temperature axis. Instead the critical temperature at which the system undergoes a transition can be thought of as projected into the $m_{u,d} - m_s$ plane, i.e. every point is considered at the respective critical temperature of the system. The order of the transition depends on the particular values of $m_{u,d}, m_s$. The heavy limit $m_{u,d}, m_s \to \infty$ that corresponds to the fully quenched theory is included in the diagram and is represented by the top right corner. The upper horizontal axis conforms to the $N_f = 2$ theory in the $m_s \to \infty$ limit whereas the right vertical axis conforms to the $N_f = 1$ theory in the $m_{u,d} \to \infty$ limit. On the diagonal line all quark masses are degenerate and hence this line represents the $N_f = 3$ theory. Every point in the diagram that does not belong to one of these three cases is included in the $N_f = 2 + 1$ theory, where the masses $m_{u,d}$ and $m_s$ are finite (or zero) and different. Of course there are also the limits $m_s \to 0$ and $m_{u,d} \to 0$ which are commonly referred to as the chiral limit of the respective theory. The diagrams of this type displayed throughout this work are not exact but rather schematic illustrations of the phase structure reflecting the

current status as it is observed or indicated from recent lattice studies. The reason for not showing a plot with exact values is that there is simply not enough data currently available. In fact for some parts of the diagram the situation is unclear and conflicts between results of different studies still have to be resolved.

In the following section I will briefly address the effect of discretization errors on the phase structure. Afterwards I am going to discuss the phase structure of this diagram for $\mu_B = 0$ and finally I will motivate the use of a purely imaginary chemical potential as some kind of analytic continuation from $\mu_B = 0$ and discuss the more complicated and richer phase structure there. I will also point out how it can help to study the structure at $\mu_B \geq 0$.

The phase diagrams presented in the following sections use color conventions that we fixed in our working group in order to have a uniform style throughout our publications. The legend listing all the relevant names denoting the respective nature of the transitions including the chosen colors is plotted in table 3.2.

### 3.5.1 Discretization and Finite Volume Effects on the Phase Structure

In order to obtain a continuum result from lattice calculations in general it is necessary to remove the systematic error introduced by the discretization of the theory by an extrapolation to vanishing lattice spacing $a \to 0$. As expected, this problem concerns the phase structure, as well. In case of the quark mass diagram the discretization effects affect the position of the $Z_2$ second order phase transition lines. The location of the latter for instance can be identified by the value of the respective quark mass $m_{\mathrm{q},Z_2}$ or by the equivalent specification of a pseudo scalar meson mass $m_{\mathrm{PS},Z_2}$ computed at the corresponding value of the lattice coupling $\beta_{\mathrm{c}}$ in a $T = 0$ simulation. Depending on the fermion discretization the computed value has a systematic error of some order of $a$. In the case of Wilson's formulation the leading order of

| Description | Color | RGB-code |
|---|---|---|
| Physical point | | (0,30,150) |
| Tricritical line | | (255,0,0) |
| $Z_2$ line | | (0,102,255) |
| $Z_2$ region | | (128,179,255) |
| 1st order line | | (255,128,0) |
| 1st order region | | (255,255,150) |
| O(4) line | | (255,0,200) |
| O(4) region | | (255,215,255) |
| 1st order triple line | | (0,180,0) |
| 1st order triple region | | (170,255,204) |
| 1st order quadruple line | | (170,0,212) |
| Crossover region | | (240,240,240) |

Table 3.2: Phase diagram color legend.

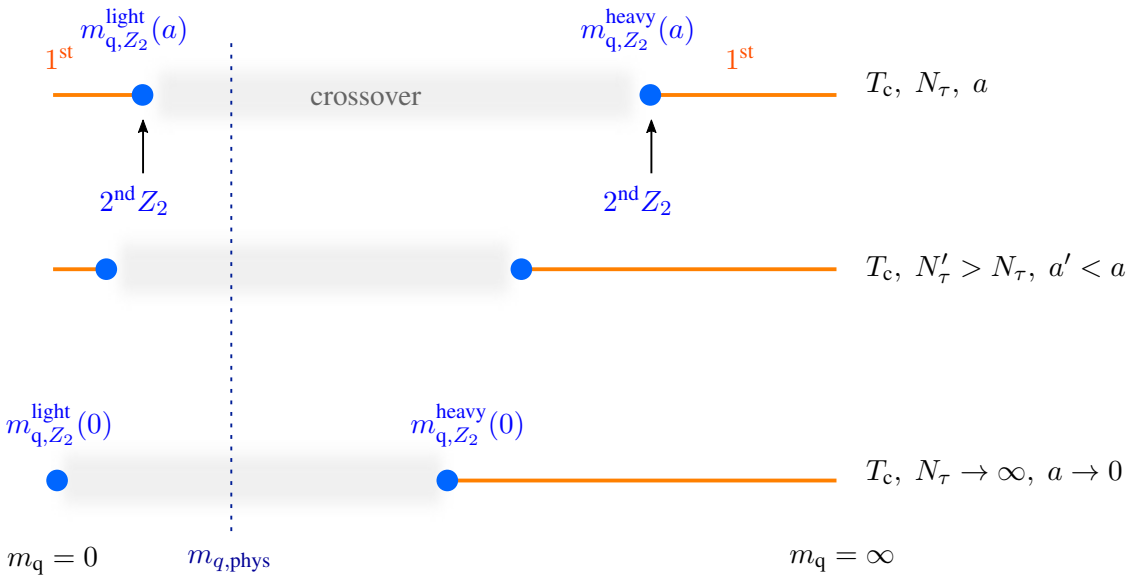


Figure 3.4: The figure shows qualitatively how the discretization error could possibly affect the phase structure. A positive coefficient $c_1$ in the leading order of $a$ term in eq. (3.77) leads to an expansion of the first order region around the heavy mass limit and a shrinking of the first order region around the chiral limit at small masses. The bottom axis corresponding to the continuum limit $a \to 0$ shows a possible but unconfirmed scenario (see discussion in section 3.5.2) where the first order transition in the chiral limit completely vanishes.

the discretization error is linear in $a$. In general this can be expressed as

$$m_{\text{q},Z_2}(a) = m_{\text{q},Z_2}(0) + \sum_{k=1}^{\infty} c_k a^k. \tag{3.77}$$

Assuming for simplicity that only the leading order $O(a)$ is significant then the direction of the shift of $m_{\text{q},Z_2}(a)$ relative to $m_{\text{q},Z_2}(0)$ only depends on the sign of $c_1$ (see fig. 3.4 for an example). While an analytical treatment of this problem turns out to be very complicated LQCD studies indicate a positive sign for $c_1$. A rather qualitative argumentation can be deduced from analyzing the pole of the quark propagator in the free theory. Reading off the mass from the pole suggests a positive sign for $c_1$. Approaching the continuum limit $a \to 0$ requires to simulate successively larger temporal lattice extents $N_\tau$ because of the relation $T_c = 1/\left(a(\beta_\text{c})N_\tau\right)$: When the temporal lattice extent gets increased, the lattice spacing $a$ has to be decreased in order to keep the system at the transition temperature $T_\text{c}$. Remember that the lattice spacing $a(\beta)$ is indirectly controlled by the inverse lattice coupling $\beta$ which is explained in section 3.2.1.

### 3.5.2 The Nature of the Phase Transition at $\mu = 0$

Following up the discussion from the beginning of section 3.5 I will describe the nature of the thermal QCD phase transition as a function of the quark masses $m_{u,d}$ and $m_s$ as it is illustrated in fig. 3.5. In the limit of infinitely heavy quark masses, i.e. excluding dynamical quarks, QCD has a first order deconfinement phase transition associated to the spontaneous breaking of the center symmetry above a critical temperature at about $T_c = 270$ MeV. Including dynamical quarks, i.e. going to finite quark masses, breaks the center symmetry explicitly. This has been discussed in section 3.2.2. Independent of the number of flavors the phase transition remains first order as long as the quark masses are sufficiently large. Decreasing the

quark masses weakens the transition until at some critical value $m_{\mathrm{q},Z_2}^{\mathrm{heavy}}$ it ends in a $Z_2$ second order point (the deconfinement critical point). For intermediate quark masses $m_q$ with $m_{\mathrm{q},Z_2}^{\mathrm{light}} < m_q < m_{\mathrm{q},Z_2}^{\mathrm{heavy}}$ the QGP and the hadronic phase are analytically connected by a crossover transition. As $m_q$ is representative for $m_{u,d}, m_s$ which span the plane of the diagram, in fact, there is a whole region of first order phase transitions that is separated from the crossover region by a line of $Z_2$ second order transitions which is commonly termed as deconfinement critical line. Starting from the opposite direction in the chiral limit at vanishing quark masses, a similar but somewhat more complex picture can be found. For $m_{u,d}, m_s = 0$ there is a first order transition associated to the spontaneous breaking of the chiral symmetry. The chiral symmetry is explicitly broken at non-vanishing quark masses but the associated transition remains first order as long as $m_{u,d}$ and $m_s$ are sufficiently small. If $m_{u,d}, m_s$ are increased the region of first order transition at some point terminates in a line of $Z_2$ second order transitions, called the chiral critical line. At larger values of $m_s$ but small $m_{u,d}$ there are different possible scenarios illustrated by the left and right side of fig. 3.5: As shown on the left-hand side there could be a small stripe of first order transitions extending all the way up to the limit $m_s \to \infty$. The alternative, illustrated on the right-hand side is that this region completely vanishes as $m_s$ grows large. In this case the transitions in the limit $m_{u,d}$ at some point become second order transitions with different possibilities for universality classes. Furthermore, note, that at the left edge ($m_{u,d} = 0$) of the diagrams there is a line of first order triple transitions, where three phases coexist: The high temperature phase where chiral symmetry is present which implies a vanishing chiral condensate $\langle\bar{\psi}\psi\rangle = 0$, and two chirally-broken phases at low temperature with a non vanishing chiral condensate $\langle\bar{\psi}\psi\rangle \neq 0$, separated by the sign (+/-) of $\langle\bar{\psi}\psi\rangle$. Finally, note that at the bottom edge ($m_s = 0$) of the diagrams the first order transitions at small values of $m_{u,d}$ do not terminate in a tricritical point. This is simply explained by the fact, that there is no chiral symmetry present with only one massless quark. For the same reason there is no first order phase transition in the right lower corner of the diagrams.

In the following I will discuss the different limits of light and heavy quark masses separately and in more detail.

### The Heavy Quark Mass Region

The limit $m_q \to \infty$ (top right corner of fig. 3.5) is better understood than the light counterpart but going to finite quark masses still offers many problems to be dealt with as all the problems linked to simulations of dynamical quarks and heavy quark masses enter. Since the quark masses in this area are academically heavy, so far less focus has been put on this region by the research community compared to the chiral limit. However, partially successful attempts have been made to understand and map out the phase structure of this region. One of the most important questions still to be clarified is where the endpoint of the first order transition, i.e. the $Z_2$ point settles in the continuum and if there is a consequence for the physical value of the quark mass (indicated by $m_{q,\mathrm{phys}}$ in fig. 3.5). One could imagine that the region of first order transitions in the heavy limit drastically expands and engulfs the physical point. This scenario has been rather ruled out by studies using the staggered fermion discretization, e.g. [28], but a continuum limit extrapolation employing Wilson fermions is not available which would be a valuable crosscheck. Moreover, the studies carried out so far took place on rather coarse lattices such that large discretization errors have to be assumed. Section 3.5.1 discusses the influence of discretization errors on the location of the $Z_2$ point. In the following I report on some selected results from the literature of the past decade.

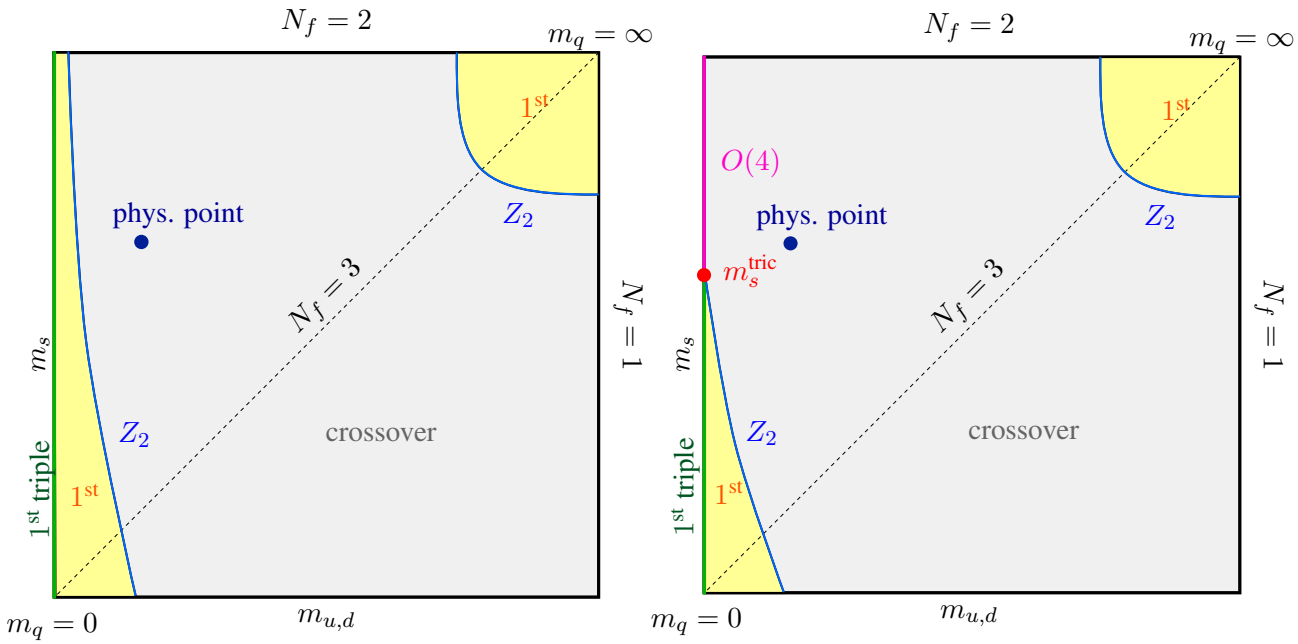


Figure 3.5: Shown are schematics of the quark mass diagram with first order transitions in the light (heavy) quark mass limit $m_q \to 0$ ($m_q \to \infty$) associated to the breaking of the chiral (center) symmetry. L.h.s.: Illustrates the first order scenario quark mass diagram, where the region of first order transitions in the light quark mass region extends all the way up to $m_s \to \infty$. R.h.s.: Illustrates the second order scenario, where the region of first order transitions in the light quark mass region terminates in a trcritical point at some finite value of $m_s$ and $m_{u,d} = 0$.

In some earlier study [124] a hopping parameter expansion was done to obtain an effective theory that was used to determine the $Z_2$ point on $N_\tau = 4$ lattices. The result is listed in table 3.3. A few years later in a study by our group [103] a combined strong coupling and hopping parameter expansion was used to derive an effective three-dimensional theory from lattice QCD with heavy Wilson quarks that shares the center symmetry and its breaking in and away from the pure gauge sector with QCD. It posseses a sign problem at non zero chemical potential that is mild enough to perform simulations even at large values of the chemical potential. In the reference the order of the expansion allowed them to simulate up to $N_\tau \sim 6$ lattices. They determined the endpoint of the first order deconfinement transition as a function of the quark mass for $N_\tau = 4$ lattices for $N_f = 1, 2, 3$ flavors. For the results see table 3.3. In different studies which took place about the same time [125, 126] the probability functions of the plaquette and the Polyakov loop were examined for changes with respect to the type of transition in order to find the $Z_2$ point. They simulated $SU(3)$ pure gauge theory on $N_\tau = 4$ lattices and subsequently performed a hopping parameter expansion together with a reweighting extrapolation to finite $\kappa$ values in order to investigate the mass dependence of the distribution functions. Their results are listed in table 3.3. Finally the results obtained from this work for $N_\tau = 4 (N_f = 3)$ and $N_\tau = 6, 8, 10 (N_f = 2)$ are listed in the last column of table 3.3. In contrast to studies listed before in this work no expansion whatsoever has been done. The results have been obtained from simulating the full theory which could be an explanation for the discrepancy between the different values in the last row of table 3.3. Note that all of the studies cited use standard Wilson fermions without improvement. For this reason the $\kappa_{Z_2}$ values listed in table 3.3 can be compared. In such studies where a transition point is identified by values of the hopping parameter $\kappa$ it is common to compute the quark mass or a corresponding pseudo-scalar meson mass at zero temperature

at the transition point, as well. This turns out to be a notoriously hard problem since in the heavy mass region the Compton-wavelength of particles is very small so that generally very fine lattices are required to resolve them. Section 3.2.1 addresses this topic. In this work pseudo-scalar meson masses were computed at the critical couplings for all $N_\tau$ but the requirement $am \leq 1$ is not met. For a detailed discussion see the results section 5.3 of this work.

| $N_f$ | $N_\tau$ | $\kappa_{Z_2}$ [103] | $\kappa_{Z_2}$ [125] | $\kappa_{Z_2}$ [124] | $\kappa_{Z_2}$ (this work) |
|---|---|---|---|---|---|
| 1 | 4 | 0.0822(11) | 0.0783(4) | ∼0.08 | |
| 2 | 4 | 0.0691(9) | 0.0658(3) | | |
| | 6 | | | | 0.0939(14) |
| | 8 | | | | 0.1167(12) |
| | 10 | | | | 0.1229(10) |
| 3 | 4 | 0.0625(9) | 0.0595(3) | | 0.0553(7) |

Table 3.3: The table shows a summary of the values $\kappa_{Z_2}$ found in different studies for $N_f = 1, 2$ and 3 flavors and several temporal lattice extents.

### The Light Quark Mass Region

Universality arguments [127] and numerous numerical studies on rather coarse lattices (just to name a few of them) with unimproved [128–132](staggered) and improved [71, 132–134](staggered), [135] (Wilson) actions give rise to certainty about a region of first order phase transitions around the chiral limit for $N_f = 3$ QCD (lower left corner in fig. 3.5). The question remains open on the position of the chiral critical line in the continuum limit as no or only partially successful attempts for a continuum extrapolation exist so far. Pseudoscalar meson masses To identify the location of the $Z_2$ point in terms of a physical quantity, pseudoscalar meson masses have been computed [7] in several studies which produced conflicting results. The reason is that different discretization schemes and lattice spacings have been used. The computed values range from $\sim 50$MeV to $\sim 300$MeV [136]. A rather recent study in which highly improved staggered quarks (HISQ) on $N_\tau = 6$ lattices were simulated produced an upper bound for the pion mass at the critical point of $50$MeV [137]. Another study that simulated non-perturbatively $O(a)$ improved Wilson-Clover fermions on up to $N_\tau = 10$ lattices claims to find a continuum value for the pion mass of $\sim 100$MeV [72]. However, there seems to be a growing agreement from the more recent studies that the region of chiral first order phase transitions could be very small and is of less relevance for real world thermodynamics [136].

The situation in the $N_f = 2$ chiral limit (top left corner in fig. 3.5) is even less clarified and considered to be more relevant for thermodynamics at the physical point. The lack of clarity about this area stems from the huge computational costs of simulating very small quark masses with currently available computer technology. Of course researchers in the field do not simply wait for faster computers but work hard to explore possibilities to circumvent the given computational limitations. The global chiral symmetry group

[7] Of course, pseudoscalar masses have been computed at zero temperature (large $N_\tau \gg N_s$) but at same simulation parameters at which the $Z_2$ point was extracted in finite temperature simulations.

of the action is $SU(2)_R \times SU(2)_L \times U_A(1)$ where $U_A(1)$ is anomalous. Since the chiral phase transition is linked to symmetry breaking a crossover transition can be excluded. This implies there are two possible scenarios currently considered:

1. The $U_A(1)$ symmetry is broken which implies a second order phase transition belonging to the universality class of a classical four component Heisenberg antiferromagnet, i.e. 3d $O(4)$ spin models (left-hand side fig. 3.5).

2. The $U_A(1)$ symmetry gets restored at the transition which allows for a first order phase transition [127] (right-hand side fig. 3.5).

In the second case of a restored $U_A(1)$ symmetry theoretical studies led to yet another alternative: In [138] a high-order field-theoretical perturbative study of the renormalization-group (RG) flow of the corresponding three-dimensional multiparameter Landau-Ginzburg-Wilson $\phi^4$ theory with the same symmetry-breaking pattern was carried out and in [139] the chiral linear sigma model in the presence of the axial anomaly was studied in the local-potential approximation of the Functional Renormalization Group (FRG). Both support the possibility for a second order transition belonging to the $O(2) \times O(4)$ universality class. In another study it was shown for a model with same chiral symmetries as $N_f = 2$ QCD that turning on the $U_A(1)$ anomaly weakens the first order transition until it vanishes at a critical anomaly strength [140]. In the case of a second order scenario in the $N_f = 2$ chiral limit the region of first order transitions at small values of $m_{u,d}$ and $m_s$ has to vanish at some point at larger values of $m_s$, i.e. the chiral critical line bounding the first order region terminates at $m_{u,d} = 0$ and some finite value $m_s^{\text{tric}}$ in a tricritical point as illustrated in the right-hand side schematic of fig. 3.5. The system at such a point would exhibit 3d mean field exponents [141] and permits to exploit tricritical scaling relations. In general the strategy is to perform simulations for several values of the quark masses and to test if scaling relations apply which describe the data properly in the vicinity of a critical point. A common approach to investigate the chiral limit is to examine the magnetic equation of state (MEoS) $M/h^{1/\delta} = f_G(t/h^{1/\beta\delta})$ (M is the magnetic order parameter) that is governed by a single scaling function $f_G$. The magnetic field $h$ and the reduced temperature $t$ describe the proximity to the critical window and $\beta, \delta$ are universal critical exponents. In this context typically the quark mass dependence of $M$ and its susceptibilities are studied so as to gather insights about the chiral transition in $N_f = 2$ QCD. The difficulty with these kinds of approaches lies in the extraction of the critical indices whose values are very close for which reason they often can't be determined reliably within the errors of a fit of the functional scaling form. Numerous studies employing both Wilson and staggered fermions following this and different approaches are listed in [136]. The author of this reference points out a more recent study [142] of his own using the described approach and reports a value of $m_s^{\text{tric}} < m_{s,\text{phys}}$, i.e. below the physical value of the strange quark mass. He cites other recent studies, e.g. [143] where simulations with improved Wilson quarks have been performed and which support his conclusion putting the second order transition in the $N_f = 2$ chiral limit into the $O(4)$ universality class. The author also cites contradicting studies with standard staggered [144] and unimproved Wilson fermions [145] employing an imaginary chemical potential approach and suggesting a first order transition in the $N_f = 2$ chiral limit. Table 3.4 gives an overview of studies supporting the first or second order scenario. Finally I want to point out the importance of the second order chiral critical line because together with the curvature of the $Z_2$ surface that emerges from switching on a

chemical potential in the $m_{u,d} - m_s - \mu$ space the position or even the existence of the critical endpoint in the QCD phase diagram (c.f. fig. 3.3) can be influenced - a problem I will discuss in section 3.5.3.

| year | pro $1^{st}$ order | pro $2^{nd}$ order |
|---|---|---|
| 1996 | | [146](O(4),Wilson) |
| 2003 | [147](no LQCD) | |
| 2006 | | [148](O(4),staggered), [149] (O(4),staggered) |
| 2008 | [150](staggered) | |
| 2009 | | [151](O(4),staggered) |
| 2013 | [152](overlap) | |
| 2014 | [144](staggered) | |
| 2016 | [145](Wilson) | [143](O(4), improved Wilson) |

Table 3.4: The table (without claiming to be exhaustive) gives an overview of studies pro and contra a first/second order scenario in the $N_f = 2$ chiral limit.

### Fractional Number of Flavors

Another very interesting approach to determine the nature of the transition in the chiral limit is currently being explored by members of our group (F. Cuteri, O. Philipsen, A. Sciarra)[153] and involves using a continuous number of flavors in the path integral. After integrating out the fermionic action the path integral for $N_f$ mass degenerate flavors of fermions has the form

$$Z(m, \mu, N_f) = \int \mathcal{D}\mathcal{U} \det \left[M\left(\mathcal{U}, m, \mu\right)\right]^{N_f} \, \mathrm{e}^{-S_G}. \tag{3.78}$$

For a fractional $N_f$ this can be simulated for instance with a rational hybrid Monte Carlo algorithm (section 4.2 explains the rhmc). The idea in this approach is that a $Z_2$ transition exists for $N_f = 3$ flavors (c.f. previous section about the light mass region) but non for $N_f = 1$. Consequently thinking in terms of a continuous $N_f$ the $Z_2$ transition has to end at some point between $N_f = 1$ and $N_f = 3$. Since there is a line of first order triple transitions starting in the $N_f = 3$ chiral limit at $m_{u,d,s} = 0$ extending along the $m_s$ axis (bottom left corner of fig. 3.5) the $Z_2$ transition must end between $N_f = 1$ and $N_f = 3$ in a tricritical point we denote as $N_f^{\text{tric}}$. The big question is whether $N_f^{\text{tric}} < 2, N_f^{\text{tric}} = 2$ or $N_f^{\text{tric}} > 2$. The schematics of fig. 3.6 should give a better idea of the problem. What was just explained can be intuitively understood in these diagrams from comparing the colored dashed framings in the $m_q - N_f$ diagram with the corresponding ones in the adjacent $m_{u,d}, m_s$ diagram. Note that at $N_f = 0$, i.e. quenched QCD there are first order transitions everywhere. This is no surprise as it describes the heavy mass limit $m_q \to \infty$ (top right corner in the $m_{u,d} - m_s$ phase diagrams in fig. 3.6) with only infinitely heavy and static quarks. The vertical mass axis has no meaning for $N_f = 0$ for which reason it should be considered "out of the diagram". The strategy in this approach consists in using the fact that scaling laws apply in the vicinity of

the tricritical point $N_f^{\text{tric}}$ from which the $Z_2$ line emanates. The functional form of the $Z_2$ line is given by

$$m_{\text{q},Z_2}^{\frac{2}{5}}(N_f) = C(N_f - N_f^{\text{tric}}). \tag{3.79}$$

The $Z_2$ line can be mapped out starting from $N_f > 2$ where the simulations are feasible. Subsequently the functional form can be fitted to the data to check whether it terminates before or if it extends beyond $N_f = 2$. The preliminary results produced in [154] currently support a first order scenario for the $N_f = 2$ chiral limit with a value of $N_f^{\text{tric}} = 1.75(32)$. It should be remarked that the approach introduces the problem of non-locality at non-integer $N_f$ which implies a quantum field theory that is not well defined in the continuum limit $a \to 0$. However, since the goal is just to find the two integer numbers between which $N_f^{\text{tric}}$ is located, the non-locality presents no problem.

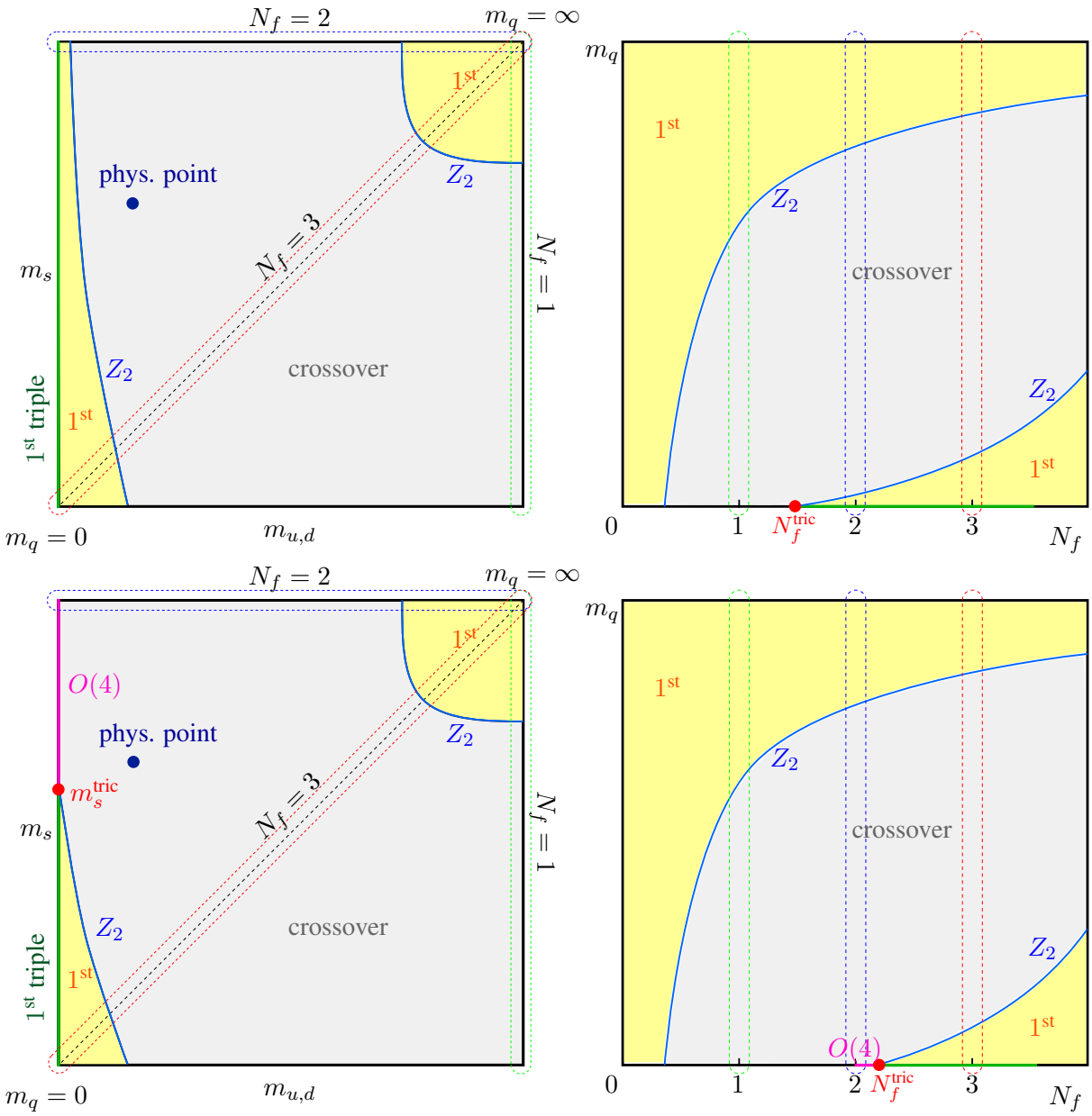


Figure 3.6: On the right-hand side the QCD phase transitions at $\mu = 0$ are plotted in a $m_q - N_f$ diagram for two different scenarios. There are first order phase transitions in the heavy mass limit each $N_f$. For small $N_f \ll 1$ the region of first order transitions extents all the way down towards the limit $m_q \to 0$. There is another region of first order transitions in the chiral region starting around $N_f \approx 2$ extending to larger masses as the $N_f$ grows. The two regions of first order transitions are separated by an area of crossover transitions from which they are separated by $Z_2$ lines. The diagram on the top shows a scenario where the $Z_2$ line in the chiral region terminates in a tricritical point $N_f^{\text{tric}}$ at $N_f < 2$ supporting the possibility for a region of first order transitions in the $N_f = 2$ chiral limit (c.f. the discussion in the previous section). The bottom diagram depicts the case in which the $Z_2$ line terminates already at $N_f > 2$ which implies a second order transitions in the $N_f = 2$ chiral limit.
On the left-hand side are plotted the corresponding quark mass phase diagrams, The corresponding quark mass diagrams are plotted on the left-hand side. Comparing the left- and right-hand side the corresponding subspaces in the diagrams on both side are identified by equally colored dashed framings. For instance consider the blue colored dashed framing in the left-hand side diagrams which corresponds to $N_f = 2$ flavor QCD for all values of quark masses. An equally colored dashed framing showing the same parameter subspace can be found in the right-hand side phase diagram at $N_f = 2$ parallel to the $m_q$ axis.

### 3.5.3 The Nature of the Phase Transition at Imaginary $\mu$

Following on from the discussion in section 3.3.4 here I will further discuss the QCD phase structure at purely imaginary chemical potential. As explained before, choosing a purely imaginary chemical potential QCD features interesting and useful properties: There is no sign problem at imaginary chemical potential, the partition function is periodic in $\mu_i/T$ and the $Z_3$ center symmetry is present despite the inclusion of dynamical quarks in the theory. In section 3.3.4 I discussed the transitions in the QCD phase diagram as a function of the temperature and the purely imaginary chemical potential by means of fig. 3.2. The points that are of particular interest are the transitions between the $Z_3$ sectors at critical values of the chemical potential $\mu_{i,c}/T$ in the partition function eq. (3.75) with $n = k + 1/2$ and $k \in \mathbb{N}$. At these values a quark mass phase diagram that corresponds to the $Z_3$ endpoint as a function of the quark masses and flavors, analogous to the one at zero density can be plotted which is shown in fig. 3.7 (right). Next to it is again plotted the one at zero density (left) so as to contrast both diagrams. In the new diagram at $\mu_{i,c}/T$ the tricritical points are assumed to be connected to tricritical lines, as it the case for the $Z_2$ points at $\mu = 0$. Due to the absence of the sign problem this can be checked with numerical simulations. Comparing both

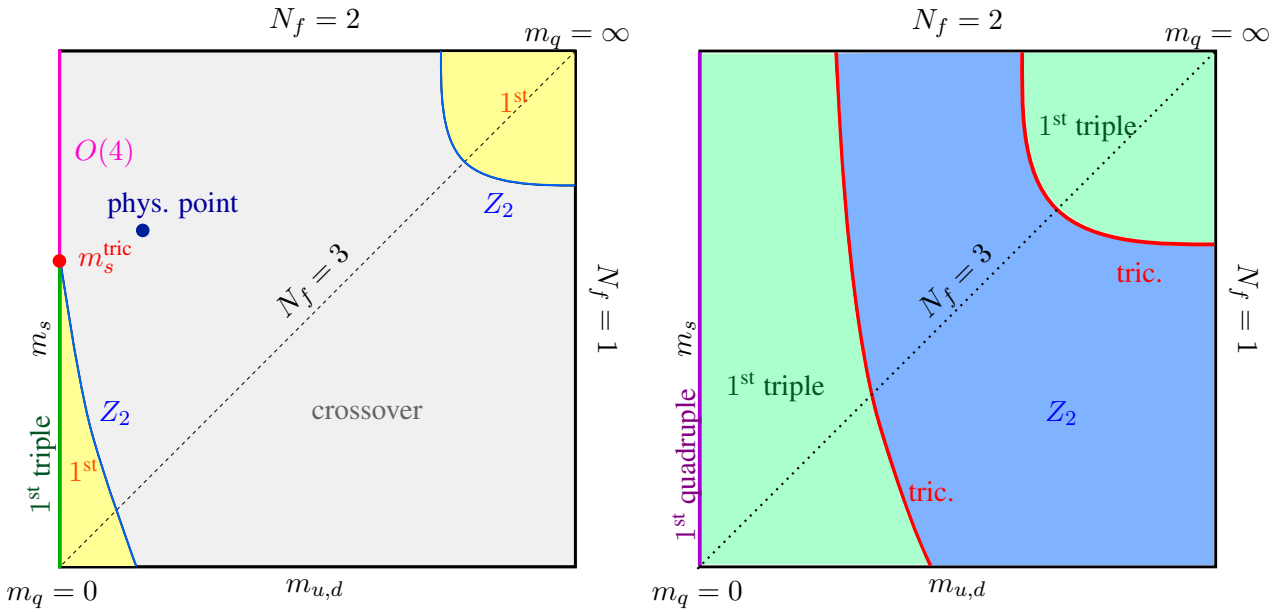


Figure 3.7: Roberge-Weiss.

diagrams several changes in the nature of the phase transitions can be observed:

- First order regions $\longrightarrow$ first order triple regions,
- $Z_2$ lines $\longrightarrow$ tricritical lines,
- crossover region $\longrightarrow$ $Z_2$ region,
- first order triple line $\longrightarrow$ quadruple line.

These changes seem natural given that at $\mu_{i,c}/T$ there is a confluence of the chiral/deconfinement phase transition and the transition between the $Z_3$ sectors. For instance a tricritical point represents the confluence of two critical points which is given by the critical point of the chiral/deconfinement transition fusing into the endpoint of the transition between the $Z_3$ sectors. The same is true for the confluence of

points in the regions with a different nature. Since the theory at $\mu/T = 0$ is analytically connected to the theory at $\mu_{i,c}/T$ both diagrams in fig. 3.7 can be combined in a three-dimensional phase diagram via a third axis that is represented by the squared chemical potential. This is done in fig. 3.8, where the resulting diagram is plotted from $(\mu/T)^2 > 0$ to the Roberge-Weiss value $(i\mu_{i,c}/T)^2 = -(\pi/3)^2$. In

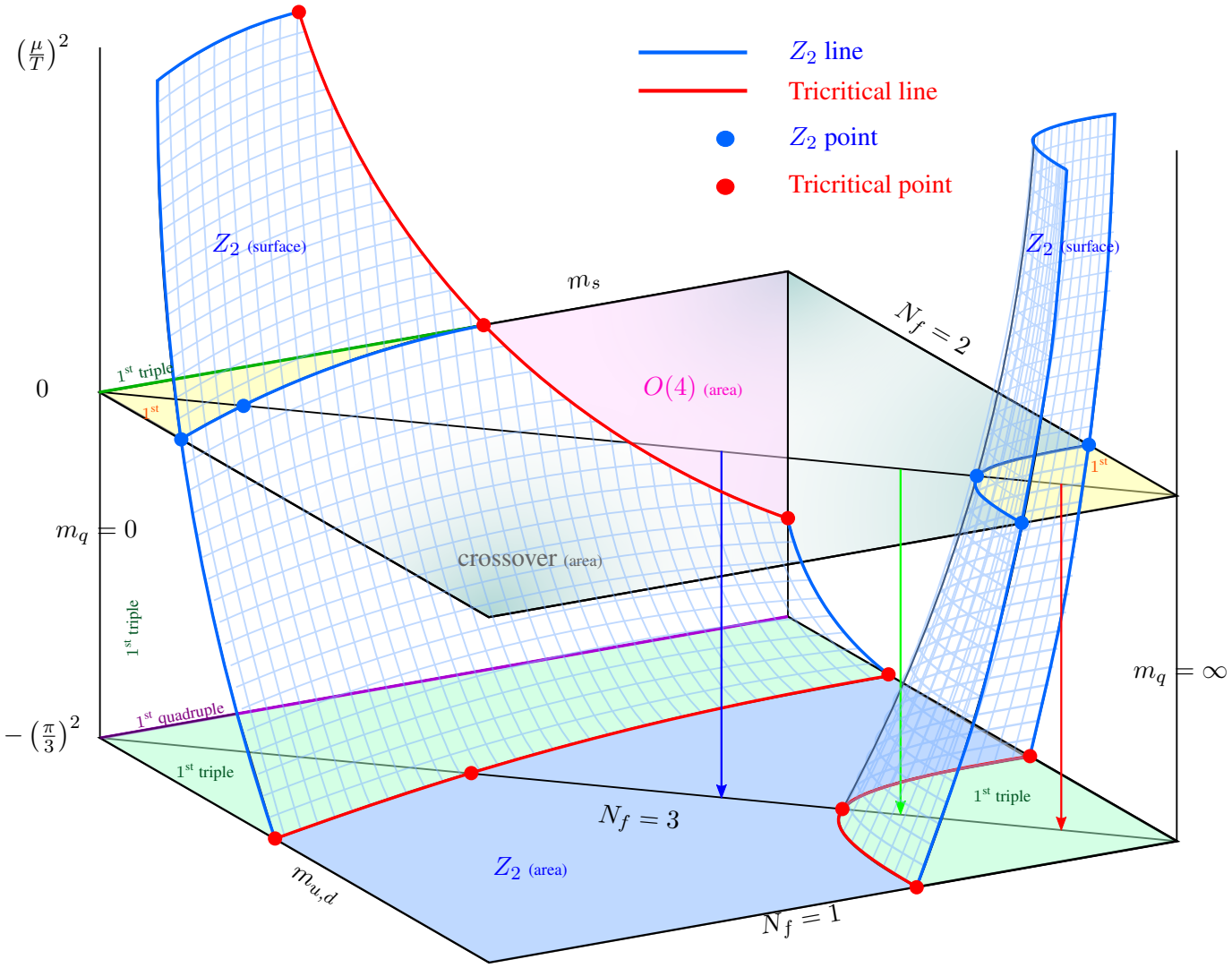


Figure 3.8: The figure shows a qualitative schematic ($O(4)$ scenario) of the extended Columbia plot ($(m_{u,d}, m_s, \mu)$-diagram) between $(\mu/T)^2 > 0$ and $(\mu/T)^2 = -(\pi/3)^2$ (Roberge-Weiss plane), where the plane at $(\mu/T)^2 = 0$ and the Roberge-Weiss plane are plotted explicitly . The $Z_2$ lines become $Z_2$ surfaces terminating in tricritical lines in the Roberge-Weiss plane, while the tricritical points extend to lines. At the Roberge-Weiss value of $(\mu_{i,c}/T)^2 = (\pi/3)^2$ the chiral/deconfinement transition fuses into the transition between the $Z_3$ sectors (c.f.fig. 3.9) which is, as it can be seen in the diagram, a function of the quark mass and the number of flavors $N_f$, thus promoting the transitions there from crossover to $Z_2$, from first order to first order triple and so forth. Note, that this schematic illustrates the possibility of a second order transition in the $N_f = 2$ chiral limit. In the alternative of a small region of first order transitions for $m_{u,d} < m_{\mathrm{u,d};Z_2}$ at $(\mu/T)^2 = 0$ the chiral $Z_2$ surface would cover the whole $m_{u,d} = 0$ backplane at least up to $(\mu/T)^2 = 0$. The filled circles mark critical and tricritical points that have been mapped out in numerical studies.

this case the $Z_2$ lines at zero chemical potential extend surfaces which terminate in the Roberge-Weiss plane in tricritical lines. This diagram, commonly referred to as the extended Columbia plot, can be

used to qualitatively complement the information about the nature of the chiral/deconfinement line that analytically continues from zero to imaginary $\mu$, represented by the dashed lines in fig. 3.2. I plotted this diagram again in fig. 3.9 for different values of $m_q$ with the frames colored equal to the arrows placed in fig. 3.8 on the $N_f = 3$ diagonal. For instance consider the green arrow (second one from the right hand-side) in fig. 3.8 starting in the crossover region at $\mu = 0$. Following this arrow down to negative values of $(i\mu_i/T)^2$ at some point it passes through a critical point on the $Z_2$ surface entering the region of first order phase transitions until it finally ends on the Roberge-Weiss plane in the region of first order triple transitions. This translates to the behavior of the deconfinement line in the top right diagram with a green frame in fig. 3.8. There the deconfinement line analytically continues from $\mu = 0$ to imaginary $\mu$ until its nature becomes first order after passing through a $Z_2$ point. Subsequently it joins the $Z_3$ endpoint which in this case is a first order triple point. The remaining diagrams can be read in the same fashion.

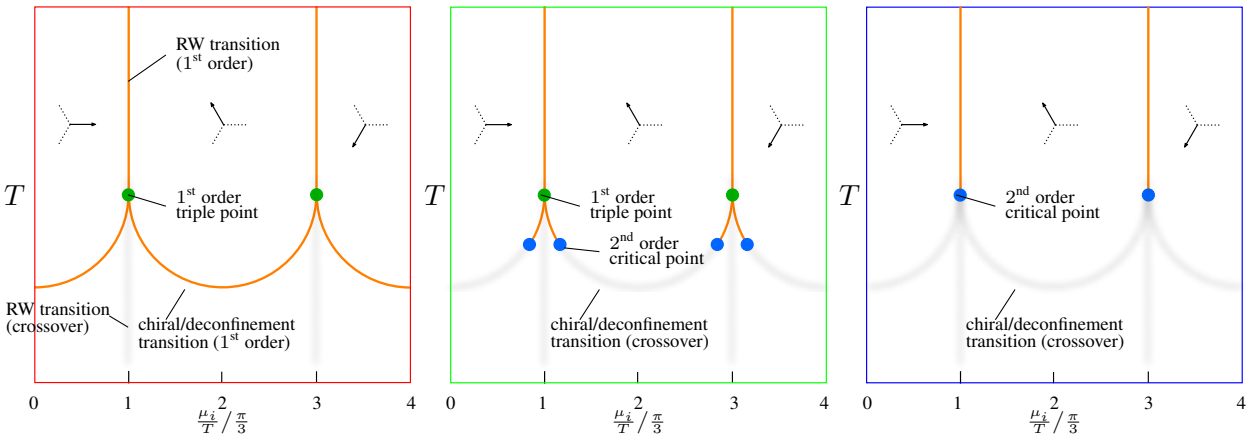


Figure 3.9: Same diagrams as in fig. 3.2, with the difference that the nature of the chiral/deconfinement line and the RW endpoint is made explicit for different values of the quark mass. The left diagram is corresponds to very large (light) quark masses $m_q > m^{\text{heavy}}_{\text{q},Z_2}$ ($m_q < m^{\text{light}}_{\text{q},Z_2}$). The middle diagram corresponds to large (light) quark masses $m^{\text{heavy}}_{\text{q},Z_2} < m_q < m^{\text{heavy}}_{\text{q,tric}}$ ($m^{\text{light}}_{\text{q,tric}} > m_q > m^{\text{light}}_{\text{q},Z_2}$). The right diagram corresponds to intermediate masses $m^{\text{light}}_{\text{q,tric}} < m_q < m^{\text{heavy}}_{\text{q,tric}}$. Note, that in the right diagram the RW endpoint would be a tricritical point for $m_q = m^{\text{light}}_{\text{q,tric}}$ or $m_q = m^{\text{heavy}}_{\text{q,tric}}$.

An important observation is that the first order regions at $\mu = 0$ are strengthened with growing purely imaginary $\mu$ (larger negative values of $(\mu/T)^2$) but weakened with growing real $\mu$. For both the chiral region [149, 155] as well as the deconfinement region [103, 126] this has been studied numerically. This is contrary to what one would expect given the conjectured QCD phase diagram, fig. 3.3, for which the first order region would expand to larger mass as $\mu$ is increased. Thus this might have important consequences for the possible existence of a critical endpoint in this diagram. I will comment on this problem in the following section. However, this property can be utilized to gain insights about the $N_f = 2$ chiral critical point at $\mu = 0$ from simulations at purely imaginary $\mu$. At purely imaginary $\mu$ the chiral critical points extend to larger masses, for which LQCD simulations are less costly compared to simulations near the chiral critical point at $\mu = 0$. The $Z_2$ line as a function of $\mu_i$ terminates in a tricritical point located in the Roberge-Weiss plane. The behavior of a $Z_2$ line in the vicinity of such a point is governed by tricritical scaling relations. Once several $Z_2$ points at different values $\mu_i$ have been found one can use these scaling laws in order to extrapolate the $Z_2$ line towards the chiral limit at $\mu = 0$, c.f. fig. 3.10 (l.h.s). This can be

done by a fit of a functional form which for $N_f = 2$ is given by

$$\frac{m_{\mathrm{q},Z_2}(\mu^2)}{T} = \frac{m_{\mathrm{q},Z_2}(0)}{T} + C\left[\frac{\pi}{3}^2 + \frac{\mu}{T}^2\right]^{\frac{2}{5}}. \tag{3.80}$$

This has already been tested successfully some time ago for the deconfinement transition in the heavy quark mass region [103, 156] where data was produced in the context of an effective three-dimensional theory based on a combined strong coupling and hopping parameter expansion for imaginary and real values of the chemical potential. The fit of the functional form eq. (3.80) could describe the data perfectly well up to large real values of the chemical potential. Somewhat later this has been repeated in a numerical study of the $N_f = 2$ chiral region with staggered fermions [144] where a first order transition was observed. Note that the study was performed on relatively coarse $N_\tau = 4$ lattices corresponding to a lattice spacing of $a \sim 0.3$ fm. The result of another more recent study [145] performed in our group for which Wilson fermions were used supports the first order scenario. In this study the approach was a similar one with the difference that studying tricritical scaling was not necessary since the chiral $Z_2$ line between $\mu_{i,c}/T$ and $\mu/T = 0$ was found at values of $m_{\mathrm{q},Z_2}$ which were still feasible to simulate, i.e. the sensitivity of $m_{\mathrm{q},Z_2}$ with respect to $\mu_i$ turned out to be relatively small within the given discretization. Note that the lattices simulated in this study have a temporal extent of $N_\tau = 4$ and are hence relatively coarse with $a \sim 0.25 - 0.3$ fm, as well. The result of the study is shown in fig. 3.10 by the red data points with error bars, denoted as $m_\pi^{Z_2,\mathrm{Wilson}}$ in the plot legend. As one can see from the data points, the mapped out $Z_2$ line starts from a tricritical point in the Roberge-Weiss plane at $(\mu_{i,c}/T)^2 = -(\pi/3)^2$ denoted by $m_\pi^{\mathrm{tric,Wilson}}$ at a mass of about $900$MeV and extends up to $(\mu_{i,c}/T)^2 = 0$ where it ends at a mass of about $550$MeV. The authors compare their findings to the result from another study, performed with the staggered discretization, which places the critical point at a lower pion mass of about 12% of the one found with Wilson fermions (see fig. 3.10). They state that this comparison, provided that both discretizations are fundamentally correct and have the same continuum limit, suggests that the discretization errors on the critical point found with Wilson fermions at a lattice spacing of $a \approx 0.25$ are of $\mathcal{O}(100\%)$.

Furthermore, briefly coming back to the region at $\mu = 0$, fig. 3.10 includes results from studies using $\mathcal{O}(a)$ improved Wilson fermions on much finer lattices ($N_\tau = 12$[157] and $N_\tau = 16$[158]) which found a crossover transition at the simulated points and can serve as an upper bound for the critical point within Wilson discretizations. In a recent study [159] (part of the present work) the $Z_2$ point obtained simulating Wilson fermions on $N_\tau = 6$ lattices was found at a value of about 70% of the $N_\tau = 4$ value. Considering the improved and unimproved results altogether, the authors of [145] plausibly conclude that on the coarse $N_\tau = 4$ lattices the $\mathcal{O}(a)$ cut-off effects seem to be far from dominant. The qualitative behavior of a shrinking $Z_2$ region for finer lattices observed throughout different studies using different discretizations remains consistent.

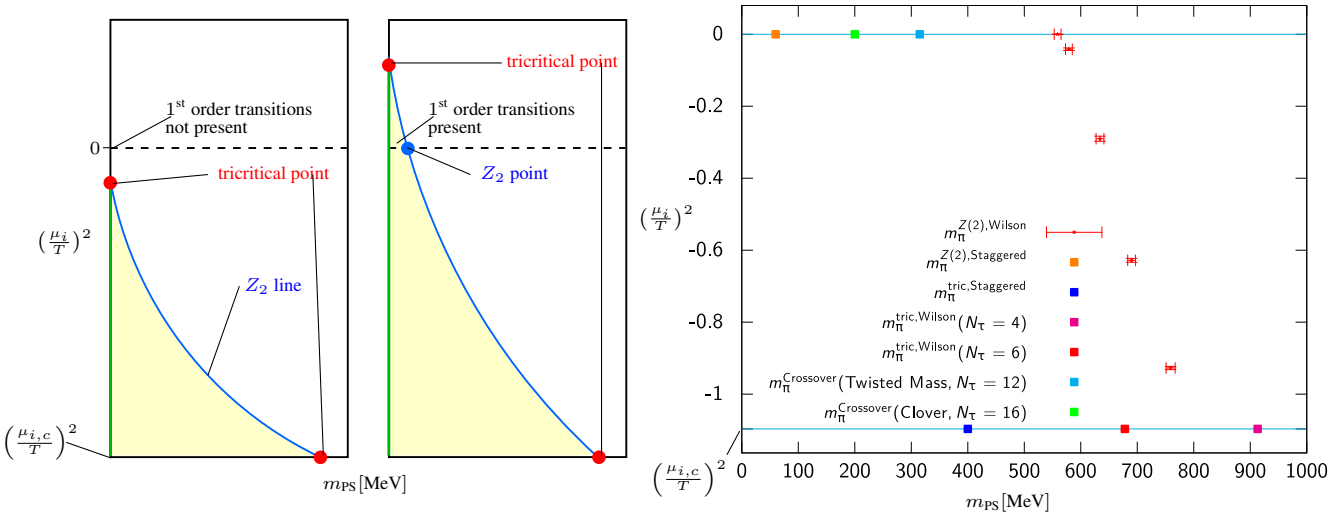


Figure 3.10: L.h.s.: Schematic showing the tricritical scaling between two tricritical points in the $N_f = 2$ backplane. The left schematic shows how the $Z_2$ line ends in a tricritical point below $\mu = 0$ implying a second order transition in the $N_f = 2$ chiral limit while in the schematic on the right-hand side the $Z_2$ line extends into the region of real chemical potential at $\mu > 0$ implying a region of first order transition in the $N_f = 2$ chiral limit. R.h.s.: The plot is taken and shows actual data from [145](Wilson, $N_\tau = 4$) where the $Z_2$ line was completely mapped out. Further results with staggered [144], Wilson [145]($N_\tau = 4$), Wilson [159]($N_\tau = 6$, results as part of this work), $\mathcal{O}(a)$ improved Wilson Twisted mass [157]($N_\tau = 12$), $\mathcal{O}(a)$ improved Wilson-Clover [158]($N_\tau = 16$) fermions are included in the plot.

### 3.5.4 From zero and Imaginary to Real Chemical Potential

In the previous section 3.5.3 I indicated that the curvature of the chiral $Z_2$ surface is of utmost importance for the nature of the phase transition at finite $\mu$. The physical point is located in the crossover region of the $\mu = 0$ quark mass diagram (c.f. fig. 3.5). The current conjecture of the $(T, \mu)$ QCD phase diagram suggests that at some value $\mu_E$ the crossover turns into a first order transition after passing through a second order point. A possible realization of this suggestion requires the $Z_2$ line in the $(m_{u,d})$ plane to move to larger masses as a function of $\mu$ and to cross the physical point at $\mu_E$, i.e. the contrary to what is depicted in fig. 3.8. Though the schematic is drawn in this way for a specific reason: The change of the $Z_2$ line under the influence of $\mu$ was studied extensively by means of Taylor series and analytic continuation and strong indications were found that it moves to smaller masses. This for instance can be calculated by fixing a value of $m_s$ (e.g. its physical value) and writing down the Taylor expansion of $m_{u,d}$

$$\frac{m_{\mathrm{u,d};Z_2}(\mu)}{m_{\mathrm{u,d};Z_2}(0)} = 1 + c_1 \left(\frac{\mu}{\pi T_{\mathrm{c}}}\right)^2 + c_2 \left(\frac{\mu}{\pi T_{\mathrm{c}}}\right)^4 + \mathcal{O}\left(\left(\frac{\mu}{T}\right)^6\right), \tag{3.81}$$

where the expansion parameter comes only in even powers due to CP-Symmetry. The task then is to compute the coefficients $c_1, c_2, \cdots$. Here I only want to roughly sketch this method and to make it short, I am being imprecise by leaving out a further step in which on the lattice the critical parameters in this equation have to be replaced by the pseudo-critical lattice couplings that again can be expanded around the critical quark mass at zero density. The interested reader can find the details in in [155]. However the coefficients in these lattice couplings can be obtained from employing the kurtosis $B_4$ introduced in section 3.1.1 and further discussed in section 3.1.2. $B_4$ behaves discontinuously when passing from a first order transition to a crossover through a second order critical point. On a finite volume this continuity is smeared out and $B_4$ can be expanded around the critical point as a function of the lattice couplings via

$$B_4(am, a\mu) = 1.604 + \sum_{i,j=1} b_{ij} L^{\frac{i+j}{\nu}} (am_{\mathrm{u,d};Z_2}(\mu) - am_{\mathrm{u,d};Z_2}(0))^i (a\mu)^{2j}. \tag{3.82}$$

The coefficients in (3.81) can apparently be related to the ones appearing in $B_4$ by formulating and evaluating derivatives like

$$\frac{d(am_{\mathrm{u,d};Z_2}(\mu)}{d(a\mu)^2}) = -\frac{\partial B_4}{\partial (a\mu)^2} \left(\frac{\partial B_4}{\partial (am_{u,d})}\right)^{-1} \tag{3.83}$$

and higher orders respectively. Once the coefficients are computed from these expressions they can be related to the ones of the continuum couplings which is a non-trivial task. In [155] this calculation was performed and the coefficients in eq. (3.81) were found to be negative implying a shift of the $Z_2$ line to smaller masses as $\mu$ is increased. Consequently if there is no rapid change in this behavior at some finite value of $\mu$, the critical endpoint in the QCD phase diagram does either not exist or belongs to a different transition unknown so far.

# Chapter 4

# Numerical Methods and Algorithmic Details

In section 4.1 I will discuss the methods used to analyze the data obtained from LQCD simulations. These will cover the error analysis techniques Jackknife and Bootstrap applied to complex observables (including the $\Gamma$-method for the autocorrelation time) but also the multiple-histogram reweighting technique which allows to efficiently interpolate between simulated ensembles in order to precisely extract observables at specific, non-simulated values of the inverse lattice coupling $\beta$. In particular the combination of error analysis and multiple-histogram reweighting poses an interesting challenge. Finally in this section the algorithm will be discussed used to filter enormous amounts of fits with respect to specific criteria which allows to filter for fits not only having good values of $\chi^2_{\text{NDF}}$ and $Q$ but also satisfy the criteria related to the underlying fitting model. In section 4.2 the Rational Hybrid Monte Carlo algorithm will be addressed which allows for simulations of odd numbers of fermion flavors $N_f$ and which has been implemented for the Wilson fermion discretization into the LQCD application CL$^2$QCD. The latter will be briefly described in the subleading section 4.3. The chapter will be concluded by a presentation of a Bash Handler to Monitor and Administrate Simulations (BaHaMAS) in section 4.4.

## 4.1 Data Analysis Methods

### 4.1.1 Error Analysis

The expectation value of an observable is estimated from a series of measurements of the observable taken on configurations produced in Markov chain Monte Carlo simulations. A necessary step in the numerical analysis of Monte Carlo data is to compute the error on the estimated value of the observable. The error is given by the standard deviation which in turn is obtained from taking the square root of the variance with respect to the expectation value of an observable. Of course the variance can only be an estimate itself since it has to be based on the estimate of the expectation value. The result for some estimated value of an observable is then quoted as

$$\hat{O} \pm \sigma, \quad \text{with } \hat{O} = \frac{1}{N}\sum_{i=1}^{N} \text{ and } \sigma = \sqrt{\frac{1}{N} 2\tau_{\text{int},O} \hat{\sigma}^2_O}. \tag{4.1}$$

In this expression $\hat{O}$ and $\hat{\sigma}_O^2$ are the well known unbiased estimators for the expectation value $\langle O \rangle$ and the variance $\sigma_O^2 = \langle O^2 \rangle - \langle O \rangle^2$. The integrated autocorrelation time $\tau_{\text{int},O}$ takes into account correlations between the measurements which are intrinsic to Monte Carlo simulations and if ignored lead to an underestimation of the error. It relates the total number of measurements to the effectively independent data by $N_{\text{indep}} = N/(2\tau_{\text{int},O})$. The size of the autocorrelation time depends on the algorithm as well as on the parameters of the simulation. For instance in lattice gauge theories $\tau_{\text{int},O}$ is expected to grow like $\tau_{\text{int},O} \sim (\xi_O)^z$, where $\xi_O$ is the correlation length of $O$ which is defined by the exponential decay of correlation functions between observables separated by some distance on the lattice. $z$ is some dynamical critical exponent of the system depending on the algorithm. Close to phase transitions, i.e. critical points, $\xi$ diverges implying the computational effort to grow with the lattice extension to the power of the exponent, $L^z$. There are numerous resources on how to compute and analyze these quantities, for instance [33, 160, 161]. Using (4.1) might suffice for the error analysis of primary quantities, i.e. observables which can be measured configuration-wise, for instance the Polyakov loop. For more complex observables like *derived quantities* which are (in general non-linear) functions of primary observables, using (4.1) will not suffice anymore. Error propagation for derived quantities, depending on the underlying observable and theory, can become very difficult or even impossible. An examples is given by $B_4$ which is constructed out of moments of fluctuations of an observable $O$:

$$B_4 = \frac{\left\langle (O - \langle O \rangle)^4 \right\rangle}{\left\langle (O - \langle O \rangle)^2 \right\rangle^2} = \frac{\left\langle O^4 \right\rangle - 4 \left\langle O^3 \right\rangle \langle O \rangle + 6 \left\langle O^2 \right\rangle \langle O \rangle^2 - 3 \langle O \rangle^4}{(\langle O^2 \rangle - \langle O \rangle^2)^2} \tag{4.2}$$

In such cases resampling methods like the Jackknife or the Statistical Bootstrap procedures are usually consulted which have a straightforward application and provide a simple way to estimate the observable as well as its variance. For the statistical analysis of the data produced in the context of this work the Jackknife procedure was used for the error computation of the raw simulated data and functions thereof. For interpolated data obtained by multiple histogram reweighting, discussed in section 4.1.2, the Statistical Bootstrap procedure was employed.

Before I proceed to the methods used for the error analysis lets introduce some notation borrowed from [162]: The term *replica* means independent Markov chains produced at the same values of the parameters of the system and are typically simulated in parallel in order to a) gather statistics faster and b) obtain more control over the statistics and related error analysis as illustrated in fig. 4.1. The difference is simply that the respective simulations are started from different points in the phase space by choosing different initial random numbers. Error analysis methods like the so called $\Gamma$-method by U.Wolff [162] explicitly employ replica in order to cancel biases occurring in the error analysis due to the way certain estimators for observables and functions thereof are defined. In the following I will use $O_\alpha$ to denote the exact statistical mean value of a primary observable where $\alpha$ identifies the specific observable (e.g. $|P|$ or Im$P$). For a Monte Carlo estimate of a primary observable I will use $o_\alpha^{i,r}$ where $i$ labels the measurements and $r$ denotes the replicum. In the following I will exemplify the error computation for $B_4$ using the Jackknife method. Later, in the section 4.1.2 about reweighting, I will explain how the error on reweighted quantities was calculated using Statistical Bootstrap. For a thorough discussion of both methods I recommend [161]. At the end of this section I will also briefly introduce the $\Gamma$-method and compare the results obtained from Jacknife and Bootstrap to the $\Gamma$-method which involves an explicit estimation of the autocorrelation function.

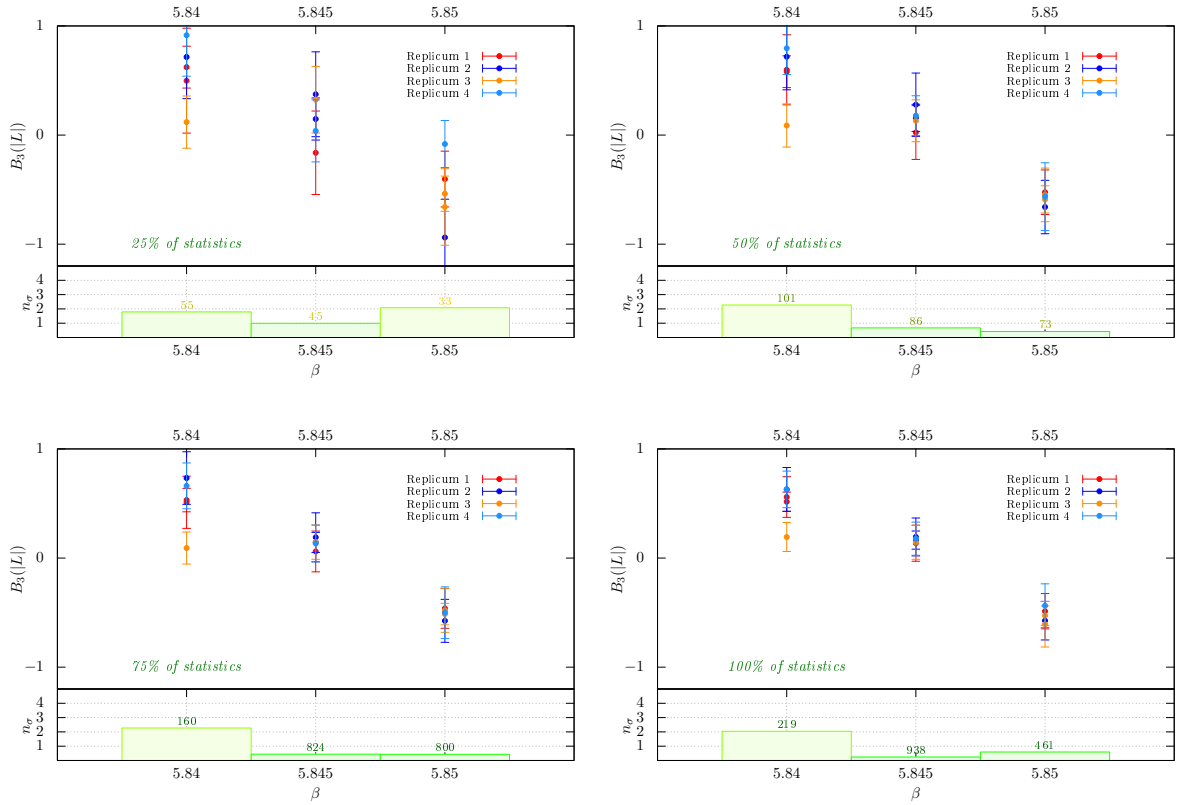


Figure 4.1: Analysis of the skewness ($B_3$) measurements at $\kappa = 0.1100$ on $N_\tau = 6$, $N_\mathrm{s} = 42$ with successively increasing statistics. The bar charts included in the lower part of the plots are intended as a guidance to judge on the statistics. $n_\sigma$ at each $\beta$ is the number of standard deviations by which the two most different chains are compatible. The numbers placed above the bars are the average numbers of independent events collected at the respective $\beta$. The colors have been chosen in order to reflect the amount of the statistics. Green color indicates that statistics are high enough while red indicates that statistics should be increased. Both $n_\sigma$ and the number of independent events have to be monitored to decide when to stop increasing statistics.

### Analyzing Data Using Jackknife

Consider a data set consisting of N uncorrelated measurements $o_\alpha^i$ (for simplicity here I omit the index $r$ labeling replica) of $O_\alpha$. The Jackknife estimator $f_\alpha^J$of a function $f(O_\alpha)$ is given by

$$f_\alpha^J = \frac{1}{N}\sum_{i=1}^{N} f(\bar{o}_\alpha^{J_n}), \quad \text{with} \quad \bar{o}_\alpha^{J_n} = \frac{1}{N-1}\sum_{j\neq n}^{N} o_\alpha^j. \tag{4.3}$$

Note that in the equation on the right in the calculation of the mean value $\bar{o}_\alpha^{J_n}$ the $n$th element is left out. Thus the estimate $f(\bar{o}_\alpha^{J_n})$, conveniently abbreviated as $f_\alpha^{J_n}$, of the function $f(O_\alpha)$ is based on $N-1$ measurements. The variance with respect to $f_\alpha^J$ reads

$$\sigma^2(f_a^J) = \frac{N}{N-1}\sum_{n=1}^{N}\left(f_\alpha^{J_n} - f_\alpha^J\right)^2. \tag{4.4}$$

Note that a possible bias, if desired, can be canceled. An estimate of a possible bias is obtained from comparing $f_\alpha^J$ with $f(O_a)$ as

$$\hat{B} = (N-1)\left(f_\alpha^J - f(O_\alpha)\right). \tag{4.5}$$

Replacing $f(O_\alpha)$ by $f(O_\alpha) - (N-1)\left(f_\alpha^J - f(O_\alpha)\right)$ gives an estimator free of or with reduced bias. Coming back to the example of $B_4$ given by eq. (4.2) one observes to have four different primary observables $O_\alpha$ given by the moments of $O^n$ with n=1,...,4. Thus we denote $O^n$ by $O_\alpha$, i.e. $n = \alpha$. In order to compute the Jackknife estimators in this case, the procedure has to be generalized which is straightforward. The function for an arbitrary number of observables is $f(O_\alpha) = f(O_1, O_2, \cdots)$. The Jackknife estimator with the $n$th element discarded now is $f(\bar{o}_1^{J_n}, \bar{o}_2^{J_n}, \ldots)$, i.e. for all observables $O_\alpha$ the function depends on, the same measurement with respect to the Monte Carlo history is discarded simultaneously. In the case of $B_4$ the estimate is obtained by computing

$$B_4^J = \frac{1}{N}\sum_{i=1}^{N} B_4\left(\bar{o}_1^{J_n}, \bar{o}_2^{J_n}, \bar{o}_3^{J_n}, \bar{o}_4^{J_n})\right). \tag{4.6}$$

The variance eq. (4.4) is computed accordingly. It was already indicated that the data subjected to this procedure must be uncorrelated to obtain correct results. This means that the autocorrelation time has to be determined in advance, which in this work was done using the $\Gamma$-method by U. Wolff which I will address further below. The data then can be made uncorrelated by dividing it into blocks or bins of length $2\tau_{\text{int},O}$ and building the average for each of these blocks. Then the Jackknife procedure is not applied anymore to the original data but to the averages made out of the data blocks of length $2\tau_{\text{int},O}$, i.e. instead of obtaining $f(\bar{o}_\alpha^{J_n})$ by leaving out the $n$th data element now the $n$th data block is discarded. Considering a quantity like $B_4$ that depends on different observables, the largest autocorrelation time $\tau_{\text{int},\alpha}$ is used. Note that dividing data of length $N$ into blocks of length $2\tau_{\text{int},\alpha}$ implies that some of the data might have to be discarded if $2\tau_{\text{int},\alpha}$ does not divide into $N$ without a reminder. Thus if one desires to use as much of the data as possible the bin size should be chosen such that it divides into $N$ with only a small reminder. This in some cases implies to choose the bin size smaller or larger than $2\tau_{\text{int},\alpha}$ and as consequence slightly under- or conservatively overestimating the error, where clearly the latter should be preferred. Another practical issue addresses the production of replica. In the resampling procedure these replica are typically sewed together to one chain of data. Then it is important to have produced replica of at least approximately equal length, since in the resampling procedures no weighting whatsoever of the single replicas is done. Sewing together replica of considerably different length results in erroneous results since replica with lower statistics are treated equally like replica with larger statistics. In the following I briefly outline the $\Gamma$-method so as to compare the computed errors with those obtained from Jackknife.

### Analyzing Data Using The $\Gamma$-method

I will only state the central quantities of the method and refrain from presenting it in detail since it was solely used to estimate the autocorrelation time of our data and to crosscheck the errors we computed using resampling methods. For the reader interested in details I recommend reading the comprehensive article [162]. The strength of this method lies in the analysis of derived quantities, i.e. (in general nonlinear) functions of primary expectation values, and autocorrelation functions which, as the authors of [162] state, is advantageous compared to popular binning or resampling methods where autocorrelations are only treated implicitly. To outline the method I need to make some more definitions: Estimates for the exact statistical mean values $O_\alpha$ of primary observables are given by $\bar{o}_\alpha$ (per replicum) and $\bar{\bar{o}}_\alpha$ (weighted average of $\bar{o}_\alpha$),

$$\bar{\bar{o}}_\alpha = \frac{1}{N}\sum_{r=1}^{R} N_r \bar{o}_\alpha, , \qquad \bar{o}_\alpha = \frac{1}{N_r}\sum_{i=1}^{N_r} o_{i,r}^\alpha. \tag{4.7}$$

A derived quantity and its estimators are defined as

$$F \equiv f(O_1, O_2, \cdots) = f(O_\alpha), \qquad \bar{\bar{F}} = f(\bar{\bar{o}}_\alpha), \qquad \bar{F} = \frac{1}{N}\sum_{r=1}^{R} N_r f(\bar{o}_\alpha). \tag{4.8}$$

A central quantity to the method is the autocorrelation function

$$\delta_{rs}\Gamma_{\alpha\beta}(j-i) = \left\langle (o_\alpha^{i,r} - O_\alpha)((o_\beta^{j,s} - O_\beta) \right\rangle. \tag{4.9}$$

which continuously appears in the analysis of eq. (4.8) by Taylor expansions in the deviations $\bar{\delta}_\alpha^r = \bar{o}_\alpha - O_\alpha$ and $\bar{\bar{\delta}}_\alpha^r = \bar{\bar{o}}_\alpha - O_\alpha$. From a Taylor expansion of $\bar{\bar{F}}$ and $\bar{F}$ involving the autocorrelation function $\Gamma$ a bias can be deduced (unless $f$ is linear),

$$\left\langle \bar{\bar{F}} - F \right\rangle \simeq \frac{1}{R-1}\left\langle \bar{F} - F \right\rangle, \tag{4.10}$$

which, if necessary, can be canceled by replacing $\bar{\bar{F}} \to (R\bar{\bar{F}} - \bar{F})/(R-1)$. The derivation of the variance $\sigma_F^2$ is based on a Taylor expansion, as well and reads

$$\sigma_F^2 = \left\langle (\bar{\bar{F}} - F)^2 \right\rangle \simeq \frac{1}{N}\sum_{\alpha\beta} f_\alpha f_\beta \sum_{-\infty}^{+\infty} \Gamma_{\alpha\beta}(t), \tag{4.11}$$

where $f_\alpha$ is a derivative of $f$ with respect to the primary observable labeled by $\alpha$. The variance $\sigma_F^2$ can be rewritten in terms of the integrated autocorrelation time $\tau_{\text{int},F}$,

$$\sigma_F^2 = \frac{2\tau_{\text{int},F}}{N} v_F, \text{ with } \tau_{\text{int},F} = \frac{1}{2v_F}\sum_{-\infty}^{+\infty}\sum_{\alpha\beta} f_\alpha f_\beta \Gamma_{\alpha\beta}(t) \tag{4.12}$$

and is estimated in terms of estimates of $\Gamma_{\alpha\beta}(t)$ given by

$$\bar{\bar{\Gamma}} = \frac{1}{N - Rt}\sum_{r=1}^{R}\sum_{i=1}^{N_r - t} (a_\alpha^{i,r} - \bar{\bar{o}}_\alpha)(a_\beta^{i+t,r} - \bar{\bar{o}}_\alpha), \tag{4.13}$$

which has a leading bias of

$$\left\langle \bar{\bar{\Gamma}} \right\rangle - \Gamma_{\alpha\beta}(t) \approx -\frac{\sum_{-\infty}^{+\infty}\Gamma_{\alpha\beta}(t)}{N}. \tag{4.14}$$

Truncation of the infinite sum as $\sum_{t=1}^{W}$ in the previous expressions leads to another bias $\sim \exp(W/\tau)$. The summation window $W$ should be chosen large compared to the decay time $\tau$ to reduce the systematic error but small enough to not include excessive noise contributions. For the computation of the derivatives $f_\alpha$ which is non-trivial the authors of [162] prefer a numerical treatment and introduce a natural scale

$$h_\alpha = \sqrt{\frac{\bar{\bar{\Gamma}}_{\alpha\alpha}(0)}{N}} \tag{4.15}$$

extracted from the data to estimate $f_\alpha$ by

$$\bar{\bar{f}} \approx \frac{1}{2h_\alpha}\left[f(\bar{\bar{o}}_1, \bar{\bar{o}}_2, \cdots, \bar{\bar{o}}_\alpha + h_\alpha, \cdots) - f(\bar{\bar{o}}_1, \bar{\bar{o}}_2, \cdots, \bar{\bar{o}}_\alpha - h_\alpha, \cdots)\right] \tag{4.16}$$

for which the numerical errors are of order $\mathcal{O}(h_\alpha^2) \sim 1/N$. The $\Gamma$-method is undoubtedly a complicated method and much more things can be said. For instance the authors also derive equations for the error of the

error and furthermore derive an algorithm to automatically determine the summation window $W$. Moreover they give a quantitative comparison to binning methods and thoroughly analyze the biases occurring in both methods. For the computation of the autocorrelation time of the data produced in the context of this work a publicly available implementation of the method was used which can for instance be found at `https://www-zeuthen.desy.de/alpha/public_software/index.html`. This implementation was used to analyze some data sets for a comparison with the error obtained from the resampling methods Jackknife and Statistical Bootstrap. The results are summarized in table 4.1. An example plot of the autocorrelation time obtained from this implementation is shown in fig. 4.2.

| $\kappa$ | $\beta$ | Raw/$\Gamma$-Method | Raw/Jackknife | Rew./Bootstrap | $\tau_{\text{int},B_4}$ |
|---|---|---|---|---|---|
| 0.0750 | 5.8870 | 4.3(9) | 4.4(2) | 3.9(5) | 2000(500) |
| | 5.8900 | 2.5(7) | 2.54(11) | 2.3(3) | 4600(1600) |
| 0.0850 | 5.8832 | 1.56(10) | 1.67(3) | 1.83(14) | 2200(400) |
| | 5.8860 | 2.5(4) | 2.56(8) | 3.6(3) | 4300(1100) |
| 0.0900 | 5.8750 | 5.0(7) | 4.8(5) | 5.3(9) | 300(60) |
| | 5.8800 | 1.66(8) | 1.67(2) | 1.67(8) | 2600(500) |
| | 5.8850 | 9.0(3.0) | 8.0(3.0) | 8.9(1.3) | 700(90) |
| 0.1000 | 5.8650 | 3.6(3) | 2.79(8) | 2.84(17) | 350(30) |
| | 5.8700 | 2.77(13) | 3.6(1) | 3.6(3) | 1150(160) |
| 0.1100 | 5.8400 | 3.24(16) | 3.21(14) | 3.1(2) | 127(9) |
| | 5.8450 | 2.58(6) | 2.57(5) | 2.57(10) | 181(14) |
| | 5.8500 | 3.03(11) | 3.03(10) | 3.07(17) | 201(16) |

Table 4.1: Comparison of estimates and errors between the $\Gamma$ and resampling methods obtained for $B_4$ from simulations of $N_\tau = 6, N_\text{s} = 42$ lattices. The Rew./Bootstrap column refers to the interpolated estimates obtained from the multiple histogram method discussed in section 4.1.2 and thus do not describe the raw data obtained from the simulations. The errors are always comparable between the different methods though not identical due to the latter being conceptually different. The deviations in the estimates of $B_4$ can be explained by data that had to be discarded during the binning of the data. For the $\Gamma$ method no binning exists and thus the different Markov chains do not get and on top are weighted with respect to their length.

### 4.1.2 Reweighting

The analysis of the data produced for this work heavily employed reweighting, for which reason I will discuss this technique more in detail. I will base the discussion on the representations given in [33, 62, 126, 160]. When simulating LQCD by means of Monte Carlo algorithms it is sometimes not possible or just to costly to access certain regions or specific values of parameters the observable of interest depends on due to a variety of reasons. In the context of finite density physics a well know example for such a situation is the sign problem, described in section 3.3.2, which prevents simulations from being carried out at real finite values of the chemical potential. Another example is given by the situation described in section 5.2.2, where the task is to precisely locate $\beta_\text{c}$, i.e. the critical value of the inverse lattice gauge coupling $\beta$ at which a thermal transition takes place. This is done by searching for the value of $\beta$ at which $B_3(\beta) = 0$.

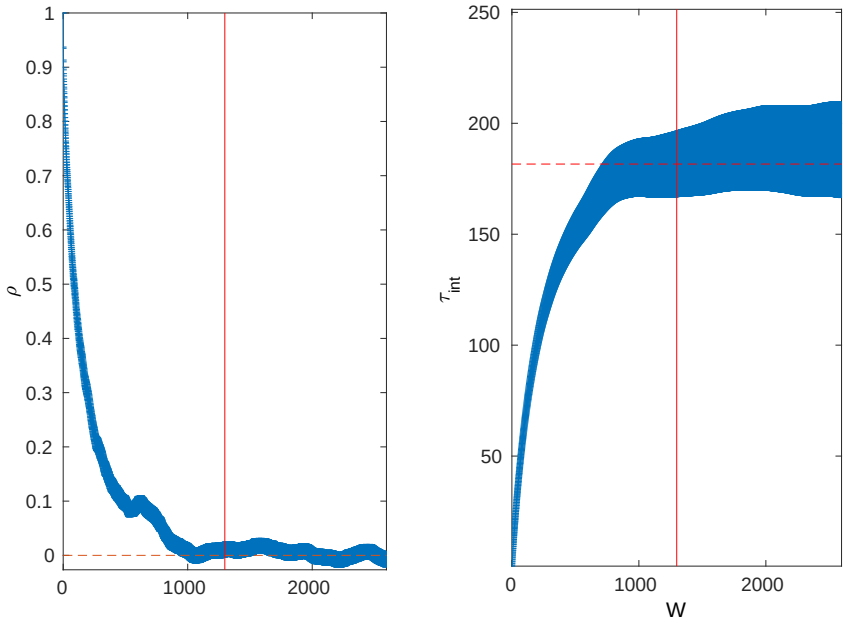


Figure 4.2: The normalized (right) and integrated (left) autocorrelation time of $B_4$ at $N_\tau = 6, \kappa = 0.11, \beta = 5.8450$.

Using only LQCD simulations for this search there are essentially two approaches. The first one is to start many simulations concurrently with a high resolution in $\beta$ where a larger desired statistical precision of $\beta_c$ implies a higher resolution in $\beta$. This could require a huge number of concurrent simulations per set of parameters of interest (quark mass $m_q$, lattice extents $N_\tau$, $N_s$, etc.)! In terms of computational costs this is extremely inefficient. The second one is to start simulations at just a few values of $\beta$. As soon as the statistics are enough to decide whether $B_3(\beta) < 0$ or $> 0$ some kind of bisection procedure could be used to track down $\beta_c$. Since LQCD simulations at relevant parameter values are very costly in terms of time and resources (e.g. close to a thermal transition at $\beta_c$ where suppression of tunneling and huge autocorrelations start to set in) this again would be overly inefficient. In such situations just described it would be desirable to have facilities to reliably perform extrapolations from more accessible parameter regions (e.g. in the case of the sign problem) or interpolations from already available data (e.g. in the case of precisely locating $\beta_c$). This is made possible by the reweighting technique, a standard tool widely used in conjunction with Monte Carlo simulations of not only LQCD but statistical physics systems in general. The idea of this method is to use the probability weight for generating a Markov chain of configurations as a reweighting factor as illustrated for LQCD in the following. The expectation value of some observable $O$ with respect to certain parameter values of $\kappa, \mu, \beta$ is formally given by the path integral

$$\langle O \rangle = \frac{1}{Z(\beta)} \int \mathcal{D}\mathcal{U}\, O \det M\,(\kappa, \mu)\ \mathrm{e}^{-S_g}, \tag{4.17}$$

which can be rewritten in terms of a probability weight for different values of the parameter set $\kappa', \mu', \beta'$, namely

$$\begin{aligned}\langle O \rangle_{(\beta,\kappa,\mu)} &= \frac{1}{Z(\beta)} \int \mathcal{D}\mathcal{U}\, O \frac{\det M\,(\kappa,\mu)\ \mathrm{e}^{-S_g}}{\det M\,(\kappa',\mu')\ \mathrm{e}^{-S'_g}} \det M\left(\kappa',\mu'\right)\ \mathrm{e}^{-S'_g} \\ &= \frac{Z(\beta')}{Z(\beta)} \left\langle O\, \mathrm{e}^{S'_g - S_g} \frac{\det M\,(\kappa,\mu)}{\det M\,(\kappa',\mu')} \right\rangle_{(\beta',\kappa',\mu')} \\ &= \frac{\left\langle O\, \mathrm{e}^{S'_g - S_g} \frac{\det M(\kappa,\mu)}{\det M(\kappa',\mu')} \right\rangle_{(\beta',\kappa',\mu')}}{\left\langle \mathrm{e}^{S'_g - S_g} \frac{\det M(\kappa,\mu)}{\det M(\kappa',\mu')} \right\rangle_{(\beta',\kappa',\mu')}}.\end{aligned} \tag{4.18}$$

The expectation value of $O$ at $\kappa, \mu, \beta$ is now extracted with respect to an ensemble generated at $\kappa', \mu', \beta'$, whereby the success of this attempt crucially depends on the distance between the parameter values, which can be quantified in terms of the overlap of the different ensembles. Depending on certain factors, like the volume or the choice of the parameters in which to reweight, the numerical evaluation of this expectation value can turn out to be very hard. However, from here on I will restrict the discussion to the case of relevance for this work which is rather simple in terms of numerical evaluation which is reweighting only in the inverse gauge coupling $\beta$. Then $\kappa', \mu' = \kappa, \mu$ and the determinant reweighting factor drops out of eq. (4.18) and we are left with $\mathrm{e}^{S'_g - S_g}$. Practical realizations of these methods are given by the single and the multiple histogram method described in the following.

### The Single Histogram Method

The single histogram method, originally introduced in [163], is included here just for the sake of completeness as it can be seen as the predecessor of the conceptually different and more elaborate multiple histogram method. It basically reflects eq. (4.18) and represents a tool to perform extrapolations to nearby parameter values. Let's start by considering a discrete series of measurements of an observable $O$ performed in a Monte Carlo simulation. The estimator $O_N$ of an expectation value $\langle O \rangle$ reads [1]

$$O_N = \frac{\sum_{i=1}^{N} O_i p_i^{-1}\ \mathrm{e}^{-\beta P_i}}{\sum_{j=1}^{N} p_j^{-1}\ \mathrm{e}^{-\beta P_j}}, \tag{4.19}$$

where $P$ is the $\beta-$independent part of the gauge action (c.f. eq. (2.31)). Generating the gauge configurations with importance sampling according to the probability

$$p_i = \frac{1}{Z}\ \mathrm{e}^{-\beta P_i} \tag{4.20}$$

we end up with the sum over the measurements $O_i$ divided by the total number of measurements $N$,

$$O_N = \frac{1}{N} \sum_{i=1}^{N} O_i. \tag{4.21}$$

If instead we define the $p_i$ to be Boltzmann probabilities of some different inverse gauge coupling, say $\beta_0$, the estimator reads

$$O_N = \frac{\sum_{i=1}^{N} O_i\ \mathrm{e}^{(\beta_0 - \beta) P_i}}{\sum_{j=1}^{N}\ \mathrm{e}^{(\beta_0 - \beta) P_j}}, \tag{4.22}$$

[1] If a reminder is needed on why to write the numerical expectation value in exactly this way I recommend reading sections 2.1 and 2.2 of [160].

which is already the central equation of the method and is ready to be used. As already stated above the method quickly breaks down if the parameter values of simulated ensemble are too far away from the ones at the ensemble of interest. Note that the method owes its name to the original formulation in terms of histograms which is legitimate for models with discrete values of the observable $O$, as it is for instance the case for the total energy $E$ in the Ising model or if memory requirements are an issue. Otherwise summarizing Monte Carlo data in histogram bins and thus producing more inaccuracies can and should be avoided. For more details about this and a discussion about practical matters like implementation and validity the reader is referred to [160].

### The Multiple Histogram Method

The Multiple Histogram Method, introduced in [164] just one year after the invention of its predecessor, is based on the observation that overlapping ensembles of sets of states, sampled from simulations at close values of the parameters, can be combined to achieve a significant improvement in the precision of an interpolation or extrapolation. Consider the case in which data has been produced in simulations at close values $\beta_1$ and $\beta_2$ of the inverse gauge coupling but an estimate of $\langle O\rangle\,(\beta')$ at a value $\beta' \in [\beta_1, \beta_2]$ is desired. Then the information from the overlapping ensembles of both states sampled at $\beta_1$ and $\beta_2$ can be combined in an elaborate way to predict an estimate of $\langle O\rangle\,(\beta')$. But how much of an overlap should be there between the ensembles and how can it be quantified? We will come back to this question and other issues later, but first I will give a description of the method and a summary of its most important equations.

We are interested in the expectation value of some observable $O(X;\beta,\vec{\kappa},\vec{\mu})$ depending on a set of physical quantities $X = (X_i)$ and parameters $(\beta,\vec{\kappa},\vec{\mu})$. The LQCD partition function of the system reads

$$Z(\beta,\vec{\kappa},\vec{\mu}) = \int \mathcal{D}\mathcal{U} \prod_{f=1}^{N_f} \det M(\kappa_f,\mu_f)\ \mathrm{e}^{-S_G}. \tag{4.23}$$

Since I will only present the method with respect to reweighting in $\beta$ the fermion determinant $\det M$ will be omitted for convenience. Furthermore I will write the gauge action as $S_G = \beta P$ where $P$ is the $\beta$-independent part of the gauge action (c.f. eq. (2.31)), i.e. the plaquette including some additional factors. The partition function can be rewritten as an integral over the possible states of the physical quantities $X$:

$$Z(\beta) = \int \mathrm{d}X \int \mathcal{D}\mathcal{U} \prod_i \delta(X_i - \hat{X}_i)\,\mathrm{e}^{-\beta P}. \tag{4.24}$$

Moreover we can choose $P$ as one of these physical quantities, i.e. $P = X_j \in (X_i)$. In this way we can write $Z(\beta)$ as

$$Z(\beta) = \int \mathrm{d}X \rho(X)\,\mathrm{e}^{-\beta P}, \tag{4.25}$$

where $\rho(X)$ is the density of states. Using $\rho(x)$ we define the probability distribution function of $X$,

$$p(X,\beta) = Z^{-1}(\beta)\ \rho(X)\ \mathrm{e}^{-\beta P}. \tag{4.26}$$

The expectation value of $O(X)$ can be written in terms of $p(X,\beta)$,

$$\langle O\rangle\,(\hat{X},\beta) = \int \mathrm{d}X O(X) p(\beta,X). \tag{4.27}$$

Now the essential idea of the method is that the density of states $\rho(X)$ which does not depend on $\beta$ is solely a function of the system. Consequently the partition function $Z(\beta)$ and the expectation value of $O$ can be computed for any $\beta$ if $\rho(X)$ is known. Of course there is no access to the true $\rho(X)$ but according to eq. (4.26) it can be estimated with high precision by combining data from Monte Carlo simulations at different couplings $\beta_i$. Each $\rho_i(X)$ obtained from a simulation at $\beta_i$ is an estimate for the true density of states $\rho(X)$. In order to combine the estimates $\rho_i(X)$ we sum up probability distribution functions from simulations at several $\beta_i$ weighted by the number of measurements $n_i$,

$$\begin{aligned}\sum_i n_i\ p(X,\beta_i) &= \sum_i n_i\ Z^{-1}(\beta_i)\ \rho_i(X)\ \ \mathrm{e}^{-\beta_i P} \\ &\approx \tilde{\rho}(X) \sum_i n_i\ Z^{-1}(\beta_i)\ \ \mathrm{e}^{-\beta_i P},\end{aligned} \tag{4.28}$$

where in the second line we made use of the fact that for infinite statistics the density of states does not depend anymore on the simulation point $\beta_i$ and thus can be removed from the sum - of course, it is not possible to gather infinite statistics and thus the second line is only an approximate equality (whose precision increases with growing statistics) where $\tilde{\rho}(X)$ represents the combined estimate for $\rho(X)$, i.e.

$$\tilde{\rho}(X) \approx \frac{\sum_i n_i\ p(X,\beta_i)}{\sum_j n_j\ Z^{-1}(\beta_j)\ \ \mathrm{e}^{-\beta_j P}}. \tag{4.29}$$

Note that $n_i p(X,\beta_i)$ can be interpreted as a histogram counting the occurrences of $X$ at $\beta_i$. Then $\sum_i n_i\ p(X,\beta_i)$ are multiple histograms combined over all simulations $i$. Inserting the estimate $\tilde{\rho}(X)$ into the partition function given by (4.25) gives

$$Z(\beta_k) = \int dX \frac{\sum_i n_i\ p(X,\beta_i)}{\sum_j n_j\ Z^{-1}(\beta_j)\ \ \mathrm{e}^{-\beta_j P}}\ \mathrm{e}^{-\beta_k P}. \tag{4.30}$$

This equation can be rearranged to form an expectation value,

$$\begin{aligned}Z(\beta_k) &= \sum_i n_i \int \frac{1}{\sum_j n_j\ Z^{-1}(\beta_j)\ \ \mathrm{e}^{-(\beta_j-\beta_k)P}} p(X,\beta_i) dX \\ &= \sum_i n_i \left\langle \frac{1}{\sum_j n_j\ Z^{-1}(\beta_j)\ \ \mathrm{e}^{-(\beta_j-\beta_k)P}} \right\rangle_{\beta_i}.\end{aligned} \tag{4.31}$$

The right-hand side of the second line is the sum of the fraction over all configurations of all simulations and can thus be written as

$$Z(\beta_k) = \sum_{i,s} \frac{1}{\sum_j n_j\ Z^{-1}(\beta_j)\ \ \mathrm{e}^{-(\beta_j-\beta_k)P_{is}}}, \tag{4.32}$$

where the index $s$ labels the configuration number and $P_{is}$ refers to $P$ measured on configuration number $s$ of simulation $i$. This equation has to be solved iteratively for $Z(\beta_k)$ for each simulated $\beta_k$. Finally, the reweighted estimate $O^R(X,\beta)$ for an expectation value of some observable $O(X)$ is obtained from

$$O^R(X,\beta) = \frac{1}{Z(\beta)} \sum_i n_i \left\langle \frac{O(\hat{X})}{\sum_j n_j\ Z^{-1}(\beta_j)\ \ \mathrm{e}^{-(\beta_j-\beta_k)P}} \right\rangle_{(\beta_i)}, \tag{4.33}$$

where again the sum times the expectation value on the right-hand side is a naive sum over all configurations of all simulations and can be written as

$$O^R(X,\beta) = \frac{1}{Z(\beta)} \sum_{i,s} \frac{o_{is}(X)}{\sum_j n_j\ Z^{-1}(\beta_j)\ \ \mathrm{e}^{-(\beta_j-\beta_k)P_{is}}}, \tag{4.34}$$

where $o_{is}$ are the measurements of $O(X, \beta)$ on every configuration $s$ and simulation $i$ at $\beta_i$. An important question mentioned in the beginning is, how close should be the values $\beta_i$ of the different simulations in order to obtain reliable interpolation result. This and further practical matters including error analysis will be briefly touched in the following.

### Practical Matters and Error Analysis

The implementation of this method involves overcoming some numerical obstacles, in particular

- avoiding over- or underflow of the partition function $Z$ by introducing a normalization factor or working with its logarithm,
- choosing the starting values for the iterative equation eq. (4.32) and
- deciding the number of iterations.

For the discussion of these issues I refer the reader to [160]. In the following I want to come back to the question about how close the values of the simulation parameters should be in order to obtain accurate interpolation results. As already mentioned above this depends on the overlap of the ensembles generated at different values of the parameters. Considering an interpolation in the inverse lattice coupling $\beta$ the overlap can be checked graphically by inspecting the overlap of histograms of $P = S_G/\beta$ for the simulated values of $\beta$ as shown in fig. 4.3. There $B_3(\beta)$ is interpolated between three $\beta$ values using the multiple histogram method. The figure shows how the accuracy of the interpolation decreases if the middle $\beta$ value is left out and how this can be understood from looking at the overlap between the ensembles of the different $\beta$ values. In [160] the ensemble overlap for the single histogram method is analyzed for the $2D$ Ising model and the author suggests for a reliable extrapolation to respect the following the criterion (translated to the case considered here),

$$|M(S_G/\beta_i) - M(S_G/\beta_j)| \leq \sigma, \tag{4.35}$$

where $M(S_G/\beta_i)$ denotes the mean value of the distribution. To say it in words, the difference between the mean values of the distribution of $S_G/\beta_i$ and $S_G/\beta_j$ should not be larger than their standard deviation. Doing this analysis for the case shown in fig. 4.3 the difference between the mean values of the distribution at $\beta = 5.8500$ and $\beta = 5.8450$ is $\approx 2250$. The standard deviation of the distribution at $\beta = 5.8500$ is $\sigma \approx 676$. Thus extrapolating from $\beta = 5.8500$ to $\beta = 5.8450$ as demonstrated in the top row of fig. 4.3 should be avoided. In most of the cases such an analysis was not performed in this work but it was always assured that the overlap between the ensembles was at least as large as the overlap of the ensembles shown in the bottom row of fig. 4.3 causing the error of the interpolated data to be of a similar size as the error on the measured data. A further point to be mentioned, which should not come as a surprise, concerns the relation between the overlap and the simulated spatial volume: assuming that all parameters are kept fixed, two ensembles which exhibit a certain overlap on a given volume will have less overlap on a larger volume. The Gaussian-like distribution of $S_G/\beta$ approaches a $\delta$-function as the volume is increased towards the infinite volume limit. Thus when increasingly larger volumes are simulated one should expect that the distance between the $\beta$ values needs to be decreased.

A further important point about the reweighting procedure concerns the application of the method on derived quantities and the computation of errors on the interpolated data. The kurtosis $B_4(\beta)$ shall serve

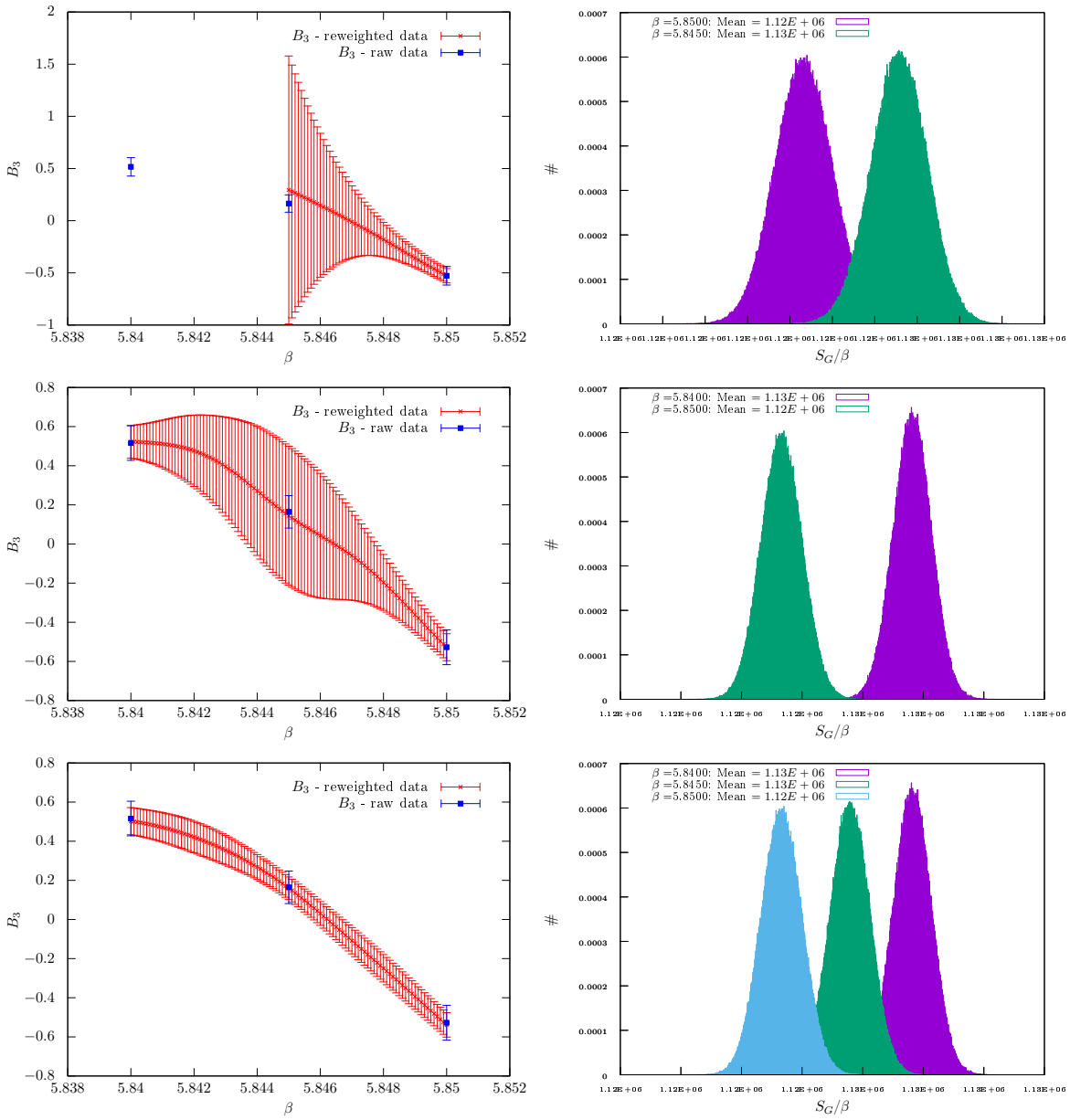


Figure 4.3: The figure shows measured (blue) and reweighted (red) $B_3(\beta)$ data for the parameter set $N_f = 2, \kappa = 0.11, N_\tau = 6, N_s = 42$. Top Row: (L.h.s.) The figure shows an extrapolation from $\beta = 5.8500$ to $\beta = 5.8450$ for which the ensembles at $\beta = 5.8400, 5.8450$ are not taken into account. From $B_3(\beta_c) \approx 0$ a critical coupling of $\beta_c = 5.8469$ is extracted. (R.h.s.) Shown is the overlap of the ensembles of $\beta \in \{5.845, 5.850\}$ in terms of histograms of $S_G/\beta$. Middle Row: (L.h.s.) The reweighting of $B_3$ in $\beta = \{5.8400, \ldots, 5.8500\}$ is performed with a resolution of $0.0001$ in $\beta$ taking into account the ensembles at $\beta = \{5.8400, 5.8500\}$ while $\beta = 5.845$ was left out. From $B_3(\beta_c) \approx 0$ a critical coupling of $\beta_c = 5.8464$ is extracted. (R.h.s.) The overlap between the ensembles of $\beta \in \{5.840, 5.850\}$ is really small and the errors on the interpolated data are still large but significantly reduced compared to the extrapolation above and the interpolation point at $\beta = 5.8450$ is slightly adjusted towards the measured point. Bottom Row: In the reweighting procedure the ensemble at $\beta = 5.8450$ was added. The curve is slightly adjusted and the errors are significantly reduced to the order of the errors of the measured data points. In this case from $B_3(\beta_c) \approx 0$ a critical coupling of $\beta_c = 5.8462$ is extracted.

as an example for a derived quantity:

$$B_4 = \frac{\left\langle (O - \langle O \rangle)^4 \right\rangle}{\left\langle (O - \langle O \rangle)^2 \right\rangle^2} = \frac{\left\langle O^4 \right\rangle - 4 \left\langle O^3 \right\rangle \langle O \rangle + 6 \left\langle O^2 \right\rangle \langle O \rangle^2 - 3 \langle O \rangle^4}{(\left\langle O^2 \right\rangle - \langle O \rangle^2)^2}. \tag{4.36}$$

Remember that the moments $O^n$ are the primary observables measured configuration-wise which I denote by $O_\alpha$. Assume we have two estimates $B_4(\beta_1)$ and $B_4(\beta_2)$ extracted from simulated ensembles with an sufficient overlap to interpolate between them. Furthermore we are interested in $B_4$ evaluated at some value of $\beta$, say $\beta'$, with $\beta_1 < \beta' < \beta_2$. Then the reweighting procedure is applied on all measurements $o_{\alpha,i}(\beta_j)$ of $O_\alpha$ (with $j = 1, 2$) to obtain the estimate $\bar{o}^R_\alpha(\beta')$, where the superscript $R$ indicates that it is obtained through reweihting. I.e. the reweighting procedure can be considered a functional $R$ acting on all measurements $o_{\alpha,i}(\beta_j)$, such that

$$\bar{o}^R_\alpha(\beta') = R[o_{\alpha,i}(\beta_i)] \tag{4.37}$$

Subsequently $B_4$ can be evaluated according to eq. (4.36) with the estimates $\bar{o}^R_\alpha(\beta')$ so as to obtain $B^R_4(\beta')$. It is as simple is that. Somewhat more involved is the determination of the errors of $B^R_4(\beta')$ which will be discussed in the following.

In section 4.1.1 I announced to discuss the Statistical Bootstrap method separately in this section since the method is used for the error analysis of reweighted data. I will explain the reason for preferring this method for reweighting over the Jackknife shortly but at first I will give a brief description of the method.

Consider a set of uncorrelated measurements $o_{\alpha,i}$ with $i = 1, \ldots, N$. This data set gets resampled $M$ times, each time randomly drawing $N$ data out of the original data set *with repetition*, yielding $M$ new data sets $o^{B_j}_{\alpha,i}$ with $i = 1, \ldots, N$ and $j = 1, \ldots, M$. This drawing with repetition implies that the new sets will include some identical data. For each of these new $M$ data sets $o^{B_j}_{\alpha,i}$ one builds the mean value

$$\bar{o}^{B_j}_\alpha = \frac{1}{N} \sum_{i=1}^{N} o^{B_j}_{\alpha,i} \tag{4.38}$$

which are the Bootstrap estimators. Bootstrap estimators of derived quantities are then given by functions evaluated using $\bar{o}^{B_j}_\alpha$, i.e. $f(\bar{o}^{B_j}_\alpha) = f^{B_j}_\alpha$. To estimate the standard deviation of a derived quantity, at first the mean value over the bootstrap estimators $f^{B_j}_\alpha$ is formed which yields

$$f^B = \frac{1}{M} \sum_{j=1}^{M} f^{B_j}_\alpha. \tag{4.39}$$

The estimated standard deviation is then given by

$$\sigma = \sqrt{\frac{1}{M} \sum_{i=1}^{M} \left( f^{B_j}_\alpha - f^B_\alpha \right)^2}. \tag{4.40}$$

Now in order to obtain the standard deviation of a reweighted estimate of a derived quantity - lets resume with the example of $B^R_4(\beta')$ - the reweighting procedure is applied on each of the $M$ newly sampled data sets $o^{B_j}_{\alpha,i}$ to obtain $\bar{o}^{R,B_j}_\alpha = R[o^{B_j}_{\alpha,i}]$. These are then used to evaluate $B_4$ to obtain a reweighted Bootstrap estimator $B^{R,B_j}_4(\beta')$ which corresponds to $f^{B_j}_\alpha$. The estimator corresponding to $f^B$ is then again the average over all $B^{R,B_j}_4(\beta')$, i.e.

$$B^{R,B}_4(\beta') = \frac{1}{M} \sum_{j=1}^{M} B^{R,B_j}_4(\beta') \tag{4.41}$$

and the standard deviation via

$$\sigma = \sqrt{\frac{1}{M} \sum_{j=1}^{M} \left( B^{R,B_j}_4(\beta') - B^{R,B}_4(\beta') \right)}. \tag{4.42}$$

Remember that both the Bootstrap procedure and the Jackknife require uncorrelated data which can be obtained by rearranging the data in blocks of size of at least $2\tau_{\text{int}}$ to end up with $K = N/(2\tau_{\text{int}})$ blocks of data. The Bootstrapping procedure is then applied on the whole blocks instead of the single data. With the exception of this step, the analysis remains as described above. There is a practical complication, though. The reweighting procedure has to be applied on $M$ resampled data sets $o_{\alpha,i}^{B_j}$ which is of the order of multiple hundreds of times. If the data set is large, say $\mathcal{O}(10^6)$, this implies huge computational costs. For this reason we alter the Bootstrap analysis slightly by taking a shortcut. We still form $K = N/(2\tau_{\text{int}})$ blocks of data but we do not resample the whole blocks and feed the resampled data set into the reweighting procedure. Instead from each block $k$ with $k = 1, \ldots, K$ only one data is drawn randomly. The $K$ drawn data represent the new data set which is fed into the reweighting to obtain the reweighted Bootstrap estimator. On the one hand-side this de-correlates the data and the time to reweight the data set decreases significantly but on the other hand-side this reduces the information content due to the decreased statistics which leads, in the worst case, to an overestimation of the error. In practice, however, this turns out not to be a problem which can be seen from table 4.1. The table shows that the estimated error on $B_4$ is always comparable to the error computed with the $\Gamma$-method. This is also supported by figures 5.4 and 4.3 (bottom, left) where one can clearly see that the errorbars of the reweighted data points are of a similar size like the errorbars of the pure data.

Now let me give a reason for preferring Statistical Bootstrap over Jackknife. The reason is similar to what was just explained. If we end up with $K = N/(2\tau_{\text{int}})$ blocks of data, in the Jackknife procedure these $K$ blocks are resampled $K$-times, each time leaving out one block, without repetition. Now if the number $K$ of blocks is large and if the Monte Carlo history is large, as well, say $\mathcal{O}(10^6)$, then the reweighting procedure, which has to be applied on all of the $K$ resampled blocks, would not be feasible in terms of computational resources anymore.

As a final remark, note that in a real application we distribute the data set on multiple Markov chains. The data $o_{\alpha,i}^r$, where $r$ labels the replica, is then sewed together to one single history before the reweighting and Bootstrap methods are applied. In this regard it is important that the replica are approximately equally long, otherwise they would have to be weighted with their respective length (as it is done in the $\Gamma$-method) which, if possible at all, would certainly imply a much more involved resampling procedure. Another point concerning a history sewed together from replica is autocorrelation. If data is to be de-correlated by blocking methods, the breaks of autocorrelation at the boundaries of the replica is simply neglected.

### Reweighting Distributions

In the section about the multiple-histogram method I stated eq. (4.27) from which the expectation value of some observable $O$ depending on some physical quantity $X$ is obtained. Sometimes it can be interesting or necessary to investigate the distribution function of an Observable $O$ rather than computing its expectation value. Let us assume for simplicity that $O(X) = X$, i.e.

$$\left\langle \hat{X} \right\rangle_\beta = \int \mathrm{d}X X p(\beta, X). \tag{4.43}$$

Then if we substitute $X \to \delta(X - X')$ in this expression we trivially obtain the probability function $p(\beta, X')$,

$$p(\beta, X') = \int \mathrm{d}X \delta(X - X') p(\beta, X). \tag{4.44}$$

The same step can be done to obtain the probability $p^R(\beta, X')$ from equation eq. (4.33) and eq. (4.34) accordingly. In the case of eq. (4.34) where we have a sum over all sampled states $s$ the $\delta$-distribution gets replaced by Kronecker-$\delta$,

$$p^R(\beta, X') = \frac{1}{Z(\beta)} \sum_{i,s} \frac{\delta_{x_{is},x'}}{\sum_j n_j \; Z^{-1}(\beta_j) \; \mathrm{e}^{-(\beta_j-\beta_k)P_{is}}}. \tag{4.45}$$

The application of this equation could be very impractical since the right-hand side of this equation has to be evaluated for every measurement $x'$ of X which could potentially be hundreds thousands of times or more. Therefore it is helpful to think in terms of histograms. A measured value $x_{is}$ of $X$ is sorted into a bin of width $\Delta X$ if $X' < x_{is} < X' + \Delta X$. Consequently, instead of a Kronecker-$\delta$ we actually have to use a heaviside function:

$$p^R(\beta, X') = \frac{1}{Z(\beta)} \sum_{i,s} \frac{\theta\left[(x_{is} - (X' - \frac{\Delta X}{2}))(X' + \frac{\Delta X}{2} - x_{is})\right]}{\sum_i n_i \; Z^{-1}(\beta_i) \; \mathrm{e}^{-(\beta_i-\beta_k)P_{is}}}. \tag{4.46}$$

With regard to the continous version of this expression one realizes that due to the heaviside function an additional factor $\Delta X$ is obtained. This can be seen from the following consideration: The probability function $p(\beta, X')$ as is given by

$$p(\beta, X') = \int_{-\infty}^{\infty} \theta\left[\left(x_{is} - \left(X' - \frac{\Delta X}{2}\right)\right)\left(X' + \frac{\Delta X}{2} - x_{is}\right)\right] p(\beta, X) dX. \tag{4.47}$$

We expect to obtain 1 from integrating $p(\beta, X')$ from $-\infty$ to $\infty$ but due to the heaviside function we instead obtain,

$$\begin{aligned}
\int_{-\infty}^{+\infty} p(\beta, X') dX' &= \int_{-\infty}^{\infty} \int_{-\infty}^{\infty} \theta\left[\left(x_{is} - \left(X' - \frac{\Delta X}{2}\right)\right)\left(X' + \frac{\Delta X}{2} - x_{is}\right)\right] p(\beta, X) dX dX' \\
&= \int_{-\infty}^{+\infty} \int_{X' - \frac{\Delta X}{2}}^{X' + \frac{\Delta X}{2}} p(\beta, X) \mathrm{d}X \mathrm{d}X' \\
&\approx \int_{-\infty}^{+\infty} p(X') \Delta X \mathrm{d}X' \\
&\approx \Delta X
\end{aligned} \tag{4.48}$$

Hence in order to obtain a normalized probability distribution function the result has to be divided by $\Delta X$. In words, the reason for obtaining the additional factor $\Delta X$ is that we put states of a theory with a continuous spectrum into bins of a finite size. For a theory with a discrete spectrum, like the $2D$ Ising model, for which the reweighting method can be completely formulated in terms of histograms, such a consideration is not necessary.

### 4.1.3 Filtering Algorithm for $\chi^2$ Fits

The two well-known key quantities to measure the quality of a fit are the reduced chi-square $\chi^2_{\mathrm{NDF}}$ and $Q$, the goodness of a fit[2]. Besides considering these quantities, fitting of data often requires to use knowledge about the underlying model or theory, as well, since the latter usually imposes further mathematical and

[2] $50\%$ is considered the optimal value for Q. For a comprehensive introduction on the goodness of a fit and to chi-square fitting in general, see for instance [165].

physical constraints on a fit. If these are ignored, there is no guarantee that a fit result with good values of $\chi^2(\approx 1)$ and $Q$ ($\approx 50\%$) is indeed the best result possible. The fitting algorithm used for the fits of the fitting form of the kurtosis $B_4$ in section 5.3 (study at $\mu = 0$) and 5.4 (study at $\mu_{i,c}$) serves exactly this purpose. Note, that here I will restrict the discussion on the application of the algorithm on the fitting form of $B_4$ at $\mu = 0$. The only difference between the fitting forms at $\mu = 0$ and $\mu_{i,c}$ is in the scaling variable, which for $\mu = 0$ is $x = (\kappa - \kappa_{Z_2})N_\mathrm{s}^{1/\nu}$ while for $\mu_{i,c}$ it is $x = (\beta - \beta_\mathrm{c})N_\mathrm{s}^{1/\nu}$. The application and criteria of the fitting-algorithm are completely analogous at purely imaginary chemical potential at $\mu_{i,c}$. In section 5.3 finite size scaling analyses are performed by fitting

$$B_4(\beta_\mathrm{c}, \kappa, N_\mathrm{s})_{(\mu=0)} = \left(B_4(\beta_\mathrm{c}, \kappa_{Z_2}, \infty)_{(\mu=0)} + a_1 x + a_3 x^3\right)\left(1 + B N_\mathrm{s}^{1/\nu}\right) \tag{4.49}$$

to $B_4$ data, obtained from Monte Carlo simulations, in order to extract $\kappa_{Z_2}$ in the infinite volume limit, i.e. the $\kappa$ value where the first order transitions change to crossover transitions. While the parameters $B_4(\beta_\mathrm{c}, \kappa_{Z_2}, \infty)_{(\mu=0)}$ and $\nu$ are usually fixed to their universal values, the parameters to be extracted are $\kappa_{Z_2}, a_1, B$. Technically this is a fit in two variables $(\kappa, N_\mathrm{s})$. An alternative approach, pursued in this work, is to treat the fit as a simultaneous or shared parameter fit of the parameters $\kappa_{Z_2}, a_1, B$ to sets of points $(\ \kappa\ ,\ B_4(\beta_\mathrm{c}(\kappa))\ )_{N_{\mathrm{s}_i}}$ that are different for each temporal extent $N_{\mathrm{s}_i}$. I.e. the data points $(\ \kappa\ ,\ B_4(\beta_\mathrm{c}(\kappa))\ )_{N_{\mathrm{s}_1}}$ belonging to $N_{\mathrm{s}_1}$ describe a different curve (with a steeper slope) compared to the data points $(\ \kappa\ ,\ B_4(\beta_\mathrm{c}(\kappa))\ )_{N_{\mathrm{s}_2}}$ belonging to $N_{\mathrm{s}_2} < N_{\mathrm{s}_1}$. An important observation here is, that the fitting range in $x = (\kappa - \kappa_{Z_2})N_\mathrm{s}^{1/\nu}$ can be different for each set of points $(\ \kappa\ ,\ B_4(\beta_\mathrm{c}(\kappa))\ )_{N_{\mathrm{s}_i}}$ and thus varying the fit interval in $x$ yields a multitude of possible fits (depending on the number of data points, $\approx \mathcal{O}(10)$ to $\mathcal{O}(10^5)$ fits) with differing results from which the "good" ones have to be chosen. This is complicated by the fact that changing the fitting range in $\kappa$ influences the fitted value of $\kappa_{Z_2}$, i.e. causes a non-trivial shift of the interval in $x$, which is only known a posteriori.

In the following, criteria are imposed on the choice of the good fits which are in accordance with the fitting form given by (4.49).

1. Extrapolation is forbidden, i.e. all fitting intervals are placed such that

$$\kappa_{Z_2} \in I = \left[\kappa_\mathrm{min}, \kappa_\mathrm{max}\right] . \tag{4.50}$$

2. Since the scaling variable is $x \equiv (\kappa - \kappa_{Z_2})N_\mathrm{s}^{1/\nu}$, the scaling region in $\kappa$ shrinks with growing $N_\mathrm{s}$. Thus, for the fitting intervals $I_1, \ldots, I_n$ of the data with $N_{\mathrm{s}_1} < \ldots < N_{\mathrm{s}_n}$, we require

$$I_1 \supseteq \cdots \supseteq I_n . \tag{4.51}$$

3. On the reduced chi-square the following condition is imposed

$$1 - \delta \leq \chi^2 \leq 1 + \delta, \qquad \text{with} \quad \delta \approx 0.2 .$$

4. The fitting range in $x$ should ideally be the same for all volumes included. The intervals $I_n$ are mapped to intervals

$$\tilde{I}_n \equiv \left[x_n^\mathrm{min}, x_n^\mathrm{max}\right] .$$

For two intervals $A = [a_1, a_2]$ and $B = [b_1, b_2]$, we define an *overlap percentage* as

$$\Omega \equiv \begin{cases} 0 & \text{if } a_2 < b_1 \vee b_2 < a_1 \\ 100 \cdot \left(1 - \dfrac{|b_1 - a_1| + |b_2 - a_2|}{a_2 - a_1 + b_2 - b_1}\right) & \text{otherwise} \end{cases} . \tag{4.52}$$

We then require $\Omega \geq 80\%$.

5. Since the scaling region is based on Taylor expansion, it should be symmetric around $x_c$,

$$I_{\text{scaling}} = \left[-\bar{x}, \bar{x}\right] ,$$

with $\bar{x}$ and the size of the region only known after the fit. Given an interval $J = [-a, b]$ with $a$ and $b$ non-negative and $a + b$ fixed, we define a *symmetry percentage* as

$$\Xi \equiv 100 \cdot \left(1 - \left|\frac{2a}{a+b} - 1\right|\right) = 100 \cdot \left(1 - \left|\frac{2b}{a+b} - 1\right|\right) . \tag{4.53}$$

Clearly, $\Xi = 0\%$ (maximally asymmetric interval) for $a = 0$ or $b = 0$ and $\Xi = 100\%$ (maximally symmetric interval) for $a = b$. Among possible fits we choose the one with maximal $\Xi$.

While in practice these criteria work fairly well for the fits performed in the study at $\mu_{i,c}$, for the fits in the study at $\mu = 0$ the criteria will be somewhat relaxed since there the finite size effects are more severe and seem to shift the scaling regions significantly (c.f. discussion in section 5.3). This means that in particular also smaller overlap and symmetry percentages of $\geq 50\%$ will be considered. An example is given in fig. 4.4, which shows one of the fits presented in section 5.3.2.

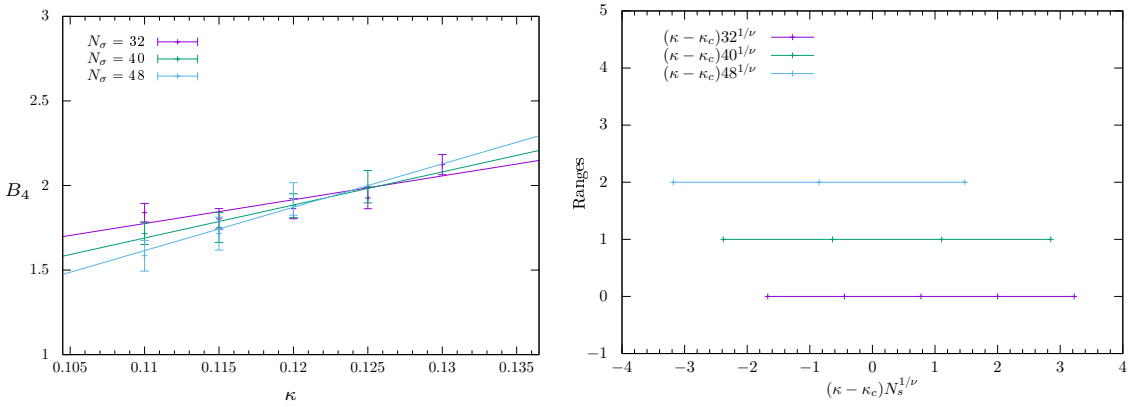


Figure 4.4: Fit of $B_4$ according to (4.49) at $\mu = 0$ and $N_\tau = 8$ with $\chi^2_{\text{NDF}} = 0.62$, NDF=9, $Q = 78$, a minimal overlap of $\Omega_{\text{min}} = 66\%$ and a minimal symmetry of $\Xi_{\text{min}} = 64\%$ in $x = (\kappa - \kappa_{Z_2})N_{\text{s}}^{1/\nu}$. The l.h.s. shows the fit for three data sets belonging to $N_{\text{s}} = 32, 40$ and $48$. The r.h.s. visualizes the fitting intervals in $x$, for which the minimal symmetry (64%) is in the fitting interval of $N_{\text{s}} = 48$ and the minimal overlap (66%) is between the fitting intervals of $N_{\text{s}} = 32$ and 48. Note, that the values on the $y$-axis serve as labels for the different fitting intervals corresponding to different $N_{\text{s}}$.

## 4.2 Rational Hybrid Monte Carlo (RHMC)

For simulations of LQCD involving $N_f = 2$ flavors (or integer multiples of 2) of standard Wilson fermions the de-facto method is the Hybrid Monte Carlo algorithm. For an uneven number of flavors, e.g. $N_f = 3$, in the Hybrid Monte Carlo algorithm the usual inverse quark matrix kernel is replaced by a rational approximation leading to the Rational Hybrid Monte Carlo algorithm . In the following I will very briefly recapitulate the Hybrid Monte Carlo algorithm [166] and starting from this I will explain the Rational Hybrid Monte Carlo algorithm for Wilson fermions. I will base this section on [167, 168].

To start with, let me write down the path integral, discussed in section 2.2, after the Grassmann-valued quark fields have been integrated out,

$$\langle O \rangle = \frac{1}{Z} \int \mathcal{D}\mathcal{U}\, O\left[\psi, \bar{\psi}, U\right] [\det M(U)]^{\alpha}\, \mathrm{e}^{-S_G[U]}, \tag{4.54}$$

in which $\alpha = N_f/2$ (for Wilson fermions) and $M = D^\dagger D$ with $D$ the Wilson fermion matrix (c.f. eq. (2.34)) in its discretized form. The fermion determinant $\det M$ is represented as a pseudofermion Gaussian functional integral, i.e.

$$\begin{aligned} \det M &= \int \mathcal{D}\phi^\dagger \mathcal{D}\phi\, \mathrm{e}^{-\phi M^{-1} \phi} \\ &= \int \mathcal{D}\phi^\dagger \mathcal{D}\phi\, \mathrm{e}^{-S_{\mathrm{PF}}} \end{aligned} \tag{4.55}$$

For a reminder about pseudofermions see for instance [33]. The form of the LQCD path integral is suited for the application of *importance sampling*, i.e. in a Monte Carlo simulation of LQCD the gauge field configurations are sampled according to the probability distribution

$$P[U] = \frac{1}{Z}\, \mathrm{e}^{-S_G} [\det M(U)]^{\alpha}. \tag{4.56}$$

Note, being a part of the probability distribution $P[U]$ the fermion determinant $\det M(U)$ must be real and non-negative. The reality is guaranteed by $\gamma_5$-hermiticity (see section 2.6). A negative fermion determinant can be ruled out by assuming mass degenerate quark masses. This is physically justified for the case of $N_f = 2$ flavor simulations for which the up and the down quark are assumed to be mass degenerate. For the Hybrid Monte Carlo algorithm a fictitious momentum field $\pi$ is introduced and included in the Hamiltonian which then reads

$$H = \frac{1}{2} \mathrm{Tr} \pi^2 + S_G + S_{\mathrm{F}}. \tag{4.57}$$

The fictitious field $\pi$ allows to evolve the gaugefields by integrating Hamilton's equations of motion in a fictitious discretized time dimension labeled by $\tau$. This is also referred to as molecular dynamics integration. The momentum and the pseudofermion fields are periodically updated by a heatbath which ensures ergodicity. The integration of Hamilton's equations along $\tau$ with a step size $\delta\tau$ introduces an error of $\mathcal{O}(\delta\tau^k)$, where $k$ is the order the integration scheme used. At the end of every Hybrid Monte Carlo step a Metropolis acceptance test is done which stochastically corrects for this error. A requirement for the Metropolis acceptance test is *detailed balance* condition for which the integration scheme used must be reversible and area preserving. This is fulfilled by symmetric symplectic integrators for which the most popular example is the second order leapfrog integrator.

These ingredients make the Hybrid Monte Carlo algorithm an exact algorithm which produces results that are independent of the step size. Of course the step size should be chose such that the rate of Hybrid Monte Carlo steps accepted (referred to as acceptance rate) is a reasonable one. If the step size is large, the integration speed is large as well but the acceptance rate will drop, leading to many Hybrid Monte Carlo steps being rejected. In this case the previous configuration will be stored. This implies that the phase space is being explored slowly and that correlations in the data are larger. In contrast, if the step size is small the integration speed is lower, as well but the data has a smaller autocorrelation time. In practice a compromise is chosen, i.e. the step size is typically chosen such that an acceptance rate between $68\%$ is $85\%$ is obtained.

One Hybrid Monte Carlo step consist of the following parts:

- Momentum refreshment heatbath $\left(P(\pi) \propto \ \mathrm{e}^{-\pi*\pi/2}\right)$,
- pseudofermion heatbath $\left(\phi \propto D^{\dagger}\chi, \text{ where } P(\chi) \propto \ \mathrm{e}^{-\chi*\chi}\right)$,
- molecular dynamics trajectory consisting of $\tau/\delta\tau$ number of steps,
- Metropolis acceptance test with $P_{\text{acc}} = \min\left(1, \ \mathrm{e}^{-\delta H}\right)$.

If the reader is unfamiliar with these steps he is referred to [33] in which a more detailed summary of the steps and discussion thereof can be found. Repetition of this Hybrid Monte Carlo step builds a Markov chain collecting the most important states of the system. The computational cost of the Hybrid Monte Carlo strongly increases if the fermion mass is decreased. This happens due to the following two reasons:

1. During the Hybrid Monte Carlo step $D^{-1}$ has to be applied to a vector which can be done using a Krylov solver for which a popular example is conjugate gradient (for a very comprehensively written article see [169]). The cost of such a solver goes up rapidly for small fermion masses due to the increase of the condition number of $D$.

2. In the integration of Hamilton's equations of motion the fermion force acting on the gauge fields increases as the fermion mass is decreased. Then the acceptance rate can only be kept constant if the step size is reduced which implies an increase of cost.

In the last years a lot of progress has been made which consists in improvements to the Hybrid Monte Carlo algorithm to considerably reduce the computational cost such that simulating small quark mass, in particular physical quark masses starts to become feasible. Among others these include mass preconditioning [170] and multi-timescale mass preconditioning [171–173].

These are the most important points to mention about the Hybrid Monte Carlo algorithm. Full descriptions and lengthy discussions about the topic can be found in textbooks like [33, 160].

For the Hybrid Monte Carlo algorithm the parameter $\alpha$ in eq. (4.54) is required to take integer values, i.e. only an even number of flavors can be simulated. If an uneven number of flavors is desired, say $N_f = 3$, the parameter $\alpha$ has to assume non-integer values. In the standard Hybrid Monte Carlo algorithm there is no way to directly evaluate the action or its variation with respect to the gauge field, needed to compute the force. One possibility for simulating uneven $N_f$ is the Rational Hybrid Monte Carlo algorithm which is at present the best algorithm for this task and is superior to two other algorithms capable of this task, the R-algorithm and Polynomial Hybrid Monte Carlo algorithm [167, 174].

The basic idea of the Rational Hybrid Monte Carlo algorithm is to replace the kernel $M^{-\alpha}$ in the bilinear in the first row of eq. (4.55) with a rational approximation ,

$$\det M = \int \mathcal{D}\phi^{\dagger}\mathcal{D}\phi \ \mathrm{e}^{-\phi r^2(M)\phi}, \tag{4.58}$$

where $r(x) = x^{-\alpha/2}$. The rational approximations can be written in partial fraction form, i.e.

$$r(x) = a_0 + \sum_{k=1}^{m} \frac{\alpha_k}{x + \beta_k}, \tag{4.59}$$

Optimal rational approximations with respect to the coefficients $\alpha_k$ and $\beta_k$ can be obtained with the Remez algorithm [175] for which the roots and poles are in general real. For a detailed discussion see

[176]. The poles are positive for $|a| < 1$, as well. This case is important when $N_f = 2 + 1$ flavors are simulated, which represents a combination of Hybrid Monte Carlo for $N_f = 2$ and Rational Hybrid Monte Carlo for $N_f = 1$.

Now the question is how to apply a rational approximation to a matrix. The ordinary way to compute a function $f(A)$ of a hermitian matrix $A$ (which is the case for $M$) is to find a matrix $U$ and a diagonal matrix $D$ such that $M = UDU^{-1}$, with $D = diag[\lambda_1, \ldots, \lambda_N]$ where $\lambda_1, \ldots, \lambda_N$ are the eigenvalues of $D$. The function $f(A)$ can then be computed by $f(A) = Uf(D)U^{-1}$, where $f(D) = diag[f(\lambda_1), \ldots, f(\lambda_N)]$. In the case of the rational approximation it turns out that the matrix $U$ and its inverse are not needed [3] , i.e. one has

$$r(A) = a_0 + \sum_{k=1}^{m} \alpha_k (A + \beta_k)^{-1}. \tag{4.60}$$

As already mentioned above, in the Hybrid Monte Carlo algorithm expressions similar to $(A + \beta_k)^{-1}\chi$ have to be evaluated which can be done using a conjugate gradient solver. The sum in eq. (4.60) contains many of these terms which can be solved altogether at a stroke using a multi-shift conjugate gradient solver [177], also referred to as CG-M. In this way the cost of evaluating a rational approximation is very similar to a single matrix inversion and moreover in leading order the cost is independent of the desired precision.

Other than the replacement of the fermion kernel in the Hybrid Monte Carlo algorithm by a rational approximation nothing changes and thus the procedure is the same like with a Hybrid Monte Carlo algorithm up to corresponding modifications in the pseudofermion heatbath, the molecular dynamics part and the Metropolis acceptance test which I will cover in the following.

Before I start with the pseudofermion refreshment heatbath part, I make two remarks: An important component of the (Rational) Hybrid Monte Carlo algorithm is the computation of the pseudofermion force which imperatively should be conducted in combination with even/odd preconditioning of the fields. Even though it is important to be familiar with it, I will not discuss the fermion force computation with even/odd preconditioning at this point since it is not strictly necessary for the discussion of the Rational Hybrid Monte Carlo algorithm and furthermore it is quite technical and lengthy. However, it might be important if the reader intends to work on or modify the CL$^2$QCD code, since identifying equations in an actual code is not always trivial. For this reason I include the computation of the pseudofermion force in the appendix section A.2. The second remark regards the notation I will use from now on, which I orient on the implementation of the Hybrid Monte Carlo and Rational Hybrid Monte Carlo algorithm in CL$^2$QCD. The reason is again that if the reader intends to read the CL$^2$QCD code, the following equations related to the Hybrid Monte Carlo and Rational Hybrid Monte Carlo algorithm can easily be identified. This notation allows to easily switch between the Wilson and the Twisted-Mass Wilson fermion discretization, which is not important for the discussion here but could be important for working with CL$^2$QCD. The

[3] Showing this a simple exercise which starts from inserting into $f(A) = Uf(D)U^{-1}$ the rational approximation for $f(D)$ according to eq. (4.60).

notation consists simply in defining $Q = \gamma_5 D$. Using this definition together with the $\gamma_5$-hermiticity of $D$

$$\begin{aligned}\left(DD^\dagger\right)^\dagger &= D^\dagger D \\ &\overset{\gamma_5\text{-herm.}}{=} (D\gamma_5 D\gamma_5)^\dagger \\ &= \gamma_5^\dagger D^\dagger \gamma_5^\dagger D^\dagger \\ &= \gamma_5 D^\dagger \gamma_5 D^\dagger \\ &\overset{\gamma_5\text{-herm.}}{=} DD^\dagger\end{aligned} \tag{4.61}$$

one can write

$$D^\dagger D = DD^\dagger = QQ, \tag{4.62}$$

which can be used to write the pseudofermion action as $S_{\text{PF}} = \phi^\dagger (QQ)^{-1} \phi$

For the pseudofermion refreshment heatbath where a field $\chi$ is created randomly according to the distribution $P(\chi) = \exp(-\chi * \chi)$ we consider the $S_{\text{PF}}$ for a general $\alpha = N_f/2$,

$$\begin{aligned}\phi^\dagger (QQ)^{-\alpha} \phi &= \phi^\dagger (QQ)^{-\frac{N_f}{2}} \phi \\ &= \underbrace{\phi^\dagger (QQ)^{-\frac{N_f}{4}}}_{\chi^\dagger} \underbrace{(QQ)^{-\frac{N_f}{4}} \phi}_{\chi}, \\ &=\end{aligned} \tag{4.63}$$

in which $\phi$ is obtained via via

$$\phi = (QQ)^{+\frac{N_f}{4}} \chi. \tag{4.64}$$

In order to evaluate eq. (4.64) a rational approximation is applied according to eq. (4.60):

$$(QQ)^{+\frac{N_f}{4}} \longrightarrow \left[\alpha_0 + \sum_{i=1}^{m} \alpha_i \left(QQ + \beta_i\right)^{-1}\right], \tag{4.65}$$

which, substituted into eq. (4.64), yields

$$\phi = \left[\alpha_0 + \sum_{i=1}^{m} \alpha_i \left(QQ + \beta_i\right)^{-1}\right] \chi. \tag{4.66}$$

At this point a multi-shift conjugate gradient solver can be applied to evaluate $\alpha_i \left(QQ + \beta_i\right)^{-1} \chi$ for $i = 1, \ldots, m$.

The next relevant part for the Rational Hybrid Monte Carlo algorithm is the molecular dynamics integration. To be more precise, only the computation of the pseudofermion force in this part is important. The total force is given by the derivative of the action

$$F\left[U, \phi\right] = \frac{\partial}{\partial V} S\left[U, \phi\right], \qquad S\left[U, \phi\right] = S_G\left[U\right] - \phi^\dagger \left(QQ\right)^{-\alpha} \phi. \tag{4.67}$$

where $\partial / \partial V$ is to be understood as derivative in the algebra direction $T_i$, i.e.

$$\partial / \partial V = \sum_i T_i \nabla^i \text{ with } \nabla^i = \partial / \partial \omega^i. \tag{4.68}$$

Let us start with the evaluation of the fermionic part of the force for the case of $N_f = 2$ flavors, i.e. $\alpha = 1$ to subsequently easily extent it to an arbitrary $N_f$: [4]

$$\begin{aligned}\nabla^{(i)}\left(\phi^\dagger (QQ)^{-1}\phi\right) &= -\phi^\dagger (QQ)^{-1}\left(\nabla^{(i)}QQ\right)(QQ)^{-1}\phi \\ &= -\left((QQ)^{-1}\phi\right)^\dagger \left(\frac{\partial Q}{\partial \omega^{(i)}}Q + Q\frac{\partial Q}{\partial \omega^{(i)}}\right)(QQ)^{-1}\phi\big).\end{aligned} \tag{4.69}$$

For an arbitrary uneven $N_f$ we start from

$$\nabla^{(i)}\left(\phi^\dagger (QQ)^{-\alpha}\phi\right), \quad \text{with} \quad \alpha = \frac{N_f}{2}. \tag{4.70}$$

Note that here a different rational approximation is needed since the exponent $\alpha$ is different compared to the pseudofermion refreshment heatbath. and substitute $(QQ)^{-\alpha}$ with its rational approximation and proceed like in eq. (4.69):

$$\begin{aligned}\nabla^{(i)}\left(\phi^\dagger (QQ)^{-\frac{N_f}{2}}\phi\right) \longrightarrow &\nabla^{(i)}\phi^\dagger\left[\alpha_0 + \sum_{j=1}^{m}\alpha_j (QQ+\beta_j)^{-1}\right]\phi \\ \overset{cf.(4.69)}{=} &-\sum_{j}^{m}\alpha_j\,\phi^\dagger (QQ+\beta_j)^{-1}\left(\nabla^{(i)}QQ\right)(QQ+\beta_j)^{-1}\phi \\ = &-\sum_{j=1}^{m}\alpha_j\Big[\phi^\dagger (QQ+\beta_j)^{-1}\left(\nabla^{(i)}Q\right)Q(QQ+\beta_j)^{-1}\phi \\ &+\phi^\dagger (QQ+\beta_j)^{-1}Q\left(\nabla^{(i)}Q\right)(QQ+\beta_j)^{-1}\phi\Big] \\ = &-\sum_{j=1}^{m}\alpha_j\left[X_j^\dagger\left(\nabla^{(i)}Q\right)Y_j + Y_j^\dagger\left(\nabla^{i}Q\right)X_j\right] \\ = &-\sum_{j=1}^{m}\alpha_j\left[X_j^\dagger\left(\nabla^{(i)}Q\right)Y_j + \left(X_j^\dagger\left(\nabla^{(i)}Q\right)Y_j\right)^\dagger\right],\end{aligned} \tag{4.71}$$

where we defined

$$X_j = (QQ+\beta_j)^{-1}\phi, \qquad Y_j = QX_j, \tag{4.72}$$

where again a multi-shift conjugate gradient is applied to obtain the solution for $X_j$. Having obtained $X_j$ the field $Y_j$ can be obtained by a simple application of $Q$. Note, that the extension to the case of even/odd-preconditioned fields is straightforward since the rational approximation can be applied to eq. (A.26) (third line) in exactly the same way as above.

The last part of the Hybrid Monte Carlo algorithm relevant for the construction of the Rational Hybrid Monte Carlo algorithm is the Metropolis accept-reject step in which the new value of the action, obtained from the refreshment heatbaths and molecular dynamics integration, is compared to the old one. To be more precise, the newly created configuration is accepted if

$$r < \exp\left(\mathrm{Tr}[\pi^2] - \mathrm{Tr}[\pi^2_{\text{new}}] + S_G[U] - S_G[U_{\text{new}}] + \phi^\dagger\left((QQ)^{-\alpha} - (QQ)^{-\alpha}_{\text{new}}\right)\phi\right), \tag{4.73}$$

where $r$ is a random number with $r \in [0,1)$. Here apparently the fermion part enters again for which reason another rational approximation has to be applied but this time it is the same procedure as eq. (4.70) since the exponent $\alpha = N_f/2$ to be approximated is the same.

[4] Remember the definition of the group elements of $SU(3)$: $U = \exp\left[i\sum_{i=1}^{8}\omega^{(i)}T_i\right]$. For details see [33].

At this point we are not done yet since a few more very important remarks have to be made which are the following: The rational approximation of $f(A)$ has a range of validity. This range must be within the interval $I = [\lambda_{\text{min}}, \lambda_{\text{max}}]$ with $\lambda_{\text{min}}$ and $\lambda_{\text{max}}$ being the minimal and maximal eigenvalues of $A$ respectively. There different algorithms to find these eigenvalues numerically. In our code CL$^2$QCD the *power method* is employed for this task. A description of this method be found for instance in [178]. This directly directly relates to the question if the rational approximation coefficients $a_k$ and $b_k$ (c.f. eq. (4.60)) have to be computed anew employing the Remez algorithm for every Rational Hybrid Monte Carlo step. This would be very costly and cause the Rational Hybrid Monte Carlo algorithm to become unfeasible in terms of computational time. Fortunately the answer is no and there is a better way explained in the following. Assume to have calculated the rational approximation of $f(y) = y^\alpha$ which is

$$y^\alpha \simeq a_0 + \sum_{k=1}^{m} \frac{a_k}{x + b_k}, \tag{4.74}$$

valid for $y \in [x_{\text{min}}, 1]$ where $x_{\text{min}}$ is known. Now the rational approximation of $f(x) = x^\alpha$ is needed which is required to be valid in the interval $I = [\lambda_{\text{min}}, \lambda_{\text{max}}]$. The functions $f(x)$ and $f(y)$ can be related by the following consideration:

$$f(x) = x^\alpha = \left(\frac{\lambda_{\text{max}}}{\lambda_{\text{max}}} x\right)^\alpha = \lambda_{\text{max}}^\alpha \left(\frac{x}{\lambda_{\text{max}}}\right)^\alpha \equiv \lambda_{\text{max}} y^\alpha. \tag{4.75}$$

Then the rational approximation of $f(x)$ can be written as

$$\begin{aligned} f(x) &\simeq \lambda_{\text{max}}^\alpha \left[ a_0 + \sum_{k=1}^{m} \frac{a_k}{\frac{x}{\lambda_{\text{max}}} + b_k} \right] \\ &= \lambda_{\text{max}}^\alpha a_0 + \sum_{k=1}^{m} \frac{\lambda_{\text{max}}^{\alpha+1} a_k}{x + \lambda_{\text{max}} b_k} \\ &= a_0' + \sum_{k=1}^{m} \frac{a_k'}{x + b_k'}, \end{aligned} \tag{4.76}$$

which is clearly valid for $x \in [x_{\text{min}}\lambda_{\text{max}}, \lambda_{\text{max}}]$. Now if

$$x_{\text{min}} \leq \frac{\lambda_{\text{min}}}{\lambda_{\text{max}}}, \tag{4.77}$$

then $x$ is valid in $I = [\lambda_{\text{min}}, \lambda_{\text{max}}]$. This means that the rational approximation coefficients $a_0', a_k', b_k'$ of $f(x)$ can be obtained by rescaling the ones of $f(y)$ by

$$a_0' = \lambda_{\text{max}}^\alpha a_0, \quad a_k' = \lambda_{\text{max}}^{\alpha+1} a_k, \quad b_k' = \lambda_{\text{max}} b_k. \tag{4.78}$$

In case the condition by eq. (4.77) is not fulfilled, a new rational approximation has to be computed.

To conclude the section I make some final. The first important remark concers the precision of the rational approximation, for which there are two sources of numerical errors - the rational approximation coefficients $a_0, a_k, b_k$ and the order of the rational approximation expansion given by the number of terms in the sum in eq. (4.74). Since the rational approximation coefficients usually only have to be evaluated once at the beginning of the Rational Hybrid Monte Carlo simulation they should be computed with a high precision, i.e. machine precision which is typically $\approx 10^{-15}$. For the order of the rational approximation expansion in contrast, which determines how well a function $f(A)$ is approximated, such a precision

would be too high since in each Rational Hybrid Monte Carlo step all the terms in the sum have to be evaluated using the multi-shift conjugate gradient solver. A too large number of terms then increases the computational cost considerably since the number of linear algebra operations like matrix-vector multiplication increases significantly, as well. Fortunately it is enough to choose the number of terms such that the precision by which $f(A)$ is approximated is just higher than the precision of the solver used. In the case of the molecular dynamics part a lower precision can be chosen, since the numerical errors occurring there are corrected for by the Metropolis acceptance test. Of course, a too low precision also implies a decrease of the acceptance rate [179]. The precision of the pseudofermion refreshment heatbath as well as the Metropolis test affect the fixed point of the Markov process for which reason it is imperative to use a high precision. The second important remark is about a comment made in [180] which states that with the Rational Hybrid Monte Carlo algorithm the measure $\sqrt{\det{}^2 D}$ is sampled. This can be a problem when very small masses in the Wilson formulation of fermions are simulated since the these $\det D$ may become negative for some background gauge fields. However, this happens only for a small number of ensembles that goes to zero in the continuum limit and thus does not affect the continuum limit of the lattice results. If desired this can be corrected by computing the sign of the determinant and multiplying the corresponding configurations by $-1$. The sign of the determinant can for instance be computed using the Arnoldi method, described in [178]. This has not been implemented in CL$^2$QCD due to temporal constraints on the project but the simulations with $N_f = 3$ flavors so far have been conducted in the heavy quark mass region only (c.f. section 5) where this phenomen is probably not an issue.

## 4.3 The CL$^2$QCD Software in a Nutshell

CL$^2$QCD is a Monte Carlo simulation code for LQCD that was used for all simulations performed for this work. In this section I will give a brief description of CL$^2$QCD without attempting to discuss the code or its performance results in detail. Attempting to do so leads beyond the scope of this work since CL$^2$QCD is a large project which originated around 2011 when it was developed by Dr. M. Bach, Dr. C. Pinke and others [181]. In the meanwhile CL$^2$QCD has grown, more developers contributed and many features, e.g. a Rational Hybrid Monte Carlo algorithm implementation, were added. A quite recent description of the code can be found in [182] in which the structure of code is depicted graphically and a discussion about the performance is available. Moreover, the code is publicly available and can be found online together with more information on [183].

The code is based on OpenCL (`Open Computing Language`) [27] which is hardware independent and enables CL$^2$QCD to run on heterogeneous computing platforms, i.e. it can make use of central processing units (CPU's) and graphics processing units (GPU's) at the same time. LQCD computations are mainly limited by memory bandwidth. Moreover LQCD functions are local, which makes them well suited for parallel computations. In both points GPU's surpass CPU's for which reason GPU's have become very popular for the environment of LQCD. An example for the memory bandwidth problem is given by the inversion of the fermion matrix $\phi = D^{-1}\chi$ which is computationally the most expensive part of LQCD simulations and is performed using Krylov solvers like conjugate gradient. The method involves computing the product $D\phi$ many times employing a large number of linear algebra operations. This computation is heavily limited by the available memory bandwidth. This can be seen from for instance considering the Wilson $\not{D}$ operator (the derivative part of $D$), which is part of this computation, requires

to read and write 2880 Bytes per lattice site for each call of the operator while it only performs 1632 FLOPs per site. This implies a relatively low numerical density (FLOPs per Byte) of $\rho = 0.57$.

OpenCL applications consist of a host program and an OpenCL part. While the OpenCL part constitutes the so-called `kernel` functions responsible for the performance critical bulk parallel computations like $D\phi$, the host program which runs solely on CPUs conducts the execution of kernels and takes over algorithmic logic involving if-else conditions and all computations which are not well suited for a parallel treatment. The way parallel GPU programming works can be well compared to parallel programming of CPUs. A kernel, executed on a GPU, can be thought of as a function of which many instances are launched concurrently and is mapped to so called `work-groups` consisting of `work-items`. The work-items are then executing the kernel in parallel. For instance a kernel that contains an algorithm to compute a vector product (e.g. $v_i, u_i, i = 1, \ldots, N$) also contains the information about the ID of the work-item by which it is currently executed. This ID can be mapped to the components $i$ of the vectors which are then multiplied by the specific work-item. This process is done in parallel until all $N$ vector entries have been multiplied, in order to be added up subsequently by another work-item. In general the work-groups together with their work-items are arranged such that they can be mapped on linear algebra operations easily.

The host program of CL$^2$QCD is written in `C++` and uses mainly the `C++11` standard but utilizes some features specific to newer standards, as well. Since it is based on OpenCL it can also be executed solely on CPUs, if desired. Initially it solely focused on Wilson fermions and was the first of its kind with respect to this discretization [184]. From the beginning on, an implementation of twisted mass Wilson fermions was provided, as well, and more recently a Rational Hybrid Monte Carlo implementation for staggered fermions was added. Now it also has an Rational Hybrid Monte Carlo implementation for Wilson fermions allowing us to simulate odd $N_f$, which was added in the present work. Moreover, improved gauge actions, standard inversion and integration algorithms are implemented and ILDG-compatible I/O as well as the RANLUX Pseudo-Random Number Generator (PRNG) [185] are available. The design of CL$^2$QCD puts emphasis on Maintainability, portability and the inclusion of unit tests (`BOOST`[186] and `CMake`) for which reason during its development the rules of *Test Driven Development* [187] and *Clean Code* [188] were strictly respected.

## 4.4 BaHaMAS Framework for Administrating Simulations

BaHaMAS stands for Bash Handler to Monitor and Administrate Simulations. As the name suggests it is a Bash command-line program (or script) to monitor and administrate simulations which we use in our group for running LQCD simulations. At present it consists of ≈13k lines of code. Since it is completely written in Bash, there is no compilation or installation involved whatsoever, but of course, some user specific files have to be set up. As a co-developer I decided to include a brief description of this program in this work since a non-negligible amount of my time as a PhD-student was used to build it and because it is the reason for being able to efficiently run and administrate hundreds of LQCD simulations on high-perfomance computing clusters (LOEWE-CSC in Frankfurt am Main and L-CSC in Darmstadt) effortlessly without committing errors.

The tool was programmed with the following motivation: LQCD simulations can be characterized by a variety of parameters and their values which one has to decide on. Usually codes simulating LQCD read these parameters from input files which have to be provided respecting certain formats. If the code

is run on a computing cluster the execution of the code is done via a job script which is processed in a queueing system like SLURM. Such a job script needs certain parameters, as well, in order to decide how the operations of the code are distributed over CPU/GPU nodes or in case parallel instances of the codes are run, how these instances are distributed among the nodes. Once the code runs reliably on the compute cluster one has to deal with the question on how to structure and organize the data constantly produced by the code. A further important point to consider is how to deal with the different phases of the simulation, i.e. how to treat the thermalization phase - is the thermalization phase separated from the real run or is this done during the analysis? Another question to think about is, what is a good way to monitor the statistics of the run, i.e. number of trajectories and other characteristic numbers like the acceptance rate of configurations and the associated change in the action, physics and numeric parameters per simulation - basically every number that helps to decide whether to continue a run or do something else. If a run has to be stopped for whatever reason, often adjustments have to be done in order to continue the run. For instance if the simulation is to be continued from a specific trajectory of the past, what happens to the more actual data? Is it simply overridden or are some cleaning operations to be done. Sometimes a node on the compute cluster simply crashes. How can such interruptions be handled efficiently? If newer technologies are used like OpenCL, errors in the computation can occur which are not necessarily related to the simulation code but rather to the software controlling the hardware (e.g. the graphical processing unit). How can such errors be spotted at the right time before the simulation produces erroneous results? In case many simulations are run in a larger project, it could be helpful to have database capabilities to output information about all simulations in a summarized format.

This might not appear to be an impressive list for somebody experienced in lattice simulations and one might ask for which reason software has to be written in order to complete it. For sure, if simulations are conducted occasionally over a very limited time span it could be feasible doing this by hand. But if these task are constantly executed over a couple of years for many simulations, doing this manually is a daunting, time inefficient and extremely error-prone task. I try to explain this more precisely using an example. In the project I discuss in section 5.3 at zero chemical potential I simulated $N_f = 2$ flavors of Wilson fermions with 3 temporal extents $N_\tau$. For each value of $N_\tau$ 5-6 different $\kappa$ values were chosen. For each value of $\kappa$ 3-4 spatial extents $N_\mathrm{s}$ were needed to be able to perform finite size scaling analyses. For each value of $N_\mathrm{s}$ simulations at 2-4 values of the coupling $\beta$ were conducted. This is roughly an amount of 150 simulations. Additionally I simulated $N_f = 3$ flavors of Wilson fermions with one temporal extent $N_\tau$ and 10 values of $\kappa$, each with 1-3 spatial extents $N_\mathrm{s}$ with about 2-4 values of $\beta$. This makes roughly another 70 simulations. In total this is an amount of about 220 simulations. Let us assume that only 35% of them are run in parallel, i.e. about 77 simulations, which is a realistic, even conservative number. Each of these simulations can have a run-time of several month or more until a reasonable amount of statistics has accumulated. This implies that the tasks I listed above have to be done for 77 simulations concurrently. Some of them need to be done only once per simulation but many others are repetitive and thus have to be completed over and over again over the duration of the project which is of order of years. I even made a crucial simplification here, by not mentioning the possibility for simulating different replica per $\beta$ which is actually a very common thing to do. In our simulations we use four replica per $\beta$ by default. This then would multiply the number of simulations to supervise by a factor 4. This should be a pretty convincing rationale on why it can be extremely beneficial to automatize some of these tasks which has been realized with BaHaMAS.

I will refrain from explaining in detail how the program completes all of the tasks mentioned above since this is beyond the scope of this work and would unnecessarily prolong this section. Instead I will briefly give a practical example to illustrate just a few features.

The data that is produced by a simulation code like CL$^2$QCD is organized in a directory structure where the tree of directories contains the information about the values of the parameters of the simulation. Therefore one starts by creating a directory structure like

```
path-to-project-directory/Nf2/mui0/k1000/nt6/ns42
```

and navigates into the top level directory (`/ns42`) in order to invoke BaHaMAS from there. Trying to invoke the program from elsewhere or having wrongly specified parameters or parameter values in the path, results in an error message output by BaHaMAS, explaining the user where he went wrong. The prefixes in the path correspond to the simulation parameters, i.e. (in this order) $N_f$, $\mu$, $\kappa$, $N_\tau$, $N_\mathrm{s}$, which are read out by BaHaMAS and used for the input file of the simulation code. In the top level directory the user creates a file (we call it *betas file*) that contains information about further simulation parameters not contained in the directory structure. The most important ones are the information about which values of $\beta$ and how many replica per $\beta$ should be simulated. Furthermore the number of integration steps per trajectory of the different molecular dynamics time scales is put in this file. This file can be created partially automatically with the help of BaHaMAS, thus greatly reducing the chance of wrong user input. If the user runs simulations at a specific $\beta$ for the first time, he can tell BaHaMAS to start a thermalization run. The difference is simply that the simulation data is stored in a specific folder for the length of the thermalization run. The different possible folders BaHaMAS creates are the following ones:

```
b5.8800_s8800_thermalizeFromHot
b5.8800_s8800_thermalizeFromConf
b5.8800_s8800_continueWithNewChain
```

The details are not important. Just note that the postfixes `_thermalizeFromHot` and `_thermalizeFromConf` refer to thermalization simulations while `_continueWithNewChain` refers to a simulation which is already thermalized. The postifx `b5.8800_s8800_` contains the information about the value of $\beta$ (prefix `b`) and about the random number (prefix `s`) used to initialize the run. The random number specification is important if multiple replica are run per value of $\beta$ since they are, of course, treated as independent simulations to be stored in separate directories. Without wanting to go into details I just remark that BaHaMAS detects and separates between unfinished and completed thermalization runs. Depending on the state of thermalization run, BaHaMAS reacts accordingly to attempts of the user to start/continue a thermalization run. The setting up of the simulation code input file, the creation of the job script and the submission of the latter is then carried out by BaHaMAS for each of the specified simulations.

During the run of the simulations the database included in BaHaMAS takes record of a variety of statistics related to the run. The database can be invoked with a simple option. Then BaHaMAS reads out again the simulation parameters of the directory to show to the user only the information about the simulations related to the current directory. An example is shown in fig. 4.5. If one desires to obtain a summary about all simulations on the compute cluster currently being tracked by the BaHaMAS database, independent on the directory one is currently in, another option exists to do exactly this. For an example see fig. 4.6.

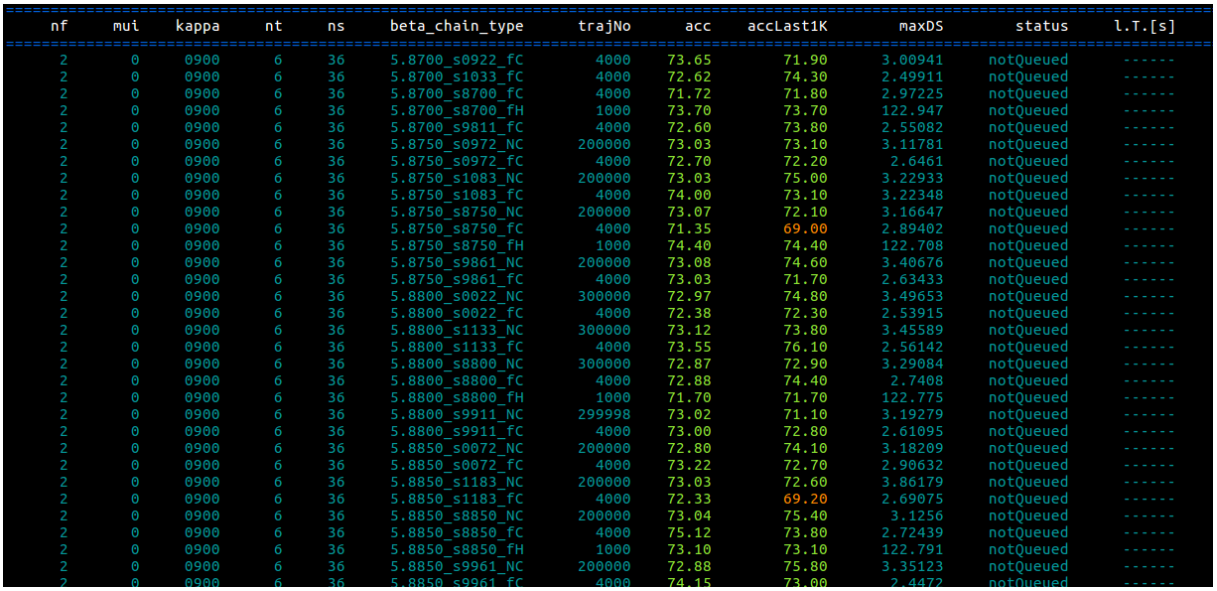

| nf | mui | kappa | nt | ns | beta_chain_type | trajNo | acc | accLast1K | maxDS | status | l.T.[s] |
|---|---|---|---|---|---|---|---|---|---|---|---|
| 2 | 0 | 0900 | 6 | 36 | 5.8700_s0922_fC | 4000 | 73.65 | 71.90 | 3.00941 | notQueued | ------ |
| 2 | 0 | 0900 | 6 | 36 | 5.8700_s1033_fC | 4000 | 72.62 | 74.30 | 2.49911 | notQueued | ------ |
| 2 | 0 | 0900 | 6 | 36 | 5.8700_s8700_fC | 4000 | 71.72 | 71.80 | 2.97225 | notQueued | ------ |
| 2 | 0 | 0900 | 6 | 36 | 5.8700_s8700_fH | 1000 | 73.70 | 73.70 | 122.947 | notQueued | ------ |
| 2 | 0 | 0900 | 6 | 36 | 5.8700_s9811_fC | 4000 | 72.60 | 73.80 | 2.55082 | notQueued | ------ |
| 2 | 0 | 0900 | 6 | 36 | 5.8750_s0972_NC | 200000 | 73.03 | 73.10 | 3.11781 | notQueued | ------ |
| 2 | 0 | 0900 | 6 | 36 | 5.8750_s0972_fC | 4000 | 72.70 | 72.20 | 2.6461 | notQueued | ------ |
| 2 | 0 | 0900 | 6 | 36 | 5.8750_s1083_NC | 200000 | 73.03 | 75.00 | 3.22933 | notQueued | ------ |
| 2 | 0 | 0900 | 6 | 36 | 5.8750_s1083_fC | 4000 | 74.00 | 73.10 | 3.22348 | notQueued | ------ |
| 2 | 0 | 0900 | 6 | 36 | 5.8750_s8750_NC | 200000 | 73.07 | 72.10 | 3.16647 | notQueued | ------ |
| 2 | 0 | 0900 | 6 | 36 | 5.8750_s8750_fC | 4000 | 71.35 | 69.00 | 2.89402 | notQueued | ------ |
| 2 | 0 | 0900 | 6 | 36 | 5.8750_s8750_fH | 1000 | 74.40 | 74.40 | 122.708 | notQueued | ------ |
| 2 | 0 | 0900 | 6 | 36 | 5.8750_s9861_NC | 200000 | 73.08 | 74.60 | 3.40676 | notQueued | ------ |
| 2 | 0 | 0900 | 6 | 36 | 5.8750_s9861_fC | 4000 | 73.03 | 71.70 | 2.63433 | notQueued | ------ |
| 2 | 0 | 0900 | 6 | 36 | 5.8800_s0022_NC | 300000 | 72.97 | 74.80 | 3.49653 | notQueued | ------ |
| 2 | 0 | 0900 | 6 | 36 | 5.8800_s0022_fC | 4000 | 72.38 | 72.30 | 2.53915 | notQueued | ------ |
| 2 | 0 | 0900 | 6 | 36 | 5.8800_s1133_NC | 300000 | 73.12 | 73.80 | 3.45589 | notQueued | ------ |
| 2 | 0 | 0900 | 6 | 36 | 5.8800_s1133_fC | 4000 | 73.55 | 76.10 | 2.56142 | notQueued | ------ |
| 2 | 0 | 0900 | 6 | 36 | 5.8800_s8800_NC | 300000 | 72.87 | 72.90 | 3.29084 | notQueued | ------ |
| 2 | 0 | 0900 | 6 | 36 | 5.8800_s8800_fC | 4000 | 72.88 | 74.40 | 2.7408 | notQueued | ------ |
| 2 | 0 | 0900 | 6 | 36 | 5.8800_s8800_fH | 1000 | 71.70 | 71.70 | 122.775 | notQueued | ------ |
| 2 | 0 | 0900 | 6 | 36 | 5.8800_s9911_NC | 299998 | 73.02 | 71.10 | 3.19279 | notQueued | ------ |
| 2 | 0 | 0900 | 6 | 36 | 5.8800_s9911_fC | 4000 | 73.00 | 72.80 | 2.61095 | notQueued | ------ |
| 2 | 0 | 0900 | 6 | 36 | 5.8850_s0072_NC | 200000 | 72.80 | 74.10 | 3.18209 | notQueued | ------ |
| 2 | 0 | 0900 | 6 | 36 | 5.8850_s0072_fC | 4000 | 73.22 | 72.70 | 2.90632 | notQueued | ------ |
| 2 | 0 | 0900 | 6 | 36 | 5.8850_s1183_NC | 200000 | 73.03 | 72.60 | 3.86179 | notQueued | ------ |
| 2 | 0 | 0900 | 6 | 36 | 5.8850_s1183_fC | 4000 | 72.33 | 69.20 | 2.69075 | notQueued | ------ |
| 2 | 0 | 0900 | 6 | 36 | 5.8850_s8850_NC | 200000 | 73.04 | 75.40 | 3.1256 | notQueued | ------ |
| 2 | 0 | 0900 | 6 | 36 | 5.8850_s8850_fC | 4000 | 75.12 | 73.80 | 2.72439 | notQueued | ------ |
| 2 | 0 | 0900 | 6 | 36 | 5.8850_s8850_fH | 1000 | 73.10 | 73.10 | 122.791 | notQueued | ------ |
| 2 | 0 | 0900 | 6 | 36 | 5.8850_s9961_NC | 200000 | 72.88 | 75.80 | 3.35123 | notQueued | ------ |
| 2 | 0 | 0900 | 6 | 36 | 5.8850_s9961_fC | 4000 | 74.15 | 73.00 | 2.4472 | notQueued | ------ |

Figure 4.5: Shows a typical example of a database output from a call to BaHaMAS invoked from a directory tree which contains the following parameters $N_f = 2$, $\mu = 0$, $\kappa = 0.0900$, $N_\tau = 6$ and $N_\mathrm{s} = 36$, shown in the first five columns. The subsequent columns contain the $\beta$ value of the simulation and the s-number referring to the random number used to start the respective replicum as well as the information about whether it is a thermalization simulation or not (`beta_chain_type`), the current trajectory or configuration number of the simulation (`trajNo`), the current acceptance rate taking into account all configurations (`acc`), the same just with the last 1k configurations (`accLast1K`), the maximal change of the action (`maxDS`), the current status of the simulation, e.g. running or waiting in the queue (`status`) and the column (`l.T.[s]`) contains the information about how many seconds have past since the last configuration. In the example shown here no simulations were running at the time for which reason the information content is somewhat limited. In the column `acc` and `accLast1K` different colors are used to indicate whether the acceptance rate is optimal or below/above optimal. Similarly colors are used in the column `beta_chain_type` where red color indicates that the simulation might be broken due to an I/O error on the computing node. In the column `maxDS` the color changes accordingly to red if the change in the action jumps to an suspiciously large value, which would not be expected if the simulation runs fine without being affected by errors like I/O errors. Of course for thermalization runs this threshold is large since there in contrast large changes in the action are expected. The column `l.T.[s]` is especially useful to spot simulations that got stuck due to some failure on the computing node. In this case the expired time since the last trajectory would grow infinitely and thus the erroneous simulation can be easily identified.

Here I will stop the description and refer the interested reader to other references like [189] which is a talk about BaHaMAS given at the Lattice 2017 conference in Granada or [190] which is the PhD thesis of my colleague A. Sciarra who is mainly developing BaHaMAS. He also has setup a GitHub repository [191] about the project which contains a very well written, continuously growing documentation. In these references the reader can also find information about how general BaHaMAS is written, i.e. how it can be applied to other codes than CL$^2$QCD.

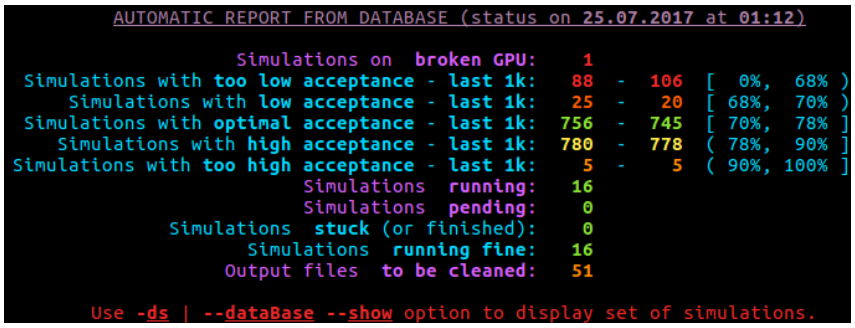


Figure 4.6: Shows a summary of the most important parameters related to all simulations on a cluster being tracked by the database. The first row shows whether a simulation is running on a GPU that might be broken and produces erroneous output. The second to sixth row classifies the simulations by their acceptance rate and prints the respective numbers. The subsequent rows are self-explanatory up to the last rows which contains the information about how many data output files (containing the measurements of observables) of simulations have to be cleaned, which is the case if identical measurements appear twice in a output data file. This can be the case when a simulation was stopped and continued from some earlier trajectory.

# Chapter 5

# Simulations, Results and Discussion

In this chapter I present the physics results obtained in the course of my work as well as the pursued approaches and strategies. These concern the exploration of the extended Columbia plot discussed in section 3.5.3. The physics represented by this diagram were studied using the standard Wilson fermion discretization at two different values of the chemical potential:

- At $\mu = 0$ in the heavy quark mass region of the
  - $N_f = 2$ theory on $N_\tau = 6, 8, 10$ lattices,
  - $N_f = 3$ theory on $N_\tau = 4$ lattices,
- and at the Roberge-Weiss value $\mu_{i,c} = \pi T/3$ of imaginary chemical potential (the Roberge-Weiss endpoint of the $Z_3$ transition) in the heavy and light quark mass region in the
  - $N_f = 2$ theory on $N_\tau = 6$ lattices.

While the $N_f = 2$ flavor QCD simulations were carried out with an existing Hybrid Monte Carlo (HMC) algorithm, the $N_f = 3$ theory was simulated with a Rational Hybrid Monte Carlo (RHMC) whose implementation into the simulation code CL$^2$QCD has been achieved as part of this work. The RHMC algorithm is presented in section 4.2. To give a visual overview I plot the simulation region listed above in the respective quark mass phase diagrams in fig. 5.1.

To start with in section 5.1 I will state the numerical setup of the theories that were simulated. Subsequently, the numerical determination of phase transitions and the different methods that were used at $\mu = 0$ and $\mu_{i,c} = \pi T/3$ will be addressed in section 5.2. Finally, in sections 5.3 and 5.4 the outcome of the simulations at the respective values of the chemical potential will be presented and discussed followed by a summary and a discussion of each section.

To handle the vast amount of simulations conducted for this work over the years it became necessary to have tools in order to efficiently administrate and bookmark the many different simulations on the computing clusters on which they were run. This led me to take part in the development of a Bash-framework named BaHaMAS, which I concisely describe in section 4.4.

Before starting, two more remarks should be made: Even though I present the results in an order that seems natural to me (first $\mu = 0$, second imaginary chemical potential) the chronological order is reversed, i.e. the project at imaginary chemical potential started first. As insights were gained over the course of time, practices and approaches were slightly improved. This implies that some insights gained during the

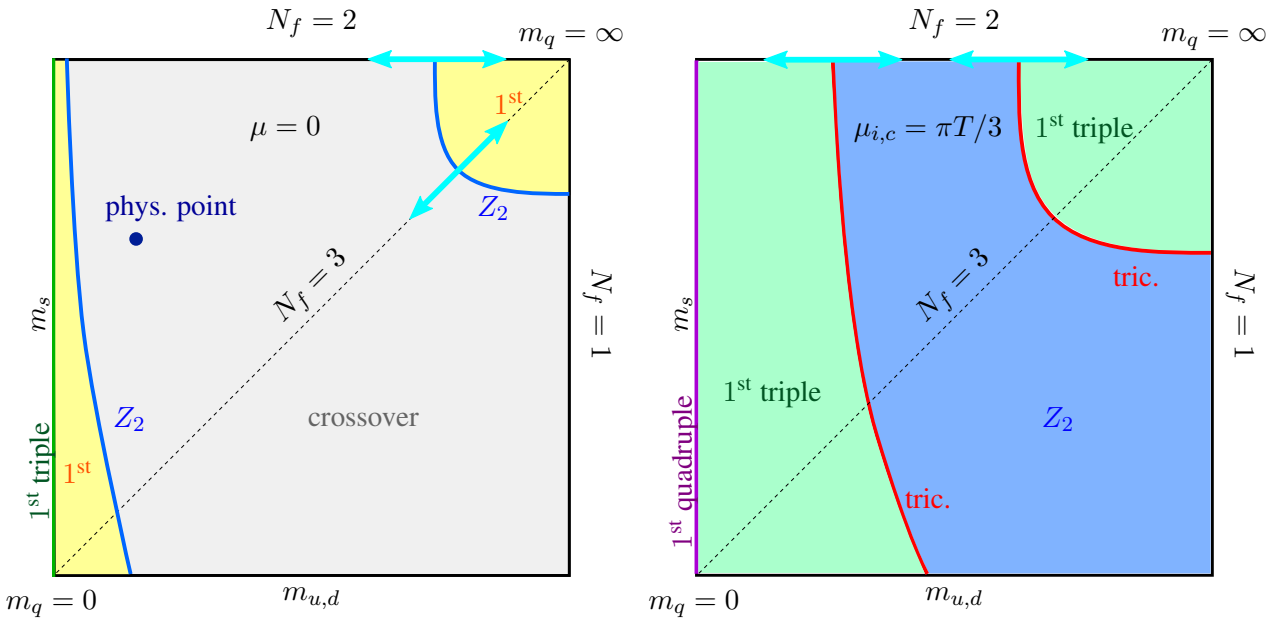


Figure 5.1: The arrow symbols in the quark mass diagrams at $\mu = 0$ (l.h.s.) and $\mu_{i,c} = \pi T/3$ (r.h.s.) indicate the regions where simulations have been performed in order to locate the $Z_2$ points in terms of the hopping parameter $\kappa$.

$\mu = 0$ project could not be applied retroactively anymore to the imaginary chemical potential project due to the complexity and temporal restrictions of the projects. Whenever this information is relevant I will make a remark about this. The second remark concerns the project at imaginary chemical potential. This project was worked out in a team of three persons, sometimes in a team of four persons and the results have been published already in [159].

## 5.1 Numerical Setup

For the gauge and fermionic sector the unimproved version of the Wilson gauge and fermion action were used which I discussed in sections 2.5 and 2.6. For convenience here I write them down once again consicely as

$$S_G = \frac{\beta}{3} \sum_n \sum_{\mu \leq \nu} \mathrm{ReTr}\left[\mathbb{1} - P_{\mu\nu}(n)\right], \qquad S_\mathrm{F} = a^4 \sum_{N_f} \sum_{n,m} \bar{\psi}^{(f)}(n) D^{(f)}(n|m) \psi^{(f)}(m) \tag{5.1}$$

where $D(n|m)$ denotes the Wilson fermion matrix

$$D(n|m) = \delta_{nm} - \kappa \sum_{i=1}^{4} \left[ (1 - \gamma_i)\, \mathrm{e}^{a\mu\delta_{|i|,0}\,\mathrm{sgn}(i)} U_{\pm i}(n) \delta_{n+\hat{i},m} \right]. \tag{5.2}$$

The fermion mass is controlled via the hopping parameter $\kappa = 2(am_f + 4)^{-1}$ and the temperature is indirectly tuned via the lattice coupling $\beta$ and is defined as $T = (a(\beta)N_\tau)^{-1}$, All numerical simulations have been performed using the publicly available OpenCl [27] based code CL$^2$QCD [182–184] that was developed in our group and designed to efficiently run on graphic processing units (GPUs). The code was run on the LOEWE-CSC [192] cluster at Goethe-University Frankfurt and on the L-CSC [193] cluster in Darmstadt. In section 4.3 I give a brief overview about CL$^2$QCD.

Note, that no $\mathcal{O}(a)$-improvement has been used for the simulations. The reason is to rule out any unphysical modifications of the phase structure by adding extra terms to the action. Furthermore if cut-off effects on the pseudoscalar mass at the $Z_2$ or tricritical point are to be studied in a quantitative way and finally removed by an extrapolation, it is necessary to see and control the transition as a function of the lattice spacing $a$. Moreover, if improved versions of the Wilson discretization are used, the available computational resources of the near future might be insufficient to simulate the very small masses marking the critical points on increasingly finer lattices, needed to perform a continuum extrapolation (c.f. the discussion at the end of section 3.5.3 and fig. 3.10).

## 5.2 Numerical Analysis of Phase Transitions

### 5.2.1 Identifying the Order of a Phase Transition

In order to map out the diagrams along the arrow symbols shown in fig. 5.1 the nature of the phase transition has to be identified for the points $(m_{u,d}, m_s)$ along these arrows. Generally this is done by evaluating suited observables $O$ and functions $F(O)$ of the latter at the critical couplings at which the system undergoes a phase transition. Then $O$ and $F(O)$ are expected to behave in a specific way or assume particular values indicating the nature of a transition. Here the main quantity will be the kurtosis (see sections 3.1.1 and 3.1.3)

$$B_4(O; \alpha_1, \cdots, \alpha_n) = \frac{\left\langle (\delta O)^4 \right\rangle}{\left\langle (\delta O)^2 \right\rangle^{\frac{4}{2}}}, \qquad \text{with } \delta O = O - \langle O \rangle . \tag{5.3}$$

where $\delta O$, as the fluctuations of $O$ and $\langle O \rangle$, refers to an ensemble average of configurations produced in a Monte Carlo lattice simulation. The parameters $\alpha_i$ are the respective couplings of the system. In

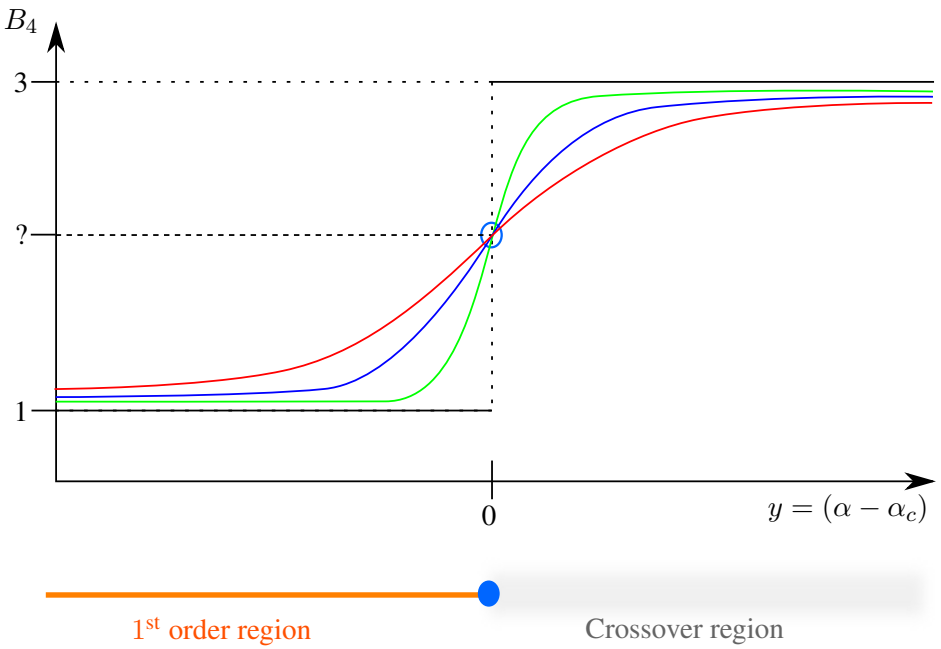


Figure 5.2: The schematic shows how the step function $B_4$ (black curve, $B_4(y<0) = 1$, $B_4(y>0)=3$) becomes an analytic function away from the thermodynamic limit and how the step function is approached by the analytic curves for a series of increasing volumes $V > V > V$. The analytic curves can be expanded around $y = 0$, where all curves intersect at a common value of $B_4$ characteristic to the universality class. The value of $B_4$ indicated by "?" at this points assumes specific values depending on $\mu$, $N_f$ and $\kappa$.

LQCD the parameters relevant for this work are the inverse lattice coupling $\beta$, the quark mass $m_q$ and the chemical potential $\mu$. Remember that in the thermodynamic limit $V \to \infty$ the kurtosis $B_4$ assumes the values 1 at a first order transition and 3 at a crossover. At a second order critical point, e.g. where a first order transition ends and turns into a crossover it assumes a value specific to the universality class of the system. Thus if $B_4$ is evaluated at the critical values of the couplings $\alpha_i$, i.e. along a phase boundary of a set of points $(m_{u,d}, m_s)$ on which the phase transition changes from first order to crossover by passing through a critical point, it behaves as a step function jumping from 1 to 3 which makes it well suited to locate the change from a first order transition to a crossover. On a finite volume no non-analyticities exist and thus there are no real phase transitions. Consequently the $B_4$ step function becomes smoothed out to an analytic curve whose slope increases with the volume. Close to the thermodynamic limit, i.e. for sufficiently large volumes the $B_4$ curves belonging to different volumes all share the same universal value at the critical point where they intersect. This is illustrated schematically in fig. 5.2. $B_4$ then can be Taylor-expanded in the couplings around the critical point, as it was discussed in section 3.1.3 and will be done later for the specific situations, and the expansion can be fitted to simulated data so as to extract the critical point where the curves intersect. The choice of the expansion variable and scaling variable $x = (\alpha - \alpha_c)N_s^{1/\nu}$ respectively depends on the parameter space being explored. Since for this work only simulations at fixed chemical potentials were carried out, at zero chemical potential the expansion will be in $\kappa$ which controls the quark mass and at the Roberge-Weiss value of imaginary chemical potential it will be in $\beta$ which controls the temperature for reasons that will be explained further below. These properties are used in the following to find the critical and tricritical points in the $(m_{u,d}, m_s)$ diagrams at $\mu = 0$ and $\mu_{i,c} = \pi T/3$, respectively.

### 5.2.2 Strategy in the Heavy Quark Mass Region at $\mu = 0$

The study at $\mu = 0$ focuses solely on the heavy quark mass region. The Polyakov loop $\langle |P| \rangle$

$$\langle |P(n)| \rangle = \left\langle \left| \frac{1}{3} \mathrm{Tr}_C \left[ \prod_{n_0=0}^{N_\tau - 1} U_0(n_0, \mathbf{n}) \right] \right| \right\rangle , \tag{5.4}$$

is an order parameter for the deconfinement transition in the limit $m_{u,d}, m_s \to \infty$ (c.f. section 3.2.2) and thus gives the strongest signal when used as an observable to study the phase transitions in the heavy quark mass region by looking at its distribution as well as functions of it like $B_4$. The distribution of $|P|$ will change from a distinct two peak structure signalling a two phase coexistence in a region of first order transitions to a Gaussian-like shape in the crossover region if the quark mass is changed from large to intermediate while the system is kept critical, see fig. 5.3 left.

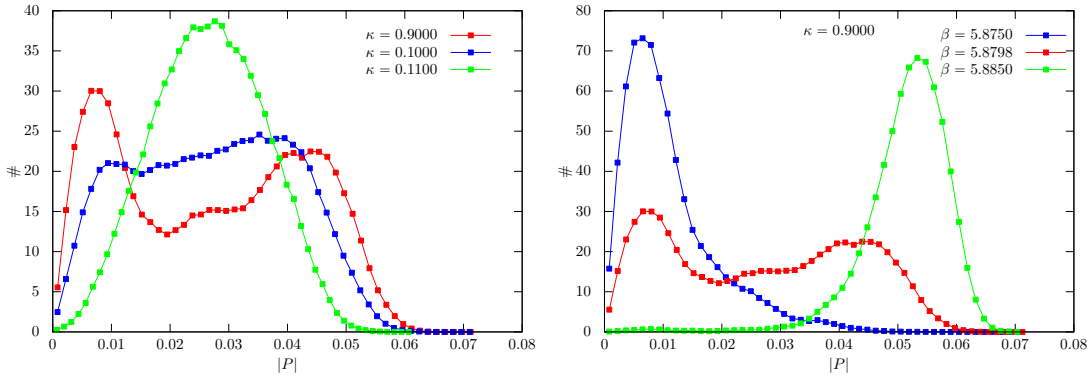


Figure 5.3: Plots created from HMC simulations of $N_f = 2$ QCD on $N_\tau = 6, N_\mathrm{s} = 42$ lattices and three values of $\kappa$. L.h.s - The distribution of $|P|$ at the pseudo-critical coupling $\beta_\mathrm{c}$ as a function of $\kappa$: The two peaks expected for a transition that for $V \to \infty$ becomes first order merge and end up as one Gaussian-like peak as the crossover region is entered. R.h.s - The distribution of $|P|$ at $\kappa = 0.0900$ as a function of $\beta$. The system goes from a confined state ($\beta = 5.8750$) over into a deconfined state ($\beta = 5.8850$). At $\beta = 5.8798$ the system is at the transition between the two states. Note that the red curves in both pictures are the same.

The pseudo-critical coupling $\beta_\mathrm{c}$ at which the system undergoes the deconfinement transition can be identified by the vanishing of the Skewness $B_3$

$$B_3(\beta_\mathrm{c}) = \frac{\left\langle (\delta |P|)^3 \right\rangle}{\left\langle (\delta |P|)^2 \right\rangle^{\frac{3}{2}}} = 0, \tag{5.5}$$

i.e. the third standardized moment that was discussed in section 3.1.1. In practice, in order to find $\beta_\mathrm{c}$ for a given value of the quark mass $m_{u,d}$ or value of $\kappa$, respectively, several simulations are performed at a series of values of the coupling $\beta_1, \cdots, \beta_n$ for each of which $B_3(\beta_i)$ is evaluated. This procedure is carried out until a crossing of the zero of $B_3(\beta_i)$ can be observed. To pin down $\beta_\mathrm{c}$ the data points $B_3(\beta_i)$ are densely interpolated using multiple histogram reweighting, which I discuss in section 4.1.2. Then $\beta_\mathrm{c}$ is extracted by determining the $B_3(\beta_i)$ value closest to zero.

The procedure is illustrated in fig. 5.4, which shows how, as $\beta$ is tuned, the system undergoes a phase transition from a confined state at lower values of $\beta$ (lower temperature) into a deconfined state (larger temperature), which is reflected by the distribution of $|P|$. The curve of the skewness $B_3$ precisely reflects the behavior of the distribution of $|P|$ shown in fig. 5.3 (right): $B_3 > 0$ in the confined state where the

distribution is skewed to the left ($\beta = 5.8750$) and $B_3 < 0$ in the deconfined state where the distribution is skewed to the right ($\beta = 5.8850$). For $B_3 = 0$ at $\beta_c = 5.8798$ the distribution is two-peaked.

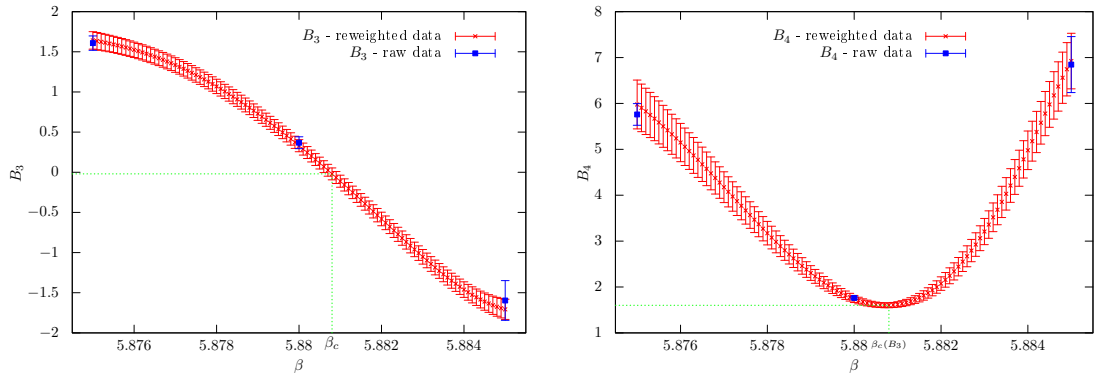


Figure 5.4: L.h.s: $B_3$ data. R.h.s.: $B_4$ data. Both obtained from simulation at $N_f = 2, N_\tau = 6, \kappa = 0.9, N_\mathrm{s} = 36$. The blue data points represent the real data while the red points represent the interpolated data by multi-histogram reweighting.

$B_4\,(\beta_i)$ is evaluated according to eq. (5.3) and gets interpolated by multiple histogram reweighting, as shown in fig. 5.4 (right). From the interpolated curve $B_4$ is extracted at $\beta_c$ obtained from $B_3(\beta_c) = 0$. At this point $B_4$ is expected to assume its minimum. Close to a first order transition and provided that the volume is sufficiently large this happens according to

$$B_4(\beta_\mathrm{c}) = -2 + \frac{c}{N_\mathrm{s}^d} + \mathcal{O}\left(\frac{1}{N_\mathrm{s}^{2d}}\right), \tag{5.6}$$

where $c$ is a constant and $d$ is the dimension of the system [194]. For each simulated value of $\kappa$ the described procedure is repeated on different volumes. The $B_4(\beta_\mathrm{c})$ data points obtained in this way are then plotted against $\kappa$ for each spatial lattice extent $N_\mathrm{s}$. As an analytic function on finite volumes $B_4$ can be expanded as a series in the scaling variable $x = (\kappa - \kappa_{Z_2})N_\mathrm{s}^{1/\nu}$ (it scales with $N_\mathrm{s}$ to the power of $1/\nu$) around $x = 0$, i.e. $\kappa = \kappa_{Z_2}$,

$$B_4(\beta_\mathrm{c}, \kappa, N_\mathrm{s})_{(\mu=0)} = B_4(\beta_\mathrm{c}, \kappa_{Z_2}, \infty)_{(\mu=0)} + a_1 x + a_3 x^3 + \cdots, \tag{5.7}$$

which can then be fitted to the $B_4(\beta_\mathrm{c})$ data points, as shown in fig. 5.5. Actual examples will be shown later on in the results sections 5.3 and 5.4.

A similar expression was derived in section 3.1.3 where the scaling variable $x = a_1 \tau N_\mathrm{s}^{1/\nu}$ was defined in terms of the reduced temperature $\tau$. However the above expansion can be reasoned in a similar way. Following the discussion in 3.1.1 to 3.1.3 and keeping in mind that near a critical point the correlation length diverges like $\xi \sim r^{-\nu}$, with $r$ being the distance to this point in the respective parameter space, it can be argued that $B_4$ is a function of the dimensionless ratio $(L/\xi)^{1/\nu}$. Since $\beta$ is kept at its critical value $\beta_\mathrm{c}$ and $\mu$ is fixed to $\mu = 0$, the distance to the critical point is given by $r = \kappa - \kappa_{Z_2}$ and thus $B_4$ is solely a function of the scaling variable $x = (\kappa - \kappa_{Z_2})L^{1/\nu}$, yielding the expansion written above. The QCD second order deconfinement transition point belongs to the $Z_2$ universality class for which $B_4(\beta_\mathrm{c}, \kappa_{Z_2}, \infty) = 1.604$, which can be fixed in the expansion for the fit. The critical exponent $\nu$ is known for this universality class, as well and can be fixed to $\nu = 0.6301$. Thus the parameters to be fitted are the slope of the curve $a_1$ (and $a_3$ if required) and the kappa value $\kappa_{Z_2}$ which represents the intersection point

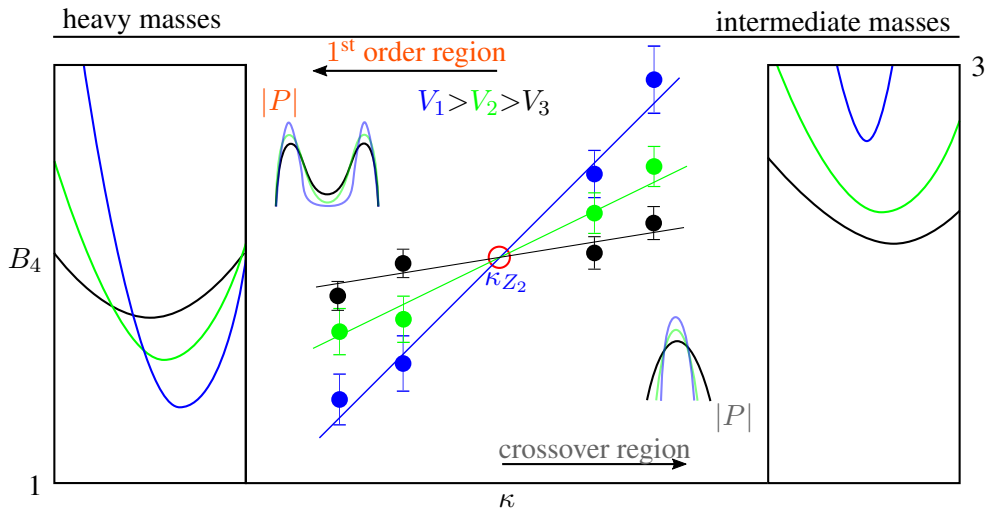


Figure 5.5: The figure schematically illustrates a finite size scaling analysis (FSS) of $B_4(\beta_c(\kappa), V)$ which is plotted against $\kappa$ for a series of increasing volumes $V_1 > V_2 > V_3$. The $B_4$ data is fitted by eq. (5.7), from which the intersection point $\kappa_{Z_2}$ is obtained. On each side (heavy and intermediate) the $B_4$ data approaches the values (one and three) characteristic for the respective transition ($1^{\text{st}}$ order and crossover). The left and the right panel of the diagram schematically show curves of $B_4(\beta)$ at a given value of $\kappa$ (c.f. r.h.s. of fig. 5.4) and how they get narrower as the volume increases. Moreover, a shift to smaller $B_4$ values and larger $\beta$ can be observed in the $1^{\text{st}}$ order region, whereas the opposite is the case in the crossover region. The figure also indicates how the shape of the distribution of $|P|$ is expected to look like in the different regions.

of the curves, i.e. the $Z_2$ point between the crossover and the first order transition region. Since eq. (5.7) is an expansion, fitting it to data certain criteria should be respected.

The fits done in this work were performed using a sophisticated procedure which takes into account that the fit should be symmetric with respect to the fitted $Z_2$ point. Moreover, the ranges in which the data belonging to different $N_s$ are fitted should be equal, i.e. they should overlap maximally. Of course in practice, depending on the quality and the ranges of the available data, this rarely can be fully respected. However, for the fits performed in the present work attention was paid to these criteria and they were respected as much as possible. The procedure is explained in detail in section 4.1.3.

The $B_4$ finite size scaling analysis can be complemented by studying the scaling of the susceptibility of $\chi(|P|)$. Plotting $\chi(|P|)/N_s^{\gamma/\nu}$ against $((\beta - \beta_c)/\beta_c)N_s^{1/\nu}$ and testing if the curves of different $N_s$ coincide for first or second order critical exponents can help to discriminate between different scenarios. A discussion is provided in section 3.1.3. Examples will be shown in sections 5.3 and 5.4.

The whole procedure described above is carried out at a fixed value of $N_\tau$, i.e. at a range of finite values of the lattice spacing $a$ which (assuming the system is kept critical, i.e. at $\beta_c(\kappa)$) changes as a function of $\kappa$ [1] . To find the continuum value of $\kappa_{Z_2}$, i.e. for $a \to 0$, the procedure has to be repeated on a series of lattices with an increasing temporal extent $N_\tau$ as explained in section 3.5.1. Once $\kappa_{Z_2}(N_\tau)$ has been extracted for several values of $N_\tau$ it can be extrapolated to vanishing lattice spacing $a \to 0$. Such a project is usually carried out over long terms (order of years) and has huge computational demands. Of course, the same is true for this work for which reason it represents only a part of our groups project,

[1] Note, since for a given $N_\tau$ the lattice spacing $a$ barely changes in a small region around $\kappa_{Z_2}$, often people familiar to such studies roughly use $N_\tau$ and $a$ synonymously. For instance, by saying *simulating at three different lattice spacings* $a$ what is really meant is *simulating at three different* $N_\tau$.

aiming at a continuum extrapolation.

### 5.2.3 Strategy at Imaginary Chemical Potential $\mu_{i,c}$ (Roberge-Weiss plane)

For the next project at imaginary chemical potential also the chiral transitions were studied for which, as an order parameter for chiral symmetry breaking, the observable of choice is naturally the chiral condensate

$$O = \bar{\psi}\psi = N_f \mathrm{Tr} D^{-1}. \tag{5.8}$$

In the previous section $B_4$ was Taylor-expanded around the point $\kappa_{Z_2}$ making it solely a function of the scaling variable $x = (\kappa - \kappa_{Z_2}) N_\mathrm{s}^{1/\nu}$. Then, while $\beta$ was kept at its critical value via $B_3(\beta_\mathrm{c}) = 0$, $B_4(\beta_\mathrm{c}, \kappa, N_\mathrm{s})$ was evaluated along the arrow symbol in fig. 5.1(left) in the $(m_{u,d}, m_s)$-plane.

For the study of the $N_f = 2$ chiral and deconfinement region of the Roberge-Weiss plane (see arrow symbols in fig. 5.1(right)) a somewhat different strategy has to be pursued. For the reader unfamiliar with the phase structure of the Roberge-Weiss plane it could be instructive to read the sections 3.3.4 and 3.5.3 beforehand.

The phase structure at $\mu_{i,c} = \pi T/3$ is slightly more complex as it represents the boundary between two $Z_3$ center sectors (c.f. fig. 3.2 and 3.9). This means that the coupling $\beta$ is pseudo-critical everywhere at $\mu_{i,c}$ and thus $B_3(\beta) = 0$ is expected for all $\beta$, irrespective of the value of $\kappa$. Consequently the $\beta$ value at which the system undergoes the chiral/deconfinement transition has to be found in a different way.

Tuning $\beta$ for a given $\kappa$ value interpolates between the crossover (low $\beta$) and the first order transition (high $\beta$) between the $Z_3$ sectors (c.f. fig. 5.6 (middle panel)). In-between at some value of $\beta$, denoted in the following as $\beta_\mathrm{c,E}$, the endpoint of the first order transition is found at which the chiral/deconfinement transition joins the $Z_3$ transition and whose nature depends on $N_f$ and the quark masses. It is exactly the nature of this endpoint we are interested in, which is schematically plotted in fig. 5.1(right) for each point $(m_{u,d}, m_s)$. In the thermodynamic limit an evaluation of $B_4$ along the phase boundary between the $Z_3$ sectors, as shown in fig. 5.6, yields $B_4 = 3$ in the crossover region, $B_4 = 1$ on the first order line and at the endpoint the kurtosis assumes the value $B_4 = 1.5$ for a triple point, $B_4 = 2$ for a tricritical point and $B_4 = 1.604$ at a $Z_2$ point. Of course in finite volumes the transitions are analytic everywhere and this step function behavior is smoothed out again. Hence, analogously to the case of $\mu = 0$ the nature of the endpoint can be extracted from a finite size scaling analysis of $B_4$ by Taylor-expanding it around the endpoint $\beta_\mathrm{c,E}$ of the transition between the $Z_3$ sectors,

$$B_4(\beta_\mathrm{c}, \kappa, N_\mathrm{s})_{(\mu_{i,c})} = B_4(\beta_\mathrm{c,E}, \kappa, \infty)_{(\mu_{i,c})} + a_1(\beta - \beta_\mathrm{c,E}) N_\mathrm{s}^{1/\nu} + \cdots , \tag{5.9}$$

making $B_4$ solely a function of the scaling variable $x = (\beta - \beta_\mathrm{c,E}) N_\mathrm{s}^{1/\nu}$ while the hopping parameter $\kappa$ and thus the quark mass is held fixed. The reasoning for this expansion has been given in the previous section as well as in section 3.1.3. The $B_4$ curves of different volumes labeled by $N_\mathrm{s}$ intersect at $\beta_\mathrm{c,E}$ which is extracted as a fit parameter. Note that in practice only a couple of measurements of $B_4$ along the phase boundary are performed. Since $B_4$ is expanded in $\beta$ these measurements can be interpolated with multi-histogram reweighting as it was done in the previous section.

Consider that, compared to the $\mu = 0$ study, here the fit parameter $B_4(\beta_\mathrm{c,E}, \kappa, \infty)_{\mu_{i,c}}$ is not known a priori since it assumes different values depending on the nature of the $Z_3$ endpoint. Together with the value of the critical exponent $\nu$, the value of $B_4(\beta_\mathrm{c,E}, \kappa, \infty)_{\mu_{i,c}}$ represents the most important piece of information to be extracted from the fit needed to determine the nature of the phase transition at the

respective point in the quark mass phase diagram.The critical exponent $\nu$ yields an equivalent information for the determination of the order of a transition (c.f. table 3.1) because it assumes specific values depending on the nature of the endpoint, as well. The extraction of $B_4(\beta_{\mathrm{c,E}}, \kappa, \infty)_{\mu_{i,c}}$ by a fit turns out to be difficult since it is very prone to finite volume effects, which will be discussed later on in sections 5.3 and 5.4. The critical exponent $\nu$ is less affected by finite volume effects and thus in practice one rather focuses on the value of $\nu$.

The fitted value of $\nu$ should be checked for consistency by using scaling relations of functions of the order parameter. An example related to the scaling relations, that was discussed in the previous section and in section 3.1.3, are *collapse plots* of the susceptibility $\chi$. The same is possible for the expansion of $B_4$ that can be plotted against its scaling variable $x = (\beta - \beta_{\mathrm{c,E}})N^{1/\nu}$, leading to the collapse of different curves corresponding to different $N_{\mathrm{s}}$ if the correct value of $\nu$ is inserted. Examples of these so-called *collapse plots* will be shown later on in the results section. However, this is just a consistency check and not to be considered as a way to obtain a definite answer since there are certain caveats about this technique that will become apparent during the presentation of the results.

Another important quantity to look at is the distribution of the imaginary part of the Polyakov loop since, due to its phase separating between different $Z_3$ sectors, it can be used as an order parameter for the deconfinement transition at $\mu_{i,c} = \pi T/3$ (c.f. section 3.3.4). Thus it is the natural choice to be used for the evaluation of $B_4$ according to eq. (5.3) (setting $O = \mathrm{Im}P$) in the heavy quark mass region. For heavy and light masses it develops a three peak structure at the $Z_3$ endpoint $\beta_{\mathrm{c,E}}$ (c.f. fig. 5.6) which in this case would be a first order triple point. This three peak structure becomes more distinct the stronger the first order transition is. Note that the imaginary part of $L$ is symmetric with respect to zero, i.e. $\langle \mathrm{Im}P \rangle = 0$, which is an important information to be used in the evaluation of functions of the fluctuations.

Once the critical exponent $\nu$ is extracted from a fit of eq. (5.9) to the actual $B_4$ data for each simulated value of $\kappa$, it can be plotted against $\kappa$. In the thermodynamic limit $V \to \infty$ a picture like fig. 5.7 would be expected. On finite volumes this step function behavior is smeared out again. An actual example will be shown later in the results section 5.4.1.

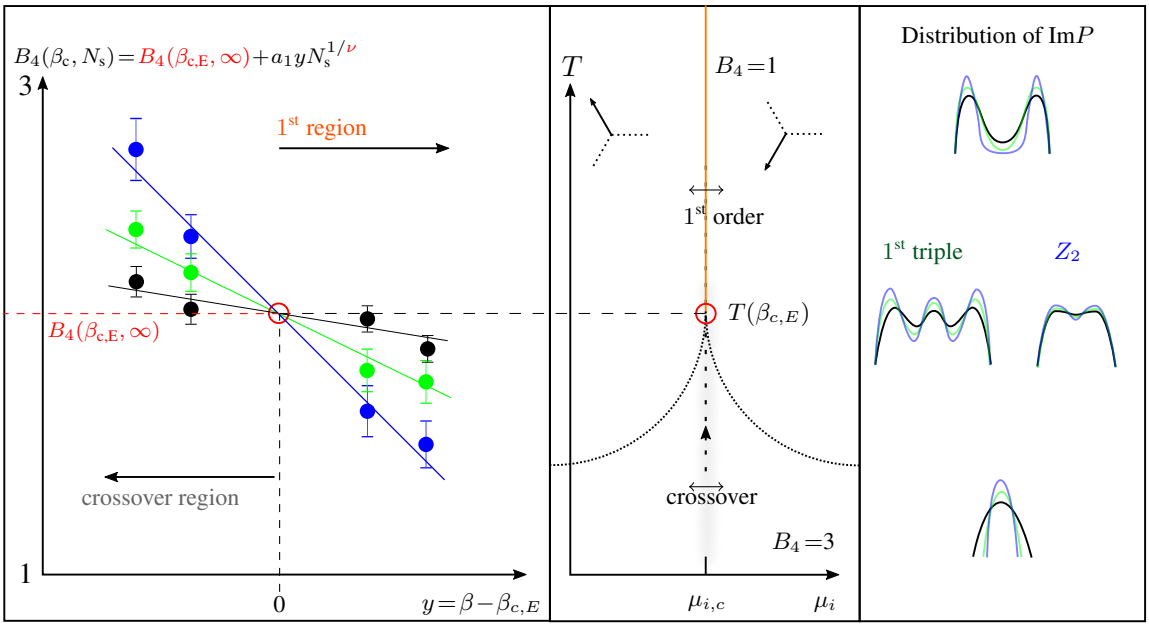


Figure 5.6: The figure sketches the method for the extraction of $B_4$ and $\nu$ by a finite size scaling analysis. The middle panel shows the transition at $\mu_{i,c}$ between the $Z_3$ center sectors in the $(T, \mu_i)$-diagram with its endpoint marked by the red circle and $T(\beta_{c,E})$. The chiral/deconfinement transition (dotted lines) joins the $Z_3$ transition in its endpoint whose nature depends on the quark mass or $\kappa$ respectively. $B_4$ is evaluated along the vertical dashed line, i.e. along the phase boundary between the $Z_3$ sectors for a series of increasing volumes $V > V > V$. Subsequently in a finite size scaling analysis, shown in the left panel, the $B_4$ data is fitted according to eq. (5.9) (or top of left panel). From the fit $B_4(\beta_{c,E}, \infty)$ and $\nu$ are extracted whose values indicate the nature of the endpoint. The expected shapes of distributions of Im$P$ are depicted in the right panel: If the chiral/deconf. transition is 1st order (heavy/light quarks), the endpoint will be 1st order triple and the respective distribution will show three peaks at $\beta_{c,E}$. If the chiral/deconf. transition is a crossover (intermediate quark masses), the distribution will show a slight two peak structure at $\beta_{c,E}$.

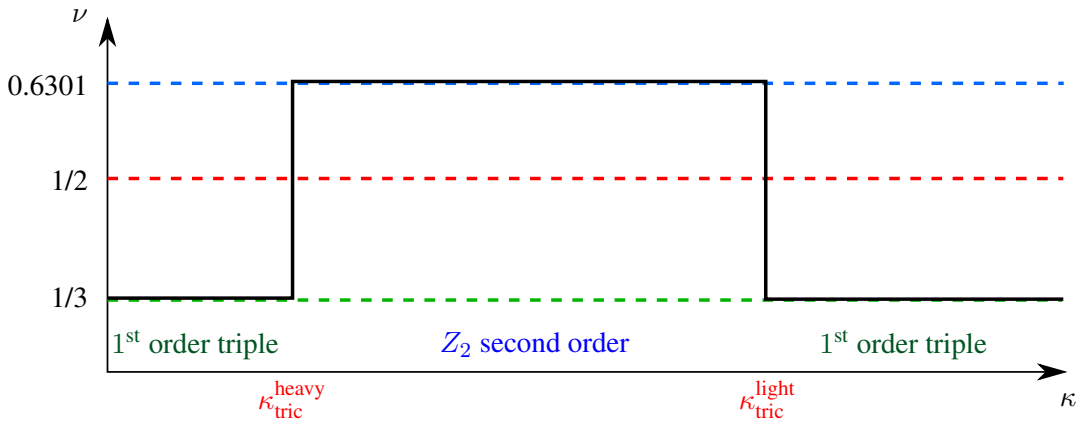


Figure 5.7: The figure shows a schematic $(\nu, \kappa)$-diagram as it is expected for $V \to \infty$. For quark masses corresponding to values of $\kappa < \kappa^{\text{heavy}}_{\text{tric}}$ (heavy) or $\kappa > \kappa^{\text{light}}_{\text{tric}}$ (light) the critical exponent $\nu$ is expected to assume the value $1/3$ characteristic to 1st order triple transitions, while for intermediate values of $\kappa^{\text{heavy}}_{\text{tric}} < \kappa < \kappa^{\text{light}}_{\text{tric}}$ it assumes $0.6301$ corresponding to $Z_2$ second order transitions. The change from 1st order triple to $Z_2$ is marked by tricritical points for which $\nu = 1/2$.

## 5.3 Simulations at Zero Chemical Potential

At chemical potential $\mu = 0$ the temporal lattice extents $N_\tau = 6, 8$ and 10 with $N_f = 2$ flavors and $N_\tau = 4$ with $N_f = 3$ flavors respectively, were simulated. For each $N_\tau$ a scan for the critical $\kappa_{Z_2}$ at the $Z_2$ point is performed in the heavy quark mass region (c.f. fig. 5.1) in a range of $\kappa$ values listed in table 5.1. To carry out a finite size scaling analysis, for each $\kappa$ value 3 to 4 spatial lattice extents $N_\mathrm{s}$ have been simulated corresponding to aspect ratios 3 to 7. The scans in temperature to locate the pseudo-critical coupling typically involved simulations at 2-3 different values of $\beta$ each with 450k to 1.15M HMC steps at $N_\tau = 6$, 330k to 1.1M HMC steps at $N_\tau = 8$, about 200k HMC steps at $N_\tau = 10$ for $N_f = 2$ and 1.2M to 3.2M HMC steps at $N_\tau = 4$ for $N_f = 3$, all of unit length and with a thermalization range of 5k trajectories in advance. Further details are listed in tables A.1, A.3, A.5 and A.8.

To accumulate statistics faster and to have a better control on the statistical errors the same parameter set was simulated on four different Markov chains per $\beta$. This helped with making the decision about when the gathered statistics were enough, for which the strategy was to run the replica until $B_3$ is compatible within at least three standard deviations between all of them. This analysis has been discussed in section 4.1.1 and an example for $B_3$ is shown in fig. 4.1. For all runs the configuration acceptance rate was held between 75% and 85% for each Markov chain.

Scale-setting was done using the Wilson flow parameter $\omega_0/a$, determined and converted to physical scales using the publicly available software described in [79]. To this purpose for each $\kappa$ about 400 (approximately) zero temperature configurations have been produced at or close to the value of the critical coupling $\beta_\mathrm{c}$ on $16^3 \times 32$ ($N_\mathrm{s}^3 \times N_\tau$) lattices. In order to provide a physical quantity for the identification of the determined critical point (identified by $\kappa_{Z_2}$) the pseudo scalar meson mass $m_\mathrm{PS}$ has been computed on the same configurations using an implementation for the computation of pseudo scalar masses which is part of the CL$^2$QCD code. A detailed description about the implementation is provided in [195]. The findings for the lattice spacings $a$, the pseudo scalar mass $m_\mathrm{PS}$ and the critical temperature $T_\mathrm{c}$ are summarized in table 5.1 for each value of $\kappa$ and $N_\tau$. Note, that $m_\mathrm{PS}$ has not been computed for the $N_f = 3$ flavor theory due to temporal and computational limitations.

The approach to locate $\kappa_{Z_2}$ has been discussed in detail in section 5.2.2. The method of the finite size scaling analysis, that consists in taylor-expanding $B_4$ (eq. (5.7)) in the scaling variable $x = (\kappa - \kappa_{Z_2}) N_\mathrm{s}^{1/\nu}$ and fitting it to the data points $B_4(\beta_\mathrm{c}, \kappa_{Z_2}, N_\mathrm{s})$, is based on the assumption that the system is close to the thermodynamic limit. If this requirement is not fulfilled, i.e. if the spatial lattice extents $N_\mathrm{s}$ are too small, the data will be affected by finite volume effects which manifest in too large values of the $B_4$ data, causing a shift and distortion of the intersection point of the $B_4$ curves. This has been observed in various studies already, for instance [159, 196], and poses a problem in this work, as well. Due to this, the data points cannot be fitted properly anymore by eq. (5.7) with the parameter $B_4(\beta_\mathrm{c}, \kappa_{Z_2}, \infty)$ fixed to its true value 1.604, resulting in a large value of $\chi^2_\mathrm{NDF}$. However, eq. (5.7) can be modified by a correction discussed in section section 3.1.3, which is adopted for this work. The modified equation reads

$$B_4(\beta_\mathrm{c}, \kappa, N_\mathrm{s})_{(\mu=0)} = \left(B_4(\beta_\mathrm{c}, \kappa_{Z_2}, \infty)_{(\mu=0)} + a_1 x + a_3 x^3\right) C(N_\mathrm{s}), \tag{5.10}$$

with $C(N_\mathrm{s}) = (1 + B N_\mathrm{s}^{1/\nu})$, where $B$ is a free parameter to be extracted from a fit. Including the term $C(N_\mathrm{s})$ will relax the situation as it corrects for a larger $B_4$ value by the volume dependent factor $B N_\mathrm{s}^{1/\nu}$ and renders eq. (5.7) volume dependent, even at $\kappa - \kappa_{Z_2} = 0$. Moreover the curves are no longer forced to intersect at a common point ($\kappa - \kappa_{Z_2} = 0, B_4(\beta_\mathrm{c}, \kappa_{Z_2}, \infty) = 1.604$) anymore. Furthermore, after

having extracted the parameter $B$ from the fit, the finite volume effects on the data can be quantified as a function of $N_\mathrm{s}$ by evaluating $BN_\mathrm{s}^{1/\nu}$.

Alternatively, instead of using this correction term, the critical exponents $B_4$ and $\nu$ could simply be left free parameters of the fit. On the one hand-side allowing deviations from their true values would then correct for the finite volume effects but on the other hand-side important information about universality will be contaminated and there is no guarantee that this leads to a proper extraction of $\kappa_{Z_2}$ because the $B_4$ curves will still be forced to intersect at a common point. In contrast, including the correction term $C(N_\mathrm{s})$ offers a systematic and theoretically motivated approach to include finite volume corrections in the fit.

In our numerical evaluation of the data we estimate the autocorrelation time of the observables using a Python implementation of the $\Gamma$-method [162]. Afterwards the data is summarized in bins of size $2\tau_\mathrm{int}$ to remove the autocorrelation in functions of the observables, c.f. section 4.1.1.

Before I continue with the finite size scaling analysis of $B_4$, the following remarks about the computed pseudo scalar meson masses (see table 5.1) shall be added: Note, that the values for $N_\tau = 6$ are between $\sim 2.2$ to $\sim 3.5$ in lattice units, i.e. much larger than one and thus large discretization errors are expected. For this reason the corresponding physical values in the sixth column of table 5.1 have to be taken with great care. A reduction of the discretization errors on $m_{\mathrm{PS},Z_2}$ by increasing $N_\tau$ (i.e. decreasing $a$) is associated with a shift of $\kappa_{Z_2}$ to smaller masses (c.f. section 3.5.1). Consequently if $N_\tau$ is increased the problem is reduced as shown in the table for $N_\tau = 8$ and 10 lattices. Aside from reducing $N_\tau$ there are not many things that can be done about this problem. A possible way to get an idea about the severeness of the discretization effects is to analyze the kinetic mass [197] by an expansion of the dispersion relation in the momentum variable $p$. An example for such an analysis can be found in [198]. Here, however, I do not try to quantify the discretization errors due to temporal constraints of the project and instead just use the computed masses to identify the $Z_2$ points keeping in mind the caveat about the possibly large discretization errors.

| $N_f \mid N_\tau$ | $\kappa$ | $\beta_c$ | $am_{\mathrm{PS}}$ | $a$[fm] | $m_{\mathrm{PS}}$[MeV] | $T$[MeV] |
|---|---|---|---|---|---|---|
| $2 \mid 6$ | 0.0750 | 5.8888 | 3.4709(3) | 0.1175(6) | 5910(30) | 284(1) |
| | 0.0850 | 5.8841 | 3.1081(3) | 0.1180(8) | 5270(40) | 282(2) |
| | 0.0900 | 5.8798 | 2.9309(3) | 0.1199(5) | 4890(20) | 278(1) |
| | 0.1000 | 5.8674 | 2.5823(4) | 0.1195(7) | 4320(30) | 279(2) |
| | 0.1100 | 5.8462 | 2.2411(3) | 0.1232(5) | 3638(15) | 271(1) |
| $2 \mid 8$ | 0.1100 | 6.0306 | 2.1310(6) | 0.0882(4) | 4830(20) | 283(1) |
| | 0.1150 | 6.0186 | 1.9490(3) | 0.0886(3) | 4400(15) | 282(1) |
| | 0.1200 | 6.0012 | 1.7673(3) | 0.0892(4) | 3963(18) | 280(1) |
| | 0.1250 | 5.9777 | 1.5866(3) | 0.0908(3) | 3495(12) | 275(1) |
| | 0.1300 | 5.9461 | 1.4073(4) | 0.0922(7) | 3050(20) | 271(2) |
| | 0.1350 | 5.9026 | 1.2325(4) | 0.0960(8) | 2570(20) | 260(2) |
| $2 \mid 10$ | 0.1150 | 6.1685 | 1.8734(3) | 0.0690(10) | 5430(80) | 290(4) |
| | 0.1200 | 6.1499 | 1.6838(3) | 0.0697(10) | 4830(70) | 287(4) |
| | 0.1250 | 6.1368 | 1.4871(3) | 0.0697(12) | 4270(70) | 287(5) |
| | 0.1300 | 6.1071 | 1.2943(4) | 0.0696(8) | 3720(40) | 287(3) |
| | 0.1350 | 6.0648 | 1.1031(5) | 0.0722(14) | 3060(60) | 277(5) |
| | 0.1400 | 5.9899 | 0.9284(5) | 0.0762(11) | 2440(40) | 262(4) |
| $3 \mid 4$ | 0.0495 | 5.6871 | – | 0.1857(4) | – | 269(1) |
| | 0.0520 | 5.6856 | – | 0.1861(5) | – | 269(1) |
| | 0.0545 | 5.6844 | – | 0.1867(5) | – | 268(1) |
| | 0.0570 | 5.6827 | – | 0.1873(4) | – | 267(1) |
| | 0.0580 | 5.6820 | – | 0.1876(5) | – | 267(1) |
| | 0.0595 | 5.6808 | – | 0.1875(6) | – | 267(1) |
| | 0.0620 | 5.6787 | – | 0.1888(3) | – | 265(0) |
| | 0.0650 | 5.6758 | – | – | – | – |

Table 5.1: The table lists for each $N_\tau$ the simulated values of $\kappa$ including the extracted values of $\beta_{\mathrm{c}}$, $am_{\mathrm{PS}}$, $a$, $m_{\mathrm{PS}}$ and $T_{\mathrm{c}}$. Further details about the spatial edge lengths $L$ of the simulated lattices as well as about the accumulated statistics can be found in tables A.1 to A.8.

### 5.3.1 $N_f = 2, N_\tau = 6$

The fits of eq. (5.7) are performed using a procedure in which the fits get repeated with many different fit ranges $\kappa$ per $N_s$. Subsequently the fit results are filtered for the largest minimal symmetry $\Xi_{\text{min}}$ (minimal regarding the comparison between the data ranges of the different $N_s$) of the fitting range around the extracted value of $\kappa_{Z_2}$ and/or the largest minimal overlap $\Omega_{\text{min}}$ between the included data ranges corresponding to the different $N_s$. The method is explained in detail in section 4.1.3, where definitions of $\Xi_{\text{min}}$ and $\Omega_{\text{min}}$ are given, as well.

| Fit | $N_s$ | $\kappa_{Z_2}$ | $a_1$ | $a_3$ | $B$ | $\chi^2_{\text{NDF}}$ | NDF | $Q[\%]$ | $\Omega_{\text{min}}$ | $\Xi_{\text{min}}$ |
|---|---|---|---|---|---|---|---|---|---|---|
| **linear fits** | | | | | | | | | | |
| $l.1.1$ | 30,36,42 | 0.093(3) | 0.084(15) | – | 1.7(1.2) | 1.38 | 4 | 24 | 74 | 29 |
| $l.1.2$ | 30,36,42 | 0.0885(12) | 0.097(11) | – | – | 1.72 | 5 | 13 | 80 | 0 |
| $l.2$ | 30,36,42 | 0.091(4) | 0.065(12) | – | 1.2(1.0) | 0.87 | 4 | 48.21 | 67 | 16 |
| **linear + cubic fits** | | | | | | | | | | |
| $c.1.1$ | 30,36,42 | 0.0939(14) | 0.02(4) | 0.017(18) | 1.7(6) | 1.00 | 2 | 37 | 74 | 78 |
| $c.1.2$ | 30,36,42 | 0.087(3) | 0.07(4) | 0.000(1) | – | 1.57 | 3 | 19 | 57 | 0 |
| $c.2$ | 30,36,42 | 0.0912(18) | 0.03 0.02 | 0.0037(19) | 1.7(1.2) | 1.47 | 6 | 18.26 | 80 | 50 |

Table 5.2: Shown are the results of the fits of eq. (5.7) to $B_4$ data. The parameters $\Omega_{\text{min}}$ and $\Xi_{\text{min}}$ describe the minimal overlap observed between the data ranges belonging to different $N_s$ and the minimal symmetry of the fitting ranges with respect to $\kappa_{Z_2}$ among all data ranges of the different $N_s$, respectively. The fits are labeled by $x.y.z$ where $x = l(c)$ indicates linear (linear + cubic) fits. $y = 1, \ldots$ labels fits differing in the filter-criteria with respect to $(\chi^2_{\text{NDF}}, Q)$, $\Omega_{\text{min}}$ and $\Xi_{\text{min}}$. A colored field indicates the best fit with respect to the parameter of the respective column while two colored fields mean either the best compromise between both parameters, chosen to be $\max(0.8 < \Omega_{\text{min}}/\Xi_{\text{min}} < 1.2)$, or that both parameters were the maximum found. $y = 1$ always represents the optimal fit for which the choice always is the best compromise between $\Omega_{\text{min}}$ and $\Xi_{\text{min}}$ unless a fit is found for which there is a gain in one of the parameters beyond the best compromise. $y > 1$ are alternatives to check for the stability of the fit with respect to $\kappa_{Z_2}$. $z = 1(2)$ (if present) indicates use of same data ranges including (excluding) the correction term $C(N_s)$.

The best fits obtained from this procedure are listed in table 5.2. The numbering convention as well as the criteria used to choose the fits are explained the table caption. The fits considered optimal, labeled in the table by $x.1.z$, have been repeated under exclusion of the correction term (z=2) to see how the quality of the fit changes.

From the table it becomes apparent that at $N_\tau = 6$ the parameter $B$, despite exhibiting a large fit-error, is significant in all fits. Comparing fits $x.y.1(2)$ in which the correction term is included (excluded), $\chi^2_{\text{NDF}}$ as well as the goodness-of-fit value $Q$ are improved when the correction is included and the value of $\kappa_{Z_2}$ is slightly increased. What is more, in the absence of the correction term (see fits $l.1.2$ and $c.1.2$) the criterion for a good symmetry of the fitting ranges with respect to $\kappa_{Z_2}$ can not be fulfilled anymore and the symmetry decreases to zero. The reason can be understood from looking at fig. 5.8, where the fits $l.1.1(2)$ (left) and $c.1.1(2)$ (right) are shown: Without the correction term (z=2), the ordinate of the intersection point of the fitted lines is decreased and forced to be at $B_4(\beta_c, \kappa_{Z_2}, \infty) = 1.604$. As a consequence, its abscissa, given by $\kappa_{Z_2}$, is reduced as well, implying a shift of the intersection point and thus a decreased

symmetry with respect to the fitting range. The intersection point can be even shifted completely out of the fitting range, as it is shown in fig. 5.8. Throughout all fits including the correction term, the $\kappa_{Z_2}$ value is consistent. The value $\kappa_{Z_2}$ extracted from fit $c.1.1$ is quoted as the final result including the corresponding pseudoscalar meson mass,

$$\kappa_{Z_2}(N_\tau = 6) = 0.0939(14) \qquad m_{\mathrm{PS},Z_2}(N_\tau = 6) = 4670(180)\mathrm{MeV}. \tag{5.11}$$

As announced before, this result is qualitatively crosschecked by collapse plots of the susceptibilities

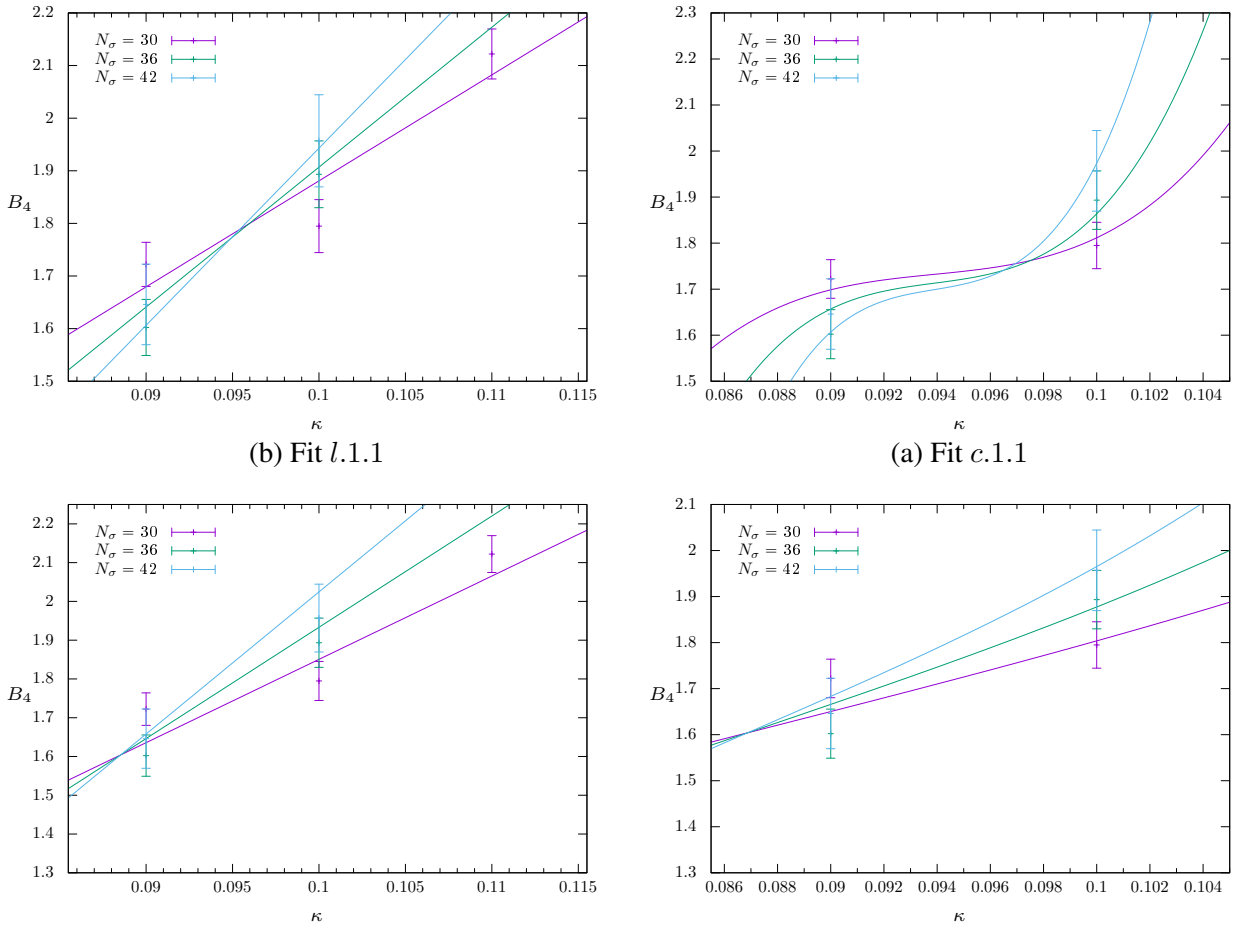


(b) Fit $l.1.1$ (a) Fit $c.1.1$

(c) Fit $l.1.2$ (d) Fit $c.1.2$

Figure 5.8: Linear (left) and cubic (right) fits of $B_4$ including (top) and excluding (bottom) the correction term given by eq. (5.10).

$\chi(|P|)$ which are shown in fig. 5.9 for three simulated values of the hopping parameter, $\kappa \in \{0.075, 0.09, 0.11\}$. For $\kappa = 0.0750$ $\chi(|P|)$ clearly collapses when scaled with first order exponents, confirming that in the thermodynamic limit the transitions in this region would be of first order. At $\kappa = 0.1100$ $\chi(|P|)$ is neither collapsing for inserting first order exponents nor for second order exponents, indicating a crossover transition. The value $\kappa = 0.0900$ is inbetween and quite close to the extracted value of $\kappa_{Z_2}$. Thus the collapse of $\chi(|P|)$ could show a tendency towards second order exponents. Though, the situation turns out to be somewhat ambiguous. Inserting first order exponents make the curves of lattice extents $N_\mathrm{s} = 30$ and 36 collapse while second order exponents cause the curves at $N_\mathrm{s} = 36$ and 42 to collapse. This conflict can probably resolved by noting that the correction parameter $B$ extracted from the fits (table 5.2) was not-vanishing and thus indicating that the data at these volumes still suffers from finite

volume effects. Though, $N_s = 42$ must be less affected by finite volume effects than $N_s = 30$ which suggests that the collapse under the second order exponent is more trustworthy. This is consistent with the result of $\kappa_{Z_2}$ obtained from the fit, which suggests that $\kappa = 0.0900$ is already very close to the $Z_2$ point. Let us now examine the available $B_4$ data to further study the finite volume effects. All

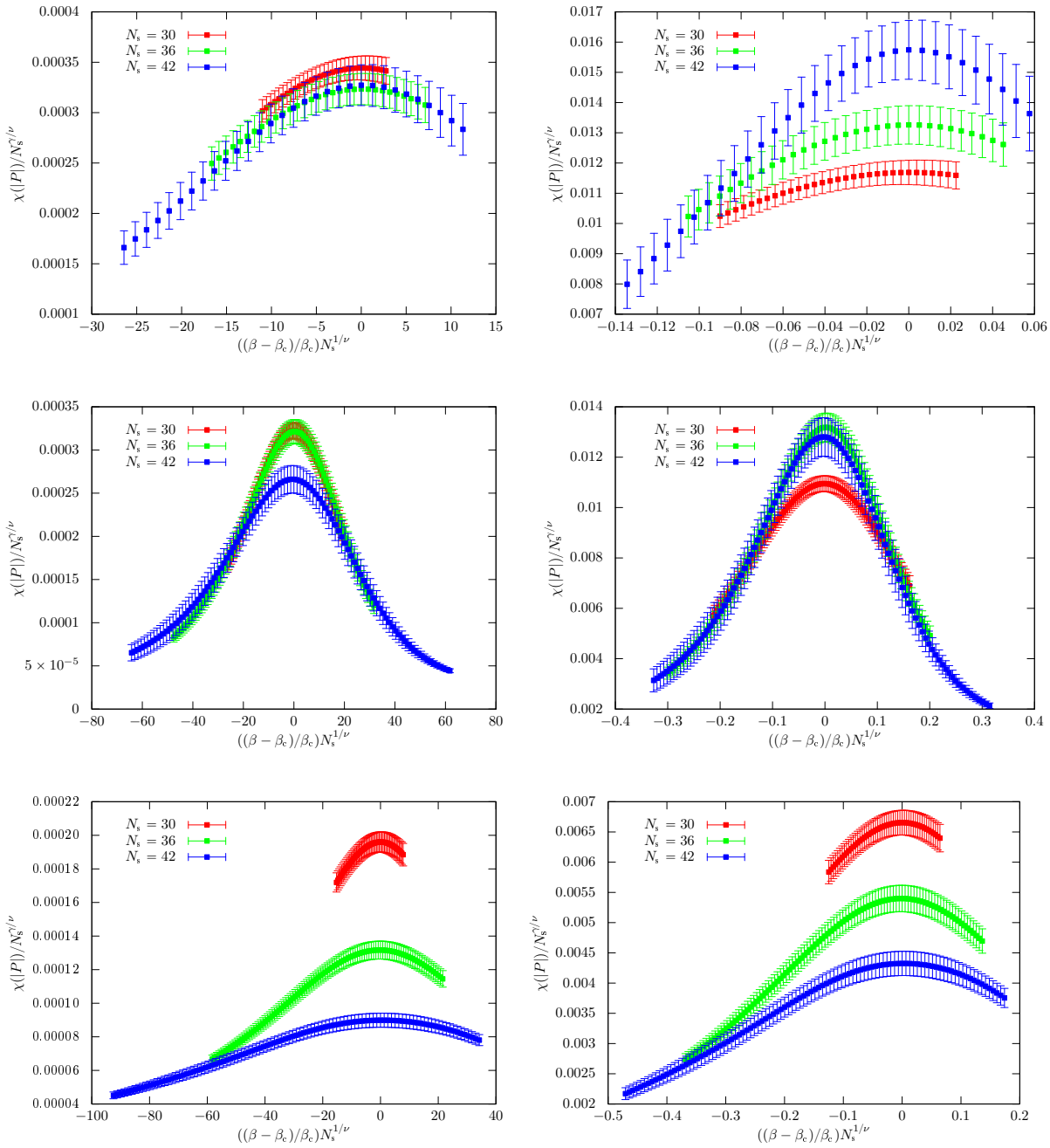


Figure 5.9: Collapse plots of $\chi(|P|)$ at $\kappa = 0.075$ (top), $\kappa = 0.09$ (middle) and $\kappa = 0.11$ (bottom) for first (left) and second order (right) critical exponents.

$B_4$ data available are shown in fig. 5.10, where the data belonging to different $N_s$ are plotted separately in fig. 5.10a to fig. 5.10c and all at once in fig. 5.10d. Normally, in the first order region for small $\kappa$ values $B_4$ is expected to approach its value characteristic for first order transitions, $B_4 = 1$. In these plots the $B_4$ data seem to reach a plateau for $\kappa < 0.1$ at significantly larger $B_4$ values than

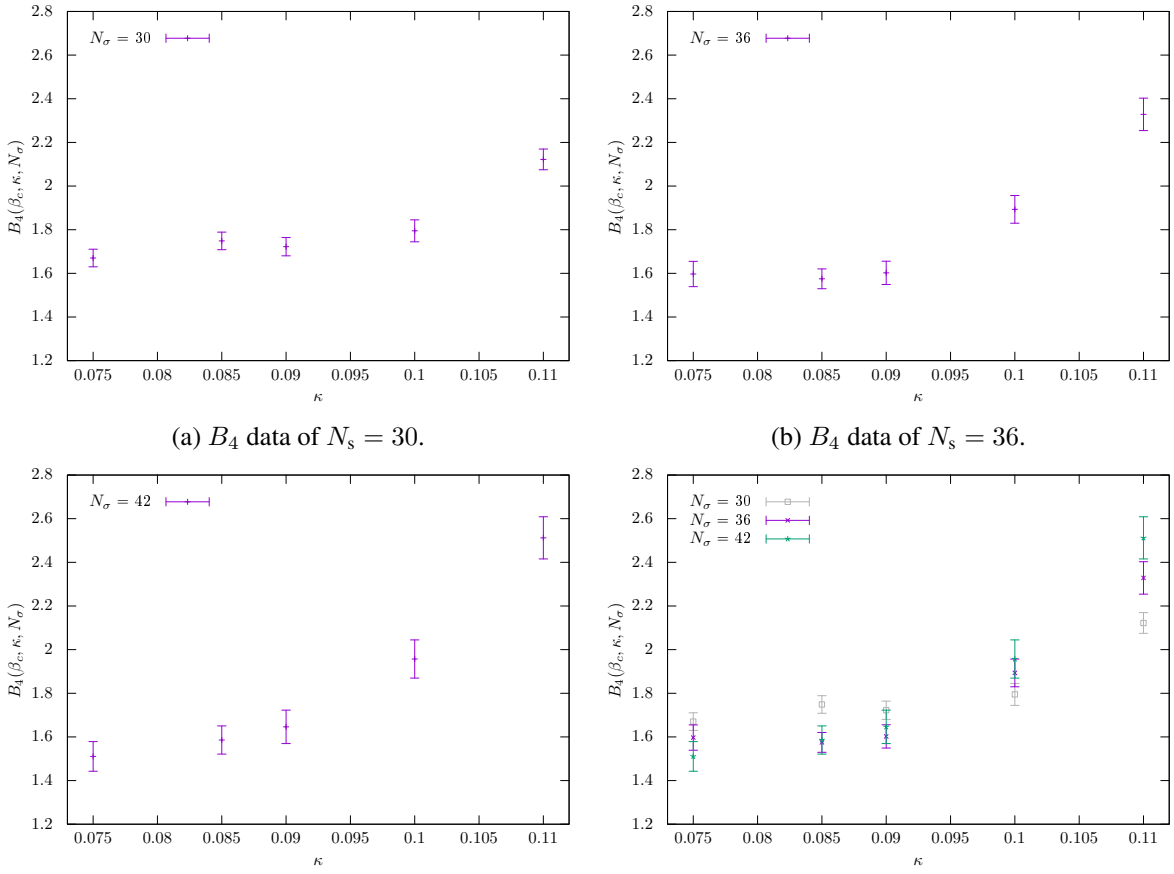


(a) $B_4$ data of $N_\mathrm{s} = 30$.

(b) $B_4$ data of $N_\mathrm{s} = 36$.

(c) $B_4$ data of $N_\mathrm{s} = 42$.

(d) Plot of $B_4$ of $N_\mathrm{s} = 30, 36, 42$.

Figure 5.10: $B_4$ data

the expected first order value. To check if $B_4$ does not decrease anymore even for very small values of $\kappa$, another simulation for $N_\mathrm{s} = 30$ was carried out at $\kappa = 0.03$ which has a considerable distance to the $\kappa$ values for which $B_4$ starts to approach the plateau. As expected, even for a very small value $\kappa = 0.03$ the kurtosis value remains $B_4 \approx 1.7$. The plateaus appear to decrease as $N_\mathrm{s}$ is increased, i.e. $B_4(\kappa \to 0, N_\mathrm{s} = 30) > B_4(\kappa \to 0, N_\mathrm{s} = 36) > B_4(\kappa \to 0, N_\mathrm{s} = 42)$. Moreover, the smaller $N_\mathrm{s}$ the larger the $\kappa$ value at which the plateau is approached, i.e. at $N_\mathrm{s} = 30$ it seems to be reached at $\kappa \lesssim 0.1$ while at $N_\mathrm{s} = 36$ this seems to happen at around $\kappa \lesssim 0.9$. The data of $N_\mathrm{s} = 42$ seems to approach the plateau at about $\kappa \lesssim 0.85$. From Intuition we would rather expect the opposite situation. The same observation can be made for $N_\tau = 8$, as it will be shown in the following, as well.

Altogether this implies that on small $N_\mathrm{s}$ the inflection point of the $B_4$ curve (which is the $Z_2$ point for $V \to \infty$) is not only shifted vertically but also horizontally to larger values of $\kappa$. In this case, a behavior of the $B_4$ curves as approximately illustrated by the schematic in fig. 5.11 (left) would be expected. This behavior is a systematic effect caused by too small volumes. A possible explanation is given in the following: The distribution $\mathcal{P}(|P|)$ of $|P|$ at $\beta_\mathrm{c}$ should show indications for the shifted first order values $B_4(\kappa \to 0, N_\mathrm{s})$. In fig. 5.11 (right) $\mathcal{P}(|P|)$ is plotted for all simulated values $\kappa$ at $N_\mathrm{s} = 30$. From looking at the distributions one can see that the minimum between the two peaks at smaller values of $\kappa < 0.1$ saturates and does not decrease anymore. This is an effect of the volumes being small which smoothens out the boundary between both phases. Then the tunneling between the phases is very frequent and the area between the two peaks is visited by the system many times. This causes the two Gaussian-like

distributions to have effectively more weight in their tails at the point where they merge. Since $B_4$ is a measure for the weights in the tails of a distribution, this causes a large value of $B_4$. Only if the two peaks are strongly separated can $B_4$ assume smaller values, which is the case for large volumes. In contrast such an effect plays no role in the crossover region where there is only one Gaussian-like distribution. Consequently there is no reason to assume that $B_4$ does not reach its crossover-value which is $B_4 = 3$. Having this in mind we remark that the correction eq. (5.10) we are using in the fits to the $B_4$ data has no $\kappa$ dependence and thus causes a total shift of $B_4$ everywhere.

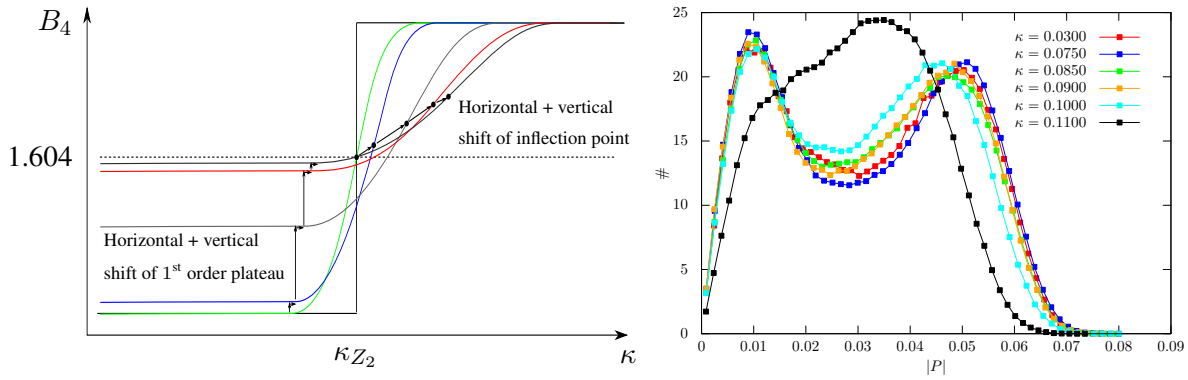


Figure 5.11: L.h.s: Schematically shows the behavior of $B_4$ at increasingly smaller volumes as observed from the data (c.f. fig. 5.10a to fig. 5.10a). The $1^{\text{st}}$ order plateau as well as the inflection point of the curves which coincides with the $Z_2$ point at $V \to \infty$ is shifted vertically and horizontally. R.h.s.: The distribution $\mathcal{P}(|P|)$ $N_\tau = 6, N_{\text{s}} = 30$ at $\beta_{\text{c}}$ for all simulated values of $\kappa$. Even at a very small value $\kappa = 0.03$ $\mathcal{P}(|P|)$ stays roughly the same.

### 5.3.2 $N_f = 2, N_\tau = 8$

As expected, for $N_\tau = 8$ a significant reduction in the lattice spacings $a$ relative to $N_\tau = 6$ can be observed, which have shifted from a range of a={0.1180(8),...,0.1232(5)} at $N_\tau = 6$ to a={0.0886(3),...,0.0960(8)} at $N_\tau = 8$ as well as in the lattice masses of the pseudo scalar meson which have shifted from a range of $am_{\mathrm{PS}} = \{2.2411(3), \ldots, 3.1081(3)\}$ at $N_\tau = 6$ to $am_{\mathrm{PS}} = \{1.2325(4), \ldots, 1.9490(3)\}$ at $N_\tau = 8$ (c.f. table 5.1). The the lattice masses are now much closer to $am_{\mathrm{PS}} = 1$

The fit results are listed in table 5.3 in the same fashion as for $N_\tau = 6$. The correction parameter $B$ extracted from the fits is considerably more significant compared to the fits at $N_\tau = 6$, indicating larger finite volume effects which are due to the smaller physical volumes $L^3$ simulated at $N_\tau = 8$ (c.f. tables A.2 to A.6). Even though larger spatial lattice extents $N_\mathrm{s}$ have been used ($N_\mathrm{s} = 32, 40, 48$ at $N_\tau = 8$ compared to $N_\mathrm{s} = 30, 36, 42$ at $N_\tau = 6$), the physical volumes are effectively decreased due to the smaller lattice spacings. The larger finite volume effects are confirmed by examining the $B_4$ data for

| Fit | $N_\mathrm{s}$ | $\kappa_{Z_2}$ | $a_1$ | $a_3$ | $B$ | $\chi^2_{\mathrm{NDF}}$ | NDF | $Q[\%]$ | $\Omega_{\mathrm{min}}$ | $\Xi_{\mathrm{min}}$ |
|---|---|---|---|---|---|---|---|---|---|---|
| **linear fits** | | | | | | | | | | |
| $l$.1.1 | 32,40,48 | 0.117(3) | 0.049(8) | – | 3.7(7) | 0.62 | 9 | 78 | 66 | 64 |
| $l$.1.2 | 32,40,48 | 0.1068(17) | 0.072(10) | – | – | 2.33 | 10 | 1 | 87 | 24 |
| $l$.2 | 32,40,48 | 0.117(4) | 0.050(12) | – | 3.6(9) | 0.88 | 6 | 51 | 53 | 67 |
| $l$.3 | 32,40,48 | 0.1149(26) | 0.056(9) | – | 3.2(8) | 0.88 | 10 | 55 | 82 | 49 |
| $l$.4.1 | 24,32,40,48 | 0.117(2) | 0.04(1) | – | 3.8(3) | 0.68 | 14 | 79 | 52 | 58 |
| $l$.4.2 | 24,32,40,48 | 0.084(11) | 0.040(13) | – | – | 9.96 | 15 | 0 | 0 | – |
| $l$.5 | 24,32,40,48 | 0.1168(18) | 0.044(9) | – | 3.8(3) | 0.76 | 16 | 73 | 24 | 91 |
| $l$.6 | 24,32,40,48 | 0.1169(23) | 0.050(11) | – | 3.8(3) | 0.87 | 17 | 61 | 60 | 25 |
| **linear + cubic fits** | | | | | | | | | | |
| $c$.1.1 | 32,40,48 | 0.1167(12) | 0.038(14) | 0.0028(10) | 3.7(5) | 1.04 | 11 | 41 | 72 | 54 |
| $c$.1.2 | 32,40,48 | 0.1091(11) | 0.092(13) | 0.0(0) | – | 3.87 | 12 | 0 | 70 | 6 |
| $c$.2 | 32,40,48 | 0.1176(18) | 0.041(16) | 0.0034(16) | 3.9(6) | 1.06 | 10 | 39 | 83 | 35 |
| $c$.3 | 32,40,48 | 0.1165(13) | 0.040(15) | 0.0027(11) | 3.7(5) | 1.13 | 10 | 34 | 54 | 52 |
| $c$.4.1 | 24,32,40,48 | 0.1171(7) | 0.028(11) | 0.0035(8) | 3.90(15) | 0.77 | 20 | 75 | 36 | 42 |
| $c$.4.2 | 24,32,40,48 | 0.097(4) | 0.080(13) | 0.0(0) | – | 10.07 | 21 | 0 | 0 | – |
| $c$.5 | 24,32,40,48 | 0.1168(8) | 0.03(1) | 0.0026(7) | 3.82(13) | 0.52 | 17 | 95 | 21 | 68 |
| $c$.6 | 24,32,40,48 | 0.1173(9) | 0.027(11) | 0.0037(10) | 3.91(16) | 0.77 | 20 | 76 | 45 | 31 |

Table 5.3: Same structure as table 5.2.

$N_\mathrm{s} = 24, 32, 40$ and 48 plotted in fig. 5.13 for which the plateaus of the different $N_\mathrm{s}$ in the first order region are overall shifted to slightly larger values of $B_4$ compared to $N_\tau = 6$. At the smallest spatial extent $N_\mathrm{s} = 24$, for which we determined a physical box length of merely $L = 2.117(10)$ fm at the smallest value of $\kappa = 0.11$, we only simulated in a range of $\kappa = \{0.112, \ldots, 0.125\}$ which assumably falls on the first order plateau since there the $B_4$ data points lie on a horizontal. The fits were done

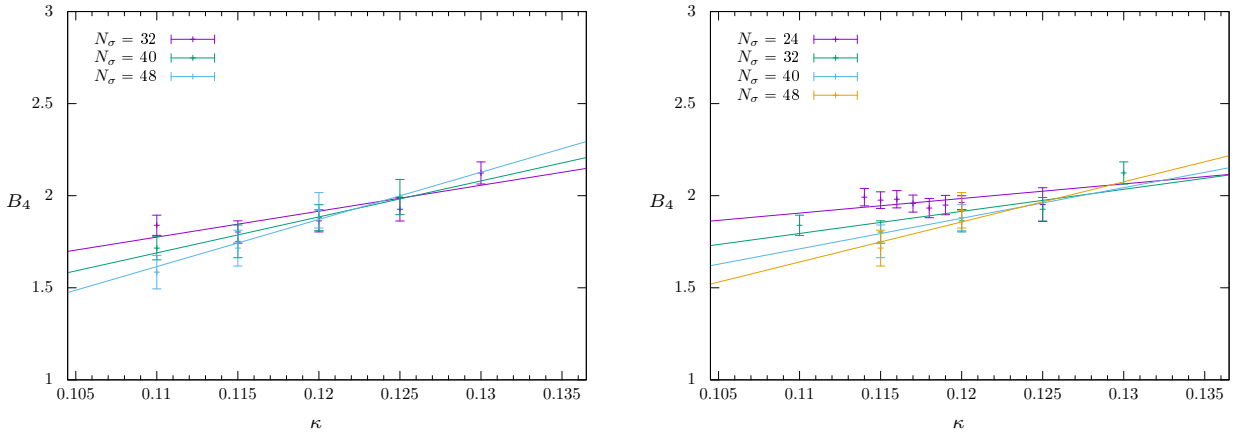


(b) Fit $l.1.1$ (a) Fit $l.4.1$

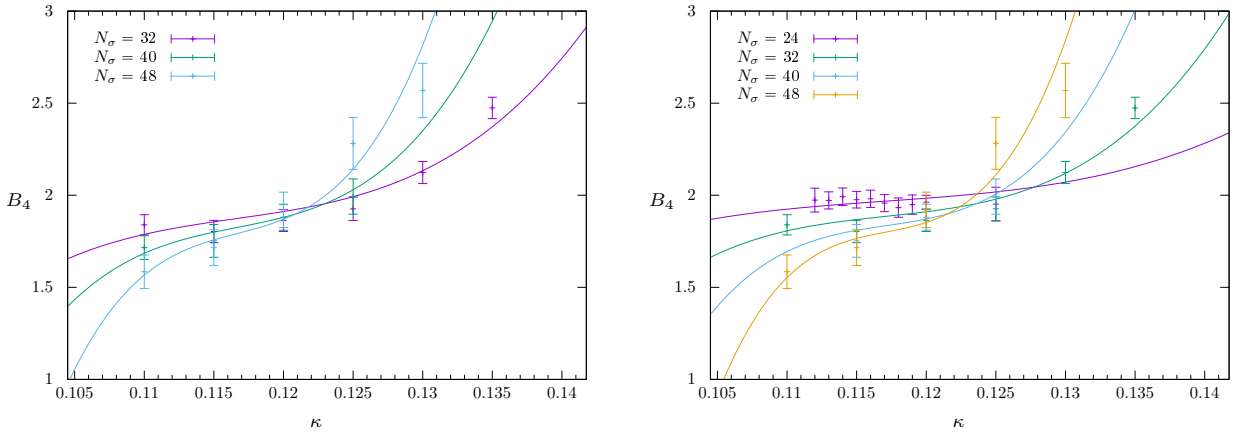


(c) Fit $c.1.1$ (d) Fit $c.4.1$

Figure 5.12: Linear (top) and linear + cubic (bottom) fits of $B_4$ to volumes $N_\mathrm{s} = (24,)32, 40, 38$ (left) right.

including and excluding $N_\mathrm{s} = 24$ (see fig. 5.12). Even though the $N_\mathrm{s} = 24$ plateau is at a large value of $B_4$ ($\approx 2$), the fits using the correction term are impressively stable with respect to quality and extracted $\kappa_{Z_2}$ when $N_\mathrm{s} = 24$ is added. We check again the effect of excluding the correction term which results in a spoiled fit, see fits $l.1.2, l.4.2$ and $c.1.2, c.4.2$. For the cubic fits overall the number of degrees of freedom increases because the fitting range is increased (under consideration of the criteria regarding symmetry and overlap of the fitting ranges imposed on the fits, c.f. section 5.3.1). The value $\kappa_{Z_2}$ extracted from fit $c.1.1$ is quoted as the final result including the corresponding pseudoscalar meson mass,

$$\kappa_{Z_2}(N_\tau = 8) = 0.1167(12) \qquad m_{\mathrm{PS},Z_2}(N_\tau = 8) = 4240(190)\mathrm{MeV}. \tag{5.12}$$

Here additionally I take a look again at the respective susceptibilities $\chi(|P|)$ plotted in fig. 5.14 as a consistency check for two simulated values of the hopping parameter, $\kappa \in \{0.115, 0.12\}$. Note, that the extracted $\kappa_{Z_2}$ value is between these two values. For $\kappa = 0.115$ the different curves $\chi(|P|)/N_\mathrm{s}^{\gamma/\nu}$ have a slightly larger spread when first order exponents are inserted which implies that $\kappa = 0.115$ is in fact close zu the $Z_2$ point. The situation is clearer for $\kappa = 0.12$ where insertion of first order exponents does not seem to cause a collpase at all, while for second order exponents the curves collapse within the error indicating the vicinity to the $Z_2$ point again. .

In this section I complement the study by examining plots of an effective potential of the Polyakov

loop for which I used the definition suggested in [125],

$$V_{\text{eff}}(|P|, \beta, \kappa) = -\ln \mathcal{P}(|P|)_{\beta,\kappa}\,, \tag{5.13}$$

which is really nothing but a different way of looking at the distribution function $\mathcal{P}(|P|)$ of the (pseudo) order parameter $|P|$. The effective potential should develop a parabola shape at the $Z_2$ point while it exhibits two neighboring minima in the first order region equivalent to the two peak-structure of $\mathcal{P}(|P|)$ shown in fig. 5.11 (right). The effective potentials were examined for fixed spatial extents as functions of $\kappa$ as shown in figures 5.15a to 5.15d as well as for fixed values of $\kappa$ as functions of $N_\text{s}$ as shown in figures 5.15e to 5.15h. Note that I refrained from including error bars so as not to clutter the plots. The errors have been checked and are always comparable to the errorbars in fig. 5.15d. The plots 5.15a to 5.15d confirm what was observed from the analysis of the previous section about $N_\tau = 6$. The moment at which the curves $B_4(\beta_\text{c}, \kappa, N_\text{s})$ reach a plateau in the first order region their respective distributions and thus also the effective potentials do not change shape anymore, c.f. fig. 5.11. Consider for instance the $B_4(\beta_\text{c}, \kappa, N_\text{s})$ curve of $N_\text{s} = 32$ in fig. 5.13a: It appears to reach the upwards shifted first order plateau at a $\kappa$ value $\lesssim 0.12$. Now, looking at the potential belonging to $N_\text{s} = 32$ in fig. 5.15b, one can see that the shape of the potential is roughly constant from $\kappa = 0.12$ on. Staying for a moment with this example, note, that

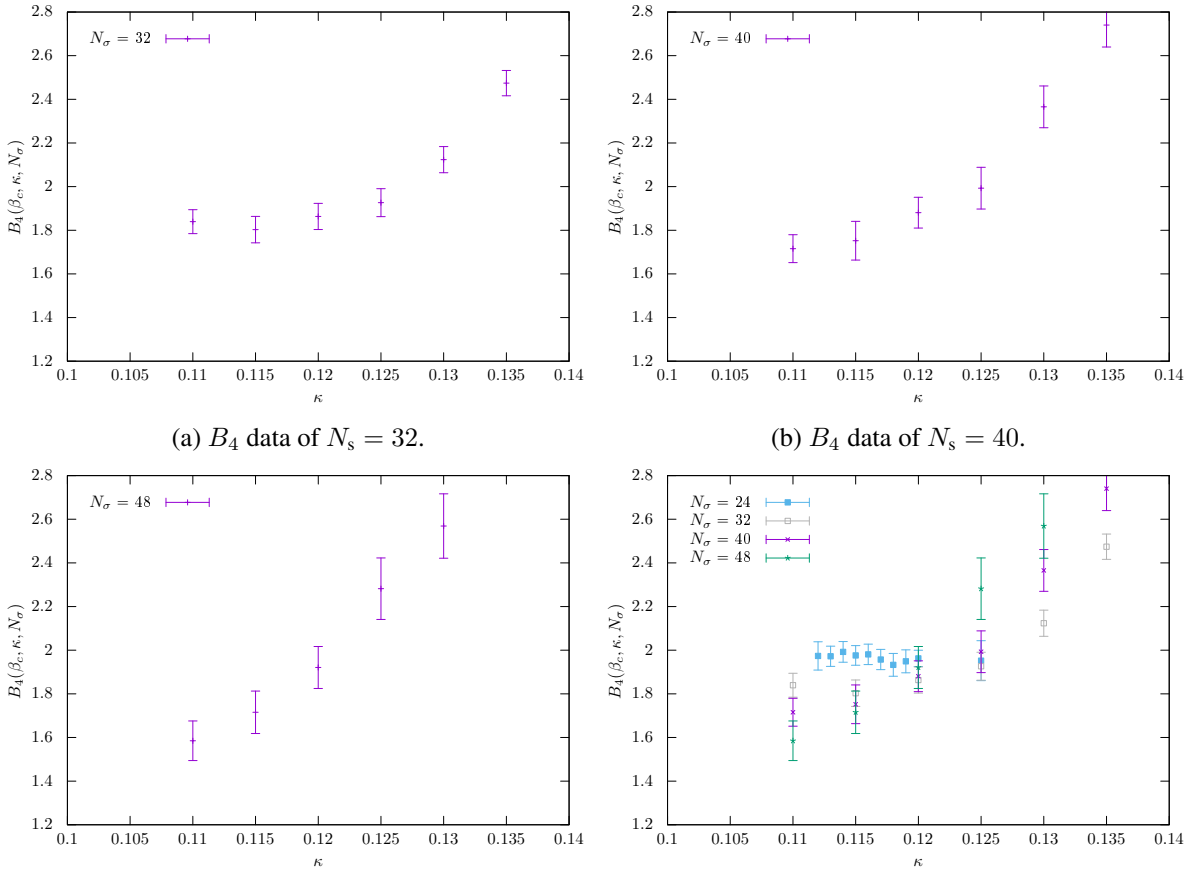


(a) $B_4$ data of $N_\text{s} = 32$.

(b) $B_4$ data of $N_\text{s} = 40$.

(c) $B_4$ data of $N_\text{s} = 48$.

(d) Plot of $B_4$ of $N_\text{s} = 24, 32, 40, 48$.

Figure 5.13: The figure shows the $B_4$ data for which fits are shown in fig. 5.12.

the fitted value of $\kappa_{Z_2}$ is $\kappa_{Z_2} = 0.1167(12)$ which is $< 0.12$. Thus one would expect the two minima of the effective potential to fuse into one minimum at values of $\kappa > 0.1167(12)$. Instead, at $\kappa = 0.12$ and even at $\kappa = 0.125$ the two minima are still clearly distinct and only merge at $\kappa \approx 0.13$. This can again

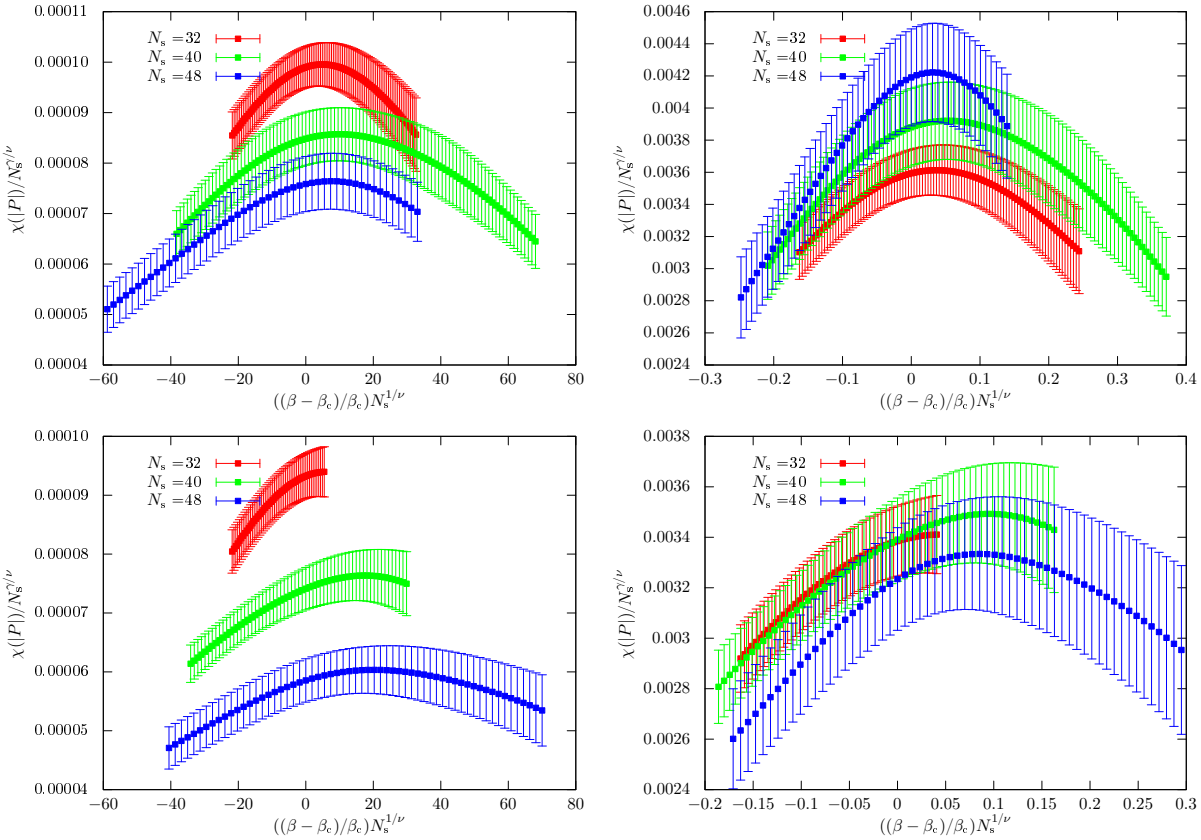


Figure 5.14: Collapse plots of $\chi(|P|)$ at $\kappa = 0.115$ (top) and $\kappa = 0.12$ (bottom) for first (left) and second order (right) critical exponents.

be explained with the behavior described by fig. 5.11: Lets assume for a moment that the fitted value $\kappa_{Z_2} = 0.1167(12)$ represents in fact the true $Z_2$ point at $V \to \infty$, i.e. $\kappa_{Z_2}(V = \infty) = 0.1167(12)$. The beginning of the first order plateau of the curve $B_4(\beta_c, \kappa, N_s = 32)$ is shifted (relatively to the $B_4$ curve at $V \to \infty$) vertically to values of $B_4 > 1$ and horizontally to values of $\kappa > 0.1167(12)$. Consequently the system with an extent of $N_s = 32$ still appears to have a first order transition at $\kappa$ values at which in the thermodynamic limit there would already be a crossover transition. Thus also the effective potential displays a shape characteristic to a first order transition.

Changing the perspective and inspecting the effective potential at a fixed $\kappa$ value as a function of $N_s$ gives more information about how the situation changes for increasing volume: Close to the thermodynamic limit the minima of the effective potentials should settle and not change anymore irrespective of the spatial extent $N_s$ considered. Looking at the plots unsurprisingly reveals that this state has not been reached so far, although, for instance considering fig. 5.15e, it seems like the distance between the minima between the different $V_{\text{eff}}(|P|, \beta, \kappa, N_s)$ decreases as $N_s$ is increased.

However, this represents merely a qualitative analysis and thus is adequate to identify trends and make instructive observations. Note that strictly speaking the comparison between the effective potentials at a fixed $N_s$ but at different values of $\kappa$ is flawed since the lattice spacing slightly varies with $\kappa$ which implies different volumes at each $\kappa$ (c.f. table A.4) an thus somewhat different finite volume effects, as well. To draw a conclusion one should probably not use this method solely for the attempt to identify the $Z_2$ point $\kappa_{Z_2}$ but consulting the distribution or the effective potential can shed additional light on the situation.

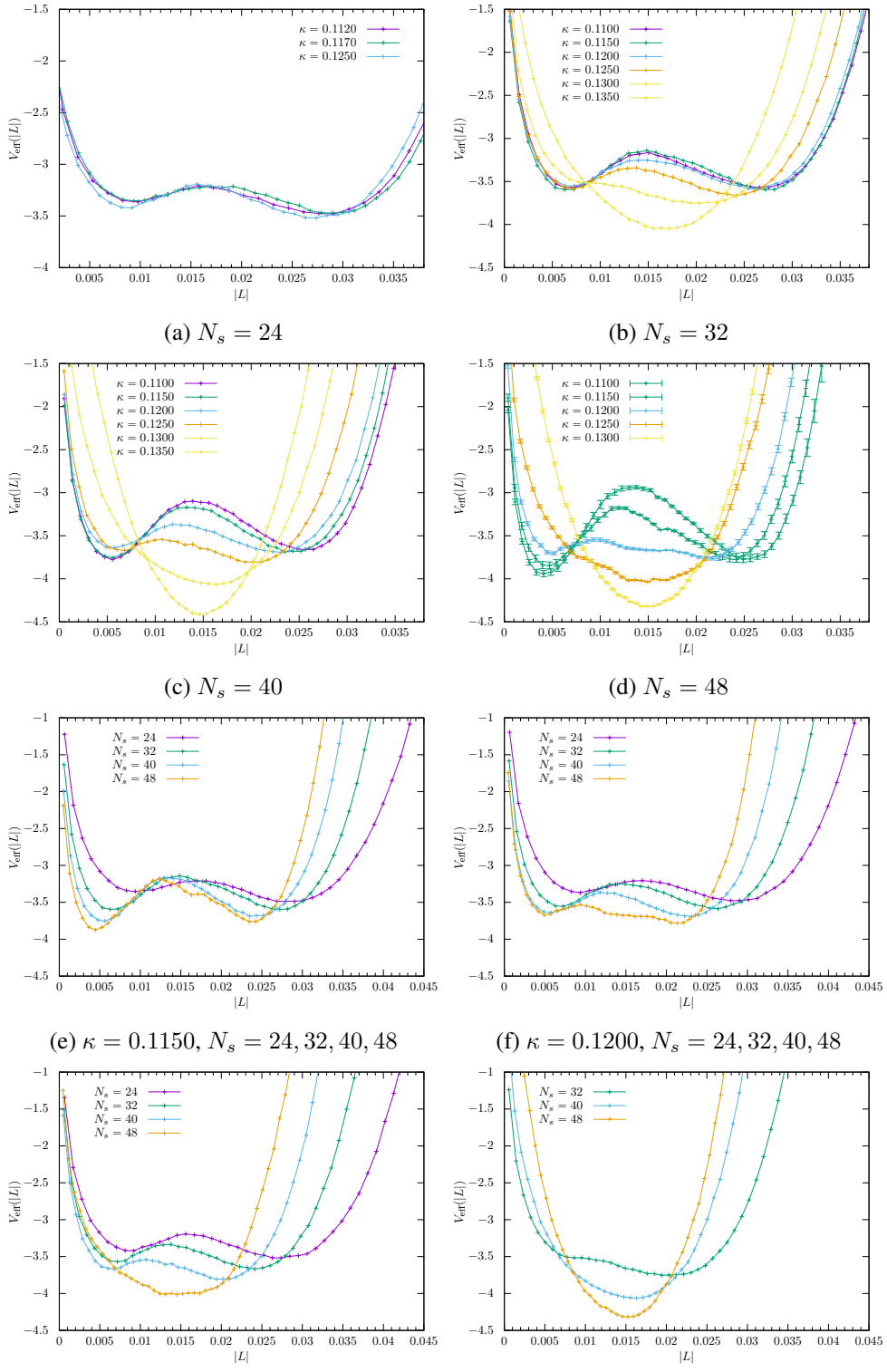


(a) $N_s = 24$ (b) $N_s = 32$

(c) $N_s = 40$ (d) $N_s = 48$

(e) $\kappa = 0.1150$, $N_s = 24, 32, 40, 48$ (f) $\kappa = 0.1200$, $N_s = 24, 32, 40, 48$

(g) $\kappa = 0.1250$, $N_s = 24, 32, 40, 48$ (h) $\kappa = 0.1300$, $N_s = 32, 40, 48$

Figure 5.15: Effective potentials of $|P|$ plotted for fixed values of $N_\text{s}$ (5.15a)-5.15d and for fixed values of $\kappa$ (5.15e-5.15h). Note that the system is always kept critical, i.e. at the pseudo-critical coupling $\beta_\text{c}$.

### 5.3.3 $N_f = 2, N_\tau = 10$

For the study of $N_\tau = 10$ lattices, only the initial steps have been taken so far, meaning that the simulated volumes are very small ($L = \{1.66(2), \dots 3.05(4)\}$ fm) and on top the accumulated statistics on the volumes are rather low. Therefore the data shown in this section is in a very preliminary state. However this state can serve as a testing ground for the insights gathered from what was presented in the preceding sections on $N_\tau = 6$ and 8 lattices. As expected, at this temporal extent the lattice spacings have decreased even further and are now found in a range of $a = \{0.0690(10), 0.0762(11)\}$. Also the pseudo scalar masses in lattice units are shifted to smaller values. At the largest simulated value of the hopping parameter with $\kappa = 0.1400$ the lattice mass dropped below one for the first time with $am_{\text{PS}} = 0.9284(5)$.

The $B_4$ data was analyzed again by fits listed in table 5.4. Due to the small volumes the correction parameter $B$ extracted from the fits further increased compared to the fits of the $N_\tau = 8$ data. The value $\kappa_{Z_2}$ extracted from fit $c.1.1$ is quoted as the final result including the corresponding pseudoscalar meson mass,

$$\kappa_{Z_2}(N_\tau = 10) = 0.1229(10) \qquad m_{\text{PS},Z_2}(N_\tau = 10) = 4500(400)\text{MeV}. \tag{5.14}$$

To summarize the findings, the values of $m_{\text{PS},Z_2}$ found in the studies at $N_\tau = 6$ and 8 as well as the preliminary value for $N_\tau = 10$ are plotted over the lattice spacing in fig. 5.17.

| Fit | $N_s$ | $\kappa_{Z_2}$ | $a_1$ | $a_3$ | $B$ | $\chi^2_{\text{NDF}}$ | NDF | $Q[\%]$ | $\Omega_{\text{min}}$ | $\Xi_{\text{min}}$ |
|---|---|---|---|---|---|---|---|---|---|---|
| **linear fits** | | | | | | | | | | |
| $l.1.1$ | 30,40,50 | 0.125(9) | 0.034(13) | – | 5.3(1.4) | 0.081 | 8 | 60 | 62 | 47 |
| $l.1.2$ | 30,40,50 | 0.1066(35) | 0.072(13) | – | – | 2.24 | 9 | 2 | 53 | - |
| $l.2$ | 30,40,50 | 0.126(11) | 0.025(12) | – | 5.2(1.3) | 0.68 | 7 | 69 | 55 | 52 |
| **linear + cubic fits** | | | | | | | | | | |
| $c.1.1$ | 30,40,50 | 0.1229(10) | -0.000(12) | 0.003(10) | 5.1(3) | 0.36 | 8 | 94 | 78 | 63 |
| $c.1.2$ | 30,40,50 | 0.1055(42) | 0.085(23) | 0.0(0) | – | 2.56 | 9 | 1 | 44 | - |
| $c.2$ | 30,40,50 | 0.1227(9) | -0.007(16) | 0.0038(16) | 5.0(3) | 0.39 | 7 | 91 | 79 | 62 |

Table 5.4: Same structure as table 5.2.

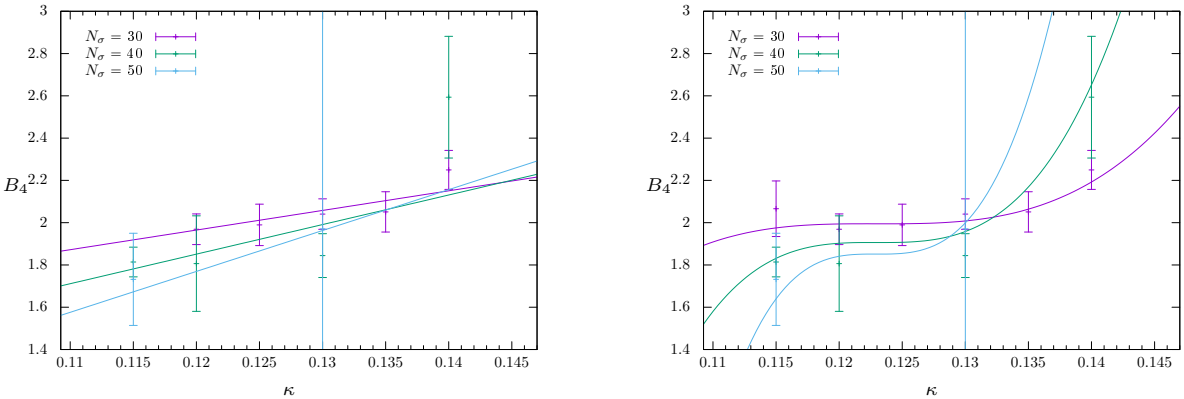


(a) Fit $l.1.1$ (b) Fit $c.1.1$

Figure 5.16: Linear (left) and cubic (right) fits of $B_4$ including the correction term given by eq. (5.10).

### 5.3.4 Discussion

For $N_f = 2$ QCD with zero chemical potential the $Z_2$ point of the heavy quark mass region has been determined by finite size scaling analyses of $B_4$ on lattices with temporal extents $N_\tau = 6, 8$ and 10. The results are summarized altogether in table 5.5. The extraction of the $Z_2$ points was complicated by finite volume effects which prevent $B_4$ to assume the value characteristic for first order transitions ($B_4(\beta_c, \kappa < \kappa_{Z_2}) = 1$) even at very small values of $\kappa$. Instead, at some value of $\kappa$, $B_4$ reaches and remains at a value $> 1$, which is further increased as the volume is decreased. Moreover, this "new first order plateau" is reached at increasingly larger $\kappa$ values at smaller volumes. This causes a positive vertical and horizontal shift of the inflection points of each individual curve $B_4(\beta_c, \kappa, N_s)$, which represent the $Z_2$ point at $B_4 = 1.604$ in or close to the thermodynamic limit, to values $B_4 > 1.604$ (and even $\kappa \gtrsim \kappa_{Z_2}$ below a certain volume). The effects can be understood from examining the distribution $\mathcal{P}(|P|)$ of the (pseudo) order parameter $|P|$. In particular the larger $B_4$ values are caused by the lack of separation of the two peaks characterizing the distribution at a first order transition. Further investigations could help to better understand and quantify the problem, for instance by means of the model that was developed in our group to explain the findings in [159] which were also caused by effects of small volumes on the distributions. However, the shifted inflection points spoil attempts to fit the $B_4$ data according to the well know expansion given by eq. (5.7), with the parameters $B_4(\beta_c, \kappa, V = \infty)$ and $\nu$ fixed to the values characteristic to the $Z_2$ universality class. For this reason a correction term given by eq. (5.10), suggested in [72], was included in this expansion. This term corrects for the finite volume effects by introducing an additional volume dependence according to a specific critical exponent. Taking into account this correction permits successfully fitting the $B_4$ data points affected by finite volumes effects with the parameters $B_4(\beta_c, \kappa, V = \infty)$ and $\nu$ fixed to their true values. The correction term is motivated by the fact that the QCD (pseudo) order parameters are mixtures of magnetic and energy-like observables [71], as discussed in section 3.1.3. Note, that the authors of [72] used the correction for finite size scaling analysis of $B_4$ in the region of small quark masses. In contrast, the present study takes place in the region of heavy quark masses. In view of this different setting, what yet needs to be understood is whether this mixing of magnetic and energy-like observables is what causes the finite volumes effects observed in the present study at small $N_s$ or if there is no theoretical connection at all and the correction term coincidentally acts as a makeshift.

The values of $m_{\mathrm{PS},Z_2}$ listed in table 5.5 are based on masses in lattice units $> 1$ for which reason large discretization errors are expected. At the largest simulated value of $\kappa$ with $\kappa = 0.14$ on $N_\tau = 10$ lattices the mass assumed a value in lattice units $< 1$. This can be seen to imply that advances to temporal extents $N_\tau \gtrsim 12$ will put forth masses in lattice units $\lesssim 1$ at the $Z_2$ point, allowing to more reliably extract pseudo scalar meson masses.

The results of the study on $N_\tau = 10$ lattices are, as explained before, in a very preliminary state at the present time but the work on the project is ongoing in our group and over a period of 1 or 2 years will presumably yield a more reliable estimate of $\kappa_{Z_2}$ and $m_{\mathrm{PS},Z_2}$. Furthermore, simulation of $N_\tau = 12$ lattices have been started in our group, as well.

Keeping in mind all the caveats about present finite volume effects and discretization errors, the results presented in the last section about $N_\tau = 6, 8$ and 10 are summarized in fig. 5.17. The left plot is rather inconclusive but the value of $m_{\mathrm{PS},Z_2}(N_\tau = 10)$ as well as its error is expected to decrease as the quality of the data improves and the spatial lattices extents included in the study are increased. In contrast the

right plot in which $1/\kappa_{Z_2}$ is plotted vs the lattice spacing $a$ shows a promising trend. Remember that $\kappa$ is defined as $\kappa = 1/(4am_q + 8)$ and thus $1/\kappa_{Z_2}$ is expected to approach 8 as $a \to 0$. Of course, this plot is specific to the standard Wilson discretization. For fig. 5.17 the lattice spacing at the respective $\kappa_{Z_2}(N_\tau)$ and $m_{\mathrm{PS},Z_2}(N_\tau)$ values were obtained by a fit to the data listed in table 5.1.

Somewhat surprising are the transition temperatures listed in table 5.5. For $N_\tau = 6$ with the largest value of $m_{\mathrm{PS},Z_2}$ the smallest value of $T_\mathrm{c}$ is found which is rather unexpected. An explanation could be found in the uncertainties that propagate into the computation of $T_\mathrm{c}$ via the relation $T = 1/(a(\beta_\mathrm{c})N_\tau)$. Remember that $\beta_\mathrm{c}$ is defined by $B_3(\beta_\mathrm{c}) = 0$. First of all, $B_3$ has a statistical error which causes uncertainties in the extraction of $\beta_\mathrm{c}$. Furthermore, $\beta_\mathrm{c}$ extracted in this way will shift at larger volumes until the system is close to the thermodynamic limit. As we have observed, the volumes that have been used in the analysis, at least for $N_\tau = 8$ and 10, still suffer considerably from finite volumes effects and thus $\beta_\mathrm{c}$ is expected to slightly change as the volumes are increased. This could also add to problems in determination of $B_4$ since, strictly speaking, it is not extracted at $T_\mathrm{c}(\infty)$. The further process of determining the lattice spacing $a$ involves employing the Wilson-flow method in which the produced $T = 0$ configurations have to be flowed. Due to the computational and time demands required by the Wilson flow method, the number of configurations flowed at each $\kappa$ is rather small ($\approx 20$) and thus a higher precision in the lattice spacing $a$ can be achieved by simply increasing this number. Taking into account all of these sources of errors suggests that the errors of the temperatures listed in table 5.1 are probably underestimated.

| $N_\tau$ | $\kappa_{Z_2}$ | $m_{\mathrm{PS},Z_2}$[MeV] | $T_\mathrm{c}$[MeV](approx.) |
|---|---|---|---|
| 6 | 0.0939(14) | 4670(180) | 278 |
| 8 | 0.1167(12) | 4240(190) | 282 |
| 10 | 0.1229(10) | 4500(400) | 287 |

Table 5.5: Summary of the determined values of $\kappa_{Z_2}$ by finize size scaling analyses of $B_4$.

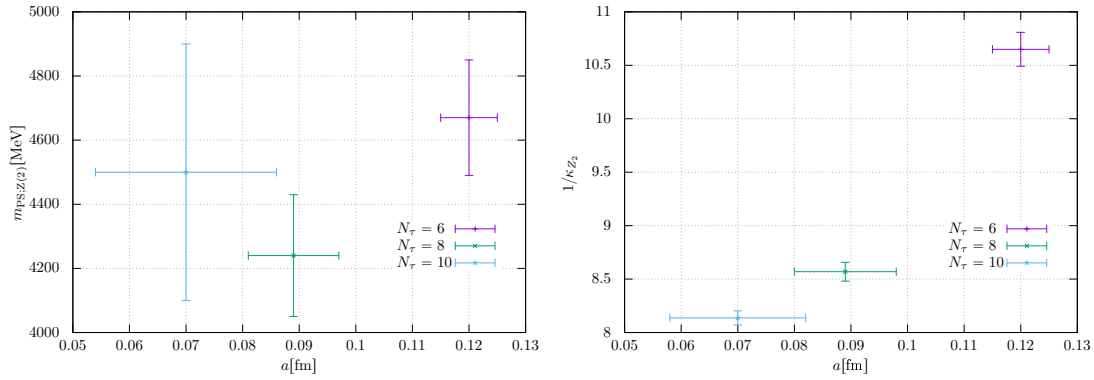


Figure 5.17: Summary of $N_\tau = 6, 8, 10$ $m_{\mathrm{PS},Z_2}$ (left) and $1/\kappa_{Z_2}$ (right) estimates.

### 5.3.5 $N_f = 3, N_\tau = 4$

The study of phase transitions on lattices with temporal extent $N_\tau = 4$ in the $N_f = 3$ theory of QCD just presents the first step of a larger set of simulations at multiple values of $N_\tau$, aiming at determining the $Z_2$ point with the same strategy as presented in the previous sections. It uses the Rational Hybrid Monte Carlo implementation for Wilson fermions in CL$^2$QCD described in section 4.2 and section 4.3. The results are compared to a study presented in [125]. Note, that at $N_\tau = 4$ we work on coarse lattices with lattice spacings around $a \approx 0.19$ (see table 5.1). Due to the large lattice spacings smaller spatial lattice extents with $N_\mathrm{s} = 16, 20, 24$ are sufficient to obtain effectively a similar physical volume compared the studies of $N_\tau = 6$ and 8 lattices. The physical edge lengths $L$ of the simulated volumes are in range a of $L \in \{2.971, \ldots, 4.531\}$ fm (see table A.7) which is very similar to the study of $N_\tau = 8$. The fits, which were performed according to the procedure described in the beginning of the section about $N_\tau = 6$, are listed in table 5.6. All fits including a cubic order gave cubic coefficients which were consistent with zero within their error for which reason they are not listed in the table. Surprisingly, the parameter $B$ of the correction term given by $C(N_\mathrm{s}) = (1 + BN_\mathrm{s}^{1/\nu})$ has been observed to be insignificant, i.e. consistent with zero within its error, for basically all fits performed. Since the simulated volumes are comparable to the volumes of the $N_\tau = 8$ study, rather large finite volume effects would be expected. Instead, excluding the correction in the fits (see fit $l.1.2$) produces a qualitatively equal result. The minimal symmetry $\Xi_\mathrm{min}$ with respect to the fitted $\kappa_{Z_2}$ and the minimal overlap $\Omega_\mathrm{min}$ of the fitting ranges of the different $N_\mathrm{s}$ hardly changes under exclusion of the correction. However, one should not be tempted to airily conclude that the finite volume effects are small. The simulations have been carried out in a rather narrow range of $\kappa$ values and on top the statistical errors of the $B_4(\beta_\mathrm{c}, \kappa, N_\mathrm{s})$ data points are still quite large which causes the data to overlap within the error. Hence statistical errors would have to be decreased and the range in $\kappa$ should be extended to obtain a more conclusive picture. From table 5.2 the value $\kappa_{Z_2}$ extracted from fit $l.1.1$ is quoted as the final result,

$$\kappa_{Z_2}(N_f = 3, N_\tau = 4) = 0.0553(7). \tag{5.15}$$

The authors of [125] find $\kappa_{Z_2} = 0.0595(3)$ which has a $4.2\sigma$ discrepancy to the result presented here.

| Fit | $N_\mathrm{s}$ | $\kappa_{Z_2}$ | $a_1$ | $a_3$ | $B$ | $\chi^2_\mathrm{NDF}$ | NDF | $Q[\%]$ | $\Omega_\mathrm{min}$ | $\Xi_\mathrm{min}$ |
|---|---|---|---|---|---|---|---|---|---|---|
| **linear fits** | | | | | | | | | | |
| $l.1.1$ | 16,20,24 | 0.0553(7) | 0.220(15) | – | 0.05(19) | 1.08 | 17 | 37 | 58 | 49 |
| $l.1.2$ | 16,20,24 | 0.0550(3) | 0.221(13) | – | – | 1.02 | 18 | 43 | 46 | 57 |

Table 5.6: Same structure as table 5.2.

To explain this discrepancy between the results not only the points already mentioned above should be considered but also the fact that in the cited study no finite size scaling is performed but only the distribution and the effective potential respectively of the plaquette is considered to deduce the $\kappa_{Z_2}$ value. To this end the quark determinant is expanded by a hopping parameter expansion to first order in $\kappa$ around the simulation point $\kappa = 0$. Subsequently a reweighting to finite values of $\kappa$ is performed. First of all have we previously learned from the presentation about $N_\tau = 8$ that the distribution functions can be heavily affected by finite volume effects. Second, the extrapolation that is used in [125] possibly introduces non-negligible systematics.

Examining the effective potential of $|P|$ plotted in fig. 5.19 one can see that the two minima only disappear at a $\kappa$ value of $\kappa = 0.0650$ implying a value $\kappa_{Z_2} = 0.0650$ which is much larger than the $\kappa_{Z_2}$ value extracted from the finite size scaling analysis of $B_4$. Since the $\kappa_{Z_2}$ value extracted in either way should be comparable for sufficiently large volumes one can conclude that the volumes considered here are affected by finite volumes effects despite the contrary impression one obtains from the vanishing of the finite volume correction parameter $B$ in the fits.

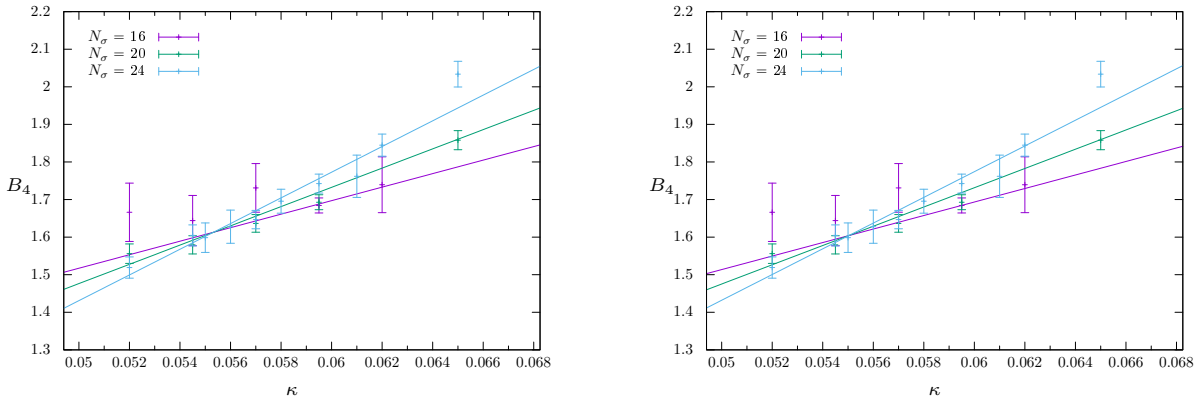


(a) Fit $l.1.1$ (b) Fit $c.1.2$

Figure 5.18: Linear fits of $B_4$ including (left) and excluding (right) the correction term given by eq. (5.10).

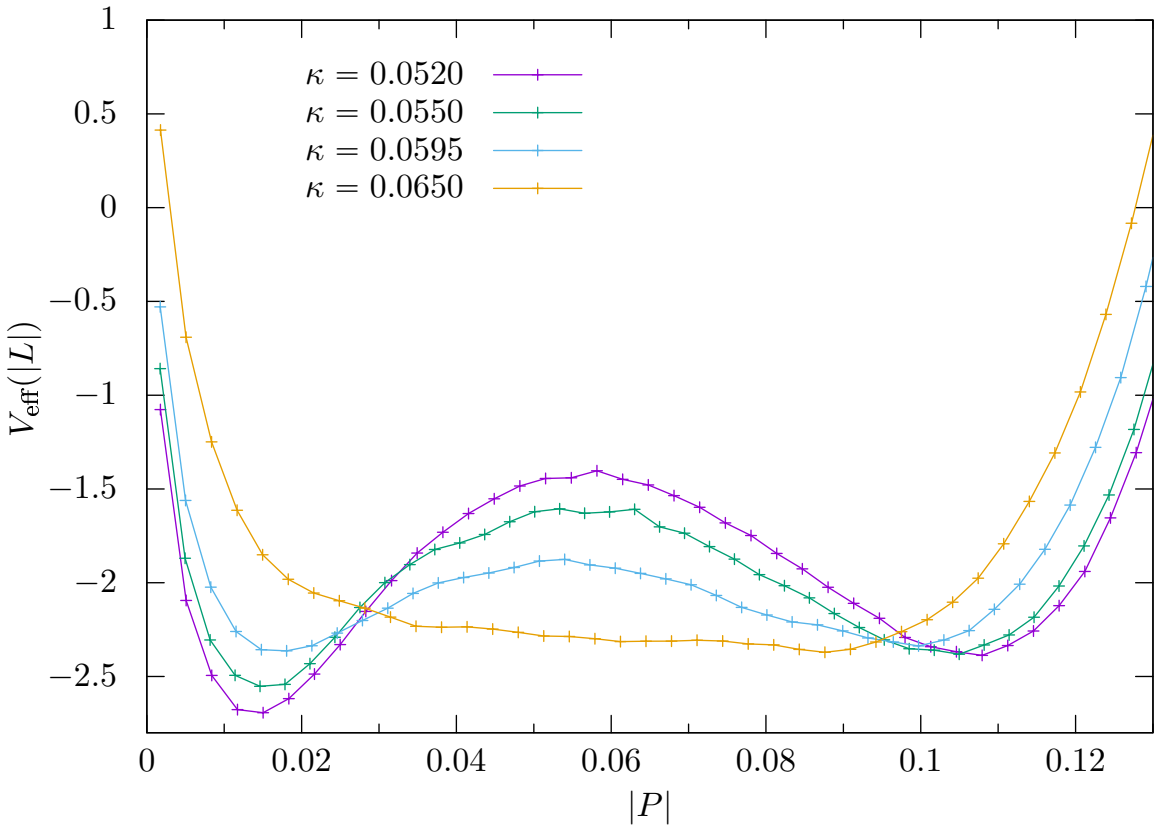


Figure 5.19: Shown is the effective potential $V_{\text{eff}}(|P|, \beta_c, \kappa)$ of $|P|$ at fixed $N_s = 24$ as a function of $\kappa$.

### 5.3.6 Discussion

The rational hybrid Monte Carlo Algorithm has been implemented in CL$^2$QCD so as to simulate at uneven values of $N_f$ which opens up the possibility to start studying the nature of the phase transition of QCD for $N_f = 3$ flavors in the Columbia phase diagram. As a test for this a first step has been successfully taken on coarse lattices with temporal extent $N_\tau = 4$ in the heavy quark mass region. The result was compared to another study [125] and was consistent within $4.2$ standard deviations. Possible reasons for the discrepancy have been discussed. To further test the correctness of the implemented algorithm another reference study is needed in which full simulations with unimproved Wilson fermions are carried out. Moreover, for the data presented in this section the statistics as well as the volumes should be increased in order to further study the finite volume effects at work.

## 5.4 Simulations at Imaginary Chemical Potential

The results presented in this section have already been published in [159] from where the content and all the figures were taken over correspondingly and adapted to fit the context of this work. To acquire the results the strategy presented in section 5.2.3 has been employed. Any further steps in the analysis not explained there will be given during the discussion when necessary.

### 5.4.1 $N_f = 2, N_\tau = 6$, $(\mu_{i,c}/T = \pi/3)$

For this project 9 values of $\kappa$ have been simulated between and including $\kappa = 0.1$ and $\kappa = 0.165$ on $N_\tau = 6$ lattices with an imaginary chemical potential value of $a\mu_{i,c} = \pi/6$. For each of these $\kappa$ values the kurtosis $B_4$ was evaluated as a function of $\beta_\mathrm{c}$ on three to four spatial lattices sizes with $N_\mathrm{s} \geq 16$ (except for $\kappa = 0.1625$ where $N_\mathrm{s} = 12$ was used additionally), giving a minimal aspect ratio of $\sim 3$. For every $N_\tau$ about 6 up to 30 values of $\beta$ have been simulated with between $40$k-$500$k standard HMC steps of unit length each after $5$k thermalization steps. For each trajectory the acceptance rate was tuned to and held at $\sim 75\%$. In each step after the thermalization Re$P$ and Im$P$ were measured. At large values of $\kappa \geq 0.16$ the Hasenbusch trick [170] for the integration of Molecular Dynamics equations has been employed in order to reduce the integrator instability causing large drops in the acceptance rate and which is generated by isolated low modes of the Dirac operator [199]. Subsequently fits to the measured data were performed according to eq. (5.9) from which the parameters $B_4(\beta_\mathrm{c,E}, V = \infty)$, $a_1$, $\beta_\mathrm{c,E}$ and $\nu$ were extracted using an intricate procedure (the method is explained in 4.1.3). Examining the change in $\nu$ as a function of $\kappa$ allows to locate the tricritical points. The fitting procedure and the extraction of parameters is particularly delicate and requires to understand at which point the gathered statistics are sufficient. For this reason the HMC steps were equally distributed on four different Markov chains per $\beta$ on which the observables were evaluated with analysis techniques discussed in section 4.1. Scale-setting was done using the Wilson flow parameter $\omega_0$. For this purpose $T = 0$ simulations at or close to the value of the critical coupling $\beta_\mathrm{c,E}(\kappa)$ of $\mathcal{O}(400)$ configurations have been carried out on $16^3 \times 32$ lattices at vanishing chemical potential. In order to provide a physical quantity for the identification of the tricritical point $\kappa_\mathrm{tric}$ the pseudo scalar meson mass, here denoted by $m_\mathrm{PS}$, has been computed on the same configurations. More details about the simulations are given in section A.4.1.

To get an idea about the nature of the phase transition at each value of $\kappa$ collapse plots of the susceptibilities $\chi$ of $|L|$ were produced according to eq. (3.15) where the different possible values for

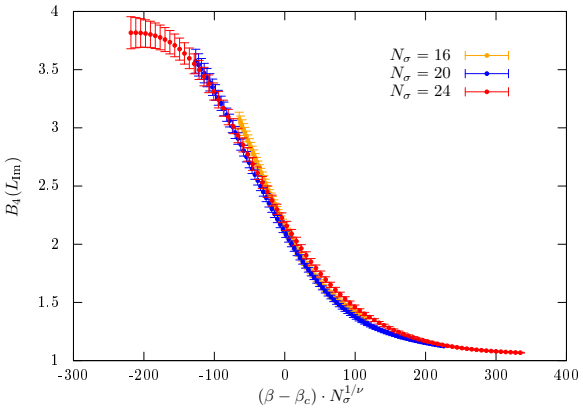


(a) $\kappa = 0.1$, first order coefficients.

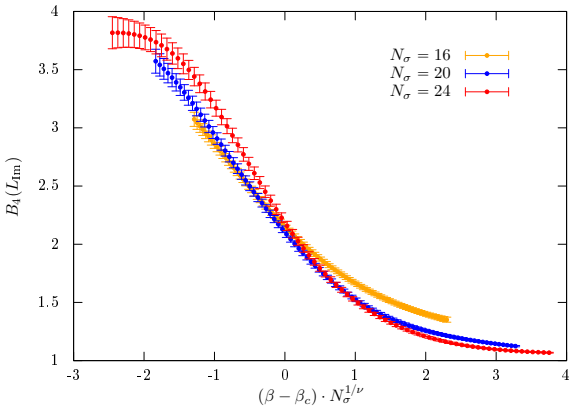


(b) $\kappa = 0.1$, second order coefficients.

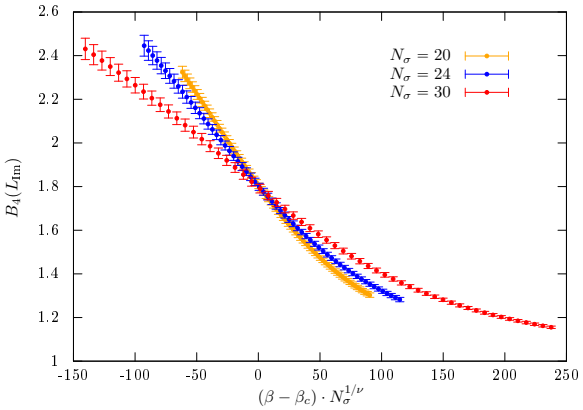


(c) $\kappa = 0.13$, first-order coefficients.

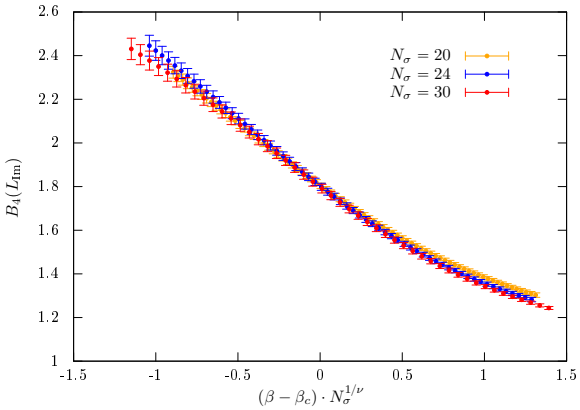


(d) $\kappa = 0.13$, second-order coefficients.

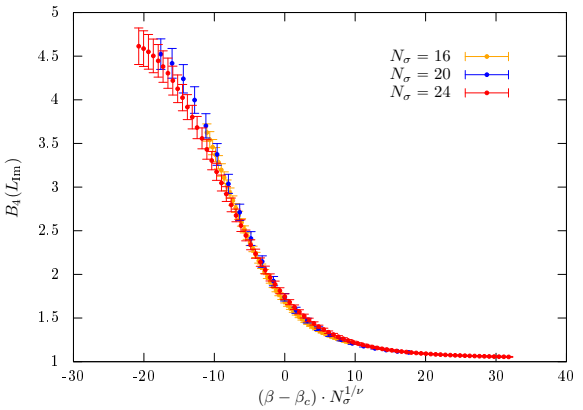


(e) $\kappa = 0.165$, first-order coefficients.

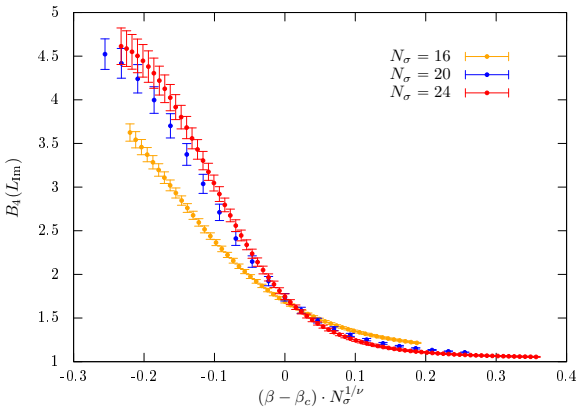


(f) $\kappa = 0.165$, second-order coefficients.

Figure 5.20: Example of collapse plots of the $B_4$ of the imaginary part of the Polyakov loop. (All figures taken from [159])

the ratio of the critical exponents $\gamma/\nu$ (first or second order values) help to exclude one of the scenarios. However, remember that the susceptibility collapse plots can be inconclusive, especially for small $N_{\mathrm{s}}$, and thus are complemented with the equivalent information from kurtosis collapse plots for which Im$P$ was used. In fig. 5.20 examples of kurtosis collapse plots are shown for $\kappa = 0.1, \kappa = 0.13$ and $\kappa = 0.165$ with first order coefficients inserted in the left column and second order coefficients inserted in the right column. In each the overlap of the different curves clearly prefers either the first or the second order coefficients. It can be observed that $\kappa = 0.1$ belongs to the region of first order deconfinement transitions.

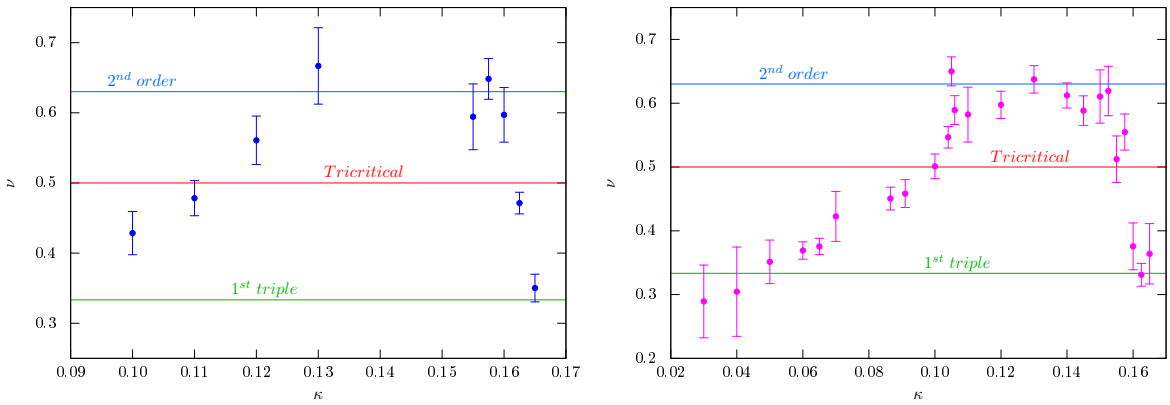


(a) $N_\tau = 6$ results of present work.

(b) $N_\tau = 4$ results of ref. [196].

Figure 5.21: Critical exponent $\nu$ as function of $\kappa$. The horizontal colored lines are the critical values of $\nu$ for some universality classes. Note the different scale on the $\kappa$-axis. Due to the much higher numerical cost, not all the $\kappa$ values simulated for $N_\tau = 4$ have been considered for $N_\tau = 6$. Refer to Figure 5.22a for a more direct comparison.(Figure taken from [159])

The phase transition at $\kappa = 0.165$ seems to be of first order, as well, but belongs to the chiral region as $\kappa$ corresponds to rather small quark masses. The value of $\kappa = 0.13$ in contrast is found to be in the second order region.

Note that at $\kappa = 0.165$ and $\kappa = 0.1$ the kurtosis unexpectedly assumes values $> 3$. This phenomenon was investigated in our group with a model introduced in [159] and discussed in detail in [190]. The model uses the definition of $B_4$ given by eq. (5.3), for which analytic expressions are inserted for the expectation values in the numerator and the denominator, namely

$$B_4\left[\mathcal{P}(x)\right] = \frac{\int_{-\infty}^{+\infty} x^4 \mathcal{P}(x) dx}{\left[\int_{-\infty}^{+\infty} x^2 \mathcal{P}(x) dx\right]^2}. \tag{5.16}$$

The distribution $\mathcal{P}$ is then constructed to be a sum of three Gaussians with respective weights. This models the situation in the chiral/deconfinement region of the Roberge-Weissplane where the distribution of Im$P$ at the end point (which is a triple point there) of the $Z_3$ transition displays a three peak structure signalling a three phase coexistence. Imposing proper conditions on the model and further algebraic evaluation shows that in fact $B_4$ can assume values $> 3$ for small volumes and thus allowing to conclude that the findings of our study can be explained by finite volume effects. However, I will not go into further detail as this model is not part of this work. The interested reader is referred to the references cited above.

Coming back to the discussion of the results, the method of collapsing curves is, as mentioned before already, only self-consistent and serves to make instructive observations. To actually extract the critical exponent $\nu$ from the data of $B_4$ it must be fitted by eq. (5.9). Since the $B_4$ data points were interpolated by multi-histogram reweighting the fitting procedure involves many data points such that the fitting ranges can be heavily varied. Thus in order to choose fitting ranges by objective criteria the same intricate procedure, explained in section 4.1.3, was used as for the $\mu = 0$ project. The outcome of the fits are shown in fig. 5.21(a) where $\nu$ is plotted as a function of $\kappa$. The plot shows the expected change from first order values of $\nu$ at small values of $\kappa$ (large quark mass) to second order values at intermediate $\kappa$ values and back again to first order values at large values of $\kappa$ (small quark mass). The behavior of $\nu$ shows a smeared out version of the step function expected in the thermodynamic limit, illustrated by the schematic

in fig. 5.7. The reason for not extracting the values of $\nu$ corresponding to $V \to \infty$ despite performing a finite size scaling analysis is presumably that the volumes are still to small. The finite slope of the $\nu$-curve implies that $\nu$ can take any value between the universal ones in the vicinity to the tricritical points which is a complication in the determination procedure of $\nu$. Producing a collapse plot based on the critical exponent $\nu$ could be rather inconclusive in this region which again is a hint that collapse plots should only be used as a supplemental technique. However, as already discussed in section 5.2.3, the critical exponent $\nu$ is less prone to finite size effects and stays confined between its first and second order values compared to $B_4(\beta_{\mathrm{c,E}}, V = \infty)$. In contrast, $B_4(\beta_{\mathrm{c,E}}, V = \infty)$ extracted from the fit gave values that are slightly larger than true universal values for which reason no plot is shown here. This is in agreement with what was found in previous studies with both Wilson [196] and staggered [156] fermions and can be explained by finite size effects (c.f. the discussion in section 3.5.1). From the analysis of the data the two tricritical values of $\kappa$ bordering the $Z_2$ region are determined as

$$\kappa_{\mathrm{tric}}^{\mathrm{heavy}} = 0.11(1), \qquad \kappa_{\mathrm{tric}}^{\mathrm{light}} = 0.1625(25) \tag{5.17}$$

The comparison with results of a former study [196] on $N_\tau = 4$ lattices (fig. 5.21(b)) shows the expected shift of $\kappa_{\mathrm{tric}}$ to smaller values of the bare mass on $N_\tau = 6$, i.e. on the finer lattice for both the chiral and deconfinement region which is explained by discretization errors (c.f. section 3.5.1). As mentioned above the pseudo scalar meson masses have been computed at the corresponding couplings $\beta_{\mathrm{c,E}}$ for all $\kappa$ values. Table 5.7 summarizes the findings for the lattice spacing $a$, the critical temperature $T_{\mathrm{c}}$ and $m_{\mathrm{PS}}$. From the table it can be clearly seen that the lattice coarsens (larger $a$) as the mass is lowered which is

| $\kappa$ | $\beta$ | # confs | $w_0/a$ | $a\,m_{\mathrm{PS}}$ | $a$ {fm} | $m_{\mathrm{PS}}$ {MeV} | $N_\tau$ | $T$ {MeV} |
|---|---|---|---|---|---|---|---|---|
| 0.0910 | 5.6655 | 1600 | 0.9161(6) | 3.0107(2) | 0.192(2) | 3101(32) | 4 | 258(3) |
| 0.1000 | 5.6539 | 1600 | 0.9017(12) | 2.7285(2) | 0.195(2) | 2766(29) | | 253(3) |
| 0.1100 | 5.6341 | 1600 | 0.8789(10) | 2.4250(3) | 0.200(2) | 2396(25) | | 247(3) |
| 0.1575 | 5.3550 | 400 | 0.7104(3) | 1.1426(17) | 0.247(3) | 913(9) | | 200(2) |
| 0.1000 | 5.8698 | 1600 | 1.4650(20) | 2.5793(6) | 0.120(1) | 4248(44) | 6 | 275(3) |
| 0.1100 | 5.8567 | 1600 | 1.4594(18) | 2.2302(2) | 0.120(1) | 3659(38) | | 273(3) |
| 0.1200 | 5.8287 | 1200 | 1.4333(20) | 1.8862(4) | 0.122(1) | 3040(31) | | 269(3) |
| 0.1600 | 5.4367 | 200 | 1.1248(14) | 0.6045(15) | 0.156(2) | 764(8) | | 211(2) |
| 0.1625 | 5.3862 | 200 | 1.0700(17) | 0.5559(23) | 0.164(2) | 669(8) | | 201(2) |
| 0.1650 | 5.3347 | 200 | 1.0082(13) | 0.5184(27) | 0.174(2) | 588(7) | | 189(2) |
| 0.1300 | 5.9590 | 1600 | 1.9357(44) | 1.3896(2) | 0.091(1) | 3024(32) | 8 | 272(3) |

Table 5.7: Results of the scale setting ($T = 0$ simulations performed on $N_\tau = 32$, $N_{\mathrm{s}} = 16$ lattices). The number of independent configurations used is reported in the third column (# confs). $w_0/a$ has been determined and converted to physical scales using the publicly available code described in [79]. For the pion mass determination, eight point sources per configuration have been used. The table also contains the lattice spacing, the pion mass and the temperature of the corresponding finite temperature ensemble in physical units.(Table taken from [159])

no surprise since $\beta$ decreases. As expected, comparing the lattice spacings of $N_\tau = 4$ with the ones of $N_\tau = 6$ shows a significant decrease of $a$. Finite size effects with respect to the pseudo scalar mesons are negligible since $m_{\mathrm{PS}} L \geq 6$ for all parameter sets. The estimates for of $m_{\mathrm{PS}}$ at the tricritical points are

$$m_{\mathrm{PS,tric}}^{\mathrm{deconf}} = 3659^{+589}_{-669}\mathrm{MeV}, \qquad m_{\mathrm{PS,tric}}^{\mathrm{chiral}} = 669^{+95}_{-81}\mathrm{MeV} \tag{5.18}$$

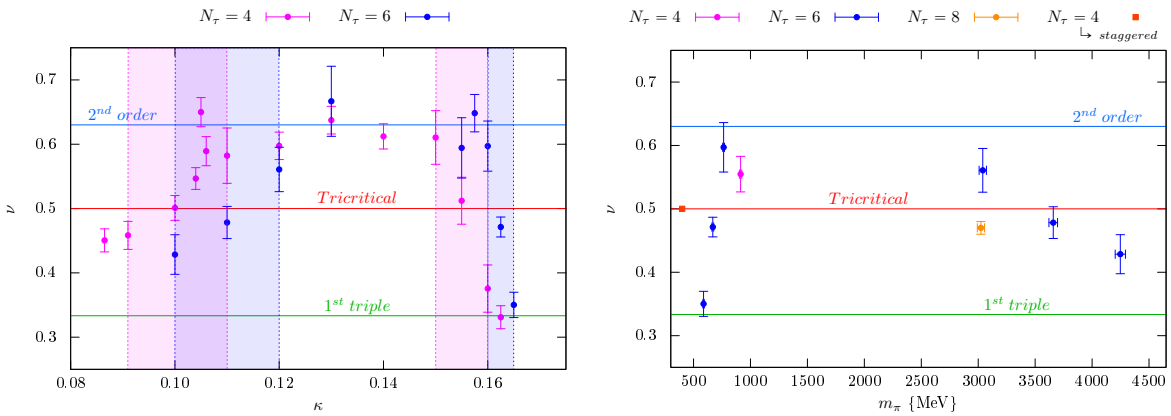


(a) $N_\tau = 4$ and $N_\tau = 6$ results.

(b) Results in terms of $m_{\mathrm{PS}}$.

Figure 5.22: Direct comparison between $N_\tau = 4$ and $N_\tau = 6$ results and comparison of $N_\tau = 4, 6, 8$ results in terms of $m_\pi$. In the latter case, the value of $m^{\mathrm{chiral}}_{\mathrm{PS,tric}}$ from [200] has been included as well. For the sake of clarity, not all the $N_\tau = 4$ points have been included. The vertical coloured bands highlight the position of the tricritical masses. A shift toward small masses (i.e. bigger $\kappa$) is evident as $N_\tau$ is increased.(Figure taken from [159])

In the deconfinement region the value of the pseudo scalar mass in lattice units is about $am^{\mathrm{deconf}}_{\mathrm{PS,tric}} \approx 2.7$ for $N_\tau = 4$ and $am^{\mathrm{deconf}}_{\mathrm{PS,tric}} \approx 2.2$ for $N_\tau = 6$ This implies large systematic errors and prevents a quantitative statement about the shift in physical units. In contrast in the chiral region the mass in lattice units is about $am^{\mathrm{chiral}}_{\mathrm{PS,tric}} \approx 1.1$ for $N_\tau = 4$ while for $N_\tau = 6$ it is even already significantly below one with $am^{\mathrm{chiral}}_{\mathrm{PS,tric}} \approx 0.55$. This values represent an acceptable range for a quantitative statement about the shift which is around $35\%$ from $N_\tau = 4$ with $m^{\mathrm{chiral}}_{\mathrm{PS,tric}} \approx 910$MeV to $N_\tau = 6$ with $m^{\mathrm{chiral}}_{\mathrm{PS,tric}} \approx 670$MeV. Note that the corresponding critical temperature $T_{\mathrm{c}}$ hardly changes with $N_\tau$ and stays roughly around 200MeV. A different study with Wilson-Clover fermions [135] of the $N_f = 3$ chiral region found a similar magnitude of shifts in the pseudo scalar meson masses at the tricritical points. Interestingly a comparison of the results of this work with the ones of a study with staggered fermions [200] shows that the Wilson value of $m^{\mathrm{chiral}}_{\mathrm{PS,tric}}$ for $N_\tau = 6$ is still larger than the staggered value for $N_\tau = 4 (\approx 400\mathrm{MeV})$. These observations suggest that the region where linear cut-off effects dominate the standard Wilson action is not reached at $N_\tau \lesssim 6$. Hence it can be concluded that much larger $N_\tau$ are needed for both Wilson and staggered fermions. This is supported by studies about the equation of state where different fermion discretizations start to agree at $N_\tau \gtrsim 12$ only. An overview can be found for instance in [201]. As an initial advance towards finer lattices at the Roberge-Weiss value of the chemical potential simulations of $\kappa = 0.13$ at $N_\tau = 8$ with spatial extents of $N_{\mathrm{s}} = 16, 24, 32, 40$ were included in this study, i.e. aspect ratios of 2-5 (simulation details are shown in table A.9). As expected significantly increased computational costs are experienced leading to lower statistics especially at $N_{\mathrm{s}} = 40$ compared to the previous simulations. Thus the critical exponent $\nu$ was computed from the three lower aspect ratios yielding a value of $\nu = 0.47(1)$ which is close to the tricritical value of $\nu = 0.5$ and thus suggests that $\kappa = 0.13$ at $N_\tau = 8$ is close to the tricritical point. The lattice spacing at these parameters decreased to $a \approx 0.09$. Calculation of the pseudo scalar meson mass corresponding to the tricritical point yielded $m^{\mathrm{deconf}}_{\mathrm{PS,tric}} = 3024(23)$. Setting aside possible issues with a large value in lattice units $(am^{\mathrm{deconf}}_{\mathrm{PS,tric}} \approx 1.4)$ this result again shows a large shift of the tricritical points towards smaller masses. The critical temperature $T_{\mathrm{c}}$ at the tricritical points again stays at about the same value when advancing from $N_\tau = 6$ to 8. The results

of this study are summarized in fig. 5.22b where the tricritical regions of the different $N_\tau$ are compared. The value of $m_{\text{PS,tric}}^{\text{chiral}}$ from the study with staggered fermions [200] mentioned above is included, as well. From the figure it becomes apparent that certainly much larger $N_\tau$ are required to approach the continuum limit.

### 5.4.2 Discussion

Previous studies about the nature of the Roberge-Weiss transition of $N_f = 2$ QCD at imaginary chemical potential on $N_\tau = 4$ lattices were progressed to $N_\tau = 6$ and for one $\kappa$ value even to $N_\tau = 8$ whereby standard Wilson fermions were used. Large amounts of data were produced in order to perform a sound finite size scaling analysis. A model (not part of this work) introduced in [159] helped to understand the reason why the kurtosis assumes values larger than the expected ones in the region where the Roberge-Weiss endpoint is a first order triple point. The observation can be explained by finite size effects related to the merging of a three peak distribution as a function of the lattice coupling. The determined phase structure qualitatively reproduces the one on coarser $N_\tau = 4$ lattices but the tricritical points were found to shift considerably to larger $\kappa$ values, i.e. to smaller masses on finer lattices both in the chiral as well as in the deconfinement region. Although discretization effects could be decreased in magnitude, the findings suggest that even much finer lattices are required for the phase structure to settle at its continuum values.

## 5.5 Linking Results from $\mu = 0$ and $\mu_{i,c}$

The information about the critical points that has been acquired in the heavy quark mass region at $\mu = 0$ and $\mu_{i,c}$ can be compared and shown to be consistent with previously established expectations: Estimates for $\kappa_{Z_2}$ at $\mu = 0$ and $\kappa_{\text{tric}}^{\text{heavy}}$ at $\mu_{i,c}$ on $N_\tau = 6$ have been produced. For $N_\tau = 8$ now an estimate of $\kappa_{Z_2}$ is available, as well and at $\mu_{i,c}$ a value of $\kappa < \kappa_{\text{tric}}^{\text{heavy}}$ has been found which can be assumed to be very close to $\kappa_{\text{tric}}^{\text{heavy}}$. On $N_\tau = 6$ the findings are $\kappa_{Z_2} = 0.0939(14)$ at $\mu = 0$ and $\kappa_{\text{tric}}^{\text{heavy}} = 0.11(1)$ at $\mu_{i,c}$, with a difference of $\Delta_{\kappa,N_\tau=6} = 0.016(10)$, which confirms a strengthening of the first order transition as the imaginary chemical potential is turned on. On $N_\tau = 8$ lattices the difference between $\kappa_{Z_2} = 0.1167(12)$ and $\kappa = 0.13(1)$ (close to $\kappa_{\text{tric}}^{\text{heavy}}$) is $\Delta_{\kappa,N_\tau=8} = 0.013(10)$ which is consistent with $\Delta_{\kappa,N_\tau=6}$. Of course this comparison is very rough since $\kappa_{\text{tric}}^{\text{heavy}}$ was not used for $N_\tau = 8$ but a value $\kappa < \kappa_{\text{tric}}^{\text{heavy}}$ just close to it.

A comparison between the pseudo scalar masses in lattice units at the $Z_2$ point at $\mu = 0$ and the tricritical point at $\mu_{i,c}$ shows a significant difference. For $N_\tau = 6$ this difference is $\approx 20\%$ ($am_{\text{PS},Z_2} \approx 2.8$ at $\mu = 0$ and $am_{\text{PS,tric}} = 2.23$ at $\mu_{i,c}$) and for $N_\tau = 8$ it is $\approx 25\%$ ($am_{\text{PS},Z_2} \approx 1.86$ at $\mu = 0$ and $am_{\text{PS,tric}} = 1.38$ at $\mu_{i,c}$), c.f. table 5.8. The point in noting this difference can have the following possible implications for the strategy pursued in the future steps of the project:

1. The smaller pseudo scalar mass in lattice units at the tricritical point at $\mu_{i,c}$ implies a smaller discretization error and hence a more reliable extraction of the mass in physical units. For instance if a similar shift of the pseudo scalar mass in lattice units between the $Z_2$ point at $\mu = 0$ and the tricritical point at $\mu_{i,c}$ occurs on $N_\tau = 10$, a value $am_{\text{PS,tric}} \approx 1$ could be expected at $\mu_{i,c}$. Consequently one could consider continuing the study in the Roberge-Weiss plane and, once a continuum extrapolation is available, use tricritical scaling relations, discussed in section 3.5.3, to find the corresponding continuum value at $\mu = 0$.

2. At larger values of $\kappa$ the transition temperature $T_c$ is lower, which implies an increase of the lattice spacing $a$. A larger lattice spacing a) is less costly to simulate in terms of computational resources and b) leads effectively to a slightly larger physical volume which helps with finite volume effects.

3. In the Roberge-Weiss plane the order parameter is not $|P|$ anymore but Im$P$. Remember that at $\mu = 0$ there is the problem, that $B_4(|P|)$ does not assume the value characteristic for a first order transition, i.e. $B_4 = 1$, but a value that is positively shifted relative to the first order value (c.f. section 5.3.1). In contrast in the Roberge-Weiss plane it has been shown (c.f. fig. 5.20) that $B_4$ approaches one, even at much smaller volumes compared to the ones used at $\mu = 0$! This is related to the fact that the distribution of Im$P$ exhibits a two/three peak structure with a more distinct separation of the peaks. Thus the kind of finite volume effects experienced at $\mu = 0$ with respect to the first order value of $B_4$ are not present at $\mu_{i,c}$.

Of course, one should not forget about the larger computational expenses implied by the smaller quark masses at the tricritical point at $\mu_{i,c}$ compared to the quark masses at the $Z_2$ point at $\mu = 0$.

| $N_\tau$ | 6 | | 8 | | 10 | |
|---|---|---|---|---|---|---|
| | $am_{\mathrm{PS}}$ | $\kappa_c$ | $am_{\mathrm{PS}}$ | $\kappa_c$ | $am_{\mathrm{PS}}$ | $\kappa_c$ |
| $\mu = 0$ | 2.8 | 0.0939(14) | 1.86 | 0.1167(12) | 1.6 | 0.1229(10) |
| $\mu_{i,c}$ | 2.23 | 0.11(1) | 1.38 | 0.13 | | |

Table 5.8: The critical $\kappa$ values ($\kappa_c = \kappa_{Z_2}$ for $\mu = 0$ and $\kappa_c = \kappa_{\mathrm{tric}}^{\mathrm{heavy}}$ for $\mu_{i,c}$) of the heavy quark mass region are summarized. Next to the $\kappa_c$ values are the respective pseudo scalar meson masses in lattice units. As expected, the $\kappa_c$ values increase from $\mu = 0$ to $\mu_{i,c}$. This implies smaller pseudo scalar masses which have smaller values in lattice units.

# Chapter 6

# Conclusions and Perspectives

The presented LQCD study of the chiral and deconfinement phase transitions of QCD by numerical means of (rational) hybrid Monte Carlo simulations, using the CL$^2$QCD software, represents an important contribution to the exploration of the Columbia plot at $\mu = 0$ (l.h.s. fig. 5.1) and $\mu_{i,c}$ (r.h.s. fig. 5.1).

In particular the study about the phase transitions for two degenerate light quark flavors in the Roberge-Weiss plane at $\mu_{i,c}$ provided a further component in the never ending debate (c.f. table 3.4) about the nature of the phase transition in the $N_f = 2$ chiral region. In this context valuable knowledge about the numerical methods and strategies used for the localization of phase transitions and the identification of the respective nature as well as about about finite volume and discretization effects was obtained. This lays the foundation for efficient future studies aiming at a continuum extrapolation of the tricritical points, separating the regions of first order triple transitions from the region of $Z_2$ transitions. Furthermore, now a large amount of data is available to compare findings to other studies using the same or different fermion discretizations as well as to use the data to employ scaling relations and analytic continuation to investigate the phase structure at $\mu = 0$. A discussion and a summary about this part is given in section 5.4.2.

These points were also achieved in the study of the $N_f = 2$ deconfinement region at $\mu = 0$ as well as at $\mu_{i,c}$. Though, at both values of the chemical potential there are different and serious problems due to an interplay of the finite (still to large) lattice spacing, the large quark masses used at the respective $N_\tau$ and the finite (still to small volumes) that need to be dealt with differently. An example is given by the finite volume effects affecting $B_4$ at $\mu = 0$ and $\mu_{i,c}$ in different ways. In the first case a shift of the first order value and in the latter case a larger value in the crossover region was observed and understood. For a discussion see section 5.4.2 and section 5.3.4.

Most of the time the research community is interested in answering the question about the nature of the phase transition in the chiral regions for which reason only few finite temperature and density projects with heavy quark masses are launched but exploring this region is important for many intents and purposes: Up to date it is unknown to which degree the first order transitions surrounding the limit $m_q \to \infty$ are strengthened as the continuum limit is approached. In section 3.5.2 I already explained that a scenario in which a reduction of the discretization errors causes the critical point ($\kappa_{Z_2}$ at $\mu = 0$ and $\kappa_{\text{tric}}^{\text{heavy}}$ at $\mu_{i,c}$) to move so far to smaller masses such that it crosses the physical point is ruled out almost with certainty. Nevertheless it is interesting and important in its own right to quantify the change of the $Z_2$ point. Furthermore the data obtained by simulations in this region can serve for input or as crosscheck for theories using Langevin or strong coupling expansion. Using this as a motivation the decision was

met to start a long term project at $\mu = 0$ to find the continuum position of the $Z_2$ point in the heavy quark mass region. This work presents the first promising steps that have been successfully taken in this direction on lattices with temporal extents of $N_\tau = 6, 8$ and 10 using the Wilson fermion discretization. On $N_\tau = 6$ and 8 the value of $\kappa_{Z_2}$ was successfully determined while for $N_\tau = 10$ a preliminary estimate was produced. The findings are discussed altogether in section 5.4.2.

Simulating on lattices with increasingly larger temporal extent will not only allow in some time ($\sim 2 - 3$ years) to locate the continuum location of the $Z_2$ points, but, since unimproved Wilson fermions haven been used, to also precisely quantify how the $Z_2$ point moves as function of the lattice spacing $a$. Moreover, possible unphysical modifications by adding extra terms to the action as it is done in the case of using improvements are excluded with certainty. From the numerical simulations presented here the expectations could be confirmed: A clear reduction of the lattice spacing $a$ is achieved as the study progressed from $N_\tau = 6$ over 8 to 10. This reduced the discretization errors on the $Z_2$ point which, in terms of the bare mass parameter $\kappa$, moved to smaller masses implying an expansion of the first order region around the heavy quark mass limit. To have a physical correspondence to $\kappa$, pseudo scalar masses haven been computed, as well. These still suffer too heavily from discretization effects to make quantitative statements. Though, the reduction in the pseudo scalar mass in lattice units from $N_\tau = 6$ over 8 to 10 allows to assume, that at temporal extents $N_\tau \gtrsim 12$ discretization errors will have decreased to an extent by which pseudo scalar masses $\lesssim 1$ in lattice units will become accessible and thus allow to make quantitative statements about the shift of the $Z_2$ point in terms of physical quantities. The conclusions of the results of $N_\tau = 6, 8$ and 10 (c.f. section 5.4.2) are that a continuum result is within reach. I assume this could possibly be established with simulations of lattices with temporal extents $N_\tau = 12, 14$ and 16. The required computational resources will be available within one to two years. A lot of work still needs to be done but if this project can be successfully brought to an end within a couple of years it represents the first LQCD project to achieve the goal of a continuum extrapolation in the heavy quark mass region.

Due to the implementation of the Rational Hybrid Monte Carlo algorithm in CL$^2$QCD the first step in a possible series of investigations of the chiral/deconfinement transitions in the $N_f = 3$ theory has been done, as well. For reasons of temporal and computational resource limitations as well as for testing purposes of the newly implemented code the study was conducted on computationally cheap lattices with temporal extents of $N_\tau = 4$ which implies coarse lattices.

In the course of this work many different problems and open issues occurred, which could not be further treated given the temporal limitations. In the following these problems will be addressed.

One of the problems of great relevance, in my opinion, is the computation of physical quantities to identify the $Z_2$ and tricritical points, respectively, in the $N_f = 2$ part of the project. Stating their position in terms of the bare parameter $\kappa$ is of very limited informative value. Computing the pseudo scalar mass $m_{\mathrm{PS}}$ is, in the heavy quark mass region, accompanied by values of the mass in lattice units $> 1$. What could be tested is to compute the masses of the constituents of the pseudo scalar meson, i.e. $m_{u,d}$. These masses are expected to be smaller in physical as well as in lattice units. At the same time the kinetic mass of $m_{\mathrm{PS}}$ could be computed and analyzed which possibly allows to make a rather quantitative statement about the severeness of the discretization effects on $m_{\mathrm{PS}}$. This possibility was briefly addressed in section 5.3. Regarding the $N_f = 3$ simulations, attempts to compute physical quantities like $m_{\mathrm{PS}}$ have not been done at all. The simulations should be progressed to finer lattices before this issue is approached, taking into account what was learned in the $N_f = 2$ simulations and analysis thereof.

In section 5.3 the kurtosis equation used for finite size scaling analyses was extended by a correction term [72], discussed in section 3.1.3, which led to a significant improvement of the finite size scaling analyses carried out to determine the $Z_2$ points. It remained unclear whether the origin of this term can be connected to the finite size effects on $B_4$ at $\mu = 0$. This should be checked in a further theoretical analysis. Alternatively, it could be checked whether the model used to explain the kurtosis bump [159, 190] briefly addressed in section 5.4.1) could be adapted to investigate the finite size effects on $B_4$ at $\mu = 0$, as well. Currently this model is based on symmetries specific to the Roberge-Weiss plane ($\mu_{i,c}$) and thus cannot simply be used for the situation at $\mu = 0$.

Another approach that could be further pursued in this project to see if the finite size effects on $B_4$ at $\mu = 0$ can be circumvented is to use tricritical scaling, starting from tricritical points at $\mu_{i,c}$. Moreover at this value of the chemical potential the pseudo scalar and quark masses at the tricritical points are smaller compared to the respective masses at the $Z_2$ points at $\mu = 0$ which might act as a workaround to the problem with the masses in lattice units $> 1$, addressed above. This possibility was discussed in section 5.5.

Having the facilities for simulating the $N_f = 2$ and 3 theory, one of the next steps definitely could be to extend the CL$^2$QCD software for simulations of more realistic physics with $N_f = 2 + 1$ flavors. This would be effectively a combination of the Hybrid Monte Carlo, used for two degenerate flavors representing the up and down quark, and the Rational Hybrid Monte Carlo algorithm, used for one flavor representing the strange quark.

Again, due to temporal limitations a proper analysis of the performance of the Rational Hybrid Monte Carlo algorithm in CL$^2$QCD could not be carried out. This however, is a minor step and should be done in order to quantify a variety of factors like how well it runs on the hardware being used, its scalability, how different fermion discretizations compare in terms of performance and how it compares to algorithmically improved codes.

Before using the Rational Hybrid Monte Carlo algorithm of CL$^2$QCD for simulations in the region of lighter quark masses, the Arnoldi method, suited to check the sign of the determinant, should be implemented. Towards smaller quark masses, this becomes increasingly important as explained in section 4.2.

There are numerous algorithmic improvements of paramount importance waiting to be implemented in order to keep CL$^2$QCD competitive among other software for simulating LQCD in the near future. These include the following. The probably most straightforward method, which is currently being implemented into the staggered part of CL$^2$QCD by members of our group, is the multiple pseudo fermions approach for small fermion masses. It brings integrator instabilities under control and vastly reduces the computational cost to generate gauge field configurations with light fermions, which represents the most costly part of lattice quantum chromodynamics computations [168]. Another approach for simulations at small quark masses are low-mode deflation techniques like domain-decomposed deflation subspaces for propagation along the HMC field trajectories. The quark forces then can be computed using a deflation-accelerated solver for the lattice Dirac operator. This leads to a significantly reduced computer time for the simulations as well as to an improved scaling behavior with respect to the quark mass [202]. Another candidate method for implementation in CL$^2$QCD and widely used nowadays to reduce critical slowing down in simulations with very small quark masses is the multigrid approach which, roughly spoken, works with smoothening and discretization on successively coarser lattice grids to accelerate the solution finding

process. An example is the adaptive multigrid algorithm for lattice QCD [203]. Apart from the algorithmic improvements another natural choice for an improvement would be to implement the possibility for multi-gpu parallelization. At the time of writing this is only possible for the temporal direction. If simulations with larger lattices are to be carried out efficiently in the future, a multi-gpu parallelization for the spatial direction is a necessity.

As last point it is worthwhile to mention the BaHaMAS software described in section 4.4. Its development helped significantly to avoid comitting errors in the management and structuring process of the hundreds of simulations conducted to obtain the results of this work. Certainly a large amount of time was invested into its development but this time was made up for easily by saving it later on in all the necessary steps involved in the process of running simulations.

# Appendix A

# Additional

## A.1 The Kurtosis Correction Term

In the following the starting point for the derivation of the correction term ((A.1)-(A.7)) is based on the presentation in [72]. As discussed in section 3.1.3, in finite size scaling theory the free energy as a function of the reduced temperature $\tau$, the external magnetic field $h$ and the inverse of the linear lattice size $N_\mathrm{s}^{-1}$ has the following scaling behavior when scaled by an arbitrary factor $b$,

$$F(\tau, h, N_\mathrm{s}^{-1}) = F(\tau b^{y_\tau}, h b^{y_h}, N_\mathrm{s}^{-1} b), \tag{A.1}$$

where $y_h$ and $y_\tau$ are the magnetic and temperature exponents, respectively. Setting $b = N_\mathrm{s}$,

$$F(\tau, h, N_\mathrm{s}^{-1}) = F(\tau N_\mathrm{s}^{y_\tau}, h N_\mathrm{s}^{y_h}, 1), \tag{A.2}$$

the free energy becomes independent of the spatial extent of the system. In the following we will use the abbreviation

$$F(\tau N_\mathrm{s}^{y_\tau}, 0, 1) = F(\tau N_\mathrm{s}^{y_\tau}). \tag{A.3}$$

For the next steps, we define the mixed derivatives with respect to the reduced temperature and external magnetic field,

$$\frac{\partial^n}{\partial \tau^n} \frac{\partial^m}{\partial h^m} F(\tau, h, N_\mathrm{s}^{-1}) = F^{nm}(\tau, h, N_\mathrm{s}^{-1}), \tag{A.4}$$

which, setting $h = 0$, evaluates to

$$\frac{\partial^n}{\partial \tau^n} \frac{\partial^m}{\partial h^m} F(\tau, h, N_\mathrm{s}^{-1}) \bigg|_{h=0} = N_\mathrm{s}^{n y_\tau + m y_h} F^{nm}(\tau N_\mathrm{s}^{y_\tau}). \tag{A.5}$$

For an obsersable that is a mixture of energy $E$ and magnetization $M$ one can write

$$O = c_E E + c_M M \longrightarrow c_E \frac{\partial}{\partial \tau} + c_M \frac{\partial}{\partial m} \tag{A.6}$$

Then the kurtosis for $h = 0$ is given by

$$K(\tau, 0, N_\mathrm{s}^{-1}) = \frac{\left(c_E \frac{\partial}{\partial \tau} + c_M \frac{\partial}{\partial m}\right)^4 F(\tau, h, N_\mathrm{s}^{-1}) \Big|_{h=0}}{\left[ \left(c_E \frac{\partial}{\partial \tau} + c_M \frac{\partial}{\partial m}\right)^2 F(\tau, h, N_\mathrm{s}^{-1}) \Big|_{h=0} \right]^2} \tag{A.7}$$

This can be expressed in terms of the binomial theorem (for readability $F(\tau N_\mathrm{s}^{y_\tau}) = F$)

$$K(\tau, 0, N_\mathrm{s}^{-1}) = \frac{\sum_{k=0}^{4} \binom{4}{k} c_E^{4-k} c_M^k N_\mathrm{s}^{(4-k)y_\tau + k y_h} F^{4-k,k}}{\sum_{l,m=0}^{2} \binom{2}{l}\binom{2}{m} c_E^{4-l-m} c_M^{l+m} N_\mathrm{s}^{(4-l-m)y_\tau + (l+m)y_h} F^{2-l,l} F^{2-m,m}} \tag{A.8}$$

In the next step the factorization yields the same term as in the last step of eq. (3.16),

$$K(\tau, 0, N_\mathrm{s}^{-1}) = \frac{F^{04}(\tau N_\mathrm{s}^{y_\tau})}{\left(F^{02}(\tau N_\mathrm{s}^{y_\tau})\right)^2} \cdot \left( \frac{1 + \sum_{k=0}^{3} \binom{4}{k} c_E^{4-k} c_M^k N_\mathrm{s}^{N(k)} \frac{F^{4-k,k}}{F^{04}}}{1 + \sum\limits_{\substack{l,m=0 \\ l,m\neq(2,2)}}^{2} \binom{2}{l}\binom{2}{m} c_E^{4-l-m} c_M^{l+m} N_\mathrm{s}^{D(l,m)} \frac{F^{2-l,l} F^{2-m,m}}{(F^{02})^2}} \right), \tag{A.9}$$

where for the exponents of $N_\mathrm{s}$ in the numerator and denominator of the second term in (A.9) we defined

$$\begin{aligned} N(k) &= (4-k)y_\tau + k y_h - 4y_h \\ D(l,m) &= (4-l-m)y_\tau + (l+m)y_h - 4y_h. \end{aligned} \tag{A.10}$$

To obtain a correction term that is of leading order in $N_\mathrm{s}^{y_\tau - y_h}$ we have to find the corresponding values of $k, l, m$ for $N(k)$ and $D(l,m)$, i.e.

$$N(k) = (4-k)y_\tau + k y_h - 4y_h \overset{!}{=} y_\tau - y_h \longrightarrow k = 3, \tag{A.11}$$

and

$$D(l,m) = (4-l-m)y_\tau + (l+m)y_h - 4y_h \overset{!}{=} y_\tau - y_h \longrightarrow l, m = (1,2), (2,1). \tag{A.12}$$

Writing the terms of sum with the above values of $k, l, m$ explicitly reads:

$$\begin{aligned} K(\tau, 0, N_\mathrm{s}^{-1}) = &\frac{F^{04}(\tau N_\mathrm{s}^{y_\tau})}{\left(F^{02}(\tau N_\mathrm{s}^{y_\tau})\right)^2} \\ &\cdot \left( \frac{1 + 4\frac{c_E}{c_M} N_\mathrm{s}^{y_\tau - y_h} \frac{F^{13}}{F^{04}} + \sum_{k=0}^{2} \binom{4}{k} c_E^{4-k} c_M^k N_\mathrm{s}^{N(k)} \frac{F^{4-k,k}}{F^{04}}}{1 + 4\frac{c_E}{c_M} N_\mathrm{s}^{y_\tau - y_h} \frac{F^{11}}{F^{02}} + \sum\limits_{\substack{l,m=0 \\ l,m\neq(2,2),(1,2),(2,1)}}^{2} \binom{2}{l}\binom{2}{m} c_E^{4-l-m} c_M^{l+m} N_\mathrm{s}^{D(l,m)} \frac{F^{2-l,l} F^{2-m,m}}{(F^{02})^2}} \right). \end{aligned} \tag{A.13}$$

Using the expansion $(1+y)/(1+x) = (1+y)(1-x) + \mathcal{O}(x^2)$ the fraction in (A.13) can be expanded as:

$$\begin{aligned} K(\tau, 0, N_\mathrm{s}^{-1}) =& \frac{F^{04}(\tau N_\mathrm{s}^{y_\tau})}{\left(F^{02}(\tau N_\mathrm{s}^{y_\tau})\right)^2} \left( 1 + 4\frac{c_E}{c_M} N_\mathrm{s}^{y_\tau - y_h} \frac{F^{13}}{F^{04}} + \sum_{k=0}^{2} \binom{4}{k} c_E^{4-k} c_M^k N_\mathrm{s}^{N(k)} \frac{F^{4-k,k}}{F^{04}} \right) \\ &\cdot \left( 1 - 4\frac{c_E}{c_M} N_\mathrm{s}^{y_\tau - y_h} \frac{F^{11}}{F^{02}} + \mathcal{O}\left( N_\mathrm{s}^{2(y_\tau - y_h)} \right) \right) \\ =& \frac{F^{04}(\tau N_\mathrm{s}^{y_\tau})}{\left(F^{02}(\tau N_\mathrm{s}^{y_\tau})\right)^2} \left( 1 + 4\frac{c_E}{c_M} N_\mathrm{s}^{y_\tau - y_h} \left( \frac{F^{13}}{F^{04}} - \frac{F^{11}}{F^{02}} \right) + \mathcal{O}\left( N_\mathrm{s}^{2(y_\tau - y_h)} \right) \right) \\ =& \frac{F^{04}(\tau N_\mathrm{s}^{y_\tau})}{\left(F^{02}(\tau N_\mathrm{s}^{y_\tau})\right)^2} \left( 1 + B N_\mathrm{s}^{y_\tau - y_h} + \mathcal{O}\left( N_\mathrm{s}^{2(y_\tau - y_h)} \right) \right), \end{aligned} \tag{A.14}$$

where in the last step we defined

$$B = 4\frac{c_E}{c_M}\left(\frac{F^{13}}{F^{04}} - \frac{F^{11}}{F^{02}}\right). \tag{A.15}$$

Expanding the first term in the last step of (A.14) around $\tau = 0$, as it is done in (3.22), yields:

$$K(\tau, 0, N_{\mathrm{s}}^{-1}) = \left(\frac{F^{04}(0)}{\left(F^{02}(0)\right)^2} + c_K \tau N_{\mathrm{s}}^{1/\nu}\right)\left(1 + BN_{\mathrm{s}}^{y_\tau - y_h} + \mathcal{O}\left(N_{\mathrm{s}}^{2(y_\tau - y_h)}\right)\right) \tag{A.16}$$

## A.2 Fermion Force Computation with Even/Odd Preconditioning

For the computation of the pseudofermion force $\delta S_{\mathrm{PF}}$ which is needed for the Rational Hybrid Monte Carlo algorithm discussed in section 4.2 it will be necessary to perform matrix inversions using the multi-shift conjugate gradient solver. In this process computational expenses can be considerably reduced by employing even/odd preconditioning and factorization of the Wilson-Dirac operator. In this way the problem size can be cut into half hence reducing significantly the number of floating point operations. The following presentation is based partially on the presentation in [204]. For the following discussion we will use the hermitian two flavor operator

$$Q \equiv \gamma_5 D = \begin{pmatrix} Q^+ & \\ & Q^- \end{pmatrix}. \tag{A.17}$$

The matrices $Q^\pm$ can be written in terms of even/odd preconditioning:

$$Q^\pm = \gamma_5 \begin{pmatrix} D_{ee}^\pm & D_{eo} \\ D_{oe} & D_{oo}^\pm \end{pmatrix} = \begin{pmatrix} 1 \pm i\tilde{\mu}\gamma_5 & D_{eo} \\ D_{oe} & 1 \pm i\tilde{\mu}\gamma_5 \end{pmatrix} \tag{A.18}$$

where $D_{ee}^\pm$ and $D_{oo}^\pm$ are defined for the case of twisted mass fermions by including the twisted mass parameter $\tilde{\mu}$. The standard Wilson-Dirac operator can be recovered from simply setting the twisted mass parameter to zero. The reason for starting from this notation is again (c.f. section 4.2) the implementation of twisted mass fermions in CL$^2$QCD. If the reader intents to work on CL$^2$QCD the equations presented here can be indentified in the code. The implementation is such that, if standard Wilson fermions are used the operators $Q^+$ and $Q^-$ simply become $Q = Q^+ = Q^-$. The block matrices $D_{ee}$ and $D_{oo}$ are site-diagonal and only mix colors and spin. The block matrices off the diagonal, $D_{eo}$ and $D_{oe}$, obey $\gamma_5$-hermiticity: $D_{eo}^\dagger = \gamma_5 D_{oe} \gamma_5$. A possible Schur decomposition based on whether the matrix elements connect even or odd sites reads:

$$Q^\pm = \begin{pmatrix} \mathbb{1} & D_{eo}\left(D_{oo}^\pm\right)^{-1} \\ 0 & \mathbb{1} \end{pmatrix} \begin{pmatrix} \gamma_5\left(D_{ee}^\pm - D_{eo}\left(D_{oo}^\pm\right)^{-1} D_{oe}\right) & 0 \\ 0 & D_{oo} \end{pmatrix} \begin{pmatrix} \mathbb{1} & 0 \\ \left(D_{oo}^\pm\right)^{-1} D_{oe} & \mathbb{1} \end{pmatrix} \tag{A.19}$$

The fermion determinant written in terms of pseudo fermion fields is given by

$$\det Q = \det Q^+ Q^- = \int \mathcal{D}\phi \mathcal{D}\phi^\dagger \exp(-S_{\mathrm{PF}}), \tag{A.20}$$

$$S_{\mathrm{PF}} = \phi^\dagger \left(Q^+ Q^-\right)^{-1} \phi. \tag{A.21}$$

The determinant factorizes and is proportional to the determinant of the submatrices:

$$\det Q^+ Q^- = \det Q^+ \det Q^- \propto \det \hat{Q}^+ \det \hat{Q}^-, \tag{A.22}$$

where we defined

$$\hat{Q}^{\pm} = \gamma_5 \left( M_{ee}^{\pm} - M_{eo}(M_{oo}^{\pm})^{-1} M_{oe} \right), \tag{A.23}$$

which is only defined on the even sites of the lattice. Due to rel. (A.22) the pseudo fermion determinant and action can be written in terms of pseudo fermion fields $\phi_e$:

$$\det \hat{Q}^{+}\hat{Q}^{-} = \int \mathcal{D}\phi_e \mathcal{D}\phi_e^{\dagger} \exp(-S_{\text{PF}}), \tag{A.24}$$

$$S_{\text{PF}} = \phi_e^{\dagger} \left( \hat{Q}^{+}\hat{Q}^{-} \right)^{-1} \phi_e. \tag{A.25}$$

The pseudo fermion force is given by the variation of the pseudo fermion action with respect to the gauge fields. Using the identity [1] it follows:

$$\begin{aligned} \delta S_{\text{PF}} = &- \Big[ \phi_e^{\dagger} \left( \hat{Q}^{+}\hat{Q}^{-} \right)^{-1} \left( \delta \hat{Q}^{+} \right) \hat{Q}^{-} \left( \hat{Q}^{+}\hat{Q}^{-} \right)^{-1} \phi_e + \\ &\quad \phi_e^{\dagger} \left( \hat{Q}^{+}\hat{Q}^{-} \right)^{-1} \hat{Q}^{+} \left( \delta \hat{Q}^{-} \right) \left( \hat{Q}^{+}\hat{Q}^{-} \right)^{-1} \phi_e \Big] \\ = &- \left[ X_e^{\dagger} \delta \hat{Q}^{+} Y_e + Y_e^{\dagger} \delta \hat{Q}^{-} X_e \right], \end{aligned} \tag{A.26}$$

where we defined

$$X_e = \left( \hat{Q}^{+}\hat{Q}^{-} \right)^{-1} \phi_e, \qquad Y_e = \hat{Q}^{-} X_e \tag{A.27}$$

Evaluating $\delta \hat{Q}^{\pm}$ gives

$$\delta \hat{Q}^{\pm} = \gamma_5 \left( -\delta M_{eo}(M_{oo}^{\pm})^{-1} M_{oe} - M_{eo}(M_{oo}^{\pm})^{-1} \delta M_{oe} \right). \tag{A.28}$$

Inserting this into eq. (A.26) yields

$$\begin{aligned} \delta S_{\text{PF}} = - \Big[ &\underbrace{-X_e^{\dagger}\gamma_5 \delta M_{eo}(M_{oo}^{+})^{-1} M_{eo} Y_e}_{(1)} \underbrace{-X_e^{\dagger}\gamma_5 M_{eo}(M_{oo}^{+})^{-1} \delta M_{oe} Y_e}_{(2)} \\ &\underbrace{-Y_e^{\dagger}\gamma_5 \delta M_{eo}(M_{oo}^{-})^{-1} M_{oe} X_e}_{(3)} \underbrace{-Y_e^{\dagger}\gamma_5 M_{eo}(M_{oo}^{-})^{-1} \delta M_{oe} X_e}_{(4)} \Big] \end{aligned} \tag{A.29}$$

In the following we rearrange the terms $(1)$-$(4)$ in eq. (A.29) and define fields on the odd sites of the lattice, indicated by the colored terms.

$$\begin{aligned} (1) = &- X_e^{\dagger}\gamma_5 \delta M_{eo}(M_{oo}^{+})^{-1} M_{eo} Y_e \\ = &X_e^{\dagger}\gamma_5 \delta M_{eo} \Big( - \left( M_{oo}^{\pm} \right)^{-1} M_{oe} Y_e \Big) \\ = &X_e^{\dagger}\gamma_5 \delta M_{eo} Y_o \end{aligned} \qquad \begin{aligned} (3) = &- Y_e^{\dagger}\gamma_5 \delta M_{eo}(M_{oo}^{-})^{-1} M_{oe} X_e \\ = &Y_e^{\dagger}\gamma_5 \delta M_{eo} \Big( - \left( M_{oo}^{-} \right)^{-1} M_{eo} X_e \Big) \\ = &Y_e^{\dagger}\gamma_5 \delta M_{eo} X_o. \end{aligned} \tag{A.30}$$

In (2) and (4) we additionally use the properties $M_{oe}^{\dagger} = \gamma_5 M_{eo} \gamma_5$ and $M_{oe}^{\dagger} = \gamma_5 M_{eo} \gamma_5$:

$$\begin{aligned} (2) = &- X_e^{\dagger}\gamma_5 M_{eo}(M_{oo}^{+})^{-1} \delta M_{oe} Y_e \\ = &- X_e^{\dagger}\gamma_5 M_{eo}\gamma_5\gamma_5 \left( M_{oo}^{+} \right)^{-1} \delta M_{oe} Y_e \\ = &- X_e^{\pm} M_{oe}^{\dagger} \left( M_{oo}^{\pm} \right)^{-1} \gamma_5 \delta M_{oe} Y_e \\ = &\Big( - \left( M_{oo}^{-} \right)^{-1} M_{oe} X_e \Big)^{\dagger} \gamma_5 \delta M_{oe} Y_e \\ = &X_o^{\dagger}\gamma_5 \delta M_{oe} Y_e \end{aligned} \qquad \begin{aligned} (4) = &- Y_e^{\dagger}\gamma_5 M_{eo}(M_{oo}^{-})^{-1} \delta M_{oe} X_e \\ = &- Y_e^{\dagger}\gamma_5 M_{eo}\gamma_5\gamma_5 \left( M_{oo}^{-} \right)^{-1} \delta M_{oe} X_e \\ = &- Y_e^{\dagger} M_{oe}^{\dagger} \left( M_{oo}^{-} \right)^{-1} \gamma_5 \delta M_{oe} X_e \\ = &\Big( - \left( M_{oo}^{+} \right)^{-1} M_{oe} Y_e \Big)^{\dagger} \gamma_5 \delta M_{oe} X_e \\ = &Y_o^{\dagger}\gamma_5 \delta M_{oe} X_e. \end{aligned} \tag{A.31}$$

[1] $\delta\left(M^{-1}M\right) = \delta\left(M^{-1}\right) M + M^{-1}(\delta M) = 0 \quad \Rightarrow \quad \delta\left(M^{-1}\right) = -M^{-1}(\delta M) M^{-1}$.
In the case of (A.24), $M = \hat{Q}^{+}\hat{Q}^{-}$

Using the definitions of $X_o$ and $Y_o$ the force can be written as

$$\delta S_{\text{PF}} = -\left[X_e^\dagger \gamma_5 \delta M_{eo} Y_o + X_o^\dagger \gamma_5 \delta M_{oe} Y_e + Y_e^\dagger \delta M_{eo} X_o + Y_o^\dagger \gamma_5 \delta M_{oe} X_e\right]. \tag{A.32}$$

Furthermore we can define fields $X$ and $Y$ for the full lattice:

$$X = \begin{pmatrix} X_e \\ X_o \end{pmatrix} = \begin{pmatrix} X_e \\ -\left(M_{oo}^-\right)^{-1} M_{oe} X_e \end{pmatrix}, \qquad Y = \begin{pmatrix} Y_e \\ Y_o \end{pmatrix} = \begin{pmatrix} Y_e \\ -\left(M_{oo}^+\right)^{-1} M_{oe} Y_e \end{pmatrix}. \tag{A.33}$$

Using the variations $\delta Q^\pm$ which are given by

$$\delta Q^\pm = \gamma_5 \delta \begin{pmatrix} M_{ee}^\pm & M_{eo} \\ M_{oe} & M_{oo}^\pm \end{pmatrix} = \gamma_5 \begin{pmatrix} 0 & \delta M_{eo} \\ \delta M_{oe} & 0 \end{pmatrix}, \tag{A.34}$$

(the variation of the constant terms $M_{ee}^\pm$ and $M_{oo}^\pm$ with respect to the gauge fields vanish, $\delta M_{ee}^\pm = 0$) and the definitions of the fields $X$ and $Y$ the force $\delta S_{\text{PF}}$ can be written in a more compact way:

$$\begin{aligned} \delta S_{\text{PF}} &= -\left(X^\dagger \delta Q^+ Y + Y^\dagger \delta Q^- X\right) \\ &= -\left(X^\dagger \delta Q^+ Y + \left(X^\dagger \delta Q^- Y\right)^\dagger\right). \end{aligned} \tag{A.35}$$

## A.3 Simulation Statistics, $\mu = 0$

### A.3.1 $N_f = 2, N_\tau = 6$

| $\kappa$ | $\beta$ range | Tot. stats. per $N_s$ ∣ # of simulated $\beta$ values | | |
|---|---|---|---|---|
| | | 30 | 36 | 42 |
| 0.0750 | 5.8870-5.8900 | 1.6M ∣ 2 | 1.4M ∣ 2 | 0.9M ∣ 2 |
| 0.0850 | 5.8832-5.8860 | 2.0M ∣ 2 | 2.3M ∣ 2 | 1.6M ∣ 2 |
| 0.0900 | 5.8750-5.8850 | 1.9M ∣ 3 | 2.8M ∣ 3 | 2.2M ∣ 3 |
| 0.1000 | 5.8650-5.8700 | 1.8M ∣ 2 | 1.9M ∣ 2 | 2.1M ∣ 2 |
| 0.1100 | 5.8400-5.8500 | 2.1M ∣ 3 | 2.4M ∣ 3 | 2.2M ∣ 3 |

Table A.1: Statistics overview of $N_\tau = 6$.

| $\kappa$ | $aN_s$[fm] | | |
|---|---|---|---|
| | $a30$ | $a36$ | $a42$ |
| 0.0750 | 3.525(18) | 4.23(2) | 4.94(3) |
| 0.0850 | 3.54(2) | 4.25(3) | 4.96(3) |
| 0.0900 | 3.597(15) | 4.316(18) | 5.04(2) |
| 0.1000 | 3.59(2) | 4.30(3) | 5.02(3) |
| 0.1100 | 3.696(15) | 4.435(18) | 5.17(2) |

Table A.2: Physical box lengths for $N_\tau = 6$.

### A.3.2 $N_f = 2, N_\tau = 8$

| $\kappa$ | $\beta$ range | Tot. stats. per $N_s$ \| # of simulated $\beta$ values | | | |
|---|---|---|---|---|---|
| | | 24 | 32 | 40 | 48 |
| 0.1100 | 6.0200-6.0350 | – | 2.9M \| 4 | 2.3M \| 3 | 1.8M \| 3 |
| 0.1120 | 6.0160-6.0260 | 1.2M \| 3 | – | – | – |
| 0.1130 | 6.0192-6.0297 | 1.5M \| 3 | – | – | – |
| 0.1140 | 6.0166-6.0216 | 1.4M \| 3 | – | – | – |
| 0.1150 | 6.0131-6.0250 | 1.6M \| 3 | 2.0M \| 3 | 2.5M \| 3 | 1.9M \| 3 |
| 0.1160 | 6.0108-6.0208 | 1.3M \| 3 | – | – | – |
| 0.1170 | 6.0125-6.0175 | 1.4M \| 2 | – | – | – |
| 0.1180 | 6.0000-6.0200 | 1.4M \| 3 | – | – | – |
| 0.1190 | 6.0000-6.0150 | 1.3M \| 3 | – | – | – |
| 0.1200 | 5.9990-6.0150 | 3.0M \| 3 | 3.2M \| 4 | 2.5M \| 3 | 1.4M \| 3 |
| 0.1250 | 5.9710-5.9810 | 2.5M \| 3 | 2.2M \| 4 | 1.6M \| 2 | 1.0M \| 3 |
| 0.1300 | 5.9400-5.9500 | 0.6M \| 3 | 4.3M \| 4 | 1.7M \| 2 | 1.2M \| 3 |
| 0.1350 | 5.8950-5.9150 | 3.0M \| 5 | 2.0M \| 3 | – | |

Table A.3: Statistics overview of $N_\tau = 8$.

| $\kappa$ | $L$[fm] | | | |
|---|---|---|---|---|
| | $a24$ | $a32$ | $a40$ | $a48$ |
| 0.1100 | 2.117(10) | 2.822(13) | 3.528(16) | 4.234(19) |
| 0.1150 | 2.126(7) | 2.835(10) | 3.544(12) | 4.253(14) |
| 0.1200 | 2.141(10) | 2.854(13) | 3.568(16) | 4.282(19) |
| 0.1250 | 2.179(7) | 2.906(10) | 3.632(12) | 4.358(14) |
| 0.1300 | 2.213(17) | 2.950(20) | 3.690(30) | 4.430(30) |
| 0.1350 | 2.304(19) | 3.070(30) | 3.840(30) | 4.610(40) |

Table A.4: Physical box lengths for $N_\tau = 8$.

### A.3.3 $N_f = 2, N_\tau = 10$

| $\kappa$ | $\beta$ range | Tot. stats. per $N_s$ ∣ # of simulated $\beta$ values | | |
|---|---|---|---|---|
| | | 30 | 40 | 50 |
| 0.1150 | 6.1620-6.1750 | 0.7M ∣ 3 | 2.6M ∣ 5 | 0.8M ∣ 4 |
| 0.1200 | 6.1450-6.1750 | 1.4M ∣ 6 | 300k | – |
| 0.1250 | 6.1325-6.1725 | 1.0M ∣ 3 | – | – |
| 0.1300 | 6.1050-6.1250 | 2.4M ∣ 5 | 1.7M ∣ 6 | 146k ∣ 4 |
| 0.1350 | 6.0590-6.0840 | 1.1M ∣ 4 | – | – |
| 0.1400 | 5.9873-5.0023 | 0.9M ∣ 3 | 0.4M ∣ 4 | – |

Table A.5: Statistics overview of $N_\tau = 10$.

| $\kappa$ | $aN_s$[fm] | | |
|---|---|---|---|
| | $a30$ | $a40$ | $a50$ |
| 0.1150 | 1.66(2) | 2.21(3) | 2.76(4) |
| 0.1200 | 1.67(2) | 2.23(3) | 2.79(5) |
| 0.1250 | 1.67(3) | 2.23(4) | 2.79(5) |
| 0.1300 | 1.67(2) | 2.23(4) | 2.78(3) |
| 0.1350 | 1.73(3) | 2.31(5) | 2.89(6) |
| 0.1400 | 1.83(3) | 2.44(4) | 3.05(4) |

Table A.6: Physical box lengths for $N_\tau = 10$.

### A.3.4 $N_f = 3, N_\tau = 4$

| $\kappa$ | $aN_s$[fm] | | |
|---|---|---|---|
| | $a16$ | $a20$ | $a24$ |
| 0.0495 | 2.971(6) | 3.714(8) | 4.457(10) |
| 0.0520 | 2.978(8) | 3.722(10) | 4.466(12) |
| 0.0545 | 2.987(8) | 3.734(10) | 4.481(12) |
| 0.0570 | 2.997(6) | 3.746(8) | 4.495(10) |
| 0.0580 | 3.002(8) | 3.752(10) | 4.502(12) |
| 0.0595 | 3.000(10) | 3.750(12) | 4.500(14) |
| 0.0620 | 3.021(5) | 3.776(6) | 4.531(7) |

Table A.7: Physical box lengths for $N_\tau = 4$.

| $\kappa$ | $\beta$ range | Tot. stats. per $N_s$ \| # of simulated $\beta$ values | | |
|---|---|---|---|---|
| | | 16 | 20 | 24 |
| 0.0495 | 5.6800-5.6900 | 1.6M \| 2 | 2.2M \| 3 | 2.4M \| 4 |
| 0.0520 | 5.6800-5.6900 | 1.6M \| 2 | 2.2M \| 3 | 2.2M \| 3 |
| 0.0545 | 5.6792-5.6892 | 1.3M \| 2 | 2.1M \| 3 | 1.7M \| 3 |
| 0.0550 | 5.6792-5.6892 | – | – | 1.4M \| 3 |
| 0.0560 | 5.6792-5.6892 | – | – | 1.1M \| 3 |
| 0.0570 | 5.6800-5.5850 | 1.6M \| 2 | 2.5M \| 3 | 2.5M \| 3 |
| 0.0580 | 5.6760-5.6860 | – | – | 1.9M \| 4 |
| 0.0595 | 5.6750-5.6850 | 2.4M \| 3 | 3.2M \| 3 | 3.2M \| 4 |
| 0.0620 | 5.6730-5.6830 | 1.6M \| 3 | – | 2.5M \| 3 |
| 0.0650 | 5.6700-5.6800 | 1.2M \| 3 | 2.4M \| 3 | 2.2M \| 3 |

Table A.8: Statistics overview of $N_\tau = 4$.

## A.4 Simulation Statistics, $(\mu_{i,c}/T = \pi/3)$

### A.4.1 $N_f = 2, N_\tau = 6$

Table A.9 is adopted from our publication [159] and provides an overview over the statistics gathered for the study of the Roberge-Weiss plane at purely imaginary chemical potential. The kurtosis $B_4$ is a numerically straightforward but computationally expensive observable since it requires large amounts of statistics and has large autocorrelations. The moments $\{O_i\}, \{O_i^2\}, \ldots, \{O_i^n\}$ of a generic observable $O$ have different integrated autocorrelation times $\tau_{\text{int},1}, \tau_{\text{int},2}, \ldots, \tau_{\text{int},n}$ which we estimated using the Wolff algorithm [162] (c.f. section 4.1.1). To obtain the number of independent measurements of a given observable, the number of HMC trajectories has to be divided by the respective autocorrelation time. We simulated long enough to obtain at least 30 independent events per run of a given parameter set for $B_4(\mathrm{Im}\, P)$. The gathered statistics are in most cases distributed on four independent equally long Markov chains For the simulation In most cases the simulations were distributed on four independent, equally long Markov chains (replica) and run long enough until $B_4(\mathrm{Im}\, P)$ was compatible within three standard deviations between all of the chains. An examples is presented in fig. A.1 for a simulation of $N_\mathrm{s} = 18$ lattices at $\kappa = 0.1625$, showing the compatibility of $B_4(\mathrm{Im}\, P)$ between the replica for 25%, 50%, 75% and 100% of the total statistics. For the finite size scaling analysis the replica were merged to a single HMC history and analyzed as discussed in section 4.1.1.

| $N_\tau$ | $\kappa$ | $\beta$ range | Total statistics per spatial lattice size $N_\mathrm{s}$ ( # of simulated $\beta$ values \| # of chains) | | | | | | | |
|---|---|---|---|---|---|---|---|---|---|---|
| | | | 16 | 18 | 20 | 24 | 30 | 32 | 12 | 36 | 40 |
| 6 | 0.1000 | 5.846-5.902 | 6.11M (24 \| 2) | | 4.36M (16 \| 2) | 4.30M (16 \| 2) | - | | - | | |
| | 0.1100 | 5.840-5.866 | - | | 3.81M (26 \| 4) | 1.49M (14 \| 4) | 4.05M (18 \| 4) | | 1.92M (13 \| 4) | | |
| | 0.1200 | 5.818-5.845 | 5.28M (10 \| 4) | | 3.89M ( 9 \| 4) | 3.23M ( 9 \| 4) | 2.19M ( 8 \| 4) | | - | | |
| | 0.1300 | 5.776-5.798 | - | | 3.94M (25 \| 4) | 3.76M (23 \| 4) | 3.56M (16 \| 4) | | - | | |
| | 0.1550 | 5.521-5.542 | 1.40M (30 \| 1) | | 1.04M (23 \| 1) | 1.12M (24 \| 1) | 0.76M ( 9 \| 4) | | - | | |
| | 0.1575 | 5.475-5.493 | 0.59M ( 7 \| 4) | | - | 0.92M ( 7 \| 4) | 1.40M ( 7 \| 4) | | - | | |
| | 0.1600 | 5.433-5.443 | 0.52M ( 6 \| 4) | | - | 0.86M ( 6 \| 4) | 1.12M ( 6 \| 4) | | - | | |
| | 0.1625 | 5.380-5.393 | 0.92M (12 \| 4) | | - | 1.12M ( 8 \| 4) | - | | 1.38M (7 \| 4) | | |
| | 0.1650 | 5.326-5.337 | 1.99M (16 \| 4) | | 1.09M (11 \| 4) | 1.71M (12 \| 4) | - | | - | | |
| 8 | 0.1300 | 5.940-5.980 | 3.69M (9 \| 4) | | - | 5.40M (9 \| 4) | 2.00M (5 \| 4) | | 1.00M (5 \| 4) | | |

Table A.9: The table gives an overview of the total statistics accumulated in all the simulations ($N_\tau = 6$ and $\mu_i = \pi/6$) for each $N_\mathrm{s}$. Additionally, the number of simulated $\beta$ values per range and the number of replica is specified in parenthesis next to the number of trajectories. Given the number of replica, the length of each chain on average can be estimated. Note, that close to the transition at the critical temperature higher statistics were needed than in the (de)confined phase.

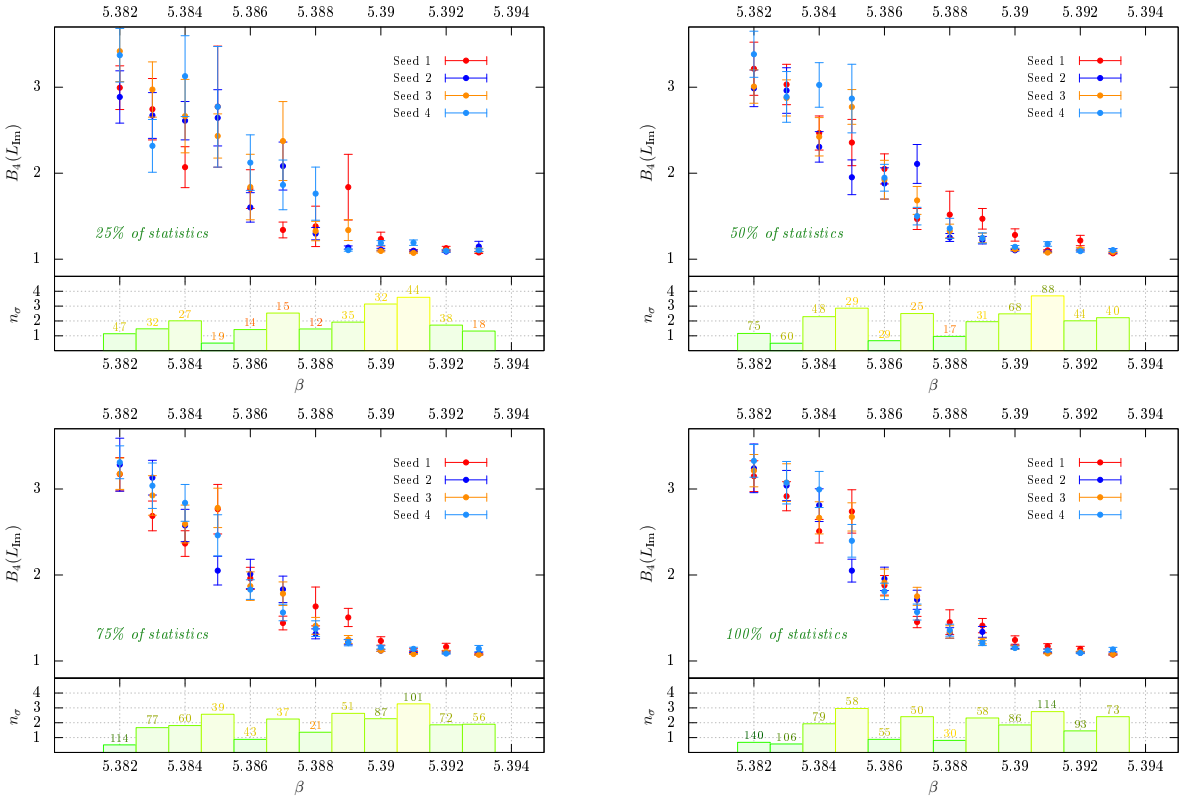


Figure A.1: The figure shows an analysis of the Kurtosis $B_4(\mathrm{Im}\, P)$ with successively increasing statistics from simulations on $N_\mathrm{s} = 18$ lattices at $\kappa = 0.1625$. The bar charts included in the lower part of the plots are intended as a guidance to judge on the statistics. $n_\sigma$ at each $\beta$ is the number of standard deviations by which the two most different chains are compatible. The numbers placed above the bars are the average numbers of independent events collected at the respective $\beta$. The colors have been chosen in order to reflect the amount of the statistics. Green color indicates that statistics are high enough while red indicates that statistics should be increased. Both $n_\sigma$ and the number of independent events have to be monitored to decide when to stop increasing statistics.

# Bibliography


[1] F. Englert and R. Brout. "Broken Symmetry and the Mass of Gauge Vector Mesons". In: *Phys. Rev. Lett.* 13 (9 Aug. 1964), pp. 321–323. DOI: 10.1103/PhysRevLett.13.321. URL: https://link.aps.org/doi/10.1103/PhysRevLett.13.321 (cit. on p. 1).

[2] Peter W. Higgs. "Broken Symmetries and the Masses of Gauge Bosons". In: *Phys. Rev. Lett.* 13 (16 Oct. 1964), pp. 508–509. DOI: 10.1103/PhysRevLett.13.508. URL: https://link.aps.org/doi/10.1103/PhysRevLett.13.508 (cit. on p. 1).

[3] Georges Aad et al. "Observation of a new particle in the search for the Standard Model Higgs boson with the ATLAS detector at the LHC". In: *Phys. Lett.* B716 (2012), pp. 1–29. DOI: 10.1016/j.physletb.2012.08.020. arXiv: 1207.7214 [hep-ex] (cit. on p. 1).

[4] Serguei Chatrchyan et al. "Observation of a new boson at a mass of 125 GeV with the CMS experiment at the LHC". In: *Phys. Lett.* B716 (2012), pp. 30–61. DOI: 10.1016/j.physletb.2012.08.021. arXiv: 1207.7235 [hep-ex] (cit. on p. 1).

[5] Harald Fritzsch and Murray Gell-Mann. "Current algebra: Quarks and what else?" In: *eConf* C720906V2 (1972), pp. 135–165. arXiv: hep-ph/0208010 [hep-ph] (cit. on p. 1).

[6] H. Fritzsch, Murray Gell-Mann, and H. Leutwyler. "Advantages of the Color Octet Gluon Picture". In: *Phys. Lett.* 47B (1973), pp. 365–368. DOI: 10.1016/0370-2693(73)90625-4 (cit. on p. 1).

[7] H. David Politzer. "Reliable Perturbative Results for Strong Interactions?" In: *Phys. Rev. Lett.* 30 (26 June 1973), pp. 1346–1349. DOI: 10.1103/PhysRevLett.30.1346. URL: https://link.aps.org/doi/10.1103/PhysRevLett.30.1346 (cit. on pp. 1, 3).

[8] David J. Gross and Frank Wilczek. "Ultraviolet Behavior of Non-Abelian Gauge Theories". In: *Phys. Rev. Lett.* 30 (26 June 1973), pp. 1343–1346. DOI: 10.1103/PhysRevLett.30.1343. URL: https://link.aps.org/doi/10.1103/PhysRevLett.30.1343 (cit. on pp. 1, 3).

[9] Murray Gell-Mann. "A Schematic Model of Baryons and Mesons". In: *Phys. Lett.* 8 (1964), pp. 214–215. DOI: 10.1016/S0031-9163(64)92001-3 (cit. on p. 1).

[10] R. P. Feynman, M. Gell-Mann, and G. Zweig. "Group $U(6) \bigotimes U(6)$ Generated by Current Components". In: *Phys. Rev. Lett.* 13 (22 Nov. 1964), pp. 678–680. DOI: 10.1103/PhysRevLett.13.678. URL: https://link.aps.org/doi/10.1103/PhysRevLett.13.678 (cit. on p. 1).

[11] M. Y. Han and Y. Nambu. "Three-Triplet Model with Double $SU(3)$ Symmetry". In: *Phys. Rev.* 139 (4B Aug. 1965), B1006–B1010. DOI: 10.1103/PhysRev.139.B1006. URL: https://link.aps.org/doi/10.1103/PhysRev.139.B1006 (cit. on p. 2).

[12] Roel Aaij et al. "Observation of $J/\psi\phi$ structures consistent with exotic states from amplitude analysis of $B^+ \to J/\psi\phi K^+$ decays". In: *Phys. Rev. Lett.* 118.2 (2017), p. 022003. DOI: 10.1103/PhysRevLett.118.022003. arXiv: 1606.07895 [hep-ex] (cit. on p. 2).

[13] Walaa I. Eshraim, Stanislaus Janowski, Francesco Giacosa, and Dirk H. Rischke. "Decay of the pseudoscalar glueball into scalar and pseudoscalar mesons". In: *Phys. Rev.* D87.5 (2013), p. 054036. DOI: 10.1103/PhysRevD.87.054036. arXiv: 1208.6474 [hep-ph] (cit. on p. 2).

[14] E. D. Bloom, D. H. Coward, H. DeStaebler, J. Drees, G. Miller, L. W. Mo, R. E. Taylor, M. Breidenbach, J. I. Friedman, G. C. Hartmann, and H. W. Kendall. "High-Energy Inelastic $e-p$ Scattering at $6^\circ$ and $10^\circ$". In: *Phys. Rev. Lett.* 23 (16 Oct. 1969), pp. 930–934. DOI: 10.1103/PhysRevLett.23.930. URL: https://link.aps.org/doi/10.1103/PhysRevLett.23.930 (cit. on p. 2).

[15] M. Breidenbach, J. I. Friedman, H. W. Kendall, E. D. Bloom, D. H. Coward, H. DeStaebler, J. Drees, L. W. Mo, and R. E. Taylor. "Observed Behavior of Highly Inelastic Electron-Proton Scattering". In: *Phys. Rev. Lett.* 23 (16 Oct. 1969), pp. 935–939. DOI: 10.1103/PhysRevLett.23.935. URL: https://link.aps.org/doi/10.1103/PhysRevLett.23.935 (cit. on p. 2).

[16] G. Myatt and D.H. Perkins. "Further observations on scaling in neutrino interactions". In: *Physics Letters B* 34.6 (1971), pp. 542–546. ISSN: 0370-2693. DOI: https://doi.org/10.1016/0370-2693(71)90676-9. URL: http://www.sciencedirect.com/science/article/pii/0370269371906769 (cit. on p. 2).

[17] Richard Phillips. Feynman. *Photon-hadron interactions [by] R. P. Feynman*. English. W. A. Benjamin Reading, Mass, 1972, xvi, 282 p. (Cit. on p. 3).

[18] G. Hanson, G. S. Abrams, A. M. Boyarski, M. Breidenbach, F. Bulos, W. Chinowsky, G. J. Feldman, C. E. Friedberg, D. Fryberger, G. Goldhaber, D. L. Hartill, B. Jean-Marie, J. A. Kadyk, R. R. Larsen, A. M. Litke, D. Lüke, B. A. Lulu, V. Lüth, H. L. Lynch, C. C. Morehouse, J. M. Paterson, M. L. Perl, F. M. Pierre, T. P. Pun, P. A. Rapidis, B. Richter, B. Sadoulet, R. F. Schwitters, W. Tanenbaum, G. H. Trilling, F. Vannucci, J. S. Whitaker, F. C. Winkelmann, and J. E. Wiss. "Evidence for Jet Structure in Hadron Production by $e^+e^-$ Annihilation". In: *Phys. Rev. Lett.* 35 (24 Dec. 1975), pp. 1609–1612. DOI: 10.1103/PhysRevLett.35.1609. URL: https://link.aps.org/doi/10.1103/PhysRevLett.35.1609 (cit. on p. 3).

[19] R. F. Schwitters, A. M. Boyarski, M. Breidenbach, F. Bulos, G. J. Feldman, G. Hanson, D. L. Hartill, B. Jean-Marie, R. R. Larsen, D. Lüke, V. Lüth, H. L. Lynch, C. C. Morehouse, J. M. Paterson, M. L. Perl, T. P. Pun, P. Rapidis, B. Richter, W. Tanenbaum, F. Vannucci, F. M. Pierre, G. S. Abrams, W. Chinowsky, C. E. Friedberg, G. Goldhaber, J. A. Kadyk, A. M. Litke, B. A. Lulu, B. Sadoulet, G. H. Trilling, J. S. Whitaker, F. C. Winkelmann, and J. E. Wiss. "Azimuthal Asymmetry in Inclusive Hadron Production by $e^+e^-$ Annihilation". In: *Phys. Rev. Lett.* 35

(20 Nov. 1975), pp. 1320–1322. DOI: 10.1103/PhysRevLett.35.1320. URL: https://link.aps.org/doi/10.1103/PhysRevLett.35.1320 (cit. on p. 3).

[20] James D. Bjorken and Stanley J. Brodsky. "Statistical Model for Electron-Positron Annihilation into Hadrons". In: *Phys. Rev. D* 1 (5 Mar. 1970), pp. 1416–1420. DOI: 10.1103/PhysRevD.1.1416. URL: https://link.aps.org/doi/10.1103/PhysRevD.1.1416 (cit. on p. 3).

[21] Murray Gell-Mann. "Symmetries of baryons and mesons". In: *Phys. Rev.* 125 (1962), pp. 1067–1084. DOI: 10.1103/PhysRev.125.1067 (cit. on p. 3).

[22] J. K. Yoh et al. "Study of Scaling in Hadronic Production of Dimuons". In: *Phys. Rev. Lett.* 41 (1978). [Erratum: Phys. Rev. Lett.41,1083(1978)], p. 684. DOI: 10.1103/PhysRevLett.41.684 (cit. on p. 3).

[23] P. Soding. "On the discovery of the gluon". In: *Eur. Phys. J.* H35 (2010), pp. 3–28. DOI: 10.1140/epjh/e2010-00002-5 (cit. on p. 4).

[24] Klaus Rabbertz. "Experimental Tests of QCD". In: *Proceedings, 9th Rencontres du Vietnam: Windows on the Universe: Quy Nhon, Vietnam, August 11-17, 2013*. 2013, pp. 85–92. arXiv: 1312.5694 [hep-ex]. URL: https://inspirehep.net/record/1272851/files/arXiv:1312.5694.pdf (cit. on p. 4).

[25] *http://www.bnl.gov/rhic/*
*http://home.web.cern.ch/about/accelerators/large-hadron-collider*
*http://www.fair-center.de* (cit. on p. 4).

[26] M. A. Clark, R. Babich, K. Barros, R. C. Brower, and C. Rebbi. "Solving Lattice QCD systems of equations using mixed precision solvers on GPUs". In: *Comput. Phys. Commun.* 181 (2010), pp. 1517–1528. DOI: 10.1016/j.cpc.2010.05.002. arXiv: 0911.3191 [hep-lat] (cit. on p. 4).

[27] *Khronos Working Group, "The OpenCL Specification,"*. URL: //www.khronos.org/registry/cl/ (cit. on pp. 4, 88, 97).

[28] Y. Aoki, G. Endrodi, Z. Fodor, S. D. Katz, and K. K. Szabo. "The Order of the quantum chromodynamics transition predicted by the standard model of particle physics". In: *Nature* 443 (2006), pp. 675–678. DOI: 10.1038/nature05120. arXiv: hep-lat/0611014 [hep-lat] (cit. on pp. 5, 48, 52).

[29] Philippe de Forcrand and Owe Philipsen. "The QCD phase diagram for small densities from imaginary chemical potential". In: *Nucl. Phys.* B642 (2002), pp. 290–306. DOI: 10.1016/S0550-3213(02)00626-0. arXiv: hep-lat/0205016 [hep-lat] (cit. on pp. 5, 45).

[30] Massimo D'Elia and Maria-Paola Lombardo. "Finite density QCD via imaginary chemical potential". In: *Phys. Rev.* D67 (2003), p. 014505. DOI: 10.1103/PhysRevD.67.014505. arXiv: hep-lat/0209146 [hep-lat] (cit. on pp. 5, 45).

[31] Owe Philipsen. "The QCD phase diagram at zero and small baryon density". In: *PoS* LAT2005 (2006). [PoSJHW2005,012(2006)], p. 016. arXiv: hep-lat/0510077 [hep-lat] (cit. on p. 5).

[32] C. Itzykson and J.B. Zuber. *Quantum Field Theory*. Dover Books on Physics. Dover Publications, 2012. ISBN: 9780486134697. URL: https://books.google.de/books?id=CxYCMNrUnTEC (cit. on p. 7).

[33] C. Gattringer and C.B. Lang. *Quantum Chromodynamics on the Lattice: An Introductory Presentation*. Lecture Notes in Physics. Springer Berlin Heidelberg, 2009. ISBN: 9783642018503. URL: https://books.google.de/books?id=qHhqCQAAQBAJ (cit. on pp. 7, 21, 66, 70, 82, 83, 86).

[34] H.J. Rothe. *Lattice Gauge Theories: An Introduction*. EBSCO ebook academic collection. World Scientific, 2005. ISBN: 9789812560629. URL: https://books.google.de/books?id=U1hBLG-%5C_WxAC (cit. on pp. 7, 18, 21).

[35] F. Knechtli, M. Günther, and M. Peardon. *Lattice Quantum Chromodynamics: Practical Essentials*. SpringerBriefs in Physics. Springer Netherlands, 2016. ISBN: 9789402409994. URL: https://books.google.de/books?id=JgZODQAAQBAJ (cit. on p. 7).

[36] J.I. Kapusta and C. Gale. *Finite-Temperature Field Theory: Principles and Applications*. Cambridge Monographs on Mathematical Physics. Cambridge University Press, 2006. ISBN: 9781139457620. URL: https://books.google.de/books?id=rll8dJ2iTpsC (cit. on pp. 9, 31).

[37] J. Glimm and A. Jaffe. *Quantum physics: a functional integral point of view*. Springer-Verlag, 1981. ISBN: 9780387905518. URL: https://books.google.de/books?id=RYp2vgAACAAJ (cit. on p. 10).

[38] M. Lüscher. "Construction of a selfadjoint, strictly positive transfer matrix for euclidean lattice gauge theories". In: *Comm. Math. Phys.* 54.3 (1977), pp. 283–292. URL: http://projecteuclid.org/euclid.cmp/1103900872 (cit. on p. 10).

[39] Kenneth G. Wilson. "Confinement of quarks". In: *Phys. Rev. D* 10 (8 Oct. 1974), pp. 2445–2459. DOI: 10.1103/PhysRevD.10.2445. URL: https://link.aps.org/doi/10.1103/PhysRevD.10.2445 (cit. on p. 13).

[40] C.B. Lang and H. Nicolai. "Monte Carlo simulation of SU(2) gauge theory with fermions on a four-dimensional lattice". In: *Nuclear Physics B* 200.1 (1982), pp. 135–148. ISSN: 0550-3213. DOI: http://dx.doi.org/10.1016/0550-3213(82)90063-3. URL: http://www.sciencedirect.com/science/article/pii/0550321382900633 (cit. on p. 14).

[41] Anna Hasenfratz, Z Kunszt, P Hasenfratz, and CB Lang. "Hopping parameter expansion for the meson spectrum in SU (3) lattice QCD". In: *Physics Letters B* 110.3-4 (1982), pp. 289–294 (cit. on p. 14).

[42] A. Hasenfratz, P. Hasenfratz, Z. Kunszt, and C.B. Lang. "Hopping parameter expansion for the baryons and p wave mesons". In: *Physics Letters B* 117.1 (1982), pp. 81–86. ISSN: 0370-2693. DOI: http://dx.doi.org/10.1016/0370-2693(82)90878-4. URL: http://www.sciencedirect.com/science/article/pii/0370269382908784 (cit. on p. 14).

[43] Marco Bochicchio, Luciano Maiani, Guido Martinelli, Giancarlo Rossi, and Massimo Testa. "Chiral symmetry on the lattice with Wilson fermions". In: *Nuclear Physics B* 262.2 (1985), pp. 331–355. ISSN: 0550-3213. DOI: http://dx.doi.org/10.1016/0550-3213(85)90290-1. URL: http://www.sciencedirect.com/science/article/pii/0550321385902901 (cit. on p. 14).

[44] Martin Lüscher, Stefan Sint, Rainer Sommer, and Peter Weisz. "Chiral symmetry and O(a) improvement in lattice QCD". In: *Nuclear Physics B* 478.1 (1996), pp. 365–397. ISSN: 0550-3213. DOI: http://dx.doi.org/10.1016/0550-3213(96)00378-1. URL: http://www.sciencedirect.com/science/article/pii/0550321396003781 (cit. on p. 14).

[45] H.B. Nielsen and M. Ninomiya. "A no-go theorem for regularizing chiral fermions". In: *Physics Letters B* 105.2 (1981), pp. 219–223. ISSN: 0370-2693. DOI: http://dx.doi.org/10.1016/0370-2693(81)91026-1. URL: http://www.sciencedirect.com/science/article/pii/0370269381910261 (cit. on p. 15).

[46] H.B. Nielsen and M. Ninomiya. "Absence of neutrinos on a lattice". In: *Nuclear Physics B* 185.1 (1981), pp. 20–40. ISSN: 0550-3213. DOI: http://dx.doi.org/10.1016/0550-3213(81)90361-8. URL: http://www.sciencedirect.com/science/article/pii/0550321381903618 (cit. on p. 15).

[47] H.B. Nielsen and M. Ninomiya. "Absence of neutrinos on a lattice". In: *Nuclear Physics B* 193.1 (1981), pp. 173–194. ISSN: 0550-3213. DOI: http://dx.doi.org/10.1016/0550-3213(81)90524-1. URL: http://www.sciencedirect.com/science/article/pii/0550321381905241 (cit. on p. 15).

[48] D. Friedan. "A proof of the Nielsen-Ninomiya theorem". In: *Communications in Mathematical Physics* 85.4 (1982), pp. 481–490. ISSN: 1432-0916. DOI: 10.1007/BF01403500. URL: http://dx.doi.org/10.1007/BF01403500 (cit. on p. 15).

[49] Martin Lüscher. "Exact chiral symmetry on the lattice and the Ginsparg-Wilson relation". In: *Physics Letters B* 428.3–4 (1998), pp. 342–345. ISSN: 0370-2693. DOI: http://doi.org/10.1016/S0370-2693(98)00423-7. URL: http://www.sciencedirect.com/science/article/pii/S0370269398004237 (cit. on p. 15).

[50] I. Montvay and G. Münster. *Quantum Fields on a Lattice*. Cambridge Monographs on Mathematical Physics. Cambridge University Press, 1997. ISBN: 9780521599177. URL: https://books.google.de/books?id=NHZshmEBXhcC (cit. on pp. 15, 21, 31).

[51] R. Frezzotti and G. C. Rossi. "Chirally improving Wilson fermions. 1. O(a) improvement". In: *JHEP* 08 (2004), p. 007. DOI: 10.1088/1126-6708/2004/08/007. arXiv: hep-lat/0306014 [hep-lat] (cit. on p. 15).

[52] B. Sheikholeslami and R. Wohlert. "Improved continuum limit lattice action for QCD with wilson fermions". In: *Nuclear Physics B* 259.4 (1985), pp. 572–596. ISSN: 0550-3213. DOI: https://doi.org/10.1016/0550-3213(85)90002-1. URL: http://www.sciencedirect.com/science/article/pii/0550321385900021 (cit. on p. 16).

[53] John Kogut and Leonard Susskind. “Hamiltonian formulation of Wilson’s lattice gauge theories”. In: *Phys. Rev. D* 11 (2 Jan. 1975), pp. 395–408. DOI: 10.1103/PhysRevD.11.395. URL: https://link.aps.org/doi/10.1103/PhysRevD.11.395 (cit. on p. 16).

[54] Paul H. Ginsparg and Kenneth G. Wilson. “A remnant of chiral symmetry on the lattice”. In: *Phys. Rev. D* 25 (10 May 1982), pp. 2649–2657. DOI: 10.1103/PhysRevD.25.2649. URL: https://link.aps.org/doi/10.1103/PhysRevD.25.2649 (cit. on p. 16).

[55] David B. Kaplan. “A Method for simulating chiral fermions on the lattice”. In: *Phys. Lett.* B288 (1992), pp. 342–347. DOI: 10.1016/0370-2693(92)91112-M. arXiv: hep-lat/9206013 [hep-lat] (cit. on p. 16).

[56] Herbert Neuberger. “A Practical Implementation of the Overlap Dirac Operator”. In: *Phys. Rev. Lett.* 81 (19 Nov. 1998), pp. 4060–4062. DOI: 10.1103/PhysRevLett.81.4060. URL: https://link.aps.org/doi/10.1103/PhysRevLett.81.4060 (cit. on p. 16).

[57] Yigal Shamir. “Chiral fermions from lattice boundaries”. In: *Nucl. Phys.* B406 (1993), pp. 90–106. DOI: 10.1016/0550-3213(93)90162-I. arXiv: hep-lat/9303005 [hep-lat] (cit. on p. 16).

[58] A.M. Polyakov. “Compact gauge fields and the infrared catastrophe”. In: *Physics Letters B* 59.1 (1975), pp. 82–84. ISSN: 0370-2693. DOI: http://dx.doi.org/10.1016/0370-2693(75)90162-8. URL: http://www.sciencedirect.com/science/article/pii/0370269375901628 (cit. on p. 16).

[59] T. DeGrand and C. DeTar. *Lattice Methods for Quantum Chromodynamics*. World Scientific, 2006. ISBN: 9789812773982. URL: https://books.google.de/books?id=HEhhDQAAQBAJ (cit. on p. 17).

[60] Christian Borgs and Erhard Seiler. “Lattice Yang-Mills theory at nonzero temperature and the confinement problem”. In: *Communications in Mathematical Physics* 91.3 (1983), pp. 329–380. ISSN: 1432-0916. DOI: 10.1007/BF01208780. URL: http://dx.doi.org/10.1007/BF01208780 (cit. on p. 18).

[61] Jan Smit. *Introduction to Quantum Fields on a Lattice*. Cambridge Lecture Notes in Physics. Cambridge University Press, 2002. DOI: 10.1017/CBO9780511583971 (cit. on p. 20).

[62] Owe Philipsen. “Lattice QCD at non-zero temperature and baryon density”. In: *Modern perspectives in lattice QCD: Quantum field theory and high performance computing. Proceedings, International School, 93rd Session, Les Houches, France, August 3-28, 2009*. 2010, pp. 273–330. arXiv: 1009.4089 [hep-lat]. URL: http://inspirehep.net/record/870483/files/arXiv:1009.4089.pdf (cit. on pp. 21, 70).

[63] J.B. Kogut and M.A. Stephanov. *The Phases of Quantum Chromodynamics: From Confinement to Extreme Environments*. Cambridge Monographs on Particle Physics, Nuclear Physics and Cosmology. Cambridge University Press, 2010. ISBN: 9780521143387. URL: https://books.google.it/books?id=79mjQwAACAAJ (cit. on p. 21).

[64] T. Lancaster, S.J. Blundell, and S. Blundell. *Quantum Field Theory for the Gifted Amateur*. OUP Oxford, 2014. ISBN: 9780199699322. URL: https://books.google.de/books?id=0rkVDAAAQBAJ (cit. on p. 21).

[65] Gregg Jaeger. “The Ehrenfest Classification of Phase Transitions: Introduction and Evolution”. In: *Archive for History of Exact Sciences* 53.1 (1998), pp. 51–81. ISSN: 1432-0657. DOI: 10.1007/s004070050021. URL: http://dx.doi.org/10.1007/s004070050021 (cit. on p. 22).

[66] Chen-Ning Yang and T. D. Lee. “Statistical theory of equations of state and phase transitions. 1. Theory of condensation”. In: *Phys. Rev.* 87 (1952), pp. 404–409. DOI: 10.1103/PhysRev.87.404 (cit. on pp. 23, 42).

[67] T. D. Lee and Chen-Ning Yang. “Statistical theory of equations of state and phase transitions. 2. Lattice gas and Ising model”. In: *Phys. Rev.* 87 (1952), pp. 410–419. DOI: 10.1103/PhysRev.87.410 (cit. on pp. 23, 42).

[68] K. Binder. “Finite size scaling analysis of ising model block distribution functions”. In: *Zeitschrift für Physik B Condensed Matter* 43.2 (1981), pp. 119–140. ISSN: 1431-584X. DOI: 10.1007/BF01293604. URL: http://dx.doi.org/10.1007/BF01293604 (cit. on p. 24).

[69] Kenneth G. Wilson and J. Kogut. “The renormalization group and the $\epsilon$ expansion”. In: *Physics Reports* 12.2 (1974), pp. 75–199. ISSN: 0370-1573. URL: http://www.sciencedirect.com/science/article/pii/0370157374900234 (cit. on p. 27).

[70] B. Widom. “Surface Tension and Molecular Correlations near the Critical Point”. In: *The Journal of Chemical Physics* 43.11 (1965), pp. 3892–3897. DOI: 10.1063/1.1696617. eprint: http://dx.doi.org/10.1063/1.1696617. URL: http://dx.doi.org/10.1063/1.1696617 (cit. on p. 27).

[71] F. Karsch, E. Laermann, and C. Schmidt. “The Chiral critical point in three-flavor QCD”. In: *Phys. Lett.* B520 (2001), pp. 41–49. DOI: 10.1016/S0370-2693(01)01114-5. arXiv: hep-lat/0107020 [hep-lat] (cit. on pp. 28, 54, 119).

[72] Shinji Takeda, Xiao-Yong Jin, Yoshinobu Kuramashi, Yoshifumi Nakamura, and Akira Ukawa. “Update on $N_f = 3$ finite temperature QCD phase structure with Wilson-Clover fermion action”. In: *PoS* LATTICE2016 (2017), p. 384. arXiv: 1612.05371 [hep-lat] (cit. on pp. 29, 30, 54, 119, 133, 135).

[73] H W J Blote, E Luijten, and J R Heringa. “Ising universality in three dimensions: a Monte Carlo study”. In: *Journal of Physics A: Mathematical and General* 28.22 (1995), p. 6289. URL: http://stacks.iop.org/0305-4470/28/i=22/a=007 (cit. on p. 30).

[74] S. Holtmann, J. Engels, and T. Schulze. “Specific heat and energy for the three-dimensional O(2) model”. In: *Nucl. Phys. Proc. Suppl.* 106 (2002), pp. 893–895. DOI: 10.1016/S0920-5632(01)01877-1. arXiv: hep-lat/0109013 [hep-lat] (cit. on p. 30).

[75] K. Kanaya and S. Kaya. “Critical exponents of a three dimensional O(4) spin model”. In: *Phys. Rev.* D51 (1995), pp. 2404–2410. DOI: 10.1103/PhysRevD.51.2404. arXiv: hep-lat/9409001 [hep-lat] (cit. on p. 30).

[76] Riccardo Guida and Jean Zinn-Justin. “Critical exponents of the N vector model”. In: *J. Phys.* A31 (1998), pp. 8103–8121. DOI: 10.1088/0305-4470/31/40/006. arXiv: cond-mat/9803240 [cond-mat] (cit. on p. 30).

[77] J. Engels, F. Karsch, H. Satz, and I. Montvay. "High temperature $SU(2)$ gluon matter of the lattice". In: *Physics Letters B* 101.1 (1981), pp. 89–94. ISSN: 0370-2693. DOI: http://dx.doi.org/10.1016/0370-2693(81)90497-4. URL: http://www.sciencedirect.com/science/article/pii/0370269381904974 (cit. on p. 31).

[78] J. Engels, F. Karsch, H. Satz, and I. Montvay. "Gauge field thermodynamics for the $SU(2)$ Yang-Mills system". In: *Nuclear Physics B* 205.4 (1982), pp. 545–577. ISSN: 0550-3213. DOI: http://dx.doi.org/10.1016/0550-3213(82)90077-3. URL: http://www.sciencedirect.com/science/article/pii/0550321382900773 (cit. on p. 31).

[79] Szabolcs Borsanyi et al. "High-precision scale setting in lattice QCD". In: *JHEP* 09 (2012), p. 010. DOI: 10.1007/JHEP09(2012)010. arXiv: 1203.4469 [hep-lat] (cit. on pp. 31, 105, 126).

[80] A.M. Polyakov. "Thermal properties of gauge fields and quark liberation". In: *Physics Letters B* 72.4 (1978), pp. 477–480. ISSN: 0370-2693. DOI: http://dx.doi.org/10.1016/0370-2693(78)90737-2. URL: http://www.sciencedirect.com/science/article/pii/0370269378907372 (cit. on p. 33).

[81] Leonard Susskind. "Lattice models of quark confinement at high temperature". In: *Phys. Rev. D* 20 (10 Nov. 1979), pp. 2610–2618. DOI: 10.1103/PhysRevD.20.2610. URL: https://link.aps.org/doi/10.1103/PhysRevD.20.2610 (cit. on p. 33).

[82] Benjamin Svetitsky and Laurence G. Yaffe. "Critical behavior at finite-temperature confinement transitions". In: *Nuclear Physics B* 210.4 (1982), pp. 423–447. ISSN: 0550-3213. DOI: http://dx.doi.org/10.1016/0550-3213(82)90172-9. URL: http://www.sciencedirect.com/science/article/pii/0550321382901729 (cit. on p. 34).

[83] G. 't Hooft. "A property of electric and magnetic flux in non-Abelian gauge theories". In: *Nuclear Physics B* 153 (1979), pp. 141–160. ISSN: 0550-3213. DOI: http://dx.doi.org/10.1016/0550-3213(79)90595-9. URL: http://www.sciencedirect.com/science/article/pii/0550321379905959 (cit. on p. 35).

[84] Jean Bricmont and Jürg Frölich. "An order parameter distinguishing between different phases of lattice gauge theories with matter fields". In: *Physics Letters B* 122.1 (1983), pp. 73–77. ISSN: 0370-2693. DOI: http://dx.doi.org/10.1016/0370-2693(83)91171-1. URL: http://www.sciencedirect.com/science/article/pii/0370269383911711 (cit. on p. 36).

[85] Zoltan Fodor. "QCD thermodynamics". In: *PoS* LAT2007 (2007), p. 011. arXiv: 0711.0336 [hep-lat] (cit. on p. 36).

[86] Frithjof Karsch. "Recent lattice results on finite temperature and density QCD. Part II." In: *PoS* LAT2007 (2007), p. 015. arXiv: 0711.0661 [hep-lat] (cit. on p. 36).

[87] Y. Aoki, Z. Fodor, S. D. Katz, and K. K. Szabo. "The QCD transition temperature: Results with physical masses in the continuum limit". In: *Phys. Lett.* B643 (2006), pp. 46–54. DOI: 10.1016/j.physletb.2006.10.021. arXiv: hep-lat/0609068 [hep-lat] (cit. on p. 36).

[88] P. Hasenfratz and F. Karsch. “Chemical potential on the lattice”. In: *Physics Letters B* 125.4 (1983), pp. 308–310. ISSN: 0370-2693. DOI: http://dx.doi.org/10.1016/0370-2693(83)91290-X. URL: http://www.sciencedirect.com/science/article/pii/037026938391290X (cit. on p. 38).

[89] E. P. Münger and M. A. Novotny. “Reweighting in Monte Carlo and Monte Carlo renormalization-group studies”. In: *Phys. Rev. B* 43 (7 Mar. 1991), pp. 5773–5783. DOI: 10.1103/PhysRevB.43.5773. URL: https://link.aps.org/doi/10.1103/PhysRevB.43.5773 (cit. on p. 40).

[90] Masanori Hanada, Yoshinori Matsuo, and Naoki Yamamoto. “Sign problem and phase quenching in finite-density QCD: models, holography, and lattice”. In: *Phys. Rev.* D86 (2012), p. 074510. DOI: 10.1103/PhysRevD.86.074510. arXiv: 1205.1030 [hep-lat] (cit. on p. 41).

[91] Z. Fodor and S. D. Katz. “Lattice determination of the critical point of QCD at finite T and mu”. In: *JHEP* 03 (2002), p. 014. DOI: 10.1088/1126-6708/2002/03/014. arXiv: hep-lat/0106002 [hep-lat] (cit. on pp. 41, 48).

[92] D. T. Son and Misha A. Stephanov. “QCD at finite isospin density”. In: *Phys. Rev. Lett.* 86 (2001), pp. 592–595. DOI: 10.1103/PhysRevLett.86.592. arXiv: hep-ph/0005225 [hep-ph] (cit. on p. 41).

[93] J. B. Kogut and D. K. Sinclair. “Lattice QCD at finite temperature and density in the phase-quenched approximation”. In: *Phys. Rev.* D77 (2008), p. 114503. DOI: 10.1103/PhysRevD.77.114503. arXiv: 0712.2625 [hep-lat] (cit. on p. 41).

[94] R. V. Gavai and Sourendu Gupta. “The Critical end point of QCD”. In: *Phys. Rev.* D71 (2005), p. 114014. DOI: 10.1103/PhysRevD.71.114014. arXiv: hep-lat/0412035 [hep-lat] (cit. on p. 42).

[95] E. Dagotto, A. Moreo, R. L. Sugar, and D. Toussaint. “Binding of holes in the Hubbard model”. In: *Phys. Rev. B* 41 (1 Jan. 1990), pp. 811–814. DOI: 10.1103/PhysRevB.41.811. URL: https://link.aps.org/doi/10.1103/PhysRevB.41.811 (cit. on p. 42).

[96] A. Hasenfratz and D. Toussaint. “Canonical ensembles and nonzero density quantum chromodynamics”. In: *Nuclear Physics B* 371.1 (1992), pp. 539–549. ISSN: 0550-3213. DOI: http://dx.doi.org/10.1016/0550-3213(92)90247-9. URL: http://www.sciencedirect.com/science/article/pii/0550321392902479 (cit. on p. 42).

[97] Mark Alford, Anton Kapustin, and Frank Wilczek. “Imaginary chemical potential and finite fermion density on the lattice”. In: *Phys. Rev. D* 59 (5 Jan. 1999), p. 054502. DOI: 10.1103/PhysRevD.59.054502. URL: https://link.aps.org/doi/10.1103/PhysRevD.59.054502 (cit. on p. 43).

[98] Slavo Kratochvila and Philippe de Forcrand. “The Canonical approach to finite density QCD”. In: *PoS* LAT2005 (2006), p. 167. arXiv: hep-lat/0509143 [hep-lat] (cit. on p. 43).

[99] Andrei Alexandru, Manfried Faber, Ivan Horvath, and Keh-Fei Liu. “Lattice QCD at finite density via a new canonical approach”. In: *Phys. Rev.* D72 (2005), p. 114513. DOI: 10.1103/PhysRevD.72.114513. arXiv: hep-lat/0507020 [hep-lat] (cit. on p. 43).

[100] K. Fukushima. “Phase diagram from PNJL models”. In: *PoS* CPOD 2009 (2009), p. 016 (cit. on p. 43).

[101] Wolfram Weise. “Chiral symmetry in strongly interacting matter: From Nuclear Matter to Phases of QCD”. In: *Prog. Theor. Phys. Suppl.* 186 (2010), pp. 390–403. DOI: 10.1143/PTPS.186.390. arXiv: 1009.6201 [nucl-th] (cit. on p. 43).

[102] Bernd-Jochen Schaefer. “Fluctuations and the QCD Phase Diagram”. In: *Phys. Atom. Nucl.* 75 (2012), pp. 741–743. DOI: 10.1134/S1063778812060270. arXiv: 1102.2772 [hep-ph] (cit. on p. 43).

[103] Michael Fromm, Jens Langelage, Stefano Lottini, and Owe Philipsen. “The QCD deconfinement transition for heavy quarks and all baryon chemical potentials”. In: *JHEP* 01 (2012), p. 042. DOI: 10.1007/JHEP01(2012)042. arXiv: 1111.4953 [hep-lat] (cit. on pp. 43, 53, 54, 61, 62).

[104] Jan Lucker and Christian S. Fischer. “Two-flavor QCD at finite temperature and chemical potential in a functional approach”. In: *Prog. Part. Nucl. Phys.* 67 (2012), pp. 200–205. DOI: 10.1016/j.ppnp.2011.12.018. arXiv: 1111.0180 [hep-ph] (cit. on p. 43).

[105] Lisa M. Haas, Jens Braun, and Jan M. Pawlowski. “On the QCD phase diagram at finite chemical potential”. In: *AIP Conf. Proc.* 1343 (2011), pp. 459–461. DOI: 10.1063/1.3575061. arXiv: 1012.4735 [hep-ph] (cit. on p. 43).

[106] André Roberge and Nathan Weiss. “Gauge theories with imaginary chemical potential and the phases of QCD”. In: *Nuclear Physics B* 275.4 (1986), pp. 734–745. ISSN: 0550-3213. DOI: http://dx.doi.org/10.1016/0550-3213(86)90582-1. URL: http://www.sciencedirect.com/science/article/pii/0550321386905821 (cit. on p. 44).

[107] S. Hands. “The phase diagram of QCD”. In: *Contemporary Physics* 42 (Apr. 2001), pp. 209–225. DOI: 10.1080/00107510110063843. eprint: physics/0105022 (cit. on p. 47).

[108] Z. Fodor and S. D. Katz. “Critical point of QCD at finite T and mu, lattice results for physical quark masses”. In: *JHEP* 04 (2004), p. 050. DOI: 10.1088/1126-6708/2004/04/050. arXiv: hep-lat/0402006 [hep-lat] (cit. on p. 48).

[109] O. Kaczmarek, F. Karsch, E. Laermann, C. Miao, S. Mukherjee, P. Petreczky, C. Schmidt, W. Soeldner, and W. Unger. “Phase boundary for the chiral transition in (2+1) -flavor QCD at small values of the chemical potential”. In: *Phys. Rev.* D83 (2011), p. 014504. DOI: 10.1103/PhysRevD.83.014504. arXiv: 1011.3130 [hep-lat] (cit. on p. 48).

[110] G. Endrodi, Z. Fodor, S. D. Katz, and K. K. Szabo. “The QCD phase diagram at nonzero quark density”. In: *JHEP* 04 (2011), p. 001. DOI: 10.1007/JHEP04(2011)001. arXiv: 1102.1356 [hep-lat] (cit. on p. 48).

[111] Claudio Bonati, Massimo D’Elia, Marco Mariti, Michele Mesiti, Francesco Negro, and Francesco Sanfilippo. “Curvature of the chiral pseudocritical line in QCD”. In: *Phys. Rev.* D90.11 (2014), p. 114025. DOI: 10.1103/PhysRevD.90.114025. arXiv: 1410.5758 [hep-lat] (cit. on p. 48).

[112] Paolo Cea, Leonardo Cosmai, and Alessandro Papa. "Critical line of 2+1 flavor QCD: Toward the continuum limit". In: *Phys. Rev.* D93.1 (2016), p. 014507. DOI: 10.1103/PhysRevD.93.014507. arXiv: 1508.07599 [hep-lat] (cit. on p. 48).

[113] R. Bellwied, S. Borsanyi, Z. Fodor, J. Günther, S. D. Katz, C. Ratti, and K. K. Szabo. "The QCD phase diagram from analytic continuation". In: *Phys. Lett.* B751 (2015), pp. 559–564. DOI: 10.1016/j.physletb.2015.11.011. arXiv: 1507.07510 [hep-lat] (cit. on p. 48).

[114] Marco Cristoforetti, Francesco Di Renzo, and Luigi Scorzato. "New approach to the sign problem in quantum field theories: High density QCD on a Lefschetz thimble". In: *Phys. Rev.* D86 (2012), p. 074506. DOI: 10.1103/PhysRevD.86.074506. arXiv: 1205.3996 [hep-lat] (cit. on p. 48).

[115] Luigi Scorzato. "The Lefschetz thimble and the sign problem". In: *PoS* LATTICE2015 (2016), p. 016. arXiv: 1512.08039 [hep-lat] (cit. on p. 48).

[116] Gert Aarts, Erhard Seiler, and Ion-Olimpiu Stamatescu. "The Complex Langevin method: When can it be trusted?" In: *Phys. Rev.* D81 (2010), p. 054508. DOI: 10.1103/PhysRevD.81.054508. arXiv: 0912.3360 [hep-lat] (cit. on p. 48).

[117] Gert Aarts, Erhard Seiler, Denes Sexty, and Ion-Olimpiu Stamatescu. "Complex Langevin dynamics and zeroes of the fermion determinant". In: (2017). arXiv: 1701.02322 [hep-lat] (cit. on p. 48).

[118] Kurt Langfeld, Biagio Lucini, and Antonio Rago. "The density of states in gauge theories". In: *Phys. Rev. Lett.* 109 (2012), p. 111601. DOI: 10.1103/PhysRevLett.109.111601. arXiv: 1204.3243 [hep-lat] (cit. on p. 48).

[119] Kurt Langfeld. "Density-of-states". In: *Proceedings, 34th International Symposium on Lattice Field Theory (Lattice 2016): Southampton, UK, July 24-30, 2016*. 2016. arXiv: 1610.09856 [hep-lat]. URL: https://inspirehep.net/record/1495254/files/arXiv:1610.09856.pdf (cit. on p. 48).

[120] Atsushi Nakamura, Shotaro Oka, and Yusuke Taniguchi. "QCD phase transition at real chemical potential with canonical approach". In: *JHEP* 02 (2016), p. 054. DOI: 10.1007/JHEP02(2016)054. arXiv: 1504.04471 [hep-lat] (cit. on p. 48).

[121] V. G. Bornyakov, D. L. Boyda, V. A. Goy, A. V. Molochkov, Atsushi Nakamura, A. A. Nikolaev, and V. I. Zakharov. "New approach to canonical partition functions computation in $N_f = 2$ lattice QCD at finite baryon density". In: (2016). arXiv: 1611.04229 [hep-lat] (cit. on p. 48).

[122] Mark G. Alford. "Color superconducting quark matter". In: *Ann. Rev. Nucl. Part. Sci.* 51 (2001), pp. 131–160. DOI: 10.1146/annurev.nucl.51.101701.132449. arXiv: hep-ph/0102047 [hep-ph] (cit. on p. 48).

[123] Y. Iwasaki, K. Kanaya, S. Kaya, S. Sakai, and T. Yoshié. "Finite temperature transitions in lattice QCD with Wilson quarks: Chiral transitions and the influence of the strange quark". In: *Phys. Rev. D* 54 (11 Dec. 1996), pp. 7010–7031. DOI: 10.1103/PhysRevD.54.7010. URL: https://link.aps.org/doi/10.1103/PhysRevD.54.7010 (cit. on p. 48).

[124] Roberto De Pietri, Alessandra Feo, Erhard Seiler, and Ion-Olimpiu Stamatescu. "A Model for QCD at high density and large quark mass". In: *Phys. Rev.* D76 (2007), p. 114501. DOI: 10.1103/PhysRevD.76.114501. arXiv: 0705.3420 [hep-lat] (cit. on pp. 53, 54).

[125] H. Saito, S. Ejiri, S. Aoki, T. Hatsuda, K. Kanaya, Y. Maezawa, H. Ohno, and T. Umeda. "Phase structure of finite temperature QCD in the heavy quark region". In: *Phys. Rev.* D84 (2011). [Erratum: Phys. Rev.D85,079902(2012)], p. 054502. DOI: 10.1103/PhysRevD.85.079902, 10.1103/PhysRevD.84.054502. arXiv: 1106.0974 [hep-lat] (cit. on pp. 53, 54, 115, 121, 123).

[126] H. Saito, S. Ejiri, S. Aoki, K. Kanaya, Y. Nakagawa, H. Ohno, K. Okuno, and T. Umeda. "Histograms in heavy-quark QCD at finite temperature and density". In: *Phys. Rev.* D89.3 (2014), p. 034507. DOI: 10.1103/PhysRevD.89.034507. arXiv: 1309.2445 [hep-lat] (cit. on pp. 53, 61, 70).

[127] Robert D. Pisarski and Frank Wilczek. "Remarks on the chiral phase transition in chromodynamics". In: *Phys. Rev. D* 29 (2 Jan. 1984), pp. 338–341. DOI: 10.1103/PhysRevD.29.338. URL: http://link.aps.org/doi/10.1103/PhysRevD.29.338 (cit. on pp. 54, 55).

[128] Norman H. Christ and Xiaodong Liao. "Locating the 3-flavor critical point using staggered fermions". In: *Nuclear Physics B - Proceedings Supplements* 119 (2003). Proceedings of the XXth International Symposium on Lattice Field Theory, pp. 514–516. ISSN: 0920-5632. DOI: http://dx.doi.org/10.1016/S0920-5632(03)01600-1. URL: http://www.sciencedirect.com/science/article/pii/S0920563203016001 (cit. on p. 54).

[129] P. de Forcrand and O. Philipsen. "The Phase diagram of N(f) = 3 QCD for small baryon densities". In: *Nucl. Phys. Proc. Suppl.* 129 (2004). [,521(2003)], pp. 521–523. DOI: 10.1016/S0920-5632(03)02628-8. arXiv: hep-lat/0309109 [hep-lat] (cit. on p. 54).

[130] Philippe de Forcrand, Seyong Kim, and Owe Philipsen. "A QCD chiral critical point at small chemical potential: Is it there or not?" In: *PoS* LAT2007 (2007), p. 178. arXiv: 0711.0262 [hep-lat] (cit. on p. 54).

[131] Dominik Smith and Christian Schmidt. "On the universal critical behavior in 3-flavor QCD". In: *PoS* LATTICE2011 (2011), p. 216. arXiv: 1109.6729 [hep-lat] (cit. on p. 54).

[132] C. Schmidt, C. R. Allton, S. Ejiri, S. J. Hands, O. Kaczmarek, F. Karsch, and E. Laermann. "The Quark mass and mu dependence of the QCD chiral critical point". In: *Nucl. Phys. Proc. Suppl.* 119 (2003). [,517(2002)], pp. 517–519. DOI: 10.1016/S0920-5632(03)01601-3. arXiv: hep-lat/0209009 [hep-lat] (cit. on p. 54).

[133] F. Karsch, C. R. Allton, S. Ejiri, S. J. Hands, O. Kaczmarek, E. Laermann, and C. Schmidt. "Where is the chiral critical point in three flavor QCD?" In: *Nucl. Phys. Proc. Suppl.* 129 (2004). [,614(2003)], pp. 614–616. DOI: 10.1016/S0920-5632(03)02659-8. arXiv: hep-lat/0309116 [hep-lat] (cit. on p. 54).

[134] C. Bernard, T. Burch, E. B. Gregory, D. Toussaint, Carleton E. DeTar, J. Osborn, Steven Gottlieb, U. M. Heller, and R. Sugar. "QCD thermodynamics with three flavors of improved staggered quarks". In: *Phys. Rev.* D71 (2005), p. 034504. DOI: 10.1103/PhysRevD.71.034504. arXiv: hep-lat/0405029 [hep-lat] (cit. on p. 54).

[135] Xiao-Yong Jin, Yoshinobu Kuramashi, Yoshifumi Nakamura, Shinji Takeda, and Akira Ukawa. "Critical endpoint of the finite temperature phase transition for three flavor QCD". In: *Phys. Rev.* D91.1 (2015), p. 014508. DOI: 10.1103/PhysRevD.91.014508. arXiv: 1411.7461 [hep-lat] (cit. on pp. 54, 127).

[136] Heng-Tong Ding. "Lattice QCD at nonzero temperature and density". In: *PoS* LATTICE2016 (2017), p. 022. arXiv: 1702.00151 [hep-lat] (cit. on pp. 54, 55).

[137] A. Bazavov, H. -T. Ding, P. Hegde, F. Karsch, E. Laermann, Swagato Mukherjee, P. Petreczky, and C. Schmidt. "Chiral phase structure of three flavor QCD at vanishing baryon number density". In: *Phys. Rev.* D95.7 (2017), p. 074505. DOI: 10.1103/PhysRevD.95.074505. arXiv: 1701.03548 [hep-lat] (cit. on p. 54).

[138] Andrea Pelissetto and Ettore Vicari. "Relevance of the axial anomaly at the finite-temperature chiral transition in QCD". In: *Phys. Rev.* D88.10 (2013), p. 105018. DOI: 10.1103/PhysRevD.88.105018. arXiv: 1309.5446 [hep-lat] (cit. on p. 55).

[139] Mara Grahl and Dirk H. Rischke. "Functional renormalization group study of the two-flavor linear sigma model in the presence of the axial anomaly". In: *Phys. Rev.* D88.5 (2013), p. 056014. DOI: 10.1103/PhysRevD.88.056014. arXiv: 1307.2184 [hep-th] (cit. on p. 55).

[140] Shailesh Chandrasekharan and Abhijit C. Mehta. "Effects of the Anomaly on the Two-Flavor QCD Chiral Phase Transition". In: *Phys. Rev. Lett.* 99 (14 Oct. 2007), p. 142004. DOI: 10.1103/PhysRevLett.99.142004. URL: https://link.aps.org/doi/10.1103/PhysRevLett.99.142004 (cit. on p. 55).

[141] I. D. Lawrie, ed. C. Domb Sarbach, and J. L. Lebowitz. *Phase transitions and critical phenomena, Volume 9*. Academic Press, London, 1984 (cit. on p. 55).

[142] Sheng-Tai Li and Heng-Tong Ding. "Chiral phase transition of (2 + 1)-flavor QCD on $N_\tau = 6$ lattices". In: *PoS* LATTICE2016 (2017), p. 372. arXiv: 1702.01294 [hep-lat] (cit. on p. 55).

[143] T. Umeda, S. Ejiri, R. Iwami, K. Kanaya, H. Ohno, A. Uji, N. Wakabayashi, and S. Yoshida. "O(4) scaling analysis in two-flavor QCD at finite temperature and density with improved Wilson quarks". In: *PoS* LATTICE2016 (2017), p. 376. arXiv: 1612.09449 [hep-lat] (cit. on pp. 55, 56).

[144] Claudio Bonati, Philippe de Forcrand, Massimo D'Elia, Owe Philipsen, and Francesco Sanfilippo. "The Chiral phase transition in two-flavor QCD from an imaginary chemical potential". In: *Phys. Rev.* D90.7 (2014), p. 074030. DOI: 10.1103/PhysRevD.90.074030. arXiv: 1408.5086 [hep-lat] (cit. on pp. 55, 56, 62, 63).

[145] Owe Philipsen and Christopher Pinke. "The $N_f = 2$ QCD chiral phase transition with Wilson fermions at zero and imaginary chemical potential". In: *Phys. Rev.* D93.11 (2016), p. 114507. DOI: 10.1103/PhysRevD.93.114507. arXiv: 1602.06129 [hep-lat] (cit. on pp. 55, 56, 62, 63).

[146] Y. Iwasaki, K. Kanaya, S. Kaya, and T. Yoshie. "Scaling of chiral order parameter in two flavor QCD". In: *Phys. Rev. Lett.* 78 (1997), pp. 179–182. DOI: 10.1103/PhysRevLett.78.179. arXiv: hep-lat/9609022 [hep-lat] (cit. on p. 56).

[147] Agostino Butti, Andrea Pelissetto, and Ettore Vicari. "On the nature of the finite temperature transition inQCD". In: *JHEP* 08 (2003), p. 029. DOI: 10.1088/1126-6708/2003/08/029. arXiv: hep-ph/0307036 [hep-ph] (cit. on p. 56).

[148] J. B. Kogut and D. K. Sinclair. "Evidence for O(2) universality at the finite temperature transition for lattice QCD with 2 flavors of massless staggered quarks". In: *Phys. Rev.* D73 (2006), p. 074512. DOI: 10.1103/PhysRevD.73.074512. arXiv: hep-lat/0603021 [hep-lat] (cit. on p. 56).

[149] Philippe de Forcrand and Owe Philipsen. "The Chiral critical line of N(f) = 2+1 QCD at zero and non-zero baryon density". In: *JHEP* 01 (2007), p. 077. DOI: 10.1088/1126-6708/2007/01/077. arXiv: hep-lat/0607017 [hep-lat] (cit. on pp. 56, 61).

[150] Massimo D'Elia, Adriano Di Giacomo, and Claudio Pica. "Two flavor QCD and confinement". In: *Phys. Rev.* D72 (2005), p. 114510. DOI: 10.1103/PhysRevD.72.114510. arXiv: hep-lat/0503030 [hep-lat]; Guido Cossu, Massimo D'Elia, Adriano Di Giacomo, and Claudio Pica. "Two flavor QCD and confinement. II." In: (2007). arXiv: 0706.4470 [hep-lat]; Cuido Bonati, Guido Cossu, Massimo D'Elia, Adriano Di Giacomo, and Claudio Pica. "A Test of first order scaling in Nf =2 QCD: A Progress report". In: *PoS* LATTICE2008 (2008), p. 204. arXiv: 0901.3231 [hep-lat]. Cit. on p. 56.

[151] S. Ejiri, F. Karsch, E. Laermann, C. Miao, S. Mukherjee, P. Petreczky, C. Schmidt, W. Soeldner, and W. Unger. "On the magnetic equation of state in (2+1)-flavor QCD". In: *Phys. Rev.* D80 (2009), p. 094505. DOI: 10.1103/PhysRevD.80.094505. arXiv: 0909.5122 [hep-lat] (cit. on p. 56).

[152] Guido Cossu, Sinya Aoki, Hidenori Fukaya, Shoji Hashimoto, Takashi Kaneko, Hideo Matsufuru, and Jun-Ichi Noaki. "Finite temperature study of the axial U(1) symmetry on the lattice with overlap fermion formulation". In: *Phys. Rev.* D87.11 (2013). [Erratum: Phys. Rev.D88,no.1,019901(2013)], p. 114514. DOI: 10.1103/PhysRevD.88.019901,10.1103/PhysRevD.87.114514. arXiv: 1304.6145 [hep-lat] (cit. on p. 56).

[153] Francesca Cuteri, Owe Philipsen, and Alessandro Sciarra. "The QCD chiral phase transition from non-integer numbers of flavors". In: (2017). arXiv: 1711.05658 [hep-lat] (cit. on p. 56).

[154] F. Cuteri, P. Philipsen, and A. Sciarra. "Updates on the Columbia plot and its extended/alternative versions". 35th International Symposium on Lattice Field Theory. 2017. URL: https://makondo.ugr.es/event/0/session/91/contribution/241/material/slides/0.pdf (cit. on p. 57).

[155] Philippe de Forcrand and Owe Philipsen. "The Chiral critical point of N(f) = 3 QCD at finite density to the order (mu/T)^ 4". In: *JHEP* 11 (2008), p. 012. DOI: 10.1088/1126-6708/2008/11/012. arXiv: 0808.1096 [hep-lat] (cit. on pp. 61, 64).

[156] Philippe de Forcrand and Owe Philipsen. "Constraining the QCD phase diagram by tricritical lines at imaginary chemical potential". In: *Phys. Rev. Lett.* 105 (2010), p. 152001. DOI: 10.1103/PhysRevLett.105.152001. arXiv: 1004.3144 [hep-lat] (cit. on pp. 62, 126).

[157] Florian Burger, Ernst-Michael Ilgenfritz, Malik Kirchner, Maria Paola Lombardo, Michael Müller-Preussker, Owe Philipsen, Carsten Urbach, and Lars Zeidlewicz. "Thermal QCD transition with two flavors of twisted mass fermions". In: *Phys. Rev.* D87.7 (2013), p. 074508. DOI: 10.1103/PhysRevD.87.074508. arXiv: 1102.4530 [hep-lat] (cit. on pp. 62, 63).

[158] Bastian B. Brandt, Anthony Francis, Harvey B. Meyer, and Daniel Robaina. "Chiral dynamics in the low-temperature phase of QCD". In: *PoS* LATTICE2014 (2015), p. 234. arXiv: 1410.5981 [hep-lat] (cit. on pp. 62, 63).

[159] Christopher Czaban, Francesca Cuteri, Owe Philipsen, Christopher Pinke, and Alessandro Sciarra. "Roberge-Weiss transition in $N_{\mathrm{f}} = 2$ QCD with Wilson fermions and $N_\tau = 6$". In: *Phys. Rev.* D93.5 (2016), p. 054507. DOI: 10.1103/PhysRevD.93.054507. arXiv: 1512.07180 [hep-lat] (cit. on pp. 62, 63, 96, 105, 119, 123–128, 133, 144).

[160] M.E.J. Newman and G.T. Barkema. *Monte Carlo Methods in Statistical Physics*. Clarendon Press, 1999. ISBN: 9780198517979. URL: https://books.google.de/books?id=J5aLdDN4uFwC (cit. on pp. 66, 70, 72, 73, 75, 83).

[161] B.A. Berg. *Markov Chain Monte Carlo Simulations and Their Statistical Analysis: With Web-based Fortran Code*. World Scientific, 2004. ISBN: 9789812389350. URL: https://books.google.de/books?id=ZAX-wg0WjDoC (cit. on p. 66).

[162] Ulli Wolff. "Monte Carlo errors with less errors". In: *Comput. Phys. Commun.* 156 (2004). [Erratum: Comput. Phys. Commun.176,383(2007)], pp. 143–153. DOI: 10.1016/S0010-4655(03)00467-3,10.1016/j.cpc.2006.12.001. arXiv: hep-lat/0306017 [hep-lat] (cit. on pp. 66, 68, 69, 106, 144).

[163] Alan M. Ferrenberg and Robert H. Swendsen. "New Monte Carlo technique for studying phase transitions". In: *Phys. Rev. Lett.* 61 (23 Dec. 1988), pp. 2635–2638. DOI: 10.1103/PhysRevLett.61.2635. URL: http://link.aps.org/doi/10.1103/PhysRevLett.61.2635 (cit. on p. 72).

[164] Alan M. Ferrenberg and Robert H. Swendsen. "Optimized Monte Carlo data analysis". In: *Phys. Rev. Lett.* 63 (12 Sept. 1989), pp. 1195–1198. DOI: 10.1103/PhysRevLett.63.1195. URL: http://link.aps.org/doi/10.1103/PhysRevLett.63.1195 (cit. on p. 73).

[165] W.H. Press, B.P. Flannery, S.A. Teukolsky, and W.T. Vetterling. *Numerical Recipes Example Book (Pascal)*. Cambridge University Press, 1989. ISBN: 9780521376754. URL: https://books.google.de/books?id=yyazAQAACAAJ (cit. on p. 79).

[166] Simon Duane, A.D. Kennedy, Brian J. Pendleton, and Duncan Roweth. “Hybrid Monte Carlo”. In: *Physics Letters B* 195.2 (1987), pp. 216–222. ISSN: 0370-2693. DOI: http://dx.doi.org/10.1016/0370-2693(87)91197-X. URL: http://www.sciencedirect.com/science/article/pii/037026938791197X (cit. on p. 81).

[167] M. A. Clark. “The Rational Hybrid Monte Carlo Algorithm”. In: *PoS* LAT2006 (2006), p. 004. arXiv: hep-lat/0610048 [hep-lat] (cit. on pp. 81, 83).

[168] M. A. Clark and A. D. Kennedy. “Accelerating dynamical fermion computations using the rational hybrid Monte Carlo (RHMC) algorithm with multiple pseudofermion fields”. In: *Phys. Rev. Lett.* 98 (2007), p. 051601. DOI: 10.1103/PhysRevLett.98.051601. arXiv: hep-lat/0608015 [hep-lat] (cit. on pp. 81, 133).

[169] Jonathan Richard Shewchuk. “An introduction to the conjugate gradient method without the agonizing pain”. In: (1994) (cit. on p. 83).

[170] Martin Hasenbusch. “Speeding up the hybrid Monte Carlo algorithm for dynamical fermions”. In: *Phys. Lett.* B519 (2001), pp. 177–182. DOI: 10.1016/S0370-2693(01)01102-9. arXiv: hep-lat/0107019 [hep-lat] (cit. on pp. 83, 123).

[171] J. C. Sexon and D. H. Weingarten. In: *Nucl. Phys.* B380 (1992) (cit. on p. 83).

[172] A. Ali Khan, T. Bakeyev, M. Gockeler, R. Horsley, D. Pleiter, Paul E. L. Rakow, A. Schafer, G. Schierholz, and H. Stuben. “Accelerating the hybrid Monte Carlo algorithm”. In: *Phys. Lett.* B564 (2003), pp. 235–240. DOI: 10.1016/S0370-2693(03)00703-2. arXiv: hep-lat/0303026 [hep-lat] (cit. on p. 83).

[173] C. Urbach, K. Jansen, A. Shindler, and U. Wenger. “HMC algorithm with multiple time scale integration and mass preconditioning”. In: *Comput. Phys. Commun.* 174 (2006), pp. 87–98. DOI: 10.1016/j.cpc.2005.08.006. arXiv: hep-lat/0506011 [hep-lat] (cit. on p. 83).

[174] M. A. Clark, Ph. de Forcrand, and A. D. Kennedy. “Algorithm shootout: R versus RHMC”. In: *PoS* LAT2005 (2006), p. 115. arXiv: hep-lat/0510004 [hep-lat] (cit. on p. 83).

[175] E. Y. Remez. In: *US Atomic Energy Commision* (1962) (cit. on p. 83).

[176] A. D. Kennedy. “Algorithms for dynamical fermions”. In: (2006). arXiv: hep-lat/0607038 [hep-lat] (cit. on p. 84).

[177] Andreas Frommer, Bertold Nockel, Stephan Gusken, Thomas Lippert, and Klaus Schilling. “Many masses on one stroke: Economic computation of quark propagators”. In: *Int. J. Mod. Phys.* C6 (1995), pp. 627–638. DOI: 10.1142/S0129183195000538. arXiv: hep-lat/9504020 [hep-lat] (cit. on p. 84).

[178] Y. Saad. *Numerical Methods for Large Eigenvalue Problems*. Society for Industrial and Applied Mathematics, 2011. DOI: 10.1137/1.9781611970739. eprint: http://epubs.siam.org/doi/pdf/10.1137/1.9781611970739. URL: http://epubs.siam.org/doi/abs/10.1137/1.9781611970739 (cit. on pp. 87, 88).

[179] M. Clark. “Rational hybrid Monte Carlo algorithm”. dissertation. The University of Edinburgh, 2005. URL: https://www.era.lib.ed.ac.uk/handle/1842/13416 (cit. on p. 88).

[180] Tetsuya Takaishi and Philippe de Forcrand. “Odd flavor hybrid Monte Carlo algorithm for lattice QCD”. In: *Int. J. Mod. Phys.* C13 (2002), pp. 343–366. DOI: 10.1142/S0129183102003152. arXiv: hep-lat/0108012 [hep-lat] (cit. on p. 88).

[181] Owe Philipsen, Christopher Pinke, Christian Schafer, Lars Zeidlewicz, and Matthias Bach. “LatticeQCD using OpenCL”. In: *PoS* LATTICE2011 (2011), p. 044. arXiv: 1112.5280 [hep-lat] (cit. on p. 88).

[182] Owe Philipsen, Christopher Pinke, Alessandro Sciarra, and Matthias Bach. “CL$^2$QCD - Lattice QCD based on OpenCL”. In: *PoS* LATTICE2014 (2014), p. 038. arXiv: 1411.5219 [hep-lat] (cit. on pp. 88, 97).

[183] *CL$^2$QCD - Lattice QCD based on OpenCL*. URL: https://github.com/AG-Philipsen/cl2qcd (cit. on pp. 88, 97).

[184] Matthias Bach, Volker Lindenstruth, Owe Philipsen, and Christopher Pinke. “Lattice QCD based on OpenCL”. In: *Comput. Phys. Commun.* 184 (2013), pp. 2042–2052. DOI: 10.1016/j.cpc.2013.03.020. arXiv: 1209.5942 [hep-lat] (cit. on pp. 89, 97).

[185] Martin Luscher. “A Portable high quality random number generator for lattice field theory simulations”. In: *Comput. Phys. Commun.* 79 (1994), pp. 100–110. DOI: 10.1016/0010-4655(94)90232-1. arXiv: hep-lat/9309020 [hep-lat] (cit. on p. 89).

[186] URL: http://www.boost.org (cit. on p. 89).

[187] K. Beck. *Test-driven Development: By Example*. Kent Beck signature book. Addison-Wesley, 2003. ISBN: 9780321146533. URL: https://books.google.de/books?id=CUlsAQAAQBAJ (cit. on p. 89).

[188] R.C. Martin. *Clean Code: A Handbook of Agile Software Craftsmanship*. Robert C. Martin Series. Pearson Education, 2008. ISBN: 9780136083252. URL: https://books.google.de/books?id=%5C_i6bDeoCQzsC (cit. on p. 89).

[189] A. Sciarra. *BaHaMAS: A Bash Handler to Monitor and Administrate Simulations*. June 2017. URL: https://makondo.ugr.es/event/0/session/102/contribution/230 (cit. on p. 92).

[190] A. Sciarra. “The QCD phase diagram at purely imaginary chemical potential from the lattice”. dissertation. Goethe University Frankfurt, 2016. URL: https://github.com/AxelKrypton/PhD_Thesis (cit. on pp. 92, 125, 133).

[191] A. Sciarra. *BaHaMAS*. https://github.com/AG-Philipsen/BaHaMAS. 2017 (cit. on p. 92).

[192] Matthias Bach, Matthias Kretz, Volker Lindenstruth, and David Rohr. “Optimized HPL for AMD GPU and multi-core CPU usage”. In: *Computer Science - Research and Development* 26.3 (Apr. 2011), p. 153. ISSN: 1865-2042. DOI: 10.1007/s00450-011-0161-5. URL: https://doi.org/10.1007/s00450-011-0161-5 (cit. on p. 97).

[193] David Rohr, Matthias Bach, Gvozden Nešković, Volker Lindenstruth, Christopher Pinke, and Owe Philipsen. "Lattice-CSC: Optimizing and Building an Efficient Supercomputer for Lattice-QCD and to Achieve First Place in Green500". In: *High Performance Computing: 30th International Conference, ISC High Performance 2015, Frankfurt, Germany, July 12-16, 2015, Proceedings*. Ed. by Julian M. Kunkel and Thomas Ludwig. Cham: Springer International Publishing, 2015, pp. 179–196. ISBN: 978-3-319-20119-1. DOI: 10.1007/978-3-319-20119-1_14. URL: https://doi.org/10.1007/978-3-319-20119-1_14 (cit. on p. 97).

[194] A. Billoire, R. Lacaze, and A. Morel. "A numerical study of finite-size scaling for first-order phase transitions". In: *Nuclear Physics B* 370.3 (1992), pp. 773–796. ISSN: 0550-3213. DOI: http://dx.doi.org/10.1016/0550-3213(92)90431-A. URL: http://www.sciencedirect.com/science/article/pii/055032139290431A (cit. on p. 100).

[195] Frederik Depta. "Pion and Quark Masses Along the Chiral Critical Line in the $N_f = 2$ QCD Phase Diagram". 2015. URL: http://th.physik.uni-frankfurt.de/~philipsen/theses/depta_ba.pdf (cit. on p. 105).

[196] Owe Philipsen and Christopher Pinke. "The Nature of the Roberge-Weiss transition in $N_f = 2$ QCD with Wilson fermions". In: *Phys. Rev.* D89.9 (2014), p. 094504. DOI: 10.1103/PhysRevD.89.094504. arXiv: 1402.0838 [hep-lat] (cit. on pp. 105, 125, 126).

[197] Aida X. El-Khadra, Andreas S. Kronfeld, and Paul B. Mackenzie. "Massive fermions in lattice gauge theory". In: *Phys. Rev.* D55 (1997), pp. 3933–3957. DOI: 10.1103/PhysRevD.55.3933. arXiv: hep-lat/9604004 [hep-lat] (cit. on p. 106).

[198] A. Ali Khan, V. Braun, T. Burch, M Gockeler, G. Lacagnina, A. Schafer, and G. Schierholz. "Decay constants of charm and beauty pseudoscalar heavy-light mesons on fine lattices". In: *Phys. Lett.* B652 (2007), pp. 150–157. DOI: 10.1016/j.physletb.2007.06.066. arXiv: hep-lat/0701015 [hep-lat] (cit. on p. 106).

[199] Balint Joo, Brian Pendleton, Anthony D. Kennedy, Alan C. Irving, James C. Sexton, Stephen M. Pickles, and Stephen P. Booth. "Instability in the molecular dynamics step of hybrid Monte Carlo in dynamical Fermion lattice QCD simulations". In: *Phys. Rev.* D62 (2000), p. 114501. DOI: 10.1103/PhysRevD.62.114501. arXiv: hep-lat/0005023 [hep-lat] (cit. on p. 123).

[200] Claudio Bonati, Guido Cossu, Massimo D'Elia, and Francesco Sanfilippo. "The Roberge-Weiss endpoint in $N_f = 2$ QCD". In: *Phys. Rev.* D83 (2011), p. 054505. DOI: 10.1103/PhysRevD.83.054505. arXiv: 1011.4515 [hep-lat] (cit. on pp. 127, 128).

[201] Owe Philipsen. "The QCD equation of state from the lattice". In: *Prog. Part. Nucl. Phys.* 70 (2013), pp. 55–107. DOI: 10.1016/j.ppnp.2012.09.003. arXiv: 1207.5999 [hep-lat] (cit. on p. 127).

[202] Martin Luscher. "Deflation acceleration of lattice QCD simulations". In: *JHEP* 12 (2007), p. 011. DOI: 10.1088/1126-6708/2007/12/011. arXiv: 0710.5417 [hep-lat] (cit. on p. 133).

[203] J. Brannick, R. C. Brower, M. A. Clark, J. C. Osborn, and C. Rebbi. “Adaptive Multigrid Algorithm for Lattice QCD”. In: *Phys. Rev. Lett.* 100 (2008), p. 041601. DOI: 10.1103/PhysRevLett.100.041601. arXiv: 0707.4018 [hep-lat] (cit. on p. 134).

[204] C. Urbach. “Wilson Twisted Mass Fermions: Towards Realistic Simulations of Lattice-QCD”. dissertation. Freie Universität Berlin, 2006. URL: http://edocs.fu-berlin.de/diss/receive/FUDISS_thesis_000000001941 (cit. on p. 137).